

# **Investigations of the EPR Parameters of Bioradicals by Density Functional Methods**

**DISSERTATION**

zur Erlangung des naturwissenschaftlichen Doktorgrades  
der Bayerischen Julius-Maximilians-Universität Würzburg

vorgelegt von  
Sylwia Kacprzak  
aus Puławy, Polen

Würzburg 2006



# **Investigations of the EPR Parameters of Bioradicals by Density Functional Methods**

**DISSERTATION**

zur Erlangung des naturwissenschaftlichen Doktorgrades  
der Bayerischen Julius-Maximilians-Universität Würzburg

vorgelegt von  
Sylwia Kacprzak  
aus Puławy, Polen

Würzburg 2006

Eingereicht am: \_\_\_\_\_

bei der Fakultät für Chemie und Pharmazie

1. Gutachter: \_\_\_\_\_

2. Gutachter: \_\_\_\_\_

der Dissertation

1. Prüfer: \_\_\_\_\_

2. Prüfer: \_\_\_\_\_

3. Prüfer: \_\_\_\_\_

des öffentlichen Promotionskolloquiums.

Tag des öffentlichen  
Promotionskolloquiums: \_\_\_\_\_

Doktorurkunde ausgehändigt am: \_\_\_\_\_

*To my parents*



## ABSTRACT

Quantum chemical modeling of electron paramagnetic resonance (EPR) parameters, in combination with data from the modern high-field/high-frequency EPR (HF-EPR) techniques, constitutes an invaluable analytical tool for gaining insight into radical-protein interactions, which determine the specificity and directionality of the radical-mediated biochemical processes. This thesis reports a series of density functional (DFT) studies on EPR parameters of several biologically relevant radicals and a series of molecular devices inspired by radical-protein interaction in photosystem I (PS-I). We demonstrate our methodology's accuracy and capacity to provide insight into the *in vivo* environment and reactivity of bioradicals.

Our DFT approach for the calculation of electronic  $g$ -tensors has been applied to semiquinone radical anions in the different protein environments of photosynthetic reaction centers. Supermolecular models have been constructed, based on combined crystallographic and quantum chemical structure data, for the  $Q_A$  and  $Q_B$  active sites of bacterial reaction centers, for the  $A_1$  site of PS-I, as well as for ubisemiquinone in frozen 2-propanol. After scaling of the computed  $\Delta g_x$  components by 0.92, both  $\Delta g_x$  and  $\Delta g_y$  components computed at gradient-corrected DFT level with accurate spin-orbit operators agree with HF-EPR reference data essentially to within experimental accuracy in all four systems studied. The influence of the various semiquinone-protein non-covalent interactions has been studied by successive removal of individual residues from the models. The effects of hydrogen bonding to the two carbonyl oxygen atoms of the semiquinones was found to be nonadditive, due to compensating spin-polarization effects. The effects of tryptophan-semiquinone  $\pi$ -stacking are different for  $Q_A$  and  $A_1$  sites. This may be traced back to a different alignment of the interacting fragments and to differential spin polarization.

In the next part of this work our DFT methodology has been applied to the semiquinone in the environment of the "high-affinity" binding site of quinol oxidase ( $Q_H$  site). Recent multi-frequency EPR studies of the  $Q_H$  binding site of quinol oxidase have suggested a very asymmetric hydrogen-bonding environment for the semiquinone radical anion state. Single-sided hydrogen bonding to the  $O_1$  carbonyl

position was one of the proposals, which contrasts with some previous experimental indications. The density functional calculations of the EPR parameters ( $g$ -tensors,  $^{13}\text{C}$ ,  $^1\text{H}$ , and  $^{17}\text{O}$  hyperfine tensors) for a wide variety of supermolecular model complexes have been used to provide insight into the detailed relations between structure, environment and EPR parameters of ubisemiquinone radical anions. A single-sided binding model is not able to account for the experimentally observed low  $g_x$  component of the  $g$ -tensor nor for the observed magnitude of the asymmetry of the  $^{13}\text{C}$  carbonyl hyperfine coupling (HFC) tensors. Based on the detailed comparison between computation and experiment, a model with two hydrogen bonds to  $\text{O}_1$  and one hydrogen bond to  $\text{O}_4$  was suggested for the  $\text{Q}_\text{H}$  site, but a model with one more hydrogen bond on each side could not be excluded. Additionally, several general conclusions on the interrelations between EPR parameters and hydrogen bond patterns of ubisemiquinones in proteins were provided.

The computational studies related to the mechanism of electron transfer in PS-I gave an impetus to the theoretical design, based on quantum-chemical calculations, of relatively small rotational molecular motors made up from intramolecularly connected dyads consisting of a quinone unit and a pyrrole or indole moiety. It was shown computationally for several systems, depending on the length and attachment points of the interconnecting chains, that a reduction of the quinone to the semiquinone radical anion or quinolate dianion states leads to a reversible intramolecular reorientation from a  $\pi$ -stacked to a T-stacked arrangement. In the rearranged structures, a hydrogen bond from the pyrrole or indole N-H function to the semiquinone or quinolate  $\pi$ -system is created upon reduction. In some systems, hydrogen bonds to the semiquinone or quinolate oxygen atoms are partly feasible and will be preferred over T-stacking. It was shown that the intramolecular interactions modify the quinone redox potentials. The electronic  $g$ -tensors computed for the semiquinone states reflected characteristically the presence and nature of hydrogen bonds to the semiquinone and were suggested as suitable EPR spectroscopic probes for the preferred structures. Intramolecular proton transfer was observed to be possible in the dianionic state.

In contrast to semiquinones, which represent paramagnetic states of enzyme cofactors, glycy radical are genuine protein radicals. As a step towards an in-depth



understanding of the EPR parameters of glycy radical in proteins, the hyperfine-tensors and, particularly, the  $g$ -tensor of N-acetylglycyl in the environment of a single crystal of N-acetylglycine have been studied by systematic state-of-the-art quantum chemical calculations on various suitable model systems. The quantitative computation of the  $g$ -tensors for such glycy-derived radicals is a veritable challenge, mainly due to the very small  $g$ -anisotropy combined with a non-symmetrical, delocalized spin-density distribution and several atoms with comparable spin-orbit contributions to the  $g$ -tensors. The choice of gauge origin of the magnetic vector potential, and of approximate spin-orbit operators, both turn out to be more critical than found in previous studies of  $g$ -tensors for organic radicals. Environmental effects, included by supermolecular hydrogen-bonded models, were found to be moderate, due to a partial compensation between the influences from intramolecular and intermolecular hydrogen bonds. The largest effects on the  $g$ -tensor are caused by the conformation of the radical. The DFT methods employed systematically overestimate both the  $\Delta g_x$  and  $\Delta g_y$  components of the  $g$ -tensor. This is important for investigations on the protein-glycy radicals (see next paragraph). The  $^1\text{H}_\alpha$  and  $^{13}\text{C}_\alpha$  hyperfine couplings depend only slightly on the supermolecular model chosen and appear less sensitive probes of detailed structure and environment.

The number of enzymes that require a glycy-based radical for their function is growing. Here we provide systematic quantum-chemical studies of spin-density distributions, electronic  $g$ -tensors, and hyperfine couplings of various models of protein-bound glycy radicals. Similarly to what was found for N-acetylglycyl (see previous paragraph), the small  $g$ -anisotropy for this delocalized, unsymmetrical system presents appreciable challenges to state-of-the-art computational methodology. This pertains to the quality of structure optimization, as well as to the choice of spin-orbit Hamiltonian and gauge origin of the magnetic vector potential. Environmental effects due to hydrogen bonding are complicated and depend in a subtle fashion on the different intramolecular hydrogen bonding for different conformations of the radical. Indeed, the conformation has the largest overall effect on the computed  $g$ -tensors (less so on the hyperfine-tensors). We discuss this in the context of different  $g$ -tensors obtained by recent HF-EPR measurements for three different enzymes. Based on results of calibration study for N-acetylglycyl, we support that the glycy radical observed for *E.coli* anaerobic ribonucleotide reductase (ARNR) has a fully extended

conformation, which differs from those of the corresponding radicals in pyruvate formate-lyase (PFL) or benzylsuccinate synthase (BSS).

## ZUSAMMENFASSUNG

Die quantenchemische Modellierung von Parametern der elektronenparamagnetischen Resonanz (EPR) stellt, in Kombination mit Daten aus modernen Hochfeld-/Hochfrequenz (HF) EPR-Techniken, eine überaus wichtige analytische Methode dar, um Einblicke in die Radikal-Protein-Wechselwirkung zu gewinnen. Diese Wechselwirkung bestimmt zu einem großen Teil die Abläufe radikalischer biochemischer Prozesse. In dieser Arbeit untersuchten wir in einer Reihe von Dichtefunktionaltheorie (DFT)-Studien die EPR-Parameter diverser biologisch wichtiger Radikale sowie mehrerer durch Radikal-Protein-Wechselwirkungen im Photosystem I inspirierter Modellsysteme. Wir demonstrierten die Genauigkeit sowie die Kapazität unserer Methode, um Einblicke in die *in vivo* Umgebung und Reaktivität von Bioradikalen zu erhalten.

Unser DFT-Ansatz zur Berechnung elektronischer  $g$ -Tensoren wurde auf Semichinonradikalanionen in verschiedenen Proteinumgebungen photosynthetischer Reaktionszentren angewandt. Supermolekulare Modelle wurden, basierend auf einer Kombination aus kristallographischen und quantenchemischen Strukturdaten, für die aktiven Zentren  $Q_A$  und  $Q_B$  bakterieller Reaktionszentren, für  $A_1$  des Photosystems I sowie für Ubisemichinon in gefrorenem 2-Propanol erstellt. Nach der Skalierung der berechneten  $\Delta g_x$  Komponenten um 0.92 stimmen die auf gradienten-korrigiertem DFT-Niveau mit den bestenverfügbaren Spin-Bahn-Operatoren berechneten Komponenten  $\Delta g_x$  sowie  $\Delta g_y$ , mit den Hochfeld-EPR-Referenzdaten innerhalb der experimentellen Genauigkeit in allen vier untersuchten Systemen überein. Der Einfluss verschiedener nichtkovalenter Wechselwirkungen zwischen dem Semichinon und dem Protein wurde durch das sukzessive Verkleinern der Modellsysteme studiert. Dabei wurde festgestellt, dass der Effekt der Wasserstoffbrückenbindung zu den beiden Carbonyl-Sauerstoff-Atomen der Semichinone wegen der kompensierenden Spinpolarisationseffekte nicht additiv ist. Der Effekt der Tryptophan-Semichinon  $\pi$ -Stapelung hat auf  $Q_A$  und  $A_1$  unterschiedliche Auswirkungen. Dies konnte auf die

andersartige Ausrichtung der wechselwirkenden Fragmente sowie auf die unterschiedliche Spinpolarisation zurückgeführt werden.

Im nächsten Teil dieser Arbeit wurden Semichinone der so genannten „hoch-affinen“ Bindungsstelle der Chinoloxidase ( $Q_H$ ) untersucht. Vor kurzem durchgeführte Multifrequenz-EPR-Studien der  $Q_H$  der Chinoloxidase legten asymmetrische Wasserstoffbrückenbindungen zum Semichinonradikalanion nahe. Eine einzelne Wasserstoffbrückenbindung zum  $O_1$  des Carbonyls war ein weiteres vorgeschlagenes Strukturmerkmal, das allerdings im Gegensatz zu früheren experimentellen Hinweisen stünde. Wir haben DFT Berechnungen der EPR-Parameter ( $g$ -Tensoren,  $^{13}\text{C}$ -,  $^1\text{H}$ - und  $^{17}\text{O}$ -Hyperfeinkopplungstensoren) einer großen Anzahl von supermolekularen Modellkomplexen durchgeführt, um detaillierte Einblicke in die Zusammenhänge zwischen Struktur, Umgebung und EPR-Parametern von Ubisemichinon-Radikalanionen zu gewinnen. Ein Bindungsmodell, das nur eine einzige Wasserstoffbrücke berücksichtigt, ist demnach weder in der Lage, die experimentell beobachteten niedrigen  $g_x$ -Komponenten der  $g$ -Tensoren, noch die beobachtete große Asymmetrie von  $^{13}\text{C}$ -Carbonyl HFC-Tensoren zu erklären. Basierend auf einem detaillierten Vergleich zwischen Rechnung und Experiment wurde ein Modell mit zwei Wasserstoffbrückenbindungen zu  $O_1$  und einer Wasserstoffbrückenbindung zu  $O_4$  für  $Q_H$  vorgeschlagen. Ein Modell mit jeweils einer Wasserstoffbrückenbindung mehr kann jedoch ebenfalls nicht völlig ausgeschlossen werden. Zusätzlich wurden weitere erkannte Zusammenhänge zwischen EPR-Parametern und Wasserstoffbrückenbindungen von Ubisemichinonen in Proteinen diskutiert.

Theoretische Untersuchungen bezüglich des Mechanismus des Elektronentransfers im Photosystem I gaben den Anstoß, relativ kleine rotierende molekulare Motoren, bestehend aus intramolekular verbundenen Dyaden, welche eine Chinoneinheit sowie eine Pyrrol- oder Indoleinheit verknüpfen, zu modellieren. Die Berechnungen zeigten, dass für einige Systeme, abhängig von der Länge und den Anknüpfungspunkten der verbundenen Ketten, eine Reduktion des Chinons zum Semichinonradikalanion oder Chinolatdianion mit einer reversiblen intramolekularen Neuorientierung weg von einer  $\pi$ -Stapelung und hin zu einer T-Stapelung auftritt. Durch die Umstrukturierung wird eine Wasserstoffbrückenbindung der Pyrrol- oder

Indol-N-H-Funktion zum Semichinon- oder Chinolat- $\pi$ -Systems nach der Reduktion ausgebildet. In einigen Systemen bilden sich jedoch Wasserstoffbrückenbindungen zum Semichinon- oder Chinolat-Sauerstoffatom aus, die gegenüber der T-Stapelung bevorzugt werden. Die intramolekularen Wechselwirkungen verändern das Redoxpotential des Chinons. Der elektronische  $g$ -Tensor, welcher für die Semichinone berechnet wurde, beweist eindeutig das Vorhandensein dieser Wasserstoffbrückenbindung zum Semichinon.  $g$ -Tensoren stellen somit eine geeignete Kenngröße in der EPR Spektroskopie dar, um strittige Strukturen aufzuklären. Wir halten auch einen intramolekularer Protonentransfer im dianionischen Zustand für möglich.

Im Gegensatz zu Semichinonen welche paramagnetische Zustände von Enzymen-Cofaktoren darstellen sind Glycylradikale echte Proteinradikale. Als Schritt zum tiefer gehenden Verständnis von EPR-Parametern des Glycylradikals in Proteinen wurden die Hyperfeinkopplungstensoren und insbesondere der  $g$ -Tensor des N-Acetylglycyls durch systematische hochgenaue quantenchemischen Berechnungen an diversen geeigneten Modellsystemen untersucht. Die quantitative Berechnung von  $g$ -Tensoren für solche Glycyl-ähnlichen Radikale ist eine enorme Herausforderung, insbesondere wegen der sehr kleinen  $g$ -Anisotropie. Diese ist zudem mit einer nichtsymmetrischen delokalisierten Spindichtevertelung auf verschiedene Atome des Moleküls verbunden, die mit vergleichbaren Spinbahneffekten zum  $g$ -Tensor beitragen. Die Wahl eines geeigneten Eichursprungs des magnetischen Vektorpotentials und geeigneter Spin-Bahn-Operatoren, gestaltete sich weitaus anspruchsvoller als in vorausgegangen Arbeiten zu  $g$ -Tensoren organischer Radikale. Umgebungseffekte, die durch supermolekulare Wasserstoffbrückenbindungs-Modelle berücksichtigt wurden, stellen sich hingegen als nicht so schwerwiegend heraus, zum Teil durch die gegenseitige Kompensierung des Einflusses von intramolekularen und intermolekularen Wasserstoffbrückenbindungen. Den größten Einfluss auf den  $g$ -Tensor übt die Konformation des Radikals aus. Die angewendete DFT Methode überschätzt systematisch sowohl die  $\Delta g_x$  als auch die  $\Delta g_y$  Komponente des  $g$ -Tensors. Dieses Ergebnis ist wichtig für Untersuchungen von Protein-Glycyl-Radikalen (siehe weiter unten). Die  $^1\text{H}_\alpha$  und  $^{13}\text{C}_\alpha$  Hyperfeinkopplungen hängen nur wenig von den gewählten supermolekularen Modellen ab und scheinen weniger empfindlich gegenüber der genauen Struktur und Umgebung des Moleküls zu sein.

Die Anzahl der bekannten Enzyme, die als funktionelle Gruppe ein Glycyl-Radikal besitzen, wird immer größer. Wir führten in dieser Arbeit eine systematische quantenchemische Studie zur Spindichteverteilung, elektronischem  $g$ -Tensor und Hyperfeinkopplungskonstanten diverser Modelle von Protein-gebundenen Glycylradikalen durch. Wie schon bei N-Acetylglycyl gesehen (siehe oben) stellt auch hier die geringe  $g$ -Anisotropie dieses delokalisierten, asymmetrischen Systems selbst für moderne Rechenmethoden eine beträchtliche Herausforderung dar. Dies betrifft zum einen die Qualität der Strukturoptimierung, zum anderen die Wahl des Spin-Bahn-Operators und des Eichursprungs des magnetischen Vektorpotentials. Umgebungseffekte aufgrund der Ausbildung von Wasserstoffbrückenbindungen hängen in komplizierter Weise von den verschiedenen intramolekularen Wasserstoffbrückenbindungen verschiedener Konformationen des Radikals ab. Die jeweilige Konformation hat insgesamt gesehen die größte Auswirkung auf den berechneten  $g$ -Tensor (jedoch weniger auf den Hyperfeinkopplungstensor). Wir diskutierten dies im Zusammenhang verschiedener  $g$ -Tensoren, welche vor kurzem durch Hochfeld-EPR Messungen für drei verschiedene Enzyme erhalten wurden. Basierend auf den Resultaten der Kalibrierungsstudie an N-Acetylglycyl, schlagen wir vor, dass das Glycylradikal, welches für die *E.coli* anaerobische *Ribonucleotid Reductase* (RNR) beobachtet wurde, eine gestreckte Konformation besitzt, die sich von derjenigen der entsprechenden Radikale der *Pyruvat Format-Lyase* (PFL) oder *Benzylsuccinatsynthase* (BSS) unterscheidet.

## LIST OF ABBREVIATIONS

ACM	adiabatic connection method
AMFI	one-center mean-field approximation to SO matrix elements
B (B88)	Becke (1988) exchange functional
B86	Becke (1986) exchange functional
B3PW91	hybrid functional using B exchange and PW91 correlation
BP86	B exchange and P86 correlation functionals
BP	Breit-Pauli (Hamiltonian)
B3LYP	hybrid functional using B exchange and LYP correlation
bRC	bacterial reaction center
BSS	benzylsuccinate synthase
CC	coupled-cluster (theory)
CCSD	CC with single and double substitutions
CCSDT	CCSD with triple substitutions
CCSD(T)	CCSD with perturbative estimate for connected triples
CI	configuration interaction
cw-EPR	continuous-wave EPR (method)
DCI	CI including only double electronic excitations
DFT	density functional theory
DZVP	valence double zeta basis with polarization functions
ENDOR	electron nuclear double resonance
EPR (ESR)	electron paramagnetic (spin) resonance
ESEEM	electron spin echo envelope modulation
ET	electron transfer
GGA	generalized gradient approximation
Gly/Gly <sup>•</sup>	glycine/glycyl
HF	Hartree-Fock (theory)
HH	half-and-half hybrid functional using 50% of exact and 50% of B exchange
HP	Hartree product
imd	imidazole

ind	indole
KS	Kohn-Sham (theory)
LCAO	linear combination of atomic orbitals
LDA	local density approximation
LSDA	local spin density approximation
LYP	Lee-Yang-Parr correlation functional
MBPT	many-body perturbation theory
MCSCF	multi-configuration self-consistent field
MOs	molecular orbitals
MP2	second-order Møller-Plesset (perturbation theory)
MP $n$	$n$ -th-order Møller-Plesset (perturbation theory)
NAGH/NAG <sup>•</sup>	N-acetylglycine/N-acetylglycyl
nmf	N-methylformamide
NMR	nuclear magnetic resonance
P86	Perdew (1986) correlation functional
PBE	Perdew-Burke-Ernzerhof functional
PFL	pyruvate formate lyase
PS-I/PS-II	photosystem I/photosystem II
PT	perturbation theory
PW91	Perdew-Wang (1991) correlation functional
PQQ	pyrroloquinolinequinones
Q	quinone
Q <sub>A</sub> , Q <sub>B</sub>	quinone binding sites of bRC
Q <sub>H</sub> , Q <sub>L</sub>	quinone binding sites of QOX
Q <sub>K</sub> (A <sub>1</sub> )	quinone binding site of PS-I
QOX	ubiquinol oxidase
RC	reaction center
RHF	restricted Hartree-Fock
RNR	ribonucleotide reductase
ROHF	restricted open-shell Hartree-Fock
SCF	self-consistent field
SD	Slater determinant
SDCI	CI including single and double electronic excitations
SOS-DFPT	sum-over-states density functional perturbation theory



SOO	spin-other-orbit
SSO	spin-same-orbit
Trp	tryptophan
UHF	unrestricted Hartree-Fock
VWN	Vosko-Wilk-Nusair correlation functional



# CONTENTS

Abstract.....	i
Zusammenfassung.....	v
List of Abbreviations .....	ix
Contents .....	xiii
1 Introduction.....	1
2 Electronic Structure. Non-Relativistic Quantum Mechanical Methods .....	5
2.1 Wave Function Methods.....	5
2.1.1 Hartree-Fock Method.....	7
2.1.2 Self-Consistent Field Theory .....	9
2.1.3 The Configuration Interaction Method .....	10
2.1.4 The Coupled-Cluster Method .....	11
2.1.5 Møller-Plesset Perturbation Theory .....	12
2.2 Density Functional Theory .....	12
2.2.1 The Kohn-Sham Approach .....	12
2.2.2 Exchange-Correlation Functionals.....	14
3 The Calculation of EPR Parameters Using One-Component Density Functional Methods .....	17
3.1 Introduction.....	17
3.2 The Effective Spin Hamiltonian .....	19
3.3 The Microscopic Spin Hamiltonian .....	21
3.3.1 The Breit-Pauli Hamiltonian.....	22
3.3.2 Operators Relevant for the Electron Zeeman Effect.....	26
3.3.3 Operators Relevant for the Hyperfine Interaction .....	29
3.4 Perturbation-Theory Expressions for the Electron Zeeman and Hyperfine Interaction Coupling Parameters.....	30
3.4.1 Rayleigh-Schrödinger Perturbation Theory .....	31
3.4.2 Perturbation-Theory Expressions for Electronic $g$ -Tensor .....	33
3.4.3 Perturbation-Theory Expressions for Hyperfine $A$ -Tensor.....	35
3.5 Computational Details .....	36

3.5.1	Basis Sets and Exchange-Correlation Functionals .....	36
3.5.2	Treatment of the Spin-Orbit Operators .....	37
3.5.3	Gauge Dependence of the $g$ -Tensor .....	39
3.5.4	Studies of Biologically Relevant Radicals. Cooperation of Experiment and Theory .....	40
4	Calculations of EPR Parameters for Bioradicals .....	45
4.1	Electronic $g$ -Tensors of Semiquinones in Photosynthetic Reaction Centers .....	47
4.1.1	Introduction .....	47
4.1.2	Computational Details .....	49
4.1.2.1	Structures .....	49
4.1.2.2	$g$ -Tensor Calculations .....	54
4.1.3	Results and Discussion .....	55
4.1.4	Conclusions .....	62
4.2	Protein-Cofactor Interactions and EPR Parameters for the $Q_H$ Quinone Binding Site of Quinol Oxidase .....	63
4.2.1	Introduction .....	63
4.2.2	Computational Details .....	66
4.2.2.1	Structure Optimizations and Models .....	66
4.2.2.2	$g$ -Tensor Calculations .....	69
4.2.2.3	Hyperfine Tensor Calculations .....	70
4.2.3	Results and Discussion .....	71
4.2.3.1	Structures of Model Complexes .....	71
4.2.3.2	$g$ -Tensors .....	74
4.2.3.3	$^{13}\text{C}$ -Carbonyl Hyperfine Tensors .....	78
4.2.3.4	$^1\text{H}(\text{CH}_3)$ Hyperfine Tensors .....	87
4.2.3.5	$^1\text{H}$ Hyperfine Tensors for Hydrogen Bonded Protons .....	90
4.2.3.6	$^{17}\text{O}$ Hyperfine Tensors .....	93
4.2.3.7	A Model for Cofactor-Protein Interactions in the $Q_H$ Binding site .....	97
4.2.4	Conclusions .....	98
4.3	Molecular Mechanical Devices Based on Quinone-Pyrrole and Quinone-Indole Dyads .....	101

4.3.1	Introduction.....	101
4.3.2	Computational Details .....	102
4.3.2.1	Choice of Model Systems .....	102
4.3.2.2	Structure Optimizations and Energy Calculations.....	105
4.3.2.3	<i>g</i> -Tensor Calculations .....	107
4.3.3	Results and Discussion .....	107
4.3.3.1	Structures of Model Complexes.....	107
4.3.3.2	Influence of the Interactions on Reduction Energies .....	111
4.3.3.3	<i>g</i> -Tensor Results .....	115
4.3.3.4	Nature of the Interaction and Comparison to Related Systems .....	116
4.3.4	Conclusions.....	118
4.4	Understanding the EPR Parameters of Glycine-Derived Radicals. The case of N-Acetylglycyl in the N-Acetylglycine Single-Crystal Environment.....	121
4.4.1	Introduction.....	121
4.4.2	Computational Details .....	123
4.4.2.1	Structure Optimizations .....	123
4.4.2.2	<i>g</i> -Tensor Calculations .....	127
4.4.2.3	Hyperfine Tensor Calculations .....	128
4.4.3	Results and Discussion .....	128
4.4.3.1	Optimized Structures .....	128
4.4.3.2	Influence of the Level of Structure Optimization on Computed <i>g</i> -Tensors.....	130
4.4.3.3	Dependence of <i>g</i> -Tensors on Gauge Origin and Spin- Orbit Operator .....	132
4.4.3.4	Basis-Set Effects on <i>g</i> -Tensors .....	135
4.4.3.5	Atomic Analyses of the <i>g</i> -Shift Tensor of CC-NAG <sup>•</sup> ...	136
4.4.3.6	Structural Results and Spin Densities for Supermolecular Models .....	138
4.4.3.7	Conformational and Environmental Effects on <i>g</i> - Tensors.....	139

4.4.3.8	$^1\text{H}_\alpha$ and $^{13}\text{C}_\alpha$ Hyperfine Tensors .....	144
4.4.4	Conclusions .....	145
4.5	Understanding the EPR Parameters of Protein-Bound Glycyl Radicals .....	147
4.5.1	Introduction .....	147
4.5.2	Computational Details .....	149
4.5.2.1	Structure Optimizations .....	149
4.5.2.2	<i>g</i> -Tensor Calculations .....	155
4.5.2.3	Hyperfine Tensor Calculations .....	156
4.5.3	Results and Discussion .....	156
4.5.3.1	Influence of the Level of Structure Optimization on Computed <i>g</i> -Tensors .....	156
4.5.3.2	Optimized Structures and Spin Densities of Gas-Phase Conformers .....	160
4.5.3.3	Conformational Effects on <i>g</i> -Tensors for Gas-Phase Radicals .....	162
4.5.3.4	Analyses of Gas-Phase <i>g</i> -Tensors in Terms of Atomic Spin-Orbit Contributions .....	164
4.5.3.5	Structural Results and Spin Densities for Supermolecular Models .....	166
4.5.3.6	Environmental Effects on <i>g</i> -Tensors .....	169
4.5.3.7	Comparison with Experimental <i>g</i> -Tensors .....	171
4.5.3.8	$^1\text{H}_\alpha$ and $^{13}\text{C}_\alpha$ Hyperfine Tensors .....	176
4.5.3.9	Effects of Out-of-Plane Twisting .....	179
4.5.4	Conclusions .....	181
5	Summary and Outlook .....	183
6	Bibliography .....	187
Acknowledgments .....		199
Curriculum Vitae .....		201
List of Publications .....		202

# 1 Introduction

The electron paramagnetic resonance (EPR) method has become a major tool, in diverse fields ranging from biology and chemistry to solid-state physics, for investigation of the structures and properties of systems containing unpaired electrons. Two spectral parameters, the  $g$ -tensor and the hyperfine coupling constants ( $A$ -tensors) between the unpaired electron spin and the magnetic nuclei of the system, can be measured for bioorganic free radicals (bioradicals) in the doublet state. They provide information on the electronic structure of the radical either globally ( $g$ -tensor) or locally ( $A$ -tensor). As the magnitudes of both parameters depends strongly on intra- and intermolecular interactions, their interpretation gives detailed insight into the local geometry of the radical and into its immediate environment.<sup>1-3</sup> While the subtle interrelation between EPR and structure parameters can be often obtained from analysis of experimental spectra, for difficult cases an in-depth quantum chemical analysis is indispensable. Accurate theoretical predictions of hyperfine coupling constants have become available with the development of high-level ab initio methods which, however, are applicable only to small organic radicals or other light main-group systems.<sup>4-24</sup> The treatment of larger systems became possible only with the introduction of density functional theory (DFT). After development of gradient-corrected and hybrid DFT schemes, numerous validation and application studies proved the hybrid DFT methods to provide the best quality of the hyperfine coupling constants (HFCs) for organic radicals.<sup>22,25-27</sup> But a quite different situation pertained to the theoretical prediction of  $g$ -tensors. Even though the theoretical methods were used in calculations of  $g$ -tensors for quite a long time, they could provide only qualitative understanding of the experimental results.<sup>28-32</sup> Within the last ten years, immense progress in experimental EPR techniques has inspired renewed interest in quantum chemical calculations of electronic  $g$ -tensors. The modern ab initio calculations<sup>33-41</sup> of  $g$ -tensors are limited to small molecules and serve best as benchmark methods. In the late 1990s, a few independent DFT implementations for calculations of  $g$ -tensors became available,<sup>42-48</sup> including two-component (employing relativistic wave function) and one-component (employing non-relativistic or scalar-

relativistic wave function) approaches. At present, only the one-component methods can be applied to relatively large organic radicals. The newly-developed methods differ mainly in the treatment of the spin-orbit (SO) matrix elements (see Chapters 3.3.2. and 3.5.2). In general, the one-component DFT approaches employing local density approximation (LDA) or generalized gradient approximation (GGA) functionals provide astonishingly accurate  $g$ -tensors for organic radicals. The calculations of  $g$ -tensors for transition metal systems imposes much higher demands on the computational methodology, although we will not discuss this in the following.<sup>49</sup>

In this work, we have used the one-component DFT approach for calculation of the EPR parameters, as implemented in the ReSpect-MAG code.<sup>50</sup> The predictive power of the method was already demonstrated in earlier studies for a number of *in vitro* organic-radical systems.<sup>51</sup> The main goal of this work has been twofold. Firstly, we wanted to confirm the predictive power of the method for organic  $\pi$ -radicals in protein environment; and secondly we used the validated method to solve problems of biological relevance. We also have proposed EPR as the technique of choice for confirming the structure of newly-designed molecular devices when these will be synthesized. In our calculations we have often used molecular models of sizes that would not be treatable by many of the other quantum chemical methods for calculations of EPR parameters.

Interest in protein-derived radicals (bioradicals), their structure, function and dynamics, has grown rapidly over the last decades, especially since the advent of the high-field/high-frequency (HF) EPR techniques.<sup>52-55</sup> The number of protein systems in which radicals have been proven to play a vital role is enormous and still growing. Stable and transient protein radicals are created in the photosynthetic and respiratory processes of electron transfer as well as in other reactions catalyzed by a large number of the enzymes.<sup>52,56</sup> Up until recently, EPR studies of bioradicals focused mainly on the conventional continuous-wave X-band EPR technique (operating at a microwave frequency of around 9.5 GHz); however, for low-symmetry systems, such as organic radicals in protein environments, X-band EPR suffers from low spectral resolution, and only seldom fully resolved spectra are obtained. The primary reason for this is the very small  $g$ -anisotropy displayed by organic radicals, which can be easily subsumed within the linewidth of the typical X-band spectrum. The usual deviation of the  $g$ -



tensor components from the free electron value for bioradicals rarely exceeds  $10^{-4}$ - $10^{-3}$ . Only for radicals, for which a significant part of the spin density is localized on heavier atoms, with relatively large spin-orbit coupling constants (e.g., oxygen or sulphur in tyrosyl or thiyl radicals, respectively), larger  $g$ -anisotropies are found. The spectral line can be also broadened due to slight variations in the local interactions between the radical and environment within the binding sites studied ( $g$ -strain) or by coexistence of two or more radicals with very similar  $g$ -values. An additional problem can be the weakness of signals caused by a low concentration of the bound radical. The complete tensor information can be extracted most easily if a single crystal is at hand. Unfortunately, this is very seldom the case for proteins. The main obstacle is the nondestructive isolation of proteins, especially of the membrane proteins.

The solution to this problem has been provided by developments in electronics. Nowadays, instead of the conventional X-band experiment, one can carry out high-field/high-frequency (HF) experiment, of which the most commonly used is W-band (95 GHz). If necessary, frequencies of 300-500 GHz and magnetic fields up to 24 T can be used; even higher frequencies and magnetic fields can be achieved at high costs.<sup>52-55</sup> HF-EPR takes advantage of the fact that Zeeman splitting depends on the magnetic field, and thus by increasing the field strength one increases the separation between the  $g$ -tensor components of the studied radical as well as between lines from the radicals with similar  $g$ -values. Additionally, HF-EPR benefits from independence of the hyperfine interaction on the magnitude of the magnetic field making it easy to separate the Zeeman and hyperfine interactions.

To summarize, the quality of the experimental results obtainable for protein radicals are very strictly constrained by the quality of the available sample, and this is valid not only for EPR but also for any other spectroscopic techniques like e.g. X-ray crystallography. For difficult cases, only fragmentary information is available, coming piecemeal from a number of different experimental techniques. The method of choice for combining the pieces of the puzzle and improving the understanding of the interactions in *in vivo* systems is quantum chemical analysis.

The present thesis consists of five parts. Chapter 1 provides the general introduction to the subject of theoretical and experimental EPR studies of bioradicals the detailed discussion of which is provided in the following chapters. Chapter 2 is devoted to an overview of non-relativistic *ab initio* computational methods for

obtaining the electronic structure of the molecular ground state in the field-free framework. Chapter 3 describes the theory of the EPR spectral parameters, introduces the concept of the spin Hamiltonian and details of perturbational approach to the calculations of *g*- and *A*-tensors. The main part of the thesis, the work of the author, is presented in Chapter 4, which consists of the five subchapters reporting a number of theoretical studies of EPR parameters for bioradicals. Chapter 4.1 presents the systematic DFT studies of *g*-tensors for semiquinone radical anions in the different protein environments of photosynthetic reaction centers. In Chapter 4.2, based on DFT calculations of the EPR parameters (*g*-tensor,  $^{13}\text{C}$ ,  $^1\text{H}$ , and  $^{17}\text{O}$  hyperfine tensors) for a wide variety of supermolecular model complexes, the putative binding-mode of semiquinone in the “high-affinity” quinone binding site of quinol oxidase is proposed. Chapter 4.3 presents a number of relatively small rotational molecular motors made up from intramolecularly connected dyads, consisting of a quinone unit and pyrrole or indole moiety, the design of which was inspired by computational studies related to the mechanism of electron transfer in photosystem I. EPR is proposed as the technique of choice for confirming the structure of newly-designed molecular devices when these will be synthesized. In Chapters 4.4 and 4.5 we focus on different type of bioradicals – glycyI-derived radicals. In contrast to semiquinones, which represent paramagnetic states of enzyme cofactors, the glycyI radicals represent genuine protein radicals. In Chapter 4.4, as a step towards an in-depth understanding of the EPR parameters of glycyI radicals in proteins, the hyperfine tensors and, particularly, the *g*-tensor of N-acetylglycyI in the environment of a single crystal of N-acetylglycine are studied by systematic state-of-the-art quantum chemical calculations on various suitable model systems. Chapter 4.5 following the study on N-acetylglycyI, reports on systematic quantum-chemical studies of spin-density distributions, electronic *g*-tensors, and hyperfine couplings of various models of protein-bound glycyI radicals. A number of general conclusions summarizing the work and outlook is provided in Chapter 5.

## 2 Electronic Structure. Non-Relativistic Quantum Mechanical Methods

In this chapter a brief review of some fundamental aspects of the theory of electronic structure will be presented. The available computational methods for obtaining the field-free molecular ground state will be introduced. The Hartree-Fock approach will be presented as a basic one-electron approximation, then the ideas behind the post-Hartree-Fock methods will be sketched, and finally the theorems of density functional theory will be discussed, along with the exchange-correlation potentials available. In-depth discussion of the topics presented in this chapter can be found in a number of quantum chemistry textbooks, see e.g., refs 57-60. All equations will be given in a compact way, without any fundamental physical constants, employing the system of atomic units.

### 2.1 Wave Function Methods

One of the crucial tasks of quantum mechanics is to find the solution to the non-relativistic, time-independent Schrödinger equation

$$\hat{H}\Psi = E\Psi, \quad (2.1)$$

where  $\Psi$  is the wave function depending on electronic and nuclear coordinates and  $\hat{H}$  is the Hamiltonian operator which acts on the wave function to return the energy  $E$  of the system as the eigenvalue. For the system of  $N$  electrons and  $M$  nuclei the general form of the Hamiltonian operator (in the absence of magnetic or electric fields) is

$$\hat{H} = -\sum_{i=1}^N \frac{1}{2} \nabla_i^2 - \sum_{A=1}^M \frac{1}{2M_A} \nabla_A^2 - \sum_{i=1}^N \sum_{A=1}^M \frac{Z_A}{r_{iA}} + \sum_{i=1}^N \sum_{j>i}^N \frac{1}{r_{ij}} + \sum_{A=1}^M \sum_{B>A}^M \frac{Z_A Z_B}{R_{AB}}. \quad (2.2)$$

It consists of five basic contributions: the kinetic energy of the electrons and nuclei, the attractive electrostatic interaction between the electrons and the nuclei, and the interelectronic and internuclear repulsive interactions. The exact solutions to the Schrödinger equation can be obtained only for the  $\text{H}_2^+$  molecule and similar one-

electron systems. In order to solve it for more complicated many-particle problems a number of approximations have to be introduced.

To decouple electronic and nuclear motion, one usually uses the *Born-Oppenheimer* (BO) approximation, which is based on well-justified assumption that nuclei move much slower compared to electrons and that electrons respond instantaneously to the nuclear motion. In consequence the electronic energies are computed for the fixed nuclear positions. The Hamiltonian (2.2) is then reduced to the electronic Hamiltonian and equation (2.1) is reduced to the pure electronic problem

$$\hat{H}_{el}(R_N)\Psi_{el}(r_i; R_N) = E_{el}(R_N)\Psi_{el}(r_i; R_N), \quad (2.3)$$

which depends only parametrically on the nuclear coordinates  $R_N$ . The electronic Hamiltonian  $\hat{H}_{el}$  is derived from equation (2.2) by leaving out the nuclear kinetic energy and internuclear repulsion terms. Accepting such a form of the Hamiltonian we implicitly neglect the relativistic effects (normally negligible for the first 3 rows in the periodic table, i.e.  $Z < 36$ , but important for the fourth and fifth rows and for transition metals<sup>61</sup>). The nuclear motion has to be considered only if one is interested in the vibration, rotation or translation of the system. We will hereafter drop the subscript “*el*” and all further equations will apply only to the electronic problem.

The exact wave function  $\Psi$  for a many-electron system is extremely difficult to express explicitly due to the correlated motion of electrons. In the simplest possible approach this correlation is ignored and the many-electron wave function  $\Psi$  is constructed from one-electron wave functions  $\psi_i$  (*molecular orbitals*, MOs). Because of the non-relativistic regime, the electron spin variables are introduced as *ad hoc* quantum numbers, whereas they arise naturally in the relativistic formalism (see e.g. Chapter 8 in ref 58), and the atomic *spin orbitals*  $\phi_i$  are used instead of the MOs  $\psi_i$ . The spin orbitals are the products of MOs (dependent only on spatial coordinates) and the spin functions:  $\alpha(\omega)$  and  $\beta(\omega)$ , i.e., spin up ( $\uparrow$ ) and spin down ( $\downarrow$ ), where  $\omega$  is an unspecified spin variable. An additional requirement (also originating from relativistic quantum mechanics) is that of the *antisymmetry* of the total electronic wave function with respect to the interchange of the coordinates of any two electrons – known as *Pauli’s exclusion principle*, i.e., no two electrons can occupy the same state.

The total wave function, if expressed as a simple product of atomic spin orbitals, is called the *Hartree product* (HP) wave function

$$\Psi_{\text{HP}}(1, 2, 3, \dots, N) = \phi_1(1)\phi_2(2)\phi_3(3)\dots\phi_N(N). \quad (2.4)$$

However, such a wave function is fundamentally flawed because it does not satisfy the Pauli exclusion principle.

The antisymmetry of the total wave function can be assured by constructing it as a *Slater determinant* (SD)

$$\Psi_{\text{SD}}(1, 2, 3, \dots, N) = \frac{1}{\sqrt{N!}} \begin{vmatrix} \phi_1(1) & \phi_2(1) & \dots & \phi_N(1) \\ \phi_1(2) & \phi_2(2) & \dots & \phi_N(2) \\ \vdots & \vdots & \ddots & \vdots \\ \phi_1(N) & \phi_2(N) & \dots & \phi_N(N) \end{vmatrix}. \quad (2.5)$$

Additionally, the SD accounts for the *indistinguishability of electrons* and the so-called *non-classical exchange*. The latter is a correlation effect unique to the electrons of the same spin and means that the probability of finding two electrons with the same spin simultaneously at the same place is zero; this so-called *Fermi hole* is said to surround each electron.

### 2.1.1 Hartree-Fock Method

The *Hartree-Fock* (HF) method is based on the following approximations: (i) the instantaneous Coulomb repulsion of every pair of electrons is replaced with the repulsion, which the particular electron would feel when moving in a time-averaged field of the other electrons (*Hartree approximation*), (ii) the total electronic wave function is approximated by the single Slater determinant of the form (2.5), and (iii) the *self-consistent field* (SCF) method is used to find a set of spin orbitals  $\phi_i$  such that the SD formed from them is the best possible approximation to the ground state of the system (see Chapter 2.1.2).

The general form of the Hartree-Fock equation is

$$\hat{f}|\phi_i\rangle = \varepsilon_i|\phi_i\rangle, \quad (2.6)$$

where  $\hat{f}(1)$  is the one-electron Fock operator consisting of the *core-Hamiltonian operator*  $h(1)$  and the *Hartree-Fock potential*  $v^{\text{HF}}(1)$

$$\begin{aligned}\hat{f}(1) &= h(1) + v^{\text{HF}}(1) \\ &= -\frac{1}{2}\nabla_i^2 - \sum_A^M \frac{Z_A}{r_{iA}} + v^{\text{HF}}(1).\end{aligned}\quad (2.7)$$

The HF potential is the average repulsive potential experienced by the electron due to the remaining N-1 electrons

$$v^{\text{HF}}(1) = \sum_j^{\text{occ}} [J_j(1) - K_j(1)], \quad (2.8)$$

where  $J$  and  $K$  are Coulomb and exchange operators, respectively,

$$J_j(1)\phi_i(1) = \left[ \int d\mathbf{x}_2 \phi_j^*(2) r_{12}^{-1} \phi_j(2) \right] \phi_i(1), \quad (2.9)$$

$$K_j(1)\phi_i(1) = \left[ \int d\mathbf{x}_2 \phi_j^*(2) r_{12}^{-1} \phi_i(2) \right] \phi_j(1). \quad (2.10)$$

The corresponding orbitals  $\phi_i$  are canonical HF orbitals and the eigenvalues  $\varepsilon_i$  are referred to as the orbital energies.

When calculating the HF wave function two types of spin orbitals may be used: (i) the restricted spin orbitals (the same spatial functions are used for  $\alpha$  and  $\beta$  spin functions) and (ii) the unrestricted spin orbitals (different spatial functions for  $\alpha$  and  $\beta$  spins). The former spin orbitals are commonly used for the closed-shell systems, leading to the *restricted Hartree-Fock* (RHF) method. For open-shell systems two methods can be used: the *restricted open-shell Hartree-Fock* (ROHF) method, using the former type of spin orbitals, or the more popular and less complicated *unrestricted Hartree-Fock* (UHF) method, using the latter one. The main advantage of the UHF method is inclusion of spin polarization, although, the drawback is that the UHF wave function does not correspond to the pure spin state.

The HF method describes the electron-electron interaction only approximately, and is thus called an uncorrelated treatment. The difference between the HF energy and the exact ground state energy  $E_0$  (within Born-Oppenheimer approximation and neglect of relativistic effects) is called the *correlation energy* ( $E_{\text{Corr}}^{\text{HF}}$ )

$$E_{\text{Corr}}^{\text{HF}} = E_0 - E_{\text{HF}}. \quad (2.11)$$

The HF method is an important starting point for more accurate approximations, which include the effects of electron correlation. The three main methods for calculating electron correlation are: Configuration Interaction (CI), Coupled Cluster

(CC), and Many Body Perturbation Theory (MBPT); a short overview of the main features of each method will be given in Chapters 2.1.3, 2.1.4, and 2.1.5, respectively.

### 2.1.2 Self-Consistent Field Theory

The main difficulty of the HF method is that the Fock operator, eq. (2.7), depends on all occupied MOs (via the Coulomb  $J$  and exchange  $K$  operators eqs. (2.9) and (2.10)). A specific Fock orbital can only be determined if all the other occupied orbitals are known, and therefore iterative methods must be employed for determining the orbitals. For small and highly symmetric systems, like atoms or diatomic molecules, the HF equations (2.6) may be solved by mapping the orbitals on a set of grid points (numerical HF methods<sup>62</sup>). For all other systems, the spatial molecular orbitals  $\psi_i$  are expanded as a *linear combination of atomic orbitals* (LCAO)

$$\psi_i = \sum_{\alpha}^M c_{\alpha i} \chi_{\alpha} . \quad (2.12)$$

Although,  $\chi_{\alpha}$  are conventionally called *atomic orbitals*, they are generally not the solutions to the atomic HF problem and are just the functions of the coordinates of a single electron, the so-called basis functions. To find a solution for HF equations, the energy is minimized with respect to under the orthonormality constraint  $\mathbf{c}^{\dagger} \mathbf{S} \mathbf{c} = 1$ , where  $\mathbf{c}$  is a  $M \times M$  square matrix of the coefficients  $c_{\alpha i}$  and  $\mathbf{S}$  is the overlap matrix  $S_{\alpha\beta} = \langle \chi_{\alpha} | \chi_{\beta} \rangle$ . This is achieved in the Roothaan-Hall equations

$$\mathbf{F} \mathbf{c} = \mathbf{S} \mathbf{c} \boldsymbol{\epsilon} , \quad (2.13)$$

where  $\mathbf{F}$  is the Fock matrix and  $\boldsymbol{\epsilon}$  is a diagonal matrix containing orbital energies. In the *self-consistent field* (SCF) procedure a set of orbitals is guessed and used to construct the Fock operator, which after diagonalisation provide a new set of orbitals. These orbitals replace the previous ones in the construction of the new Fock operator. This procedure is repeated until a satisfactory convergence is found, i.e. the orbitals no longer change within some threshold. At this point the orbitals satisfy the HF equations.

### 2.1.3 The Configuration Interaction Method

The *configuration interaction* (CI) method is conceptually (but not computationally!) the simplest of the correlated methods. The basic idea is that the total wave function is written as a linear combination of Slater determinants with expansion coefficients determined by requiring the energy to be a minimum. The Slater determinants are constructed from the HF MOs. Assuming a molecule with an even number of electrons and adequately, to the first approximation, represented by a closed-shell restricted HF determinant, the CI wave function is written as

$$\Psi_{\text{CI}} = c_0 \Psi_{\text{HF}} + \sum_i^{\text{occ}} \sum_r^{\text{vir}} c_i^r \Psi_i^r + \sum_{i<j}^{\text{occ}} \sum_{r<s}^{\text{vir}} c_{ij}^{rs} \Psi_{ij}^{rs} + \dots, \quad (2.14)$$

where  $i$  and  $j$  are occupied MOs in the HF ‘reference’ wave function ( $\Psi_{\text{HF}}$ ),  $r$  and  $s$  are virtual MOs in  $\Psi_{\text{HF}}$ . The consecutive determinants in the summation are generated by substituting an electron(s) from the occupied orbital(s) indicated by the subscripts into the virtual orbital(s) indicated by the superscripts. Thus, the first summation includes all possible single electronic substitutions, the second includes all possible double substitutions and so on, and the respective determinants are often referred to as *Singles* (S), *Doubles* (D), etc. If all possible excited configurations that can be generated from the HF determinant are considered, the full CI wave function is obtained. Additionally, if the basis was complete, the exact energies of not only the ground state but also of all excited states of the system could be calculated. However, “exact” here is not the same as the experimental value, because it is a solution to the non-relativistic, Born-Oppenheimer, time-independent Schrödinger equation.

For all but the smallest molecules, even with a minimal basis set, full CI is a computationally impractical procedure. To obtain a computationally viable scheme one must truncate the full CI expansion of the wave function. In a systematic procedure only the configurations which differ from the HF wave function by no more than  $m$  spin orbitals are considered. Assuming, e.g.,  $m=2$ , one would include single and double substitutions in the CI wave function (SDCI). Limitation to only single and double (SDCI) or only double (DCI) substitutions can be carried out up to systems of moderate size. A serious drawback of truncated CI methods is that they are not size consistent; and thus the total energy of a system of non-interacting molecules does not scale linearly with the number of molecules.



### 2.1.4 The Coupled-Cluster Method

In the Coupled-Cluster (CC) method,<sup>63</sup> the wave function is not written as a linear (as in CI) but as an exponential expansion, which ensures the size-extensivity and size-consistency

$$\Psi_{\text{CC}} = e^{\mathbf{T}} \Psi_{\text{HF}}, \quad (2.15)$$

$$e^{\mathbf{T}} = 1 + \mathbf{T} + \frac{1}{2!} \mathbf{T}^2 + \frac{1}{3!} \mathbf{T}^3 + \dots + \frac{1}{n!} \mathbf{T}^n = \sum_{n=0}^{\infty} \frac{1}{n!} \mathbf{T}^n. \quad (2.16)$$

The *cluster operator*  $\mathbf{T}$  is defined as

$$\mathbf{T} = \mathbf{T}_1 + \mathbf{T}_2 + \mathbf{T}_3 + \dots + \mathbf{T}_n, \quad (2.17)$$

where  $n$  is the total number of electrons and the various  $\mathbf{T}_i$  operators generate all possible determinants having  $i$  substitutions from the HF reference. For example,

$$\mathbf{T}_2 = \sum_{i>j}^{occ} \sum_{r>s}^{vir} t_{ij}^{rs} \Psi_{ij}^{rs}, \quad (2.18)$$

where the expansion coefficients  $t$  are customarily called *cluster amplitudes* and are determined by the constraint that equation (2.15) has to be satisfied. The exponential operator (2.16) may be rewritten as

$$\begin{aligned} e^{\mathbf{T}} = & \mathbf{1} + \mathbf{T}_1 + \left(\frac{1}{2!} \mathbf{T}_1^2 + \mathbf{T}_2\right) + \left(\frac{1}{3!} \mathbf{T}_1^3 + \mathbf{T}_1 \mathbf{T}_2 + \mathbf{T}_3\right) \\ & + \left(\frac{1}{4!} \mathbf{T}_1^4 + \mathbf{T}_1 \mathbf{T}_3 + \frac{1}{2!} \mathbf{T}_1^2 \mathbf{T}_2 + \frac{1}{2!} \mathbf{T}_2^2 + \mathbf{T}_4\right) + \dots \end{aligned} \quad (2.19)$$

The CC method in its untruncated form is implicitly equivalent to the full CI. However, as in CI, the CC expansion, due to very high computational costs, must be truncated. A commonly used truncation includes single and double substitutions (CCSD).<sup>64</sup> Including triple substitutions leads to the CCSDT method,<sup>65</sup> which is computationally too demanding for all but the smallest systems. An alternative method (CCSD(T))<sup>66</sup> evaluates the triples contribution by perturbation theory and adds them to the CCSD results. The CCSD(T) method is widely regarded as the best single-reference correlation treatment with computational cost low enough to be applicable to chemically interesting systems.

### 2.1.5 Møller-Plesset Perturbation Theory

Perturbation theory (PT) provides yet another approach for the treatment of correlation energy. The basic idea of this method is to divide the total Hamiltonian of the system in two parts: a zeroth-order part,  $H_0$ , which has known eigenfunctions and eigenvalues, and a so-called perturbation  $V$ . The general formulation of the perturbation theory is known as *Rayleigh-Schrödinger PT* and is presented in more detail in Chapter 3.4.1. When the Fock operator (2.7) is chosen as the unperturbed Hamiltonian the method is called *Møller-Plesset perturbation theory* (MP $n$ , where  $n$  indicates the order of correction).<sup>67</sup> The MP2 method is the most commonly used not only among perturbational MP $n$  methods but also among all ab initio methods of quantum chemistry treating electron correlation. Alternatively, the name *Many-Body Perturbation Theory* (MBPT) can be used to emphasize the more general nature of the theory.<sup>68</sup> The Coupled-Cluster method may also be considered as an MBPT method involving summation to infinite order.

## 2.2 Density Functional Theory

Density functional theory (DFT)<sup>60,69,70</sup> enjoys ever-increasing popularity in the chemical community due to its capability to treat electron correlation with low computational cost as compared to correlated ab initio post-HF methods. The accuracy and efficiency offered by the DFT method is especially important for large systems. All modern-day density functional theories are based on two theorems presented by Hohenberg and Kohn<sup>71</sup> in 1964: (i) the electron density  $\rho(\vec{r})$  uniquely determines the external potential  $V_{ext}(\vec{r})$  (i.e., the Hamiltonian operator) and hence the total energy and all other properties of the system, and (ii) the ground state energy can be obtained variationally, meaning the density that minimizes the total energy is the exact ground state density  $\rho_0$ .

### 2.2.1 The Kohn-Sham Approach

The fundamental idea in the DFT method that makes the calculations actually feasible is that an electron density can ordinarily be represented as the sum of squares

of  $N$  orbital densities, with the orbitals themselves defining a single Slater determinant. This idea gives rise to the Kohn-Sham method.<sup>72</sup> The complete ground state energy as a functional of the ground state electron density is written

$$E[\rho(\vec{r})] = T[\rho(\vec{r})] + E_{ee}[\rho(\vec{r})] + E_{Ne}[\rho(\vec{r})]. \quad (2.20)$$

The terms on the right-hand side of eq. (2.20) are the kinetic energy  $T$ , electron-electron repulsion  $E_{ee}$  and nuclear-electron  $E_{Ne}$  interaction, respectively. By further breakdown of the terms we arrive at the expression

$$E[\rho(\vec{r})] = T_s[\rho(\vec{r})] + J[\rho(\vec{r})] + E_{Ne}[\rho(\vec{r})] + T_C[\rho(\vec{r})] + E_{ncl}[\rho(\vec{r})], \quad (2.21)$$

where the terms on the right-hand side of eq. (2.21) are the kinetic energy of the non-interacting electrons  $T_s$ , the classical Coulomb electron-electron repulsion  $J$ , the nuclear-electron interaction  $E_{Ne}$ , the correction to the kinetic energy derived from the interacting nature of the electrons  $T_C$ , and the non-classical correction to the electron-electron repulsion due to self-interaction, exchange (i.e., antisymmetry) and electron correlation effects  $E_{ncl}$ . The two last terms sum up to give the *exchange-correlation* energy

$$\begin{aligned} E_{xc}[\rho(\vec{r})] &= T_C[\rho(\vec{r})] + E_{ncl}[\rho(\vec{r})] \\ &= (T[\rho(\vec{r})] - T_s[\rho(\vec{r})]) + (E_{ee}[\rho(\vec{r})] - J[\rho(\vec{r})]), \end{aligned} \quad (2.22)$$

containing everything that is unknown - in other words, everything that is not known how to be handled exactly. Within the orbital expression for the density eq. (2.21) can be written ( $N, M$  being the number of electrons and nuclei, respectively)

$$\begin{aligned} E[\rho(\vec{r})] &= -\frac{1}{2} \sum_i^N \langle \varphi_i | \nabla^2 | \varphi_i \rangle + \frac{1}{2} \sum_i^N \sum_j^N \iint |\varphi_i(\vec{r}_1)|^2 \frac{1}{r_{12}} |\varphi_j(\vec{r}_2)|^2 d\vec{r}_1 d\vec{r}_2 \\ &\quad - \sum_i^N \int \sum_A^M \frac{Z_A}{r_{1A}} |\varphi_i(\vec{r}_1)|^2 d\vec{r}_1 + E_{xc}[\rho(\vec{r})] \end{aligned} \quad (2.23)$$

To find the orbitals  $\varphi_i$  that minimize  $E[\rho(\vec{r})]$  we need to solve the *Kohn-Sham (KS)* equation

$$\hat{h}_i^{\text{KS}} \varphi_i = \varepsilon_i \varphi_i, \quad (2.24)$$

where the one-electron operator is defined as

$$\hat{h}_i^{\text{KS}} = -\frac{1}{2} \nabla_1^2 + \int \frac{\rho(\vec{r}_2)}{r_{12}} d\vec{r}_2 - \sum_A^M \frac{Z_A}{r_{1A}} + V_{xc}(\vec{r}_1). \quad (2.25)$$

Since the exact expression of the exchange-correlation energy  $E_{XC}$  is not known, no explicit form of the corresponding potential  $V_{XC}$  is available. Hence,  $V_{XC}$  is simply defined as the functional derivative of  $E_{XC}$  with respect to the density  $\rho$

$$V_{XC} = \frac{\partial E_{XC}}{\partial \rho}. \quad (2.26)$$

It is important to realize that if the exact form of  $E_{XC}$  and  $V_{XC}$  were known (which is not the case), the Kohn-Sham strategy would lead to the exact energy, i.e. the correct eigenvalue of the Hamilton operator of the Schrödinger equation. The first approximation to the Kohn-Sham approach appears when the explicit form of the unknown exchange-correlation energy  $E_{XC}$  and corresponding potential  $V_{XC}$  have to be decided. The central goal of modern density functional theory is therefore to find better and better approximations to these two quantities.

### 2.2.2 Exchange-Correlation Functionals

The conventional wave function methods can, in principle, be systematically improved from the HF description all the way to the full CI. In the density functional method there is no such systematic way towards improved approximated functionals. The reason for this is that the explicit form of the exact functional is unknown. Searching for better functionals relies largely on physical or mathematical intuition and has a strong “trial and error” component. A reasonable functional has to fulfill a few physical constraints;<sup>73,74</sup> peculiarly, functionals which strictly meet these requirements are not necessarily better than others that do not.

The simplest approximation is the *Local Density Approximation* (LDA) which assumes that the density can be locally treated as a uniform electron gas. The main advantage of LDA is that the exact analytical form of the exchange energy functional is known (*Slater exchange*)<sup>75</sup> and high-accuracy correlation energy functionals can be obtained from quantum Monte-Carlo simulations<sup>76</sup> (the most widely used is the correlation energy functional of Vosko, Wilk and Nusair, VWN<sup>77</sup>). In the more general case, where  $\alpha$  and  $\beta$  densities are not equal, LDA is replaced by the *Local Spin Density Approximation* (LSDA). The LDA (LSDA) model is relatively far removed from any realistic situation in atoms or molecules, which are usually characterized by a rapidly varying density.

Improvement was provided by the *Gradient Corrected* or *Generalized Gradient Approximation* (GGA) that applies to a model system where the density is not uniform but varies very slowly

$$E_{\text{XC}}^{\text{GGA}}[\rho_{\alpha}, \rho_{\beta}] = \int f(\rho_{\alpha}, \rho_{\beta}, \nabla\rho_{\alpha}, \nabla\rho_{\beta}) d\vec{r} . \quad (2.27)$$

A widely used correction to the LDA (LSDA) exchange energy was proposed by Becke (B or B88)<sup>78</sup> which included only one adjustable parameter fitted to the exactly known exchange energies of the six rare gas atoms. A different group of GGA exchange functionals containing no empirically optimized parameters is represented by the early functionals of Becke (B86)<sup>79</sup> and Perdew (P),<sup>80</sup> or Perdew, Burke, and Ernzerhof (PBE).<sup>81</sup> Among the most widely-used choices of GGA correlation functionals is the correlation counterpart of the Perdew (P) exchange functional, the parameter-free Perdew and Wang (PW91)<sup>82</sup> correlation functional. Another very popular correlation functional came from Lee, Yang and Parr (LYP).<sup>83</sup> All these correlation functionals are based on systems (the uniform electron gas or the helium atom), which include only short-range correlation effects (so-called *dynamical correlation*). Long-range correlation (*non-dynamical correlation*) is not covered by these correlation functionals.

To obtain an exchange-correlation functional, in general, one can combine any of the exchange with any of the correlation functionals. The examples of commonly used GGA exchange-correlation functionals are those combining Becke exchange with the correlation functionals of Perdew (BP86), Lee, Yang, and Parr (BLYP), or Perdew and Wang (BPW91). During the last several years, the so-called meta-GGA functionals have been developed, in which the gradient of the electronic density is augmented by some additional parameter(s) of inhomogeneity: either the Laplacian of the density, the local kinetic energy density, or both (for review see, e.g., ref 84).

Very successful approximations to the exact exchange-correlation functional were obtained after introduction of the *Adiabatic Connection Method* (ACM), which incorporates a certain amount of exact, non-local Hartree-Fock exchange into the local GGA exchange-correlation functionals resulting in *hybrid functionals*. The simplest hybrid functional is the *half-and-half* (HH) functional.<sup>85</sup> More complex mixing schemes were obtained by introducing semiempirical coefficients to determine the weights of the various components. The first such functional was the 3-parameter (*a, b, c*) functional of Becke (B3PW91)<sup>86</sup>

$$E_{XC}^{B3PW91} = (1-a)E_X^{LSDA} + aE_X^{HF} + b\Delta E_X^B + E_C^{LSDA} + cE_C^{PW91}. \quad (2.28)$$

where  $a$ ,  $b$ , and  $c$  were optimized to 0.20, 0.72, and 0.81, respectively. The most popular hybrid functional is B3LYP<sup>83,86,87</sup> in which the PW91 correlation functional is replaced by the LYP (the values of  $a$ ,  $b$ , and  $c$  remain the same as in B3PW91)

$$E_{XC}^{B3LYP} = (1-a)E_X^{LSDA} + aE_X^{HF} + b\Delta E_X^B + (1-c)E_C^{LSDA} + cE_C^{LYP}. \quad (2.29)$$

Conventional implementations of hybrid functionals in self-consistent calculations result in non-local and non-multiplicative potentials  $V_X^{HF,NL}$ . Recently, the proper Kohn-Sham local and multiplicative self-consistent treatment of hybrid functionals within the framework of the optimized effective potential (OEP) was reported.<sup>88-91</sup> The localized hybrid potentials have been obtained within the localized Hartree-Fock/CEDA approximation<sup>92,93</sup> to the OEP method.<sup>94,95</sup>

## 3 The Calculation of EPR Parameters Using One-Component Density Functional Methods

### 3.1 Introduction

Quantum chemical methods for the calculation of electron paramagnetic resonance (EPR) parameters were developed in close correspondence to the progress in experimental techniques.<sup>96</sup> From the very beginning, they were tailored to special classes of substances of interest rather than being formulated in a more general way. The two distinguished classes of substances were: transition metal complexes and organic  $\pi$ -radicals. In this thesis we focus on the biologically relevant organic  $\pi$ -radicals (bioradicals). Thus, in the following, the aspects of calculations for transition metal complexes will be omitted (a comprehensive treatment of the subject can be found, e.g., in ref 49).

For a long time quantum chemical calculations of EPR parameters for organic radicals were entirely dominated by calculations of isotropic hyperfine coupling constants (HFCs). Responsible for this situation was mainly the quality of experimental spectra, typically measured for radicals in fluid solutions where the anisotropy in the  $g$ - and hyperfine-tensors is averaged out due to rapid molecular tumbling. Anisotropic HFCs or  $g$ -values were rarely measured. The anisotropic HFCs, however, were easy to calculate and in cases when the experimental data was available the agreement was very satisfactory. The  $g$ -tensors of organic radicals, showing very small deviations from the free electron  $g$ -value, are very difficult to measure and thus were usually not considered in the quantum chemical analysis.

Ab initio quantum chemical studies of HFCs were initiated with pioneering work of Meyer in the late 1960s.<sup>97</sup> But results of these early Hartree-Fock calculations deviated significantly from experiment indicating that an account of electron correlation is mandatory for quantitative calculations of HFCs. It was not until the configuration interaction (CI) techniques were fully developed for HFCs calculations,

that theoretical predictions of high accuracy were possible for atomic and molecular radicals.<sup>4-16</sup> In later years, HFCs calculations have also been carried out with great success using various levels of multi-configuration SCF (MCSCF),<sup>17</sup> multi-reference CI (MRCI)<sup>18-22</sup> and coupled cluster (CC) theory.<sup>23,24</sup> These ab initio methods provided quantitative agreement with experiment, but due to use of large and flexible basis sets restricted the studied systems only to systems such as small organic radicals or other light main group systems. The situation has changed radically in the early 1990s when the gradient-corrected and hybrid methods of density functional theory (DFT) became available.<sup>25-27</sup> (A number of  $X_\alpha$ -computations of HFCs has been reported earlier.<sup>31,32,98</sup>) These DFT methods provided HFCs for many radicals of the same quality as the high-level ab initio methods at moderate computational costs, if the choice of a functional along with a basis set was appropriate for a given class of systems (for case of organic  $\pi$ -radicals see Chapter 3.5.1).

The best-known early method for calculation of the  $g$ -tensor is that of Stone<sup>28</sup> who derived a gauge invariant formula starting from a single Slater determinant representation of the ground state as well as of the excited states that enter his sum-over-states (SOS)  $g$ -tensor theory.<sup>29</sup> Stone's theory was widely used to interpret  $g$ -tensors of organic radicals. The first ab initio  $g$ -tensor calculations date back to 1973,<sup>30</sup> which was reasonably successful but suffered from the small basis sets and limited wave functions available at the time. Only rare reports on other ab initio or semiempirical calculations of  $g$ -tensors were appearing within the next 20 years. The first modern ab initio calculations are due to Lushington et al., who reported the restricted-open-shell Hartree-Fock (ROHF) level SOS calculations<sup>33</sup> and later extended their work to the more accurate multi-reference configuration-interaction (MRCI) approach.<sup>34-36</sup> The alternative approach was proposed by Vahtras et al., which use linear response theory at the ROHF and multi-configuration self-consistent field (MCSCF) levels of ab initio theory.<sup>37-41</sup> In general, ab initio approaches up to now are most suitable for small molecules and serve best as benchmark methods. The first DFT calculations of  $g$ -tensors were reported already in 1980,<sup>31,32</sup> but the real advance in the field occurred in the late 1990s, when several groups started to develop DFT methods for the prediction of the  $g$ -tensors<sup>42-48</sup> providing results comparing remarkably well with experimental results. These newly-developed DFT methods are divided into the so-called one-component methods employing double perturbation



theory and starting from standard non-relativistic Kohn-Sham solutions,<sup>42-46</sup> and two-component methods computing the  $g$ -tensors with first-order perturbation theory and using relativistic Kohn-Sham solutions.<sup>47,48</sup> The recently increased interest in  $g$ -tensor calculations was most probably launched by the significant progress in the experimental EPR techniques over last years that allowed resolution of very small  $g$ -anisotropies, such as those typically observed for biradicals in the asymmetric protein environments.

In this chapter the theoretical basis of the one-component DFT method, as implemented into the ReSpect-MAG computer program<sup>50</sup> (successor of the deMon program<sup>99</sup> used only in Chapter 4.1) will be discussed, which was employed in this thesis for calculating  $g$ - and  $A$ -tensors. Chapter 3.2 introduces the concept of the effective spin Hamiltonian, while terms of microscopic spin Hamiltonian relevant for  $g$ - and  $A$ -tensors are given in Chapter 3.3. In Chapter 3.4, the perturbational expressions for the components of both tensors are provided, preceded by a short overview of the basics of Rayleigh-Schrödinger perturbation theory. The practical aspects of the calculations of the EPR parameters for organic  $\pi$ -radicals are discussed in Chapter 3.5. The cooperation of experimental and theoretical methods in studies of biologically relevant organic radicals is highlighted in Chapter 3.6.

## 3.2 The Effective Spin Hamiltonian

The transition energies observed in magnetic resonance experiments are best analyzed in terms of the so-called effective spin Hamiltonian  $\hat{H}_s$ , which, in general, is defined as the operator acting only on the spin variables and incorporating all pairwise interactions of the spin magnetic moments of electrons  $\mathbf{S}$  and nuclei  $\mathbf{I}$  with each other and with the external magnetic field  $\mathbf{B}$ . The coupling parameters between  $\mathbf{S}$ ,  $\mathbf{I}$ , and  $\mathbf{B}$  operators can be obtained: (i) from experiment by analysis of the magnetic resonance spectrum or (ii) from modern quantum chemical calculations.

The final form of the effective spin Hamiltonian depends on the spectroscopic method to which it is applied and in case of EPR spectroscopy it is written as

$$\hat{H}_s = \hat{H}(S, B) + \hat{H}(S, I) + \hat{H}(S, S) + \hat{H}(I, I). \quad (3.1)$$

The spin operator  $S$  is the effective spin operator for which the total effective spin is chosen in such a way that it reproduces the experimental  $(2S+1)$ -level multiplet structure (it is not necessary the “true” spin of the system).

The basic and most common effective spin Hamiltonian used in EPR spectroscopy includes only two first terms of eq. (3.1)

$$\hat{H}_S = \hat{H}(S, B) + \hat{H}(S, I) = \mathbf{S} \cdot \mathbf{g} \cdot \mathbf{B} + \sum_N \mathbf{S} \cdot \mathbf{A}_N \cdot \mathbf{I}_N, \quad (3.2)$$

which are: the *electron Zeeman* and the *hyperfine* interactions. The former term describes the coupling of the total electron spin and the external magnetic field with *electronic g-tensor* ( $\mathbf{g}$ ) as a coupling parameter. The latter term describes the coupling of the total electron spin and the nuclear magnetic moment of nucleus  $N$  with the *hyperfine A-tensor* ( $\mathbf{A}_N$ ) as a coupling parameter. The Hamiltonian in the form of eq. (3.2) applies to radical systems in the doublet state,  $S=1/2$ , like all the systems studied in this thesis. Thus, in the following, we will focus only on this form of Hamiltonian, or more exactly, on obtaining the  $g$  and  $A$  coupling parameters by means of quantum chemical methods. Nevertheless, to complete the picture, a brief discussion of other terms of eq. (3.1) is provided below.

For higher spin radical systems (containing more than one unpaired electron,  $S > 1/2$ ) the EPR Hamiltonian of eq. (3.2) has to be augmented with the term describing interaction between unpaired electrons

$$\hat{H}(S, S) = \mathbf{S} \cdot \mathbf{D} \cdot \mathbf{S}, \quad (3.3)$$

the so-called *zero field splitting*, where  $\mathbf{D}$  is the *zero field splitting* tensor.

Another term accounts for the interactions of the intrinsic electric quadrupole moments of the high-spin nuclei,  $|I_N| > 1/2$ , with the electric field gradients (due to electronic and nuclear charges)

$$\hat{H}_Q(I, I) = \sum_N \mathbf{I}_N \cdot \mathbf{Q}_{NN} \cdot \mathbf{I}_N, \quad (3.4)$$

where  $\mathbf{Q}_{NN}$  is a quadrupole coupling tensor. In practice the combination of the eqs. (3.2) and (3.4) is avoided by setting up the experimental conditions so that basic EPR transitions and transitions due to quadrupole coupling do not mix and are observed separately.

As we have already mentioned above, in this thesis we focus only on the doublet-state organic  $\pi$ -radicals, which are well-described by the EPR Hamiltonian of eq. (3.2). Our main goal is to obtain  $g$  and  $A$  coupling parameters by means of modern quantum chemical methods. Here we employ the one-component DFT approach combined with the double perturbation theory. In this theoretical approach, the components of  $g$ - and  $A$ -tensors are obtained as mixed second derivatives of the total molecular energy  $E$  with respect to magnetic field  $B$  and/or spin magnetic moments  $S$  and  $I_N$

$$g_{uv} = \frac{1}{\mu_B} \frac{\partial^2 E}{\partial B_u \partial S_v} \Big|_{\mathbf{B}=\mathbf{S}=0}, \quad (3.5)$$

$$A_{N,uv} = \frac{\partial^2 E}{\partial I_{N,u} \partial S_v} \Big|_{\mathbf{I}_N=\mathbf{S}=0}, \quad (3.6)$$

where  $g_{uv}$  and  $A_{uv}$  are the Cartesian components of the tensors and  $\mu_B=1/2$  is the Bohr magneton (the atomic units of the SI system are used). The total molecular energy of the system is obtained by means of the second-order perturbation theory (see Chapter 3.4).

### 3.3 The Microscopic Spin Hamiltonian

To obtain components of  $g$ - and  $A$ -tensors as mixed second derivatives of the total molecular energy with respect to magnetic field and/or magnetic moments (eqs. (3.5) and (3.6)), the total molecular energy must be expressed as a function of magnetic field and magnetic spin moments. In the framework of one-component DFT method the sought-after expression for energy is obtained by means of the second-order perturbation theory. This method requires the Hamiltonian operator describing the interactions of electronic and nuclear spin moments with each other, with an external magnetic field and with magnetic moments due to orbital motions of electrons.

The interaction between spin magnetic moment of an electron and the external magnetic field is parameterized by the  $g$ -tensor, which is dominated by the free-electron value ( $g_e$ ). The deviation of the  $g$ -tensor from the free-electron value is defined as  $g$ -shift-tensor. The main contribution to the  $g$ -shift tensor is coming from

the coupling between spin and orbital magnetic moments of electrons (spin-orbit coupling, SO). Spin variables arise naturally only in the relativistic theory and thus the  $g$ -tensor is an intrinsically relativistic property. The hyperfine coupling tensor ( $A$ -tensor) parameterizes the interaction between the spin magnetic moment of an electron and a nucleus and also comes most naturally from the relativistic description.

The consistent relativistic treatment of both parameters is offered by a number of *two-component* DFT methods, which employ the relativistic wave function and treat the SO coupling variationally. However, at the moment, these methods can be applied only to relatively small systems. An alternative applicable to larger systems is the *one-component* DFT method, which uses the non-relativistic ground state wave function and treats the spin-orbit effects and other relativistic terms as well as the magnetic field as perturbations. The suitable microscopic Hamiltonian including operators describing these perturbations can be derived from the many-electron quasi-relativistic Breit-Pauli (BP) Hamiltonian.

### 3.3.1 The Breit-Pauli Hamiltonian

To take the magnetic interactions into consideration properly one has to start with relativistic quantum mechanics and, in principle, take into account small corrections following from the quantum field theory.<sup>3,61,100-104</sup> However, the Dirac equation is a common starting point to treat magnetic interactions. Since the Dirac equation can be solved exactly only for a few simple model cases, different approximations must be used.<sup>3,61,100-104</sup> The perturbational approach to the quantum chemical calculations of  $g$ - and  $A$ -tensors employed in this thesis is based on the Breit-Pauli (BP) Hamiltonian. The detailed derivation of the terms that occur in the BP Hamiltonian for an open-shell system in the presence of an external magnetic field, starting from the Dirac equation, may be found, e.g., in ref 3. Here we only report the final form of the BP Hamiltonian, which, in general, can be written as the sum of pure electronic terms, pure nuclear terms and electron-nuclear terms

$$\hat{H} = \hat{H}_e + \hat{H}_n + \hat{H}_{en} . \quad (3.7)$$

All terms of the BP Hamiltonian are given following ref 100.

The pure electronic part consists of twelve terms

$$H_e = \sum_{m=1}^{12} H_m^e, \quad (3.8)$$

where ( $\kappa_0$  denotes  $4\pi\epsilon_0$ )

$$H_1^e = \sum_i \frac{\boldsymbol{\pi}_i^2}{2m_e}, \quad (3.9)$$

$$H_2^e = -e \sum_i \phi_i, \quad (3.10)$$

$$H_3^e = g_e \beta_e \sum_i \left( 1 - \frac{\boldsymbol{\pi}_i^2}{2m_e \kappa_0 c^2} \right) \mathbf{s}_i \cdot \mathbf{B}_i, \quad (3.11)$$

$$H_4^e = -\frac{1}{8m_e^3 c^2} \sum_i \boldsymbol{\pi}_i^4, \quad (3.12)$$

$$H_5^e = -\frac{g_e \beta_e}{4m_e c^2} \sum_i [\mathbf{s}_i \cdot \boldsymbol{\pi}_i \times \mathbf{E}_i - \mathbf{s}_i \cdot \mathbf{E}_i \times \boldsymbol{\pi}_i], \quad (3.13)$$

$$H_6^e = \frac{\hbar \beta_e}{4m_e c^2} \sum_i \text{div} \mathbf{E}_i, \quad (3.14)$$

$$H_7^e = \frac{e^2}{2\kappa_0} \sum_{i,j} \frac{1}{r_{ij}}, \quad (3.15)$$

$$H_8^e = -\frac{2\pi \beta_e^2}{\kappa_0 c^2} \sum_{i,j} \delta(\mathbf{r}_{ij}), \quad (3.16)$$

$$H_9^e = -\frac{g_e \beta_e^2}{\hbar \kappa_0 c^2} \sum_{i,j} \left[ \frac{\mathbf{s}_j \cdot (\mathbf{r}_{ij} \times \boldsymbol{\pi}_j)}{r_{ij}^3} + 2 \frac{\mathbf{s}_i \cdot (\mathbf{r}_{ij} \times \boldsymbol{\pi}_j)}{r_{ij}^3} \right], \quad (3.17)$$

$$H_{10}^e = -\frac{\beta_e^2}{\hbar \kappa_0 c^2} \sum_{i,j} \left[ \frac{\boldsymbol{\pi}_i \cdot \boldsymbol{\pi}_j}{r_{ij}} + \frac{(\boldsymbol{\pi}_i \cdot \mathbf{r}_{ij})(\mathbf{r}_{ij} \cdot \boldsymbol{\pi}_j)}{r_{ij}^3} \right], \quad (3.18)$$

$$H_{11}^e = \frac{g_e^2 \beta_e^2}{2\kappa_0 c^2} \sum_{i,j} \left[ \frac{\mathbf{s}_i \cdot \mathbf{s}_j}{r_{ij}^3} - \frac{3(\mathbf{s}_j \cdot \mathbf{r}_{ij})(\mathbf{s}_i \cdot \mathbf{r}_{ij})}{r_{ij}^5} \right], \quad (3.19)$$

$$H_{12}^e = -\frac{4\pi g_e^2 \beta_e^2}{3\kappa_0 c^2} \sum_{i,j} (\mathbf{s}_i \cdot \mathbf{s}_j) \delta(\mathbf{r}_{ij}). \quad (3.20)$$

The pure nuclear part consists of four terms

$$H_N = \sum_{m=1}^4 H_m^N, \quad (3.21)$$

where (within the fixed-nucleus approximation)

$$H_1^N = e \sum_N Z_N \phi_N, \quad (3.22)$$

$$H_2^N = -\beta_N \sum_N g_N \mathbf{I}_N \cdot \mathbf{B}_N, \quad (3.23)$$

$$H_3^N = \frac{e^2}{2\kappa_0} \sum_{N,N'} \frac{Z_N Z_{N'}}{R_{NN'}}, \quad (3.24)$$

$$H_4^N = \frac{\beta_N^2}{2\kappa_0 c^2} \sum_{N,N'} g_N g_{N'} \left[ \frac{\mathbf{I}_N \cdot \mathbf{I}_{N'}}{R_{NN'}^3} - \frac{3(\mathbf{I}_N \cdot \mathbf{R}_{NN'})(\mathbf{I}_{N'} \cdot \mathbf{R}_{NN'})}{R_{NN'}^5} \right]. \quad (3.25)$$

Finally, the electron-nuclear part consists of six terms

$$H_{eN} = \sum_{m=1}^6 H_m^{eN}, \quad (3.26)$$

where

$$H_1^{eN} = -\frac{e^2}{\kappa_0} \sum_{i,N} \frac{Z_N}{r_{iN}}, \quad (3.27)$$

$$H_2^{eN} = -\frac{g_e \beta_e \beta_N}{\kappa_0 c^2} \sum_{i,N} g_N \left[ \frac{\mathbf{s}_i \cdot \mathbf{I}_N}{r_{iN}^3} - \frac{3(\mathbf{s}_i \cdot \mathbf{r}_{iN})(\mathbf{I}_N \cdot \mathbf{r}_{iN})}{r_{iN}^5} \right], \quad (3.28)$$

$$H_3^{eN} = \frac{8\pi}{3} \frac{g_e \beta_e \beta_N}{\kappa_0 c^2} \sum_{i,N} g_N \mathbf{s}_i \cdot \mathbf{I}_N \delta(\mathbf{r}_{iN}), \quad (3.29)$$

$$H_4^{eN} = \frac{2\beta_e \beta_N}{\hbar \kappa_0 c^2} \sum_{i,N} g_N \frac{\mathbf{I}_N \cdot (\mathbf{r}_{iN} \times \boldsymbol{\pi}_i)}{r_{iN}^3}, \quad (3.30)$$

$$H_5^{eN} = \frac{g_e \beta_e^2}{\hbar \kappa_0 c^2} \sum_{i,N} Z_N \frac{\mathbf{s}_i \cdot (\mathbf{r}_{iN} \times \boldsymbol{\pi}_i)}{r_{iN}^3}, \quad (3.31)$$

$$H_6^{eN} = \frac{2\pi \beta_e}{\kappa_0 c^2} \sum_{i,N} Z_N \delta(\mathbf{r}_{iN}). \quad (3.32)$$

In the formulae given above all the signs are explicitly taken care of, thus  $e$  and  $Z_N$  should be entered in them as positive numbers,  $\beta_e$  and  $\beta_N$  are the Bohr and the nuclear magnetons, respectively, and the electron and the nuclear moments are  $\boldsymbol{\mu}_i = -g_e \beta_e \mathbf{s}_i$  and  $\boldsymbol{\mu}_N = g_N \beta_N \mathbf{I}_N$ ,  $\mathbf{s}_i$  is the spin angular momentum vector of  $i$ -th electron,  $\mathbf{I}_N$  is the spin angular momentum of nucleus  $N$ ,  $\mathbf{E}_i$  is the external electric field vector derived from  $\phi$  (the external electric potential), and  $\boldsymbol{\pi}$  is the generalized momentum operator ( $\boldsymbol{\pi} = \mathbf{p} + e\mathbf{A}$ , where  $\mathbf{p} = -i\nabla$  and  $\mathbf{A}$  is a vector potential associated with the magnetic field  $\mathbf{B}$ ,  $\mathbf{A} = 1/2 \mathbf{B} \times \mathbf{r}$ ). The vectors ( $\mathbf{r}_{iN}$ ,  $\mathbf{r}_{iO}$ ,  $\mathbf{r}_{ij}$ ) are

given as  $\mathbf{r}_{iN} = \mathbf{r}_i - \mathbf{r}_N$  and define the position of the electron  $i$  with respect to the position of nucleus  $N$ , the position of some arbitrary chosen gauge origin  $O$ , or the other integration variable  $\mathbf{r}_j$ , respectively.

The descriptions of the BP Hamiltonian terms given below are based on ref 3.

The pure electronic terms represent:

- (3.9) kinetic energy of electron,
- (3.10) interaction between the electron and the external electric field,
- (3.11) electron Zeeman interaction,
- (3.12) relativistic kinetic energy mass correction,
- (3.13) one-electron spin-orbit interaction (spin-orbit type correction with respect to an external electric field),
- (3.14) Darwin correction to the electric field interaction,
- (3.15) electron-electron Coulomb interaction (electron repulsion),
- (3.16) electron-electron Darwin term,
- (3.17) electron-electron spin-orbit interaction (including spin-same-orbit and spin-other-orbit interactions),
- (3.18) orbit-orbit interaction between electrons,
- (3.19) electron spin-spin dipolar interaction,
- (3.20) electron spin-spin contact interaction.

The pure nuclear terms represent:

- (3.22) interaction between the nuclei and the external electric field,
- (3.23) nuclear Zeeman interaction,
- (3.24) nuclear-nuclear Coulomb interaction (nuclear repulsion),
- (3.25) nuclear dipole-dipole interaction.

The electron-nuclear terms represent:

- (3.27) electron-nuclear Coulomb interaction (nuclear attraction),
- (3.28) dipolar hyperfine interaction,
- (3.29) Fermi contact hyperfine interaction,
- (3.30) orbital hyperfine interaction (paramagnetic spin-orbit operator),
- (3.31) electron-electron spin-orbit hyperfine correction (one-electron part of spin-orbit operator),

(3.32) electron-nuclear Darwin term.

To single out from the Breit-Pauli Hamiltonian only those terms, which are relevant for the electron Zeeman splitting and hyperfine interactions one has to equate the energy expression obtained with the effective spin Hamiltonian with that obtained with the Breit-Pauli Hamiltonian. Only those terms of BP Hamiltonian are kept, which provide energy expression exhibiting bilinear dependence on the magnetic operators ( $B$ ,  $S$  or  $S$ ,  $I$ ). In the framework of second-order perturbation theory, the terms of BP Hamiltonian with bilinear dependence on the magnetic operators ( $B$ ,  $S$  or  $S$ ,  $I$ ) contribute in first order to the energy expression, while terms linearly dependent on the magnetic operators ( $B$ ,  $S$  or  $I$ ) contribute in second-order (see Chapter 3.4). For clarity we will discuss the operators relevant for the electron Zeeman splitting and the operators relevant for the hyperfine splitting separately.

### 3.3.2 Operators Relevant for the Electron Zeeman Effect

The Hamiltonian operator for the electronic Zeeman splitting is constructed from the Breit-Pali Hamiltonian by selecting only those terms, which provide energy expression with bilinear dependence on  $S$  and  $B$  operators. In general we can write

$$\hat{H} = \hat{H}_{SZ}(S, B) + \hat{H}_{RMC}(S, B) + \hat{H}_{OZ}(B) + \hat{H}_{SO}(S) + \hat{H}_{SO-GC}(S, B). \quad (3.33)$$

All explicit terms given below are in atomic units applying the substitution  $\alpha = 1/c$ , where  $\alpha$  is the fine structure constant.

The main contribution to the  $g$ -tensor comes from the *electron Zeeman interaction* term (the  $\pi_i$ -independent part of  $H_3^e$ , eq.(3.11)) usually referred to as the *spin-Zeeman* operator

$$\hat{H}_{SZ}(S, B) = \frac{1}{2} g_e \sum_i \mathbf{s}_i \cdot \mathbf{B}. \quad (3.34)$$

$\hat{H}_{SZ}$  gives the first-order contribution to the electronic  $g$ -tensor and results in the free-electron  $g$ -tensor ( $g_e \mathbf{1}$ ), where  $g_e = 2.002319$ . Since all other contributions are small compared to  $g_e$  it is convenient to separate them and define the overall  $g$ -tensor as

$$\mathbf{g} = g_e \mathbf{1} + \Delta \mathbf{g}. \quad (3.35)$$



The *g-shift-tensor* ( $\Delta\mathbf{g}$ ) defines the deviation of the total *g*-tensor from the free-electron value ( $g_e$ ) and results from the contributions coming from all remaining terms of eq. (3.33).

The dominant contribution to the *g*-shift tensor is coming from the spin-orbit operator, more exactly from the one-electron term of the spin-orbit operator. The total spin-orbit operator gives rise to the second-order contribution to the *g*-shift-tensor and consists of one-electron and two-electrons terms, described by the  $H_5^{eN}$  and  $H_9^e$  terms (eqs. (3.31) and (3.17)) of the Breit-Pauli Hamiltonian, respectively

$$\hat{H}_{SO}(S) = \hat{H}_{SO(1e)}(S) + \hat{H}_{SSO(2e)}(S) + \hat{H}_{SOO(2e)}(S). \quad (3.36)$$

The first term of eq. (3.36) is the one-electron spin-orbit operator that describes the interaction of the spin and the orbital magnetic moments of an electron which takes place under an electric field arising from electron-nuclear attraction. The one-electron SO operator is often referred in the literature as *electron-nuclear spin-orbit*

$$\hat{H}_{SO(1e)}(S) = \frac{1}{4} \alpha^2 g' \sum_{N,i} Z_N \frac{\mathbf{s}_i \cdot \mathbf{l}_{iN}}{r_{iN}^3}. \quad (3.37)$$

To keep all equations as simple as possible the angular momentum operators ( $\mathbf{l}_{iM}, \mathbf{l}_{iO}, \mathbf{l}_{ij}$ ) thereafter will be given in the following form

$$\mathbf{l}_{iN} = \mathbf{r}_{iN} \times \mathbf{p}_i. \quad (3.38)$$

The constant  $g'$  is the electronic spin-orbit *g*-factor and is related to the  $g_e$  by  $g' = 2(g_e - 1)$ . However, one should note, that at the present level of accuracy of both theory and experiment, it is not necessary to distinguish between  $g_e$  and  $g'$ .<sup>3,45</sup>

The second term of eq. (3.36) is the two-electron *spin-same-orbit* operator describing the interaction of the electronic spin with the magnetic field generated by its own movement

$$\hat{H}_{SSO(2e)}(S) = -\frac{1}{4} \alpha^2 g' \sum_{i,j} \frac{\mathbf{s}_i \cdot \mathbf{l}_{ij}}{r_{ij}^3}. \quad (3.39)$$

The negative sign of the term is due to the fact that the magnetic interactions take place under an electric field arising from electron-electron Coulomb repulsion.

The last term of eq. (3.36) is the *spin-other-orbit* term describing the interaction of an electronic spin with the magnetic field generated by the movement of the other electrons.

$$\hat{H}_{\text{SOO}(2e)}(S) = -\alpha^2 \sum_{i,j} \frac{\mathbf{s}_j \cdot \mathbf{l}_{ij}}{r_{ij}^3}. \quad (3.40)$$

Comparing the explicit forms of eqs. (3.37), (3.39), and (3.40) and of the  $H_5^{eN}$  and  $H_9^e$  BP Hamiltonian terms (eqs. (3.31) and (3.17)) one notices immediately that only the field-independent parts of operators are considered. As some of the terms of the BP Hamiltonian include the field-dependent  $\boldsymbol{\pi}_i$  momentum operator ( $\boldsymbol{\pi} = \mathbf{p} + e\mathbf{A}$ ), they can be expanded into their field-dependent and field-independent parts. The field-independent parts of  $H_5^{eN}$  and  $H_9^e$  terms contribute to the SO operator of eq. (3.36), while the field-dependent parts contribute to the *spin-orbit gauge-correction* operator (see below).

Two so-called *correction terms* are included in eq. (3.33): the *relativistic mass correction* ( $\hat{H}_{\text{RMC}}$ ) and the *spin-orbit gauge-correction* ( $\hat{H}_{\text{SO-GC}}$ ). Both terms contribute to the  $g$ -shift tensor in first-order.

The *relativistic mass correction* to the *spin-Zeeman* operator arises from the field-dependent kinematic relativistic effects (derived from  $H_3^e$  term of the BP Hamiltonian, eq. (3.11)):

$$\hat{H}_{\text{RMC}}(S, B) = -\frac{1}{4} \alpha^2 g_e \sum_i p_i^2 \mathbf{s}_i \cdot \mathbf{B}, \quad (3.41)$$

where  $p_i^2 = \mathbf{p}_i \cdot \mathbf{p}_i$  is the square of the linear momentum operator for the  $i$ -th electron.

The *spin-orbit gauge-correction* is necessary to provide the gauge-invariant results. *Gauge-correction* refers to the dependence of this term on the origin  $O$  of the computational coordinate system (the origin of the magnetic vector potential)

$$\hat{H}_{\text{SO-GC}}(S, B) = \hat{H}_{\text{SO-GC}(1e)}(S, B) + \hat{H}_{\text{SO-GC}(2e)}(S, B). \quad (3.42)$$

The *one-electron spin-orbit gauge-correction* term is derived from the field dependent part of the  $H_5^{eN}$  term of the BP Hamiltonian (eq. (3.31))

$$\hat{H}_{\text{SO-GC}(1e)}(S, B) = \frac{1}{8} \alpha^2 g' \sum_{N,i} Z_N \frac{\mathbf{s}_i \cdot (\mathbf{B}(\mathbf{r}_{iN} \cdot \mathbf{r}_{iO}) - \mathbf{r}_{iO}(\mathbf{r}_{iN} \cdot \mathbf{B}))}{r_{iN}^3}, \quad (3.43)$$

and the *two-electron spin-orbit gauge-correction* term is derived from the field dependent part of the  $H_9^e$  term of the BP Hamiltonian (eq. (3.17)).

$$\hat{H}_{\text{SO-GC}(2e)}(S, B) = \frac{1}{8} \alpha^2 g' \sum_{i,j} \frac{(\mathbf{s}_i - 2\mathbf{s}_j) \cdot (\mathbf{B}(\mathbf{r}_{ij} \cdot \mathbf{r}_{iO}) - \mathbf{r}_{iO}(\mathbf{r}_{ij} \cdot \mathbf{B}))}{r_{ij}^3}. \quad (3.44)$$

This term provides corrections to both the spin-same-orbit (3.39) and spin-other-orbit (3.40) operators.

Finally, the *orbital Zeeman* operator, which, in double perturbation expression of the  $g$ -shift tensor components (see Chapter 3.4.2.), couples with the spin-orbit operator of eq. (3.36) to provide the main contribution to the  $g$ -shift tensor

$$\hat{H}_{\text{OZ}}(B) = -\frac{1}{2} \sum_i \mathbf{l}_{iO} \cdot \mathbf{B}. \quad (3.45)$$

$\hat{H}_{\text{OZ}}$  arises from the  $H_1^e$  operator of the BP Hamiltonian (eq. (3.9)) by expanding the field-dependent momentum  $\boldsymbol{\pi}_i$  and taking only the part linear in the magnetic field. It describes the interaction between the external magnetic field and the orbital magnetic moment of electron,  $\boldsymbol{\mu}_l = \mu_B \mathbf{l}$ .

### 3.3.3 Operators Relevant for the Hyperfine Interaction

The Hamiltonian operators describing the hyperfine interactions between unpaired electron(s) and magnetic nuclei collect only those terms of the Breit-Pauli Hamiltonian which provide the energy expression that is bilinear in  $S$  and  $I$  operators

$$\hat{H} = \hat{H}_{\text{FC}}^N(S, I) + \hat{H}_{\text{SD}}^N(S, I) + \hat{H}_{\text{HC-SO}}^N(S, I) + \hat{H}_{\text{PSO}}^N(I) + \hat{H}_{\text{SO}}(S). \quad (3.46)$$

All explicit terms given below are in atomic units applying the substitution  $\alpha = 1/c$ , where  $\alpha$  is the fine structure constant.

The dominant, first-order contributions to the  $A$ -tensor of nucleus  $N$  are coming from the *Fermi-contact* operator (from  $H_3^{eN}$  eq. (3.29))

$$\hat{H}_{\text{FC}}^N(S, I) = \frac{4\pi}{3} \alpha^2 g_e g_N \beta_N \sum_i \mathbf{s}_i \cdot \mathbf{I}_N \delta(\mathbf{r}_{iN}), \quad (3.47)$$

and the *spin-dipolar* operator (from  $H_2^{eN}$  eq. (3.28))

$$\hat{H}_{\text{SD}}^N(S, I) = \frac{1}{2} \alpha^2 g_e g_N \beta_N \sum_i \left[ \frac{3(\mathbf{s}_i \cdot \mathbf{r}_{iN})(\mathbf{r}_{iN} \cdot \mathbf{I}_N)}{r_{iN}^5} - \frac{\mathbf{s}_i \cdot \mathbf{I}_N}{r_{iN}^3} \right]. \quad (3.48)$$

The third term of eq. (3.46),  $\hat{H}_{\text{HC-SO}}^N$ , provides an additional but only small first-order contribution to the  $A$ -tensor.  $\hat{H}_{\text{HC-SO}}^N$  collects one- and two-electron operators, analogous to the eq. (3.42). However, instead of the external magnetic vector potential they include the vector potential  $\mathbf{A}_N(\mathbf{r}_i)$  due to the magnetic nucleus  $N$

$$\mathbf{A}_N(\mathbf{r}_i) = \alpha^2 g_N \beta_N \frac{\mathbf{I}_N \times \mathbf{r}_{iN}}{r_{iN}^3}. \quad (3.49)$$

The *one-electron spin-orbit hyperfine correction* term (from  $H_s^{eN}$  eq. (3.31)) is

$$\hat{H}_{\text{HC-SO}(1e)}^N(S, I) = \frac{1}{4} \alpha^4 g_e g_N \beta_N \sum_i' \sum_{N, N'} \frac{Z_{N'}}{r_{iN}^3 r_{iN'}^3} \times [(\mathbf{r}_{iN} \cdot \mathbf{r}_{iN'}) (\mathbf{s}_i \cdot \mathbf{I}_N) - (\mathbf{s}_i \cdot \mathbf{r}_{iN'}) (\mathbf{I}_N \cdot \mathbf{r}_{iN})]. \quad (3.50)$$

The *two-electron hyperfine correction* term can be divided into: *spin-same-orbit* and *spin-other-orbit hyperfine correction* terms (from  $H_o^e$  eq.(3.17))

$$\hat{H}_{\text{HC-SO}(2e)}^N(S, I) = \hat{H}_{\text{HC-SSO}}^N(S, I) + \hat{H}_{\text{HC-SOO}}^N(S, I). \quad (3.51)$$

Both terms, usually, are treated together and only for clarity are given separately

$$\hat{H}_{\text{HC-SSO}}^N(S, I) = \frac{1}{4} \alpha^4 g_e g_N \beta_N \sum_{i,j}' \sum_N \frac{1}{r_{ij}^3 r_{iN}^3} \times [(\mathbf{r}_{ij} \cdot \mathbf{r}_{iN}) (\mathbf{s}_i \cdot \mathbf{I}_N) - (\mathbf{s}_i \cdot \mathbf{r}_{iN}) (\mathbf{I}_N \cdot \mathbf{r}_{ij})], \quad (3.52)$$

$$\hat{H}_{\text{HC-SOO}}^N(S, I) = \frac{1}{4} \alpha^4 g_e g_N \beta_N \sum_{i,j}' \sum_N \frac{1}{r_{ij}^3 r_{iN}^3} \times [(\mathbf{r}_{ji} \cdot \mathbf{r}_{jN}) (\mathbf{s}_i \cdot \mathbf{I}_N) - (\mathbf{s}_i \cdot \mathbf{r}_{jN}) (\mathbf{I}_N \cdot \mathbf{r}_{ji})]. \quad (3.53)$$

Second-order contributions to the hyperfine tensor (see Chapter 3.4.3) arise as a cross-term between the spin-orbit operator (eq.(3.36)) and the *paramagnetic nuclear spin-electron orbit* operator

$$\hat{H}_{\text{PSO}}^N(I) = \alpha^2 g_N \beta_N \sum_{i,j} \frac{\mathbf{I}_{iN}}{r_{iN}^3}. \quad (3.54)$$

### 3.4 Perturbation-Theory Expressions for the Electron Zeeman and Hyperfine Interaction Coupling Parameters

In the framework of one-component DFT method,  $g$ - and  $A$ -tensor are calculated as second-order properties by means of double perturbation theory. The perturbational treatment can be applied only when the total molecular Hamiltonian can be divided into a zeroth-order part ( $H_0$ ) and a perturbation ( $V$ ) with the assumption that eigenfunctions and eigenvalues of the unperturbed Hamiltonian ( $H_0$ )

are known and the perturbation ( $V$ ) is small. In calculations of EPR parameters the natural choice of  $H_0$  is the non-relativistic field-free Hamiltonian while  $V$  is the Hamiltonian including field- and spin-dependent terms (see Chapters 3.3.2 or Chapter 3.3.3). The double perturbation-theory approach to  $g$ - and  $A$ -tensor, treating spin-orbit coupling (SO) as a perturbation, is appropriate only for radical systems consisting of relatively light atoms (like organic  $\pi$ -radicals) thus having only small SO couplings. The radical systems with significant SO coupling must be thus treated by means of two-component DFT methods, in which SO coupling is treated variationally. Before the explicit perturbation-theory expressions for  $g$ - and  $A$ -tensor will be given (Chapters 3.4.2 and 3.4.3), the basic features of the perturbation theory are recapitulated in Chapter 3.4.1.

### 3.4.1 Rayleigh-Schrödinger Perturbation Theory

In the general case, one wishes to solve the following eigenvalue problem

$$H|\Phi_i\rangle = (H_0 + \lambda V)|\Phi_i\rangle = E_i|\Phi_i\rangle. \quad (3.55)$$

The operator  $H$  can be written as a sum of unperturbed operator  $H_0$  for which we know the eigenfunctions and eigenvalues

$$H_0|\Psi_0\rangle = E_0|\Psi_0\rangle, \quad (3.56)$$

and a perturbing operator  $V$ .  $\lambda$  is a dimensionless ordering parameter which later will be set equal to unity. If the perturbation  $V$  is small, one can expect  $|\Phi_i\rangle$  and  $E_i$  to be reasonably close to  $|\Psi_0\rangle$  and  $E_0$ . Then, the exact eigenfunctions and eigenvalues can be expanded in a Taylor series in  $\lambda$

$$|\Phi_i\rangle = |\Psi_0\rangle + \lambda|\Psi_1\rangle + \lambda^2|\Psi_2\rangle + \dots, \quad (3.57)$$

$$E_i = E_0 + \lambda E_1 + \lambda^2 E_2 + \dots. \quad (3.58)$$

The terms having superscripts ( $n$ ) are referred to as ‘ $n$ th-order corrections’ to the zeroth-order term. Additionally the assumption is made that the unperturbed wave function  $|\Psi_0\rangle$  is normalized  $\langle\Psi_0|\Psi_0\rangle=1$  and the exact wave function is intermediately normalized  $\langle\Psi_0|\Phi_i\rangle=1$  (e.i.  $\langle\Psi_0|\Psi_n\rangle=0$  for  $n\neq 0$ ). After substituting eqs. (3.57) and (3.58) into eq. (3.55), equating coefficients of  $\lambda^n$ , multiplying all

equations by  $\langle \Psi_0 |$  and applying orthogonality relations (the detailed derivation can be found, e.g., in refs 57 and 59) the following expressions for the  $n$ th-order energies are obtained

$$E_0 = \langle \Psi_0 | H_0 | \Psi_0 \rangle, \quad (3.59)$$

$$E_1 = \langle \Psi_0 | V | \Psi_0 \rangle, \quad (3.60)$$

$$E_2 = \langle \Psi_0 | V | \Psi_1 \rangle. \quad (3.61)$$

The zero-order wave function defines the zeroth- and first-order energies. Expanding  $|\Psi_1\rangle$  in terms of eigenfunctions  $\varphi_n$  of  $H_0$  with eigenvalues  $\varepsilon_n$  ( $\Psi_0 = \varphi_0$  and  $E_0 = \varepsilon_0$ ) provides similar expressions for the second-order energy

$$E_2 = \sum_{n>0} \frac{\langle \varphi_0 | V | \varphi_n \rangle \langle \varphi_n | V | \varphi_0 \rangle}{\varepsilon_0 - \varepsilon_n}. \quad (3.62)$$

In non-degenerate perturbation theory, many of the spectroscopic properties can be formulated in terms of derivatives of the total molecular energy  $E$ . The first- and second-order energy derivatives with respect to perturbation parameters  $x_i, x_j$  are known as *first-* and *second-order* molecular properties and are given by

$$\frac{\partial E(\mathbf{x})}{\partial x_i} = \langle \varphi_0 | \frac{\partial H}{\partial x_i} | \varphi_0 \rangle, \quad (3.63)$$

$$\frac{\partial^2 E(\mathbf{x})}{\partial x_i \partial x_j} = \langle \varphi_0 | \frac{\partial^2 H}{\partial x_i \partial x_j} | \varphi_0 \rangle + 2 \sum_{n>0} \frac{\langle \varphi_0 | \frac{\partial H}{\partial x_i} | \varphi_n \rangle \langle \varphi_n | \frac{\partial H}{\partial x_j} | \varphi_0 \rangle}{\varepsilon_0 - \varepsilon_n}, \quad (3.64)$$

where the derivatives are taken at  $x_i=0$  and  $x_j=0$ . The perturbation parameters can represent the same or two different perturbations. In the latter case, the mixed spectroscopic property is evaluated and the method is commonly called *double perturbation theory*. Both  $g$ - and  $A$ -tensors are such mixed second-order molecular properties. Thus final expression for the total molecular energy must be bilinear in both perturbational parameters. The evaluation of the *first-order* properties is straightforward and requires only knowledge of the unperturbed state  $\varphi_0$ . The expression for the *second-order* property eq. (3.64) contains an expectation value term equivalent to the expression for the first-order property eq. (3.63) but additionally a sum-over-states contribution from each excited state  $\varphi_n$  with energy  $\varepsilon_n$ . For magnetic

properties, the first term of eq. (3.64) is known as the *diamagnetic* part, and the second term is known as the *paramagnetic* part.

### 3.4.2 Perturbation Theory Expressions for the Electronic $g$ -Tensor

As was already mentioned above, in the second-order perturbation theory treatment of the  $g$ -tensor the external magnetic field, spin-orbit coupling and other relativistic terms are treated as perturbations. All operators relevant to the Zeeman splitting are provided in Chapter 3.3.2 and when summed up together give the perturbing operator  $\hat{V}$

$$\hat{V} = \hat{H}_{SZ} + \hat{H}_{RMC} + \hat{H}_{OZ} + \hat{H}_{SO} + \hat{H}_{SO-GC}. \quad (3.65)$$

The magnitude of the Zeeman splitting (transition energy between split levels) does not depend on the energy of the unperturbed system. Thus, the zero-order energy (energy of the unperturbed system) can be ignored. However, the perturbational expressions (see eqs. (3.60), (3.61) and (3.62)) employ the wave function of the unperturbed system, which is constructed in our implementation from the Kohn-Sham orbitals obtained in the prior DFT electronic structure optimization.

Three of the terms in eq. (3.65),  $\hat{H}_{SZ}$ ,  $\hat{H}_{RMC}$ ,  $\hat{H}_{SO-GC}$ , depend bilinearly on the external magnetic field  $\mathbf{B}$  and the effective electronic spin  $\mathbf{s}$ . All of them provide the first-order corrections to the energy and thus contribute to the  $g$ -tensor in first order. It can be easily shown that the first-order corrections to the energy coming from  $\hat{H}_{SO}$  and  $\hat{H}_{OZ}$  of eq. (3.65), which depend linearly on the effective electronic spin  $\mathbf{s}$  and on the external magnetic field  $\mathbf{B}$ , respectively, are equal to zero.<sup>3</sup> From the terms arising from the second-order corrections to the energy only those that have the bilinear dependence on  $\mathbf{B}$  and  $\mathbf{s}$  are kept, namely the cross term between the spin-orbit  $\hat{H}_{SO}$  and orbital Zeeman  $\hat{H}_{OZ}$  operators. The  $g$ -tensor in the framework of double perturbation theory is calculated as mixed second-order molecular property (see eq. (3.5)). Thus the final expression for the total molecular energy must be bilinear in both perturbational parameters.

We recall that the spin-Zeeman operator  $\hat{H}_{SZ}$  results in the free-electron  $g$ -tensor ( $g_e\mathbf{1}$ ), while all the other operators of eq. (3.65) contribute to the  $g$ -shift-tensor ( $\Delta g$ ) defined as the deviation of the  $g$ -tensor from the free-electron value.

The final expression for the Cartesian  $uv$ -components of the  $g$ -shift-tensor up to  $O(\alpha^2)$  is the sum of three contributions

$$\Delta g_{uv} = \Delta g_{SO/OZ,uv} + \Delta g_{RMC,uv} + \Delta g_{SO-GC,uv}. \quad (3.66)$$

The first term of eq. (3.66), the cross term between spin-orbit and orbital-Zeeman operators dominates the  $g$ -shift tensor and is given as<sup>45</sup>

$$\begin{aligned} \Delta g_{SO/OZ,uv} = \frac{1}{S} & \left[ \sum_k^{occ(\alpha)} \sum_a^{virt(\alpha)} \frac{\langle \psi_k^\alpha | H_{SO,u} | \psi_a^\alpha \rangle \langle \psi_a^\alpha | H_{OZ,v} | \psi_k^\alpha \rangle}{\varepsilon_k^\alpha - \varepsilon_a^\alpha} \right. \\ & \left. - \sum_k^{occ(\beta)} \sum_a^{virt(\beta)} \frac{\langle \psi_k^\beta | H_{SO,u} | \psi_a^\beta \rangle \langle \psi_a^\beta | H_{OZ,v} | \psi_k^\beta \rangle}{\varepsilon_k^\beta - \varepsilon_a^\beta} \right]. \end{aligned} \quad (3.67)$$

$\psi_k^{\alpha/\beta}$  and  $\psi_a^{\alpha/\beta}$  are unperturbed occupied and virtual  $\alpha/\beta$  Kohn-Sham molecular orbitals,  $\varepsilon_k$  and  $\varepsilon_a$  are the corresponding Kohn-Sham eigenvalues,  $H_{SO,u}$  denotes the  $u$  component of the spatial part of the spin-orbit Hamiltonian (eq. (3.36)),  $H_{OZ,v}$  denotes the orbital-Zeeman Hamiltonian of eq. (3.45) derived with respect to the  $v$  component of magnetic field,  $S$  is the effective spin quantum number allowing the application of the equation to the high-spin systems.

The ‘‘diamagnetic’’ relativistic mass correction to the spin-Zeeman interaction provides the small diagonal (isotropic) contribution to the  $g$ -shift-tensor

$$\Delta g_{RMC,uv} = \frac{1}{S} \delta_{uv} \left[ \sum_k^{occ(\alpha)} \langle \psi_k^\alpha | H_{RMC,uv} | \psi_k^\alpha \rangle - \sum_k^{occ(\beta)} \langle \psi_k^\beta | H_{RMC,uv} | \psi_k^\beta \rangle \right], \quad (3.68)$$

where  $H_{RMC,uv}$  denotes the  $u$  component of the spatial part of eq.(3.41) derived with respect to the  $v$  component of magnetic field.

The ‘‘diamagnetic’’ spin-orbit gauge correction term reflects the magnetic-field dependence of the SO operators

$$\Delta g_{SO-GC,uv} = \frac{1}{S} \left[ \sum_k^{occ(\alpha)} \langle \psi_k^\alpha | H_{SO-GC,uv} | \psi_k^\alpha \rangle - \sum_k^{occ(\beta)} \langle \psi_k^\beta | H_{SO-GC,uv} | \psi_k^\beta \rangle \right], \quad (3.69)$$

where  $H_{SO-GC,uv}$  is the  $u$  component of the spatial part of eq. (3.42) derived with respect to the  $v$  component of magnetic field.



The  $g$ -tensor calculations reported in this thesis, as implemented in the ReSpect-MAG computer program,<sup>50</sup> include all the contributions discussed above except for the two-electron part of the spin-orbit gauge correction (eq. (3.44)), which is neglected due to expected relatively small contribution but high computational costs. The various treatments of spin-orbit operators available in the implementation are discussed in Chapter 3.5.2.

### 3.4.3 Perturbation Theory Expressions for Hyperfine $A$ -Tensor

In the second-order perturbation theory treatment of the hyperfine  $A$ -tensor the perturbing Hamiltonian  $\hat{V}$  consists of terms depending on the nuclear spin moment  $\mathbf{I}$  and the effective electronic spin  $\mathbf{s}$ .

$$\hat{V} = \hat{H}_{\text{FC}}^N + \hat{H}_{\text{SD}}^N + \hat{H}_{\text{HC-SO}}^N + \hat{H}_{\text{PSO}}^N + \hat{H}_{\text{SO}}^N. \quad (3.70)$$

The explicit expressions for the terms of eq. (3.70) are given in Chapter 3.3.3. Here we apply a similar procedure as in case of the  $g$ -tensor. We look for the first- and second-order corrections to the molecular energy choosing only the terms which are bilinear in the nuclear spin moment  $\mathbf{I}$  and the effective electronic spin  $\mathbf{s}$ .

The final expression for the Cartesian  $uv$ -components of  $A$ -tensor up to  $O(\alpha^2)$  and including spin-orbit terms up to  $O(\alpha^4)$  is given as

$$A_{uv}^N = A_{\text{FC},uv}^{N(1)} + A_{\text{SD},uv}^{N(1)} + A_{\text{HC-SO},uv}^{N(1)} + A_{\text{SO/PSO},uv}^{N(2)}. \quad (3.71)$$

Two first terms of eq. (3.71), the Fermi-contact term and the spin-dipolar term, contribute in first-order and for light-atom systems dominate the overall  $A$ -tensor

$$A_{\text{FC},uv}^{N(1)} = \frac{1}{S} \left[ \sum_k^{\text{occ}(\alpha)} \langle \psi_k^\alpha | H_{\text{FC},uv} | \psi_k^\alpha \rangle - \sum_k^{\text{occ}(\beta)} \langle \psi_k^\beta | H_{\text{FC},uv} | \psi_k^\beta \rangle \right], \quad (3.72)$$

$$A_{\text{SD},uv}^{N(1)} = \frac{1}{S} \left[ \sum_k^{\text{occ}(\alpha)} \langle \psi_k^\alpha | H_{\text{SD},uv} | \psi_k^\alpha \rangle - \sum_k^{\text{occ}(\beta)} \langle \psi_k^\beta | H_{\text{SD},uv} | \psi_k^\beta \rangle \right]. \quad (3.73)$$

The  $H_{\text{FC},uv}$  and  $H_{\text{SD},uv}$  denote the  $u$  components of the spatial parts of the Hamiltonians given by eqs. (3.47) and (3.48), respectively, derivated with respect to the  $v$  component of magnetic field.

All the other contributions arise only when the spin-orbit effects play an important role like, e.g., for transition metal systems. This is not the case for free

organic radicals. Therefore all hyperfine tensors presented in this thesis include only the first-order contributions (eqs. (3.72) and (3.73)) neglecting the contributions due to spin-orbit coupling (see below). For completeness of the chapter, however, we will present also the terms including the spin-orbit operators.

The first-order contribution comes from the spin-orbit hyperfine correction operators given by eqs. (3.50) and (3.51)

$$A_{\text{HC-SO},uv}^{N(1)} = \frac{1}{S} \left[ \sum_k^{\text{occ}(\alpha)} \langle \psi_k^\alpha | H_{\text{HC-SO},uv}^N | \psi_k^\alpha \rangle - \sum_k^{\text{occ}(\beta)} \langle \psi_k^\beta | H_{\text{HC-SO},uv}^N | \psi_k^\beta \rangle \right]. \quad (3.74)$$

The  $H_{\text{HC-SO},uv}^N$  denotes the sum of the  $u$  components of the spatial parts of Hamiltonians given by eqs. (3.50), (3.52) and (3.53), derivated with respect to the  $v$  component of magnetic field.

The second-order contribution is obtained as a cross term between the spin-orbit operator of eq. (3.36) and the paramagnetic nuclear spin-electron orbit operator of eq. (3.54)

$$A_{\text{SO/PSO},uv}^{N(2)} = \frac{1}{S} \left[ \sum_k^{\text{occ}(\alpha)} \sum_a^{\text{virt}(\alpha)} \frac{\langle \psi_k^\alpha | H_{\text{SO},u} | \psi_a^\alpha \rangle \langle \psi_a^\alpha | H_{\text{PSO},v} | \psi_k^\alpha \rangle}{\epsilon_k^\alpha - \epsilon_a^\alpha} - \sum_k^{\text{occ}(\beta)} \sum_a^{\text{virt}(\beta)} \frac{\langle \psi_k^\beta | H_{\text{SO},u} | \psi_a^\beta \rangle \langle \psi_a^\beta | H_{\text{PSO},v} | \psi_k^\beta \rangle}{\epsilon_k^\beta - \epsilon_a^\beta} \right]. \quad (3.75)$$

$H_{\text{SO},u}$  denotes the  $u$  component of the spatial part of eq. (3.36) and  $H_{\text{PSO},v}$  denotes the  $v$  component of eq. (3.54), derivated with respect to the  $uv$  component of magnetic field.

## 3.5 Computational Details

### 3.5.1 Basis Sets and Exchange-Correlation Functionals

The  $g$ -tensor is essentially a valence and semi-core property<sup>105</sup> and, differently than many other magnetic properties, is relatively insensitive to the choice of basis set.<sup>42,44,45</sup> Modest split-valence basis sets, with one polarization function in the valence region, already produce reasonable results, with polarized triple zeta basis sets being close to saturation,<sup>42,45</sup> both for Slater- and Gaussian-type basis sets.

The dependence of  $g$ -tensor on exchange-correlation functional was investigated in the number of studies.<sup>44-46,106-108</sup> In case of organic radicals, various GGA functionals provided nearly identical  $g$ -tensors<sup>44,45</sup> and only modest but nonnegligible improvement over the LDA functionals. Thus all  $g$ -tensor calculations presented in this thesis were performed with polarized valence double zeta (DZVP) basis sets and the BP86 GGA functional. Additional tests of basis sets presented in Chapter 4.4 supported this choice.

In calculations of hyperfine coupling constants (HFCs), in general, anisotropic coupling constants are much less sensitive to the exchange-correlation functional and basis set than isotropic ones. For isotropic couplings, the requirements for exchange-correlation functional and basis set are much less stringent if the unpaired spin populates  $s$ -type orbitals ( $^7\text{Li}$ ) rather than  $p$ -type orbitals (organic  $\pi$ -radicals). The transfer of unpaired spin from  $p$  orbitals to the magnetic nuclei takes place exclusively via a spin-polarization mechanism. The description of this mechanism represents the major challenge in calculations of HFCs for atoms as well as for organic  $\pi$ -radicals. Extensive studies of hyperfine coupling constants for large organic  $\pi$ -radicals<sup>109-111</sup> concluded that the reasonable data can be calculated for most nuclei of these systems with either PWP86 GGA or B3LYP hybrid exchange-correlation functionals used along with basis sets of extended triple zeta quality; advisable are EPR-II, EPR-III or IGLO-III basis sets. All the calculations of HFCs presented in this thesis were then performed using the B3LYP functional and EPR-II basis sets.

### 3.5.2 Treatment of the Spin-Orbit Operators

The energy of a system in the presence of a magnetic field depends on the electron density and the current density.<sup>112-114</sup> Therefore, for a proper description of a system in the presence of the magnetic field in the framework of density functional theory one should use an exchange-correlation functional depending not only on the electron density but also on the current density. Such an exchange-correlation functional would contain both two-electron contributions to the spin-orbit operator, eqs. (3.39) and (3.40), where spin-other-orbit term would appear as a current dependence of the functional. However, no sufficiently accurate functional of this kind has been developed so far. Thus practical  $g$ -tensor calculations are constrained to

an approximate introduction of the spin-orbit operators. A number of approximations are used in different implementations. Most of them neglect the spin-other-orbit term, which is opposite in sign to the dominant one-electron spin-orbit term. Thereby this calculations overestimate the spin-orbit/orbital-Zeeman contribution to the  $g$ -tensor, see eq. (3.67).

A few different spin-orbit operators are implemented in the Respect-MAG program.<sup>50</sup> Two operators, denoted as AMFI and FULL, include the one-electron as well as both two-electron spin-orbit operators and use explicitly the Kohn-Sham determinant as approximation to the wave function. AMFI (atomic mean-field approximation<sup>115,116</sup>) is an accurate and efficient approximation to the exact spin-orbit operator replacing the explicit treatment of the integrals by integrals over a sum of effective atomic spin-orbit operators. Importantly, the AMFI approximation is easily applicable to large systems. The FULL operator is the explicit treatment of all one- and two-electron spin-orbit operators. For comparison with other implementations, another effective one-electron spin-orbit operator was also implemented in the ReSpect-MAG program. This is the simplest approach, widely used in early DFT calculations, approximating the total spin-orbit coupling only by the one-electron (electron-nuclear) spin-orbit operator of eq. (3.37), where  $Z_N$  is replaced by an effective nuclear charge  $Z_{N,eff}$  adjusted to reproduce experimental spin-orbit term splittings.<sup>117</sup> Particularly useful for calculations of  $g$ -tensors for compounds containing heavy elements are spin-orbit pseudopotentials (SO-ECPs), which treat only valence electrons explicitly and are used in conjunction with scalar-relativistic pseudopotentials inserted at the Kohn-Sham stage of the calculation.<sup>45,118</sup> They are not used in the calculations of  $g$ -tensors for organic radicals.

The amazing progress in computer hardware over the last few years made it possible to apply the exact spin-orbit operator (FULL) to larger and larger systems. This was especially important for the studies of glycol-derived radicals (Chapters 4.4 and 4.5).

The one-center nature of the AMFI spin-orbit operator (a superposition of effective atomic spin-orbit operators) allows a breakdown of the  $\Delta g_{SO/OZ}$  term (eq. (3.67)) into atomic (or fragment) spin-orbit contributions. The atomic analysis is performed by carrying out a number of separate calculations (which employ the same Kohn-Sham wave function and thus do not require much extra computational effort),

in which atomic mean-field spin-orbit operators are only used on specific atoms (or a sets of atoms). The sums of these contributions should correspond closely to the overall  $\Delta g_{SO/OZ}$  result.

### 3.5.3 Gauge Dependence of the $g$ -Tensor

Due to presence of the external magnetic field in the operators,  $g$ -tensor calculations are subject to the so-called “gauge problem”. The results of calculations that use finite basis set depend on the gauge origin of the magnetic vector potential. This problem hampered for a long time calculations of NMR chemical shifts, until distributed-gauge methods, like *gauge including atomic orbitals* (GIAO<sup>119,120</sup>) or *individual gauges for localized orbitals* (IGLO<sup>121</sup>), have been developed. Practical experience with ab initio and DFT calculations<sup>47,122-124</sup> of  $g$ -tensors for small or moderate-size radicals indicated that the gauge dependence of the  $g$ -tensor is usually small and calculations with common gauge origin at the center of charge or at the center of nuclear charges of the molecule provide sufficiently accurate results. A similarly low dependence on gauge was found for larger organic radicals like phenoxyl, tyrosyl, or a number of semiquinone anion radicals. Only in studies on substituted tyrosyl radicals a sizable dependence of the orientation (but not the magnitude) of the principal components was found, making a gauge-independent treatment mandatory.<sup>125</sup> In this thesis we study glycyI-derived radicals, for which a large dependence on the gauge origin was found. The same was observed in test calculations for the Flavin radical (results not included in the thesis). In general, sensitivity to the gauge origin was found for organic radicals with strongly delocalized and asymmetric distribution of unpaired spin density. For accurate calculations, a distributed gauge origin method (in this case the GIAO method) had to be used in combination with the exact spin-orbit operator FULL (see Chapter 3.5.2). Such calculations are very expensive and would not be possible unless the recent remarkable progress in computer hardware.

### 3.6 Studies of Biologically Relevant Radicals. Cooperation of Experiment and Theory

Free radicals usually are associated with unidentified species that exhibit uncontrollable reactivities leading to mutations in DNA and consequently in proteins and are responsible for aging and cancer. In general, it is not recognized that free radicals are vitally important for the functional activity of many proteins. Nature, has developed methods to specifically generate free radicals within protein environments and to exquisitely control their reactivity and life-times in order to avoid any potential promiscuities. A large number of proteins have been proven to utilize free radicals, and many more are expected to do so.<sup>52,126</sup> The protein-derived radicals (bioradicals) can be either covalently bound to the protein - amino acid or modified amino acid based radicals<sup>52</sup> or non-covalently bound cofactors.<sup>56,127-131</sup> The two most prevalent amino acid based radicals are the tyrosyl or modified tyrosyl radicals and the glycyl radicals; less common are transient tyrosyl radicals, thiyl radicals and tryptophan cation radicals. Enzymatic proteins utilizing cofactor-based radicals are, e.g.: the cytochrome P450 enzyme family,<sup>127</sup> flavins and pyrroloquinoline quinone (PQQ) dependent enzymes<sup>128</sup> or heme peroxidases.<sup>129</sup> A large number of cofactor-based radicals, e.g.: semiquinone radical anions, chlorophyll radical cations or bacteriopheophytin radical anions, are employed in the electron transfer of plant (PS-I and PS-II)<sup>130</sup> or bacterial (bRC)<sup>56,131</sup> photosynthetic reactions centers as well as in various respiratory chain complexes.<sup>132</sup>

The mechanisms of biological processes and their structure-function relationship on a molecular level are of interest to scientists of many fields. A number of spectroscopic techniques for investigating protein systems are available including X-ray crystallography, solid-state NMR, site-directed mutagenesis, ultra-fast laser spectroscopy in the visible and IR regions. Yet, the method of prominent role for studying paramagnetic intermediates of biological processes is electron paramagnetic resonance (EPR). The advanced multi-frequency EPR spectroscopy, both in the continuous wave (cw) and pulse mode of operation, has proven to be very powerful for investigations of bioradicals, especially since the advent of the high-frequency/high-field (HF) EPR techniques. EPR techniques are most useful tools to detect, identify, monitor the location and characterize static and dynamic properties of

free radicals in biological systems.<sup>133,134</sup> A unique strength of HF-EPR is the ability to provide detailed information on transient intermediates of proteins in biological action, which can be observed and characterized while staying in their working states on biologically relevant time scales. Interestingly, EPR can also be very useful in studying biological processes that do not involve any stable or transient paramagnetic species or states, such as the light-driven proton transfer in bacteriorhodopsin, by introducing artificial paramagnetic probes, so-called spin labels, into the system, e.g. nitroxide radicals.<sup>135</sup>

A detailed understanding of structure-function relationship of the radical-mediated biological processes requires knowledge of the geometric and electronic structures of the radicals of interest. The subtle details of the electronic structure and distortions by environmental effects can be explored by means of electron nuclear double resonance (ENDOR) techniques by probing the local properties of the unpaired electron wave functions via hyperfine interactions. However, the unambiguous assignment of hyperfine couplings to molecular positions generally impose great problems, which can often be solved only by elaborate isotope labeling and/or single crystal experiments. The global probe of the electronic structure of the radical interacting with its protein environment is provided by the electronic  $g$ -tensor. The best resolution of individual components of hyperfine- and  $g$ -tensors is obtained for single-crystal samples. Unfortunately, the crystal preparation is often difficult or even impossible for large biological systems. The way out is offered by HF-EPR techniques which can resolve even  $g$ -tensors with very small anisotropies. Nevertheless, even fully resolved spectra do not give direct access to the radical structures. The indirect information held by  $g$ - and  $A$ -tensors is very complex and cannot be straightforwardly inferred from the experimental spectra as they depend on the subtle interplay of several different effects, which are not easily dissectable and evaluated. For such difficult cases, analysis by means of quantum chemical methods is indispensable. Theoretical studies can determine the electronic and geometric structure of radicals starting from their spectral properties. They can also provide detailed analyses of different effects determining the observed spectral parameters.

From the very beginning, experimental EPR studies of organic  $\pi$ -radicals were supported by qualitative theoretical methods to analyze spectral parameters. For interpretation of  $g$ -tensors the semi-empirical theory of Stone was used.<sup>28,29</sup> First

interpretations of HFCs of organic free radicals encountered a significant problem as non-zero hyperfine couplings have been measured for atoms lying in the nodal plane of spin-carrying molecular orbitals (SOMO), e.g., aromatic hydrogen atoms. Based on simple molecular orbital theory, there should be no spin density at the positions of the protons and thus no hyperfine couplings. However, the systematic investigation of aromatic radicals allowed one to find out several semi-empirical relationships. The non-zero spin densities on aromatic hydrogen atoms were explained with effect of spin polarization. The proportionality relation known as McConnell equation<sup>136-138</sup> allows determination of the spin density at the carbon atom starting from the experimentally measured hyperfine coupling constants of the directly bound hydrogen atom. A second important relationship is the  $\cos^2 \theta$  proportionality between the isotropic HFC and the dihedral angle  $\theta$  (angle defined by the  $p_z$  orbital on the adjacent carbon on the aromatic ring and the  $C_\beta$ -H bond) of a hydrogen atom that is bound to the  $C_\beta$  position relative to an aromatic radical.<sup>139</sup> These relationships are widely used in biochemical studies of, e.g., tyrosyl radicals.<sup>140</sup>

The quantitative analysis of  $g$ - and HFC-tensors, however, had to wait until more sophisticated treatments were developed. The developments in *ab initio* methods did not affect significantly the field of bioradicals as these methods are applicable only to relatively small systems in vacuum. Fundamental changes followed the development of density functional (DFT) methods,<sup>60,69</sup> Modern DFT approaches for calculations of  $g$ - and HFC-tensors became available allowing treatment of relatively large systems, like organic radicals in their protein environment.<sup>22,25-27,42-48</sup>

DFT methods for calculations of HFCs became available much earlier than those for calculations of  $g$ -tensors and are easily accessible not only to theoretically oriented researchers, but also to experimentalists. The number of papers reporting theoretical studies of HFCs together with experimental data is enormous. Any systematic overview of them is out of scope of this chapter. Examples of detailed theoretical studies of HFCs for various biologically relevant radicals can be found in refs 141-151. Improta and Barone<sup>152</sup> reviewed the HFC calculations for organic free radicals focusing not on aspects of method implementations but on the discussion how computations can shed light on the physicochemical effects determining the experimental results. They have analyzed role of different effects: intrinsic (electronic), environmental or vibrational, in determining isotropic HFCs.



Accurate calculations of  $g$ -tensors have become available only recently. Thus the number of detailed applications to biologically relevant radicals is yet limited. A relatively exhaustive review on ab initio and DFT calculations of  $g$ -tensors for biologically relevant organic radicals in isotropic solutions or in their protein environments is provided in ref 105. Examples have ranged from phenoxy and tyrosyl radicals via nitroxide spin labels to semiquinone radical anions. The other studies mentioned have dealt with sulfur-based radicals or with tryptophan radicals. Only a few additional application studies of  $g$ -tensor calculations have appeared since this review was published. Significant contributions came from our group.<sup>153-160</sup> Some recent works on protein-derived glycy radical focused not so much on solving specific problems as on validating the newly developed methodology for  $g$ -tensor calculations.<sup>161,162</sup> We expect that calculations of  $g$ -tensors will become a standard tool used by experimentalists for analyzing measured data. At present, only a few reports of that kind can be found in the literature, e.g., refs 163 and 164.



## 4 Calculations of EPR Parameters for Bioradicals



## 4.1 Electronic $g$ -Tensors of Semiquinones in Photosynthetic Reaction Centers<sup>153</sup>

### 4.1.1 Introduction

Photosynthesis is the central biological process in which the energy of sunlight is converted into the biochemical energy essential to power life.<sup>56</sup> A wide variety of organisms is able to carry out photosynthesis. The crucial step of photosynthesis, in which the energy of electronic excitation is transformed to chemical redox energy, takes place in the reaction center (RC). The RC is an integral membrane pigment-protein complex incorporating many non-covalently associated cofactors which directly or indirectly take part in the electron transfer (ET) process. The charge separation taking place during ET leads to the formation of various radical pairs, several of which are ideally studied by electron paramagnetic resonance (EPR) spectroscopy. Among the most important bioradicals observed by EPR during the ET process are chlorophyll radical cations, pheophytin radical anions, and semiquinone radical anions.<sup>56</sup> It is the latter anions that are studied here by quantum-chemical methods.

The information that may be extracted from EPR of bioradicals has recently been enhanced tremendously by the development of high-field/high-frequency EPR (HF-EPR).<sup>55,165</sup> In particular, the electronic  $g$ -tensor may be resolved at higher magnetic fields and microwave frequencies. Importantly, the  $g$ -tensor has been shown to depend crucially not only on the type of semiquinone, but even more on the interactions of the semiquinone with the protein environment. This makes electronic  $g$ -tensors an important spectroscopic probe of semiquinone-protein interactions. An increasing number of HF-EPR experiments have now provided  $g$ -tensor information on semiquinones, either in frozen solution or in their natural protein environment.<sup>166,167</sup> Significant differences in the semiquinone  $g$ -tensors of different RCs have been found, due to environmental influences. For example, the  $g$ -tensor anisotropy of phyllosemiquinone (Vit-K<sub>1</sub><sup>•</sup>) in the A1 binding site of Photosystem I

(PS-I) RC was found to be larger than one would expect (given the nature of the two semiquinones) from that of the ubisemiquinone ( $UQ^{\bullet}$ ) in the  $Q_A$  binding site of bacterial RCs (bRC). The  $g$ -anisotropy of the latter is in turn slightly larger than that for the same semiquinone in the  $Q_B$  binding site of bRCs.<sup>168-173</sup> These differences are thought to be mainly due to different non-covalent interactions with the protein environment. The main interactions are hydrogen bonds to the carbonyl oxygen atoms of the semiquinone, but  $\pi$ - or T-stacking interactions are also at the focus of current research.<sup>174</sup> As the same interactions influence also the redox potentials of the quinone/semiquinone redox couples and thus their function in the ET, detailed insight into the interrelations between  $g$ -tensor and environment is of considerable interest.

Quantum chemical calculations may provide central information about these interrelations. While semiempirical methods have provided important qualitative insights into the  $g$ -tensors of semiquinone radical anions,<sup>175,176</sup> quantitative treatments became possible only recently, in particular by using density functional theory (DFT). In a recent systematic DFT study of various semiquinones, quantitative agreement with experimental  $\Delta g_x$  components measured in frozen 2-propanol has been achieved after scaling by a factor of 0.92, whereas the  $\Delta g_y$  components were reproduced within experimental accuracy without scaling.<sup>51</sup> To achieve this accuracy, hydrogen bonding to solvent molecules, as well as the conformational arrangement of the substituents of the semiquinones, had to be taken into account accurately<sup>51</sup> (see refs 177 and 178 for further DFT and MCSCF studies of  $g$ -tensors for semiquinone radical anions). The same DFT method<sup>45</sup> was then applied to understand interactions between tryptophan (Trp) and quinones/semiquinones in the  $A_1$  binding site of PS-I.<sup>174</sup> It was shown that the unusually large  $\Delta g_x$  and  $\Delta g_y$  values measured in reaction centers reconstituted with smaller quinones<sup>179,180</sup> may be explained by novel T-stacking hydrogen-bonding interactions between the Trp N-H function and the  $\pi$ -system of the semiquinone. This may have appreciable consequences for the role of Trp residues in the neighborhood of quinones in biological systems.<sup>174</sup>

Here we use the same DFT approach<sup>45,51</sup> to study the  $g$ -tensors of a wider set of semiquinone active sites of photosynthetic RCs. The purpose of this study was 2-fold: (a) to confirm the predictive power of the method found for in vitro systems also for a number of realistic models from protein environments and (b) to analyze in detail the influence of the various semiquinone-protein interactions on the computed  $g$ -tensors.

The study concentrates on models for three distinct active sites of RCs, for which high-resolution X-ray structures are available:<sup>181,182</sup> the A<sub>1</sub> phylloquinone binding site of PS-I and both Q<sub>A</sub> and Q<sub>B</sub> ubiquinone binding sites of bRC. In addition, we include models for ubisemiquinone in frozen 2-propanol, in extension of the study in ref 51. We carry out calculations for realistic models of the entire active site, as well as for systems that include only a subset of the semiquinone-protein interactions. Together with further analysis tools, this is expected to shed light on the influence of specific residues on the  $g$ -tensor.

## 4.1.2 Computational Details

### 4.1.2.1 Structures

The models for ubisemiquinone in the Q<sub>A</sub> and Q<sub>B</sub> sites (see Figure 4.1.1 and Figure 4.1.2, respectively) were based on the 2.6 Å resolution X-ray structure obtained for *Rhodobacter (Rb.) sphaeroides* in the charge-separated P<sup>+</sup>Q<sub>B</sub><sup>•-</sup> state.<sup>181</sup> Three residues interact strongly with UQ<sup>•-</sup> in the Q<sub>A</sub> binding site (Ala M260, His M219, Trp M252), among which Ala M260 and His M219 hydrogen-bond to the two semiquinone carbonyl oxygen atoms, whereas Trp M252 exhibits a moderate  $\pi$ -stacking interaction with UQ<sup>•-</sup>. In our model, Ala M260 was substituted by an nmf (*N*-methylformamide) molecule, His M219 by imidazole, and Trp M252 by indole. The isoprenoid side chain of UQ<sup>•-</sup> is not expected to influence the  $g$ -tensor appreciably<sup>51</sup> and was replaced either by a methyl or an ethyl group. The same substitution was applied to all other models. Overall, the model for Q<sub>A</sub> consisted of the semiquinone UQ-M<sup>•-</sup> or UQ-EM<sup>•-</sup> [2,3-dimethoxy-5,6-dimethyl or 5-ethyl-6-methyl-1,4-benzoquinone, respectively], nmf, imidazole, and indole (Figure 4.1.1).

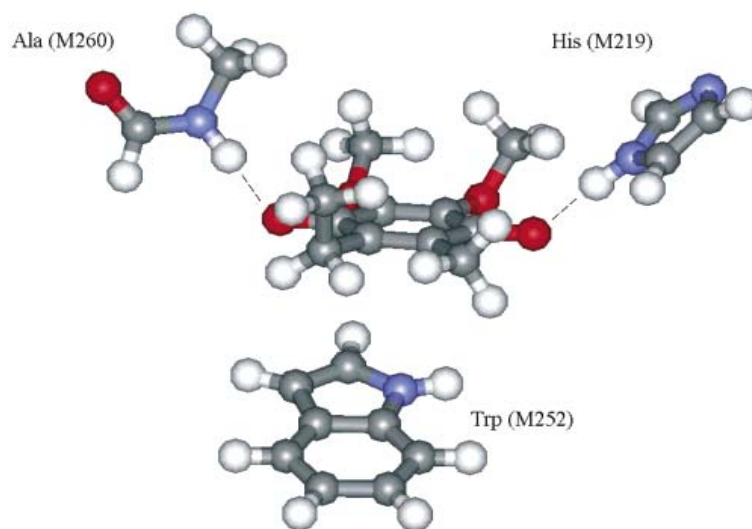


Figure 4.1.1 Model of the  $Q_A$  binding site of bRC, with  $UQ-EM^{\bullet-}$ , nmf, histidine and indole.

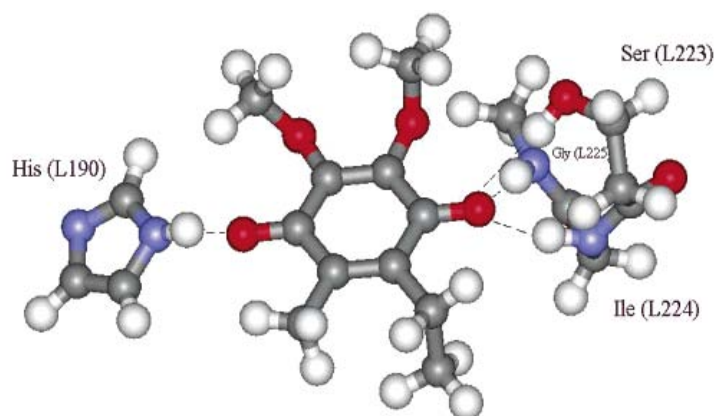


Figure 4.1.2 Model of the  $Q_B$  binding site of bRC, with  $UQ-EM^{\bullet-}$ , histidine and SIG-fragment.



Four amino acid residues (His L190, Ser L223, Ile L224, Gly L225) have been included in our model of the Q<sub>B</sub> binding site, all of which participate in hydrogen bonding to the two semiquinone carbonyl oxygen atoms. His L190 was modeled by imidazole. The part of the protein backbone consisting of Ser L223, Ile L224, and Gly L225 (SIG fragment) was directly cut out of the crystallographically determined structure and terminated by hydrogen atoms as follows: the amino group of Ser, the carbonyl group of Gly, and the hydrocarbon side chain of the Ile were each replaced by hydrogen (Figure 4.1.2). In view of the flexibility of the Q<sub>B</sub> site, we regard it as essential that intermolecular parameters could be extracted from the charge separated P<sup>+</sup>Q<sub>B</sub><sup>•-</sup> state. As this should provide more realistic hydrogen bonding, we chose this 2.6 Å resolution structure<sup>181</sup> over available “ground-state structures” at higher resolution. Note that a recent 3.0 Å resolution structure of the P<sup>+</sup>Q<sub>A</sub><sup>•-</sup> state indicated no structural changes in the Q<sub>A</sub> site relative to the P<sup>+</sup>Q<sub>B</sub><sup>•-</sup> state (see results quoted in ref 166), and therefore we regard it as appropriate to use the data for this state also as a starting point for our model of the Q<sub>A</sub> site (see above). Note that, in addition to the X-ray data, EPR and ENDOR have provided further evidence for the presence or absence of semiquinone-protein interactions in these sites.<sup>166,167,183</sup> In the present study we neglect the potential influence of the iron atom that is located between the Q<sub>A</sub> and Q<sub>B</sub> sites, coordinated to His M219 on the Q<sub>A</sub> side and to His L190 on the Q<sub>B</sub> side. We cannot exclude completely the possibility that this center (or the zinc atom by which iron is often replaced to obtain simplified EPR spectra) might provide a small additional influence on the *g*-tensors of the semiquinones in both sites. This could be either by direct electrostatic effects or by an indirect slight polarization of the hydrogen bonds from histidine to the corresponding semiquinone. These potential influences will be the subject of further studies.

Our model for the A<sub>1</sub> binding site of PS-I is based on the 2.5 Å resolution X-ray structure for the cyanobacterium *Synechococcus elongatus*.<sup>182</sup> The relevant interactions include phyllosemiquinone (Vit-K<sub>1</sub><sup>•-</sup>) and two amino acid residues (Leu A722 and Trp A697). Vit-K<sub>1</sub><sup>•-</sup> was modeled by DMNQ<sup>•-</sup> or EMNQ<sup>•-</sup> (2,3-dimethyl or 2-ethyl-3-methyl-1,4-naphthosemiquinone), Leu A722 was substituted by nmf, and Trp A697 by indole (see Figure 4.1.3). Again, the choice of interacting residues is consistent with further EPR and ENDOR data, and also with recent mutation studies

that indicate negligible spectroscopic changes upon modification of a nearby hydrogen bonding network that includes residues Tyr A696, Ser A692, and Met A688.<sup>184,185</sup>

To reproduce the *g*-tensors accurately, it was mandatory to account properly for hydrogen bonding to the carbonyl oxygen atoms, as well as for the conformational arrangement of the substituents of the semiquinone. We kept intermolecular structure parameters, as well as the dihedral angles of the methoxy substituents in UQ<sup>•</sup>, at their crystallographic values. However, in view of the limited accuracy of the protein crystallographic data, all other intramolecular parameters were substituted by values obtained from full DFT optimizations performed for each individual component of the models. The optimizations were carried out at the gradient-corrected DFT level (BP86 functional<sup>78,80</sup>), with the Gaussian 98 program.<sup>186</sup> As in the previous studies,<sup>51,174</sup> effective-core potentials (ECPs) and DZP valence basis sets were used for C, O, and N,<sup>187</sup> and a DZV basis set for hydrogen.<sup>188</sup> As the crystallographic data files contain only information about the positions of heavy atoms, most hydrogen atom positions were fully optimized for a given fragment. The available information on hydrogen bond lengths from ENDOR data is not very accurate.<sup>166</sup> Therefore, the positions of most hydrogen atoms participating in hydrogen bonds (with the exception of the SIG fragment in the Q<sub>B</sub> site, see above) were obtained by restricted optimizations of bimolecular complexes of the semiquinone with the corresponding hydrogen bond donor, keeping all further inter- and intramolecular structural parameters constant. The following hydrogen bond lengths have been obtained and were employed in the *g*-tensor calculations. Q<sub>A</sub> site: UQ-EM<sup>•</sup>-nmf 1.82 Å, UQ-EM<sup>•</sup>-imidazole 1.78 Å. Q<sub>B</sub> site: UQ-EM<sup>•</sup>-imidazole 1.81 Å, UQ-EM<sup>•</sup>-SIG 2.24 Å (Ser L223), 1.98 Å (Ile L224), and 2.39 Å (Gly L225).<sup>189</sup> A<sub>1</sub> site: EMNQ<sup>•</sup>-nmf 1.85 Å. These values agree reasonably well with spectroscopic estimates.<sup>166</sup>

To model UQ<sup>•</sup> in frozen 2-propanol, the fully DFT-optimized structures of dimethyl-substituted model complexes [UQ-M<sup>•</sup>(2-PrOH)<sub>6</sub> or UQ-M<sup>•</sup>(2-PrOH)<sub>4</sub>] were taken from ref 51. In addition, the corresponding complexes with UQ-EM<sup>•</sup> were also fully optimized at the BP86/DZP level (see, e.g., Figure 4.1.4). The optimized hydrogen bond lengths were 1.74-1.78 Å for the four hydrogen-bonds to the carbonyl oxygen atoms and 1.80 Å for the two hydrogen-bonds to the methoxy substituents.

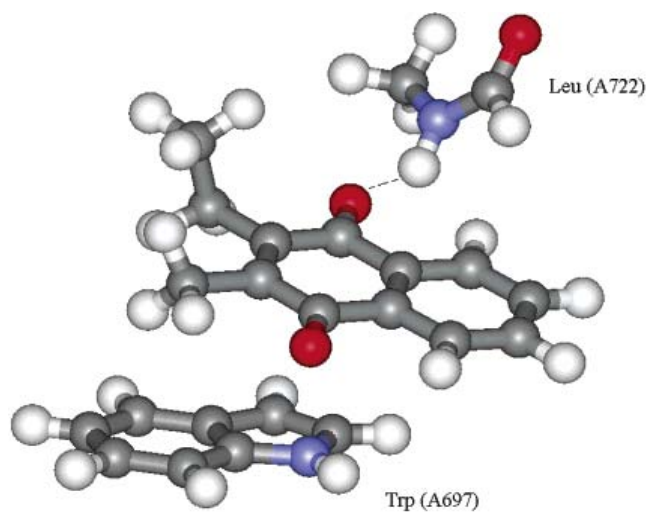


Figure 4.1.3 Model of the  $A_1$  binding site of Photosystem I, with  $EMNQ^{\bullet-}$ , nmf and indole.

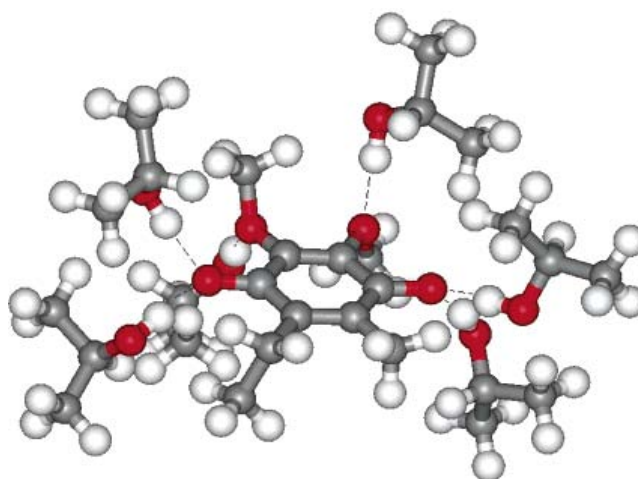


Figure 4.1.4  $UQ-EM^{\bullet-}(2-PrOH)_6$  model of ubisemiquinone in frozen 2-propanol solution.

### 4.1.2.2 g-Tensor Calculations

All details of the *g*-tensor calculations were as described in ref 51 and in Chapter 3. Here only the features specific to the studies presented in this chapter are summarized. The calculations used the deMon program<sup>99</sup> and the associated *g*-tensor module.<sup>45</sup> The uncoupled DFT level was employed, with the BP86 functional<sup>78,80</sup> and DZVP basis sets.<sup>188</sup> As has been shown previously,<sup>45,51</sup> the modest DZVP basis set provides a good compromise between accuracy and computational effort. The one- and two-electron spin-orbit (SO) operators were treated by the accurate and efficient all-electron atomic mean-field approximation (AMFI),<sup>115,116</sup> which has the main advantage of covering the important spin-other orbit contributions<sup>45,106</sup> (cf. Chapter 3.5.2). The common gauge origin for the magnetic vector potential was chosen to be at the midpoint between the two carbonyl oxygen atoms. This is justified by previous experience, and by the overall low gauge dependence of the *g*-tensor components (compared to, e.g., the NMR chemical shift tensor). As discussed already in Chapter 3, the *g*-tensor is defined as  $\mathbf{g} = g_e(\mathbf{1}) + \Delta\mathbf{g}$ , where  $g_e = 2.002319$ . In the following we present and discuss *g*-shift ( $\Delta g$ ) values defined as a correction to the free-electron value in ppm (that is, in units of  $10^{-6}$ ).

The calculations in this chapter are on supermolecular model complexes that account for the direct interactions of the semiquinones with the neighboring amino acid residues, whereas further long-range electrostatic contributions are neglected. The use of continuum solvent models in *g*-tensor calculations has been recently evaluated.<sup>190</sup> After accounting for explicit hydrogen-bond interactions in protic solvents using supermolecular models, the continuum solvent model made only very small further contributions to the *g*-tensor. This was even the case when the dielectric constant for water of  $\epsilon = 78.39$  was employed.<sup>190</sup> Given the much smaller dielectric constants of  $\epsilon = 4$  that are usually considered for proteins, we do not expect major effects of continuum solvent models when added to our supermolecular systems. Obviously, these considerations do not apply to charged residues, where generally more important long-range effects might be expected (see discussion above). A consideration of dynamical effects on the *g*-tensor is outside the scope of this study but these was currently investigated by ab initio molecular dynamics simulations for

semiquinones in aqueous solution.<sup>159,160</sup>

### 4.1.3 Results and Discussion

The computed g-shift components of the investigated model complexes are collected in Table. 4.1.1, which includes also the experimental HF-EPR reference values. In the following, we will focus mostly on the most characteristic  $\Delta g_x$  component (parallel to the carbonyl C-O vectors), which depends particularly on the environment. We will also point out specific features in  $\Delta g_y$  (in-plane but perpendicular to the C-O vectors). The  $\Delta g_z$  component (out-of-plane) cannot be discussed meaningfully, as it is too small (and dominated by diamagnetic contributions). Note that in all cases studied here, the orientation of the tensor deviates by less than 5°, but usually even by less than 2°, from ideal alignment with the semiquinone framework.

As was found in the comparison between computed and experimental values for a series of semiquinones in frozen 2-propanol,<sup>51,174</sup> deficiencies in the currently available state-of-the-art gradient-corrected density functionals cause a systematic overestimate of  $\Delta g_x$  by ca. 8-10%. This may be corrected via scaling by 0.92.<sup>51,191</sup> After scaling (values in parentheses in Table. 4.1.1), the computed  $\Delta g_x$  results for the best (complete) models agree remarkably well with experiment in all four cases studied here. Maximum deviations from experiment are typically in the range of ca. 100 ppm, which has also been reported as the typical experimental uncertainty in current HF-EPR experiments.<sup>168,169</sup> As found for the previously studied in vitro systems,<sup>51</sup> results for  $\Delta g_y$  are generally within these limits without any scaling.<sup>191</sup> In the following discussion, we will use the scaled  $\Delta g_x$  and unscaled  $\Delta g_y$  values. Table. 4.1.1 also provides previous results<sup>174</sup> for the DMNQ•<sup>-</sup> (indole-nmf) model of the A<sub>1</sub> site. The  $\Delta g_x$  component is about 100 ppm larger in these calculations than in the presented here studies, due to the fact that MP2- rather than DFT-optimized fragment structures were employed (MP2 optimizations were used consistently in ref 174, to account for dispersion contributions to  $\pi$ -stacking interactions, in particular for neutral quinone-indole complexes).

Table 4.1.1 Computed and Experimental g-Shift Components (in ppm) for Semiquinone Radical Anions with a Breakdown of Active-Site Models into their Constituent Contributions.

<b>Model</b>	$\Delta g_x^a$	$\Delta g_y$	$\Delta g_z$
<b>exp Q<sub>A</sub><sup>•-</sup> in Zn-bRCs<sup>b</sup></b>	<b>4300</b>	<b>3100</b>	<b>-100</b>
<b>exp Q<sub>A</sub><sup>•-</sup> in Zn-bRCs<sup>c</sup></b>	<b>4170</b>	<b>3000</b>	<b>-220</b>
UQ-M <sup>•-</sup> (imidazole - nmf – indole)	4659 (4286)	3061	12
UQ-EM <sup>•-</sup> (imidazole - nmf – indole)	4730 (4352)	3052	11
UQ-EM <sup>•-</sup> (nmf – indole)	5070 (4664)	3153	23
UQ-EM <sup>•-</sup> (imidazole – indole)	5171 (4757)	3136	7
UQ-EM <sup>•-</sup> (indole)	5439 (5224)	3301	24
UQ-EM <sup>•-</sup> (imidazole – nmf)	4629 (4259)	2998	-61
UQ-EM <sup>•-</sup> (nmf)	4983 (4584)	3120	-43
UQ-EM <sup>•-</sup> (imidazole)	5053 (4649)	3110	-16
UQ-EM <sup>•-</sup>	5298 (4874)	3243	-5
<b>exp UQ-10<sup>•-</sup> in 2-PrOH<sup>d</sup></b>	<b>4140</b>	<b>3100</b>	<b>-100</b>
<b>exp UQ-3<sup>•-</sup> in 2-PrOH<sup>e</sup></b>	<b>3900</b>	<b>2940</b>	<b>-220</b>
UQ-M <sup>•-</sup> (2-PrOH) <sub>6</sub>	4425 (4071)	2944	20
UQ-EM <sup>•-</sup> (2-PrOH) <sub>4</sub>	4269 (3927)	2880	47
UQ-EM <sup>•-</sup> (2-PrOH) <sub>6</sub>	4393 (4042)	2927	70
UQ-EM <sup>•-</sup>	5853 (5385)	3325	1
<b>exp. Q<sub>B</sub><sup>•-</sup> in Zn-bRCs<sup>c</sup></b>	<b>3940</b>	<b>2950</b>	<b>-190</b>
UQ-M <sup>•-</sup> (imidazole – SIG)	4202 (3866)	2902	-68
UQ-EM <sup>•-</sup> (imidazole – SIG)	4254 (3914)	2874	-68
UQ-EM <sup>•-</sup> (SIG)	4716 (4339)	3014	-60
UQ-EM <sup>•-</sup> (imidazole)	5004 (4604)	3110	-41
UQ-EM <sup>•-</sup>	5251 (4831)	3234	-30
<b>exp. A<sub>1</sub><sup>•-</sup> in PS-I<sup>f</sup></b>	<b>3900</b>	<b>2750</b>	<b>-140</b>
DMNQ <sup>•-</sup> (indole – nmf)	4082 (3755)	2699	-12
DMNQ <sup>•-</sup> (indole – nmf), MP2 <sup>g</sup>	4227 (3889)	2707	14
EMNQ <sup>•-</sup> (indole – nmf)	4129 (3799)	2683	-9
EMNQ <sup>•-</sup> (indole)	4458 (4101)	2785	32
EMNQ <sup>•-</sup> (nmf)	4219 (3881)	2679	36
EMNQ <sup>•-</sup>	4548 (4184)	2791	-5

<sup>a</sup> Values in parentheses have been scaled by 0.92 (cf. ref 51). <sup>b</sup> W-band EPR for zinc-substituted bRC.<sup>168</sup> <sup>c</sup> Q-band EPR in zinc-substituted bRC of *Rb. sphaeroides* R-26, with fully deuterated UQ-10<sup>•-</sup>.<sup>173</sup> <sup>d</sup> W-band EPR in frozen 2-propanol.<sup>168,169</sup> <sup>e</sup> Q-band EPR in 2-propanol-*d*<sub>8</sub> (ref 192). <sup>f</sup> Transient spin-polarized W-band EPR on P<sub>700</sub><sup>•+</sup>A<sub>1</sub><sup>•-</sup> in a PS-I single crystal.<sup>170</sup> <sup>g</sup> MP2-optimized structure employed, cf. ref 174

We note in passing that differences between methyl- and ethyl-substituted model semiquinones are rather small (the largest difference is 66 ppm for  $\Delta g_x$  in the  $Q_A$  site). The computed results for the isolated semiquinones ( $\Delta g_x = 4184$  ppm for  $EMNQ^{\bullet-}$  and  $\Delta g_x \approx 4800$  ppm for  $UQ-EM^{\bullet-}$ ) show that part of the difference between observed  $g$ -anisotropies for the PS-I and bRC active sites arises from the intrinsic properties of the semiquinone (see also refs 175,176 and 51 for analyses). Large effects of methoxy group conformations in ubisemiquinone models on  $g$ -shifts have already been identified in ref 51. In our models, both angles and dihedral angles defining the conformations of the methoxy substituents were taken unchanged from the X-ray structure files. The small difference in the  $\Delta g_x$  values (43 ppm) for isolated  $UQ-EM^{\bullet-}$  in the  $Q_A^{\bullet-}$  and  $Q_B^{\bullet-}$  models reflects slight differences in the out-of-plane dihedral angles and bond angles of the methoxy substituents (see also below).

While the intrinsic properties of the semiquinone contribute to the differences between the  $A_1$  site of PS-I and the bacterial reaction centers, it is mainly the environmental interactions that modify the  $\Delta g_x$  values for the different ubisemiquinone-based systems. As is well-known, the decisive influence is that of the hydrogen bonding to the carbonyl oxygen atoms. This reduces  $\Delta g_y$  to some extent, but in particular  $\Delta g_x$  is reduced noticeably (Table 4.1.1). In the  $A_1$  binding site model, the single hydrogen bond to nmf (model for Leu A722) reduces  $\Delta g_x$  of isolated  $EMNQ^{\bullet-}$  by 303 ppm (7%). The two hydrogen bonds (models for Ala M260, His M219) in the  $Q_A$  binding site of bRC decrease  $\Delta g_x$  of isolated  $UQ-EM^{\bullet-}$  by 615 ppm (13%), whereas in the  $Q_B$  binding site the reduction is 917 ppm (19%), due to four hydrogen bonds of variable orientation and strength (models for His L190, Ser L223, Ile L224, Gly L225). Interestingly, the effect of four hydrogen-bonds in the  $Q_B$  site is not twice larger than that of two hydrogen-bonds in the  $Q_A$  site, probably due to the fact that some of the bonds in the  $Q_B$  site are noticeably longer than the hydrogen-bonds to Ala M260 and His M219 in the  $Q_A$  site. As discussed further below, the effects of different hydrogen bonds do not necessarily have to be additive.

Experimentally, both  $\Delta g_x$  and  $\Delta g_y$  in the  $Q_B$  site are somewhat lower than in the  $Q_A$  site. This is well reproduced by the calculations and reflects the more pronounced hydrogen bonding in the  $Q_B$  site, which is furthermore known to be open to the cytoplasm via a hydrophilic channel.<sup>56</sup> Interestingly, the calculations suggest that both

$\Delta g_x$  and  $\Delta g_y$  in the models for UQ-10 $\bullet^-$  in 2-propanol are intermediate between the  $Q_A$  and  $Q_B$  results (experimental results for UQ-10 $\bullet^-$  agree with this notion, whereas the values for UQ-3 $\bullet^-$  are lower). As may be seen clearly from the comparison of results for UQ-EM $\bullet^-$  (2-PrOH) $_4$  and UQ-EM $\bullet^-$  (2-PrOH) $_6$ , this is in part due to the extra hydrogen bonds to the methoxy substituents of ubisemiquinone. These additional interactions, which are apparently absent in the two protein environments, have been shown previously to increase both  $\Delta g_x$  and  $\Delta g_y$ .<sup>51</sup>

In addition, comparison of the free ubisemiquinones reveals a significantly larger  $\Delta g_x$  (by more than 500 ppm) and a somewhat larger  $\Delta g_y$  (by ca. 100 ppm) for UQ-EM $\bullet^-$  when taken from the optimized UQ-EM $\bullet^-$  (2-PrOH) $_6$  structure rather than from the  $Q_A$  or  $Q_B$  models. This must reflect the different methoxy-group conformations. The previous analyses showed<sup>51</sup> that dihedral angles between 40° and 60° (as found for optimized isolated ubisemiquinone models) provide particularly low  $\Delta g_x$  and  $\Delta g_y$  values, whereas maximal values are obtained in the range between 90° and 120° (dihedral angles found for solvated supermolecular models<sup>51</sup>). Closer inspection of the methoxy out-of-plane dihedral angles in the systems of interest in this study provides interesting insights: the two methoxy out-of-plane angles in the UQ-EM $\bullet^-$ (2-PrOH) $_6$  system are 92.0° and 98.7°, i.e., both in the range of maximal  $\Delta g_x$  and  $\Delta g_y$ . In contrast, in the  $Q_A$  site, the dihedral angles are ca. 72.5° for the methoxy group closer to the hydrogen bond with His M260, and 125.6° for that close to the hydrogen-bond with Ala M219 (Figure 4.1.1). In particular the former dihedral angle is already in a range that will lead to lower  $\Delta g_x$  and  $\Delta g_y$ . Inspection of the bRC X-ray data<sup>181</sup> indicates much higher steric demand of the protein backbone near Ala M219 than near His M260. We presume that this forces the lower dihedral angle of the methoxy group near His M260 and thus the lower  $\Delta g_x$  and  $\Delta g_y$  values compared to UQ-EM $\bullet^-$  in the conformation of the UQ-EM $\bullet^-$  (2-PrOH) $_6$  model. Similarly, in the  $Q_B$  site, the steric demand of the backbone near the Ser L223, Ile L224, and Gly L225 residues (SIG fragment in the model, cf. Figure 4.1.2) forces a larger dihedral angle of 99.7°, whereas His L190 hydrogen bonds from the side of the semiquinone opposite the methoxy groups and thus allows a very small dihedral angle of 61.2° for the closest methoxy substituent. Part of this lowering of the  $\Delta g_x$  and  $\Delta g_y$  values for the isolated semiquinones in the structures derived from  $Q_A$  and  $Q_B$  compared to the UQ-



EM<sup>•</sup> (2-PrOH)<sub>6</sub> model survives in the full supermolecular models, i.e., when the environmental effects are taken into account. Together with the extra hydrogen bonds to the methoxy oxygen atoms in solution (see above) these conformational effects explain the relatively low values found experimentally for the protein environment compared to 2-propanol solution (Table 4.1.1), despite the more extensive hydrogen bonding in the latter environment. Note that the conformation of the methoxy substituents is thought to influence also the redox potential of the quinone/semiquinone pair.<sup>166,193</sup>

As was noted previously,<sup>51</sup> the reduction of  $\Delta g_x$  by simultaneous hydrogen bonds to both carbonyl oxygens is more pronounced than the sum of the individual effects of hydrogen bonding to each carbonyl oxygen separately. The same lack of additivity is apparent for both the Q<sub>A</sub> and Q<sub>B</sub> models. While in the Q<sub>A</sub> models the sum of individual reductions of  $\Delta g_x$  from isolated UQ-EM<sup>•</sup> by nmf and imidazole is calculated to be -415 ppm, the total effect of both hydrogen bonds is computed to be -615 ppm. Similarly, the reduction of  $\Delta g_x$  by the sum of individual contributions from the imidazole and SIG fragments in the Q<sub>B</sub> model is -719 ppm, but the total reduction is computed to be -917 ppm. Closer analysis of the nonadditivity showed<sup>51</sup> that in the case of asymmetric hydrogen-bonding the spin density is polarized in the direction of the non-coordinated carbonyl oxygen. The reduced spin-orbit contributions to the  $g$ -shift tensor from the coordinated oxygen are thus partly compensated by an enhancement of SO effects from the non-coordinated oxygen.<sup>51</sup> This compensation by spin polarization ceases to work when hydrogen-bonds exist to both carbonyl oxygen atoms. Spin polarization effects should bear also on the model for the A<sub>1</sub> site, where only one of the carbonyl oxygen atoms is involved in hydrogen bonding. This is expected to keep the reduction of  $\Delta g_x$  by hydrogen-bonding small in this case. The polarization of spin density by unsymmetrical hydrogen bonding is also apparent in experimental and computed  $\beta$ -hydrogen hyperfine coupling constants.<sup>142,145,194,195</sup>

In the Q<sub>A</sub> and A<sub>1</sub> binding sites, further non-covalent interactions arise from  $\pi$ -stacking of the semiquinone with a nearby Trp residue, which has been modeled here by an indole molecule, as in ref 174. The effect of this  $\pi$ -stacking on the  $g$ -tensor is moderate but nonnegligible (see also ref 174), and it appears to be rather different for the Q<sub>A</sub> and A<sub>1</sub> models. In the A<sub>1</sub> model, the effect is small on  $\Delta g_x$  (ca. -80 ppm) and

negligible on  $\Delta g_y$ . In contrast, both  $\Delta g_x$  and  $\Delta g_y$  are *increased* in the  $Q_A$  models. In this case, strong nonadditivity is found for  $\Delta g_x$ ; while a significant effect of +350 ppm is predicted when indole is added to isolated UQ-EM $\bullet$ , the effect is only +93 ppm when the indole is added in the presence of the two hydrogen bonds. Apparently, the presence of hydrogen bonding reduces the influence of  $\pi$ -stacking on  $\Delta g_x$ .

The effect of  $\pi$ -stacking with a nearby Trp residue seems thus to be slightly more pronounced and in the opposite direction in the  $Q_A$  site compared to the  $A_1$  site, although the average  $\pi$ -stacking distance is larger (4.1 Å in  $Q_A$  vs 3.4 Å in  $A_1$ ). These differences appear to be related to the relative arrangements of semiquinone and indole molecules (Figure 4.1.1 and Figure 4.1.3). In the  $A_1$  model they are aligned nearly parallel, with the pyrrole ring of indole eclipsed by the benzosemiquinone ring of EMNQ $\bullet$ . This allows genuine  $\pi$ - $\pi$  interactions. In the  $Q_A$  model, the indole molecule is not only shifted to a side of semiquinone but is also tilted slightly from the parallel alignment ( $\sim 15^\circ$ ), thus reducing  $\pi$ - $\pi$  interactions but potentially enhancing electrostatic polarization effects. The different relative alignment in the two systems results in different polarization of spin densities (Figure 4.1.5), the net effect of which actually turns out to be larger for  $Q_A$  than for  $A_1$ . In the case of the UQ-EM $\bullet$ -indole bimolecular model complex for  $Q_A$ , the intermolecular interaction moderately increases the spin density on both semiquinone carbonyl oxygen atoms in an asymmetric fashion (Figure 4.1.5a). In contrast, in the EMNQ $\bullet$ -indole model for  $A_1$ , the spin density on one carbonyl oxygen O(4) is increased slightly, but that on the other oxygen atom O(1) is reduced much more (Figure 4.1.5b). As oxygen spin-orbit coupling is mainly responsible for the  $g$ -shifts,<sup>51</sup> an overall increase/decrease of spin-density on the carbonyl oxygens will enhance/reduce the  $\Delta g_x$  component (the  $\Delta g_y$  component is affected much less). It should be noted that a recent computational study suggested the  $\pi$ -interactions between semiquinones and indole to be repulsive, or at least inferior to other arrangements, whereas they are clearly attractive for the neutral quinone.<sup>174</sup> In the anionic systems, the computations strongly favored a T-stacking arrangement. This should be kept in mind when we discuss the  $\pi$ -stacking based on the X-ray structure obtained for the neutral quinone.

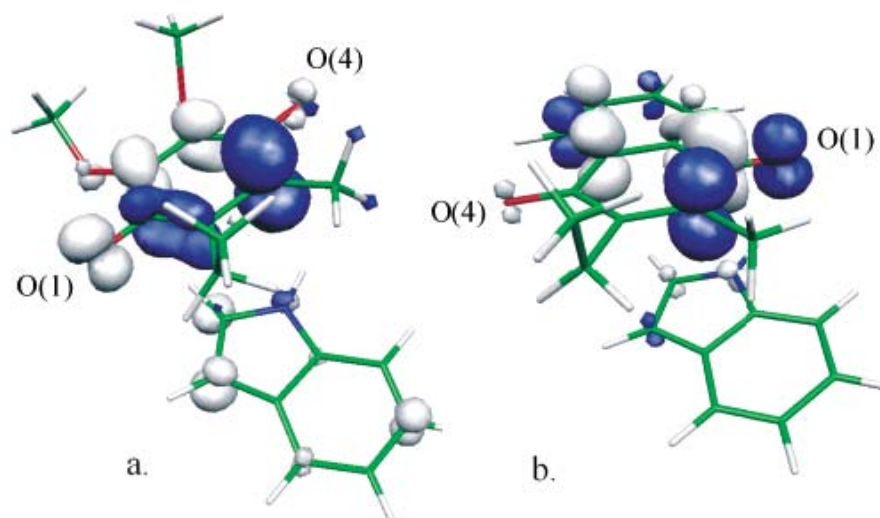


Figure 4.1.5 Plots of differences in spin density ( $\pm 10^{-4}$  au) with and without an indole  $\pi$ -stacking to the semiquinone. Blue isosurfaces indicate a reduction of spin density, gray ones indicate an enhancement due to intermolecular interactions. (a) UQ-EM $\dot{\text{C}}^-$  (indole) from the  $Q_A$  site of bRC; (b) EMNQ $\dot{\text{C}}^-$  (indole) from the  $A_1$  of PS-I.

In view of the rather different  $g$ -tensors computed for isolated (gas-phase) EMNQ $\dot{\text{C}}^-$  and UQ-EM $\dot{\text{C}}^-$  radicals (Table. 4.1.1), the overall  $\Delta g_x$  components in the  $A_1$  and  $Q_B$  sites are remarkably similar. Obviously, the intrinsically lower  $\Delta g_x$  of EMNQ $\dot{\text{C}}^-$  is compensated by the stronger hydrogen-bonding to UQ-EM $\dot{\text{C}}^-$  in the  $Q_B$  site.

A similar breakdown of the individual environmental contributions to the  $g$ -tensor of Vit-K $_1\dot{\text{C}}^-$  in the  $A_1$  site has been attempted recently.<sup>177</sup> Unfortunately, neither the computational methods nor the structural models employed were adequate for a precise analysis. The two-component ZORA method employed neglects spin polarization (as well as spin-other-orbit contributions) and overestimates  $\Delta g_x$  and  $\Delta g_y$  considerably. The environmental effects, which were computed to be much larger than we find here, are therefore probably severely overestimated.

#### 4.1.4 Conclusions

The density functional approach of ref 45 reproduces experimental  $g$ -tensors for semiquinones remarkably well in a variety of protein environments, as well as for frozen protic solution, provided that the  $\Delta g_x$  component is scaled by a factor of 0.92 to account for systematic deficiencies of the currently used density functionals.<sup>45,51,191</sup> We believe that these types of DFT calculations are a valuable tool to augment experimental studies of biradicals, and the computations provide both quantitative predictive power and qualitative insights. A recent application to PS-I is a good further example.<sup>174</sup>

The supermolecular models for the binding sites have been decomposed to analyze the influence of specific semiquinone-protein interactions in detail. The effects of hydrogen-bonding interactions are nonadditive, due to compensating effects of spin polarization in unsymmetrically hydrogen-bonded systems. In addition,  $\pi$ -stacking with nearby Trp residues provides further moderate contributions to the  $g$ -tensor, which are notably different for the  $Q_A$  site of bacterial reaction centers and the  $A_1$  site of PS-I. These differences have been traced back to the different alignment of Trp relative to the semiquinone in the two systems, leading to different spin-polarization contributions. Last but not least, in ubisemiquinone model systems the conformations of the methoxy substituents (and hydrogen-bonding to the methoxy-oxygen atoms) have important influences on the  $g$ -tensor<sup>51</sup> and need to be considered in a full interpretation of EPR data.

## 4.2 Protein-Cofactor Interactions and EPR

### Parameters for the $Q_H$ Quinone Binding Site of Quinol Oxidase<sup>155</sup>

#### 4.2.1 Introduction

Quinone cofactors are found in a remarkable multitude of redox enzymes.<sup>132,196,197</sup> Most often, the quinones employed by nature are ubiquinones (Figure 4.2.1), but phylloquinones, plastoquinones or menaquinones are also frequently found.

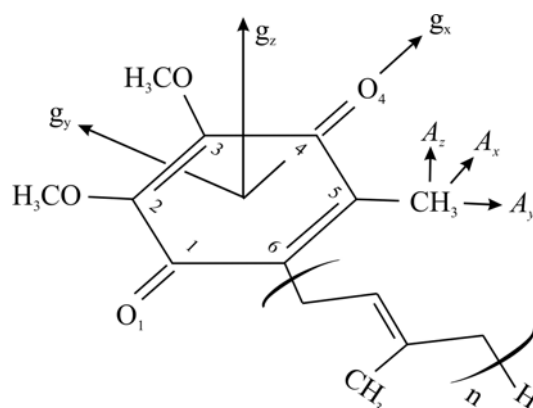


Figure 4.2.1 Structure of a general ubiquinone with atom labelling used throughout this chapter and with orientations of the semiquinone principal  $g$ -tensor and  $^1\text{H}(\text{CH}_3)$  hyperfine tensor components.

More than 50 distinct types of quinone (Q) binding sites associated with respiratory or photosynthetic electron transfer processes are known, and it has been suggested that many more may be discovered.<sup>198</sup> The function of the quinone is often that of a mediator between one-electron and two-electron redox processes. While binding initially either the oxidized quinone or fully reduced quinol, the Q binding sites stabilize the intermediate semiquinone oxidation state in form of the paramagnetic semiquinone radical anion  $Q^{\bullet-}$ . Via spatial confinement of the quinone, the cofactor-protein interactions in the binding site serve to control electron-transfer

processes from other parts of the protein to the quinone and vice versa. The interactions with the protein environment alter the potentials of the various redox states, thereby controlling the specific redox function of the quinone in a given system.<sup>132,196,197</sup> The relevant interactions include a) hydrogen bonds, mainly to the quinone/semiquinone carbonyl oxygen atoms and b)  $\pi$ -stacking, e.g. with tryptophan residues. To understand the function of quinone cofactors in biological redox processes, knowledge of the cofactor-protein interactions is thus essential. Notably, information for the different relevant redox states should ideally be available. While protein crystallography typically provides information only about the neutral quinone or quinol states (but see, e.g., ref 181), the paramagnetic semiquinone state is often most effectively studied by spectroscopic methods, in particular by EPR spectroscopy.<sup>166,167,199</sup> The structurally best characterized quinone binding sites are certainly the  $Q_A$  and  $Q_B$  sites in photosynthetic reaction centers of purple bacteria.<sup>56,181,200,201</sup> The  $A_1$  ( $Q_K$ ) binding sites in photosystem I of higher organisms have also been studied in detail by crystallography<sup>182</sup> and spectroscopy.<sup>170,172,202</sup> Crystal structure information has recently been provided also for the  $Q_0$  and  $Q_i$  sites of the respiratory  $bc_1$  complexes,<sup>203-205</sup> and for the menaquinone binding site of bacterial fumarate reductase.<sup>206,207</sup> At this point we will neglect the large number of characterized pyrroloquinolinequinones (PQQ) and flavins that may also be viewed as quinone redox cofactors.<sup>208</sup>

Often, however, less structural information is available, and what information there is may be incomplete or less direct. Then spectroscopy and computations may help to better understand the structures of the binding sites. In this chapter we will use quantum chemical methods, combined with recently obtained multi-frequency EPR data<sup>209</sup> and further available information, to elucidate the principal semiquinone binding mode in the “high-affinity” quinone binding site ( $Q_H$ ) in cytochrome  $bo_3$  ( $bo_3$  ubiquinol oxidase, QOX). The  $bo_3$  QOX belongs to the family of terminal copper-heme oxidases of the respiratory chain.<sup>210</sup> In bacteria like *Escherichia coli*, the function of this enzyme is thus analogous to that of the mitochondrial cytochrome *c* oxidase,<sup>211-214</sup> that is the four-electron reduction of molecular oxygen to water in the cytoplasmic membrane. While the mechanism of dioxygen reduction is closely similar to cytochrome *c* oxidase (and the structural and functional elements involved are almost identical), in  $bo_3$  QOX the electrons needed for reduction of  $O_2$  do not derive

from cytochrome *c* but from membrane-soluble ubiquinol-8. Ubiquinol oxidase is thought to have two ubiquinol binding sites, a low-affinity  $Q_L$  and a high-affinity  $Q_H$  site.<sup>215</sup> The  $Q_H$  binding site has been suggested to act as a redox mediator between the two-electron oxidation of the quinol pool and the individual one-electron processes involved in reduction of oxygen at the heme-copper center.<sup>215</sup> It changes redox states between a quinone and a reduced semiquinone state. The X-ray structure of the bacterial *bo*<sub>3</sub> complex has been solved recently at 3.5 Å resolution,<sup>216</sup> but no quinones were bound in the crystal form. Functional studies combined with site-directed mutagenesis suggested a putative  $Q_H$  binding site, and four residues were postulated to be involved in direct binding to the cofactor (labels as for *Escherichia coli*): Asp75, Arg71, His98, and Gln101.<sup>198</sup> Clear information on individual interactions is, however, not available from these studies.

In this situation, EPR spectroscopy may provide additional important information, specifically on the semiquinone state.<sup>166,167</sup> Indeed, there have been several recent EPR and ENDOR studies of the  $Q_H$  semiquinone signal in the bacterial *bo*<sub>3</sub> QOX complex.<sup>209,217-221</sup> X-band EPR spectra provided evidence for the stabilization of a semiquinone radical anion in the  $Q_H$  site.<sup>217,218</sup> Numerical simulations of Q-band cw-EPR spectra<sup>219</sup> suggested that features seen in X-band spectra arise from hyperfine coupling to the protons of the ubisemiquinone methyl group in position 5 (Figure 4.2.1). Indications for exchangeable protons by ENDOR provided evidence for hydrogen bonds, to either one or to both semiquinone oxygens.<sup>219</sup> Based on ESEEM spectra, coupling of the unpaired electron density of the semiquinone radical anion to a nitrogen nucleus was identified, which was assigned as a peptide backbone nitrogen<sup>221</sup> (however an arginine<sup>209</sup> was not be excluded), hydrogen-bonded to the 1-carbonyl oxygen atom (cf. Figure 4.2.1).

Using ubiquinone selectively <sup>13</sup>C-labelled at either the 1- or 4-carbonyl carbon position (Figure 4.2.1), Grimaldi et al. performed multifrequency EPR (X-, Q-, and W-band) measurements.<sup>209</sup> On the one hand, they found an extremely low *g*-tensor anisotropy (low *g<sub>x</sub>* value), which is usually attributed to strong hydrogen bonding.<sup>28,29,126,168,169,173,192,222,223</sup> On the other hand, a large asymmetry of the *A<sub>z</sub>* components of the two <sup>13</sup>C carbonyl hyperfine tensors providing evidence for an appreciably asymmetrical spin density distribution was attributed to very asymmetrical hydrogen bonding. Single-sided hydrogen bonding to the 1-oxygen

position was even suggested.<sup>209</sup> Previous detailed quantum chemical studies of the  $g$ -tensors of semiquinones in various environments showed, however, that single-sided hydrogen bonding to just one of the two carbonyl oxygen atoms will reduce the  $g_x$  component of the  $g$ -tensor much less than the same number of hydrogen bonds distributed over both oxygens, for reasons that we will review further below.<sup>51</sup> Therefore, very low  $g$ -anisotropies appear incompatible with single-sided hydrogen bonding. ENDOR data from plastoquinone-substituted samples were also interpreted in terms of a more symmetrical hydrogen-bonding framework.<sup>220</sup> To characterize the hydrogen bonding environment of the semiquinone radical anion in the  $Q_H$  site of  $bo_3$  quinol oxidase in more detail, these somewhat contradictory findings require further investigation. Here we employ modern density functional methods to compute the  $g$ - and  $A$ -tensors of suitable hydrogen-bonded model complexes. Based on a detailed comparison between computed and experimental  $g$ -tensors and hyperfine tensors, we arrive at an improved binding model for the  $Q_H$  site that involves asymmetric but not single-sided hydrogen bonding. The relevance of the presented here study extends beyond the insight into the target system, quinol oxidase, and provides a systematic investigation of the effects of hydrogen bonding on EPR parameters of ubisemiquinone anions in proteins.

## 4.2.2 Computational Details

### 4.2.2.1 Structure Optimizations and Models

Previous experience in comparison with experiment and with more sophisticated computational approaches suggests that the effects of hydrogen bonds on the EPR parameters of semiquinone radical anions may be modeled well by density functional (DFT) calculations on relatively small supermolecular complexes. This holds for both  $g$ -tensors<sup>51,149,153,159,160,174,190</sup> and hyperfine tensors.<sup>141,143,144,148,193,224-229</sup> In the absence of more specific structural information, we have chosen to employ either water molecules or N-methyl-formamide (nmf), or both, as hydrogen-bond donors to the semiquinone. As the nature of the isoprenoid side chain of the ubisemiquinone radical anion (cf. Figure 4.2.1) has been found both experimentally and computationally to influence the  $g$ -tensor and most hyperfine parameters only negligibly,<sup>168,169,230</sup> it has been replaced by an ethyl group in our

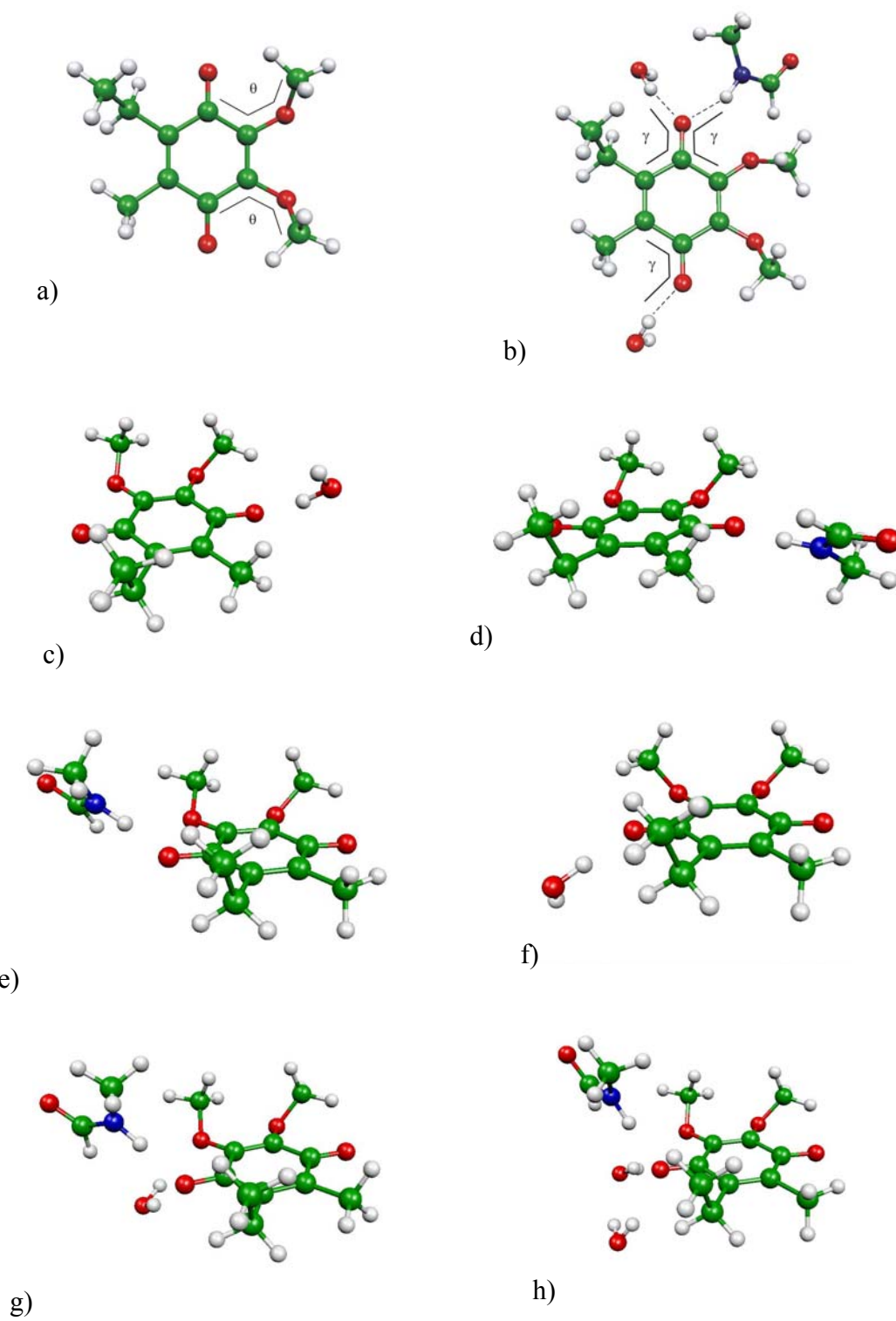


models (UQ-E $\bullet^-$ ). For the majority of models, all substituents were on the same side of the semiquinone ring in the starting structure, as found in the X-ray structure of  $Q_A\bullet^-$ .<sup>181</sup> However, in view of the low rotational barriers,<sup>230</sup> other conformations, such as represented by models 2/1-c and 2/1-d, cannot be excluded. Most of the resulting model complexes are shown in Figure 4.2.2.

All structures have been fully optimized at DFT level, using the gradient-corrected BP86 functional<sup>78,80</sup> and a DZVP Gaussian-type-orbital basis set.<sup>188</sup> SVP auxiliary basis sets<sup>231</sup> were used to fit the electron density (RI-DFT approximation). Unless stated otherwise, the calculations were performed with the TURBOMOLE program<sup>232,233</sup> (version 5.6). In some calculations, we have simulated roughly the electrostatic influence of *heme a*,<sup>216</sup> using a +2 point charge at positions relative to the semiquinone model 2/1-a 1HO-1HN-4HO (Figure 4.2.2b) that are compatible with the suggested binding site.<sup>216</sup> The possibility of a weak single hydrogen bond to O<sub>4</sub> has been evaluated by examining structures, again based on the 2/1-a 1HO-1HN-4HO model (Figure 4.2.2b), in which the hydrogen-bond distance to O<sub>4</sub> was increased in steps of 0.05 Å from the optimized 1.79 Å up to 2.34 Å. Using the same 2/1-a model, the potential effect of very strong hydrogen bonding was investigated by shortening all or only selected hydrogen bonds to 1.60 Å.<sup>155</sup>

Four more specific supermolecular models from a previous computational study presented in Chapter 4.1<sup>153</sup> have been included for comparison: models for ubisemiquinone anion radicals in both the  $Q_A\bullet^-$  and  $Q_B\bullet^-$  binding sites of bacterial reaction centers, one model for ubisemiquinone in frozen 2-propanol (with six isopropanol molecules hydrogen-bonded to ubisemiquinone), and a model for phyllosemiquinone in the  $A_1\bullet^-$  binding site of PS-I. The models from Chapter 4.1<sup>153</sup> were prepared based on crystal structure data for the intermolecular arrangement and on DFT-optimized fragments (with optimization of the positions of the hydrogen-bonded hydrogen atoms in bimolecular complexes<sup>153</sup>). We have initially used those structures directly for the EPR parameter calculations (note that the *g*-tensor results will nevertheless differ slightly from those presented in Chapter 4.1<sup>153</sup> due to a somewhat different *g*-tensor implementation). For the  $Q_A\bullet^-$ ,  $Q_B\bullet^-$ , and  $A_1\bullet^-$  binding-site models, we have additionally performed partial optimizations in which the heavy atoms of the hydrogen-bond donors have been kept at fixed positions, but the entire semiquinone and the hydrogen-bonded protons were free to move (see Table 4.2.2

below for details, as well as Figures 4.1.1-4.1.4 in Chapter 4.1<sup>153</sup>). All these partial optimizations were performed with the Gaussian 03 program.<sup>234</sup>



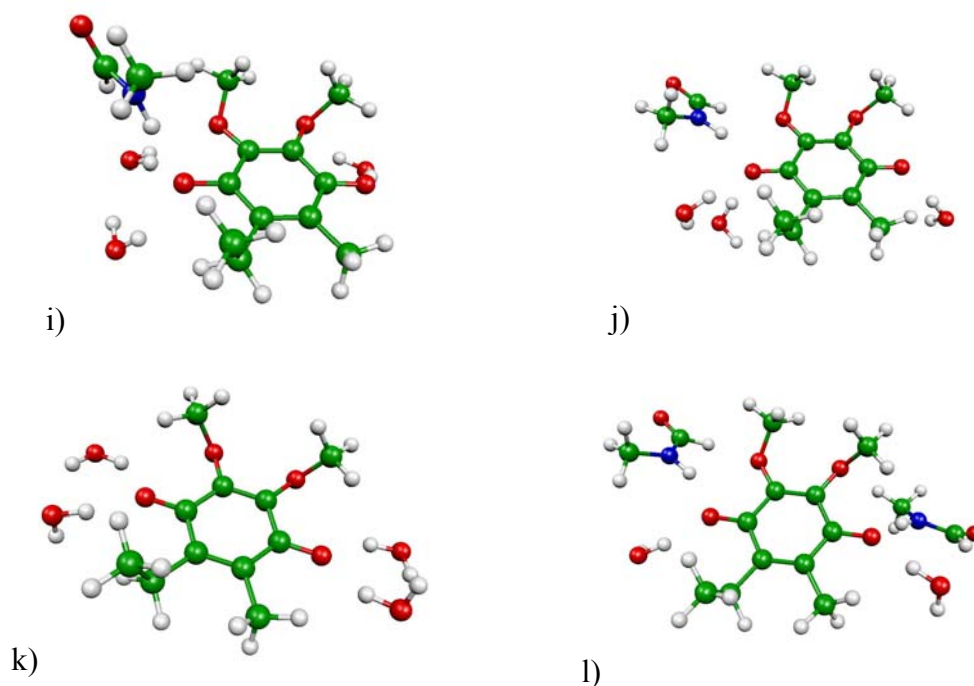


Figure 4.2.2 Optimized structures of supermolecular model complexes studied. Numbers  $n/m$  indicate the number of hydrogen bonds to  $O_1$  and  $O_4$ , respectively, and the labels HO and HN indicate a water molecule and an N-methylformamide molecule, respectively: a) naked  $UQ-E^{\bullet-}$ , 0/0 model; definition of methoxy dihedral angles  $\theta_1$  and  $\theta_2$ ; b) 2/1-a model 1HO-1HN-4HO; definition of hydrogen-bonding dihedral angle  $\gamma$ ; c) 0/1 model 4HO; d) 0/1 model 4HN; e) 1/0 model 1HN; f) 1/0 model 1HO; g) 2/0 model 1HO-1HN; h) 3/0 model 1HO-1HO-1HN; i) 3/1-a model 1HO-1HO-1HN-4HO (this model involves bridging hydrogen bonds to the methoxy oxygen atoms); j) 3/1-b model 1HO-1HO-1HN-4HO; k) 2/2-a model 1HO-1HO-4HO-4HO; l) 2/2-b model 1HO-1HN-4HO-4HN.

#### 4.2.2.2 $g$ -Tensor Calculations

The  $g$ -tensor calculations employed the second-order perturbation approach delineated in refs 45 and 106 and in Chapter 3. The method has been demonstrated to provide unprecedented accuracy in calculations of  $g$ -tensors for organic radicals (see also a recent review on  $g$ -tensor calculations for organic radicals<sup>105</sup>). Unlike most of the previous static calculations of semiquinones,<sup>51,153,174</sup> but analogous to recent dynamical studies of aqueous benzosemiquinone,<sup>159,160</sup> the Kohn-Sham orbitals were

obtained with the TURBOMOLE program and involved fitting of charge density but not of exchange-correlation potential. This provides about 5% larger  $\Delta g_x$  components of the  $g$ -shift tensors compared to previous extensive studies within the deMon program framework, where both density and potential were fitted.<sup>51,153,174</sup> In the latter case, we found RI-BP86/DZVP calculations to overestimate the most sensitive  $\Delta g_x$  tensor component systematically, and a scaling factor of 0.92 was found to provide best agreement between supermolecular model calculations and experimental data in protic solution.<sup>51</sup> Given the larger  $\Delta g_x$  components obtained in the current procedure (also at RI-BP86/DZVP level), a scaling factor of 0.88 is more appropriate<sup>159,160</sup> and will be used throughout this chapter. The unrestricted Kohn-Sham MO information from TURBOMOLE was transferred by appropriate interface routines to the MAG (magnetic resonance) property module of the in-house program ReSpect.<sup>50</sup> The one- and two-electron spin-orbit (SO) operators were treated by the accurate and efficient all-electron atomic mean-field approximation (AMFI).<sup>115,116</sup> The common gauge origin for the external magnetic vector potential was chosen to be at the midpoint between the two carbonyl oxygen atoms. This is expected to be close to the center of spin density. As discussed in Chapter 3, the  $g$ -tensor is defined as  $\mathbf{g} = g_e(\mathbf{1}) + \Delta\mathbf{g}$ , where  $g_e = 2.002319$ , and we present and discuss  $g$ -shift components ( $\Delta g$ ) defined as corrections to the free electron value in ppm (that is, in units of  $10^{-6}$ ).

### 4.2.2.3 Hyperfine Tensor Calculations

All hyperfine coupling parameters were computed in the usual non-relativistic first-order approach (cf. Chapter 3), using the MAG-ReSpect<sup>50</sup> code based on unrestricted Kohn-Sham wave functions obtained with the TURBOMOLE<sup>232,233</sup> program. It is well-known that gradient-corrected functionals like BP86 underestimate the spin polarization in  $\pi$ -radicals and thus provide less accurate hyperfine couplings. In contrast to the optimizations and  $g$ -tensor calculations the hyperfine calculations used therefore the B3LYP<sup>83,86,87</sup> hybrid functional (in non-local implementation, cf. refs 88 and 89 for a discussion) in combination with the somewhat larger EPR-II<sup>235</sup> basis set (which was specifically designed for hyperfine calculations). Further test calculations with other functionals, and also with the more extended EPR-III basis, provided only relatively minor modifications of the results.

## 4.2.3 Results and Discussion

### 4.2.3.1 Structures of Model Complexes

Figure 4.2.2 shows optimized structures for the chosen model systems. In most cases, the hydrogen bonds occur not too far outside the plane of the semiquinone, with dihedral angles  $\gamma$  typically below  $30\text{-}40^\circ$  (Table 4.2.1; cf. definition of  $\gamma$  in Figure 4.2.2b). Somewhat larger out-of-plane angles occur particularly for models with more than two hydrogen bonds to an oxygen, or when the overall hydrogen-bond situation becomes crowded for other reasons. Some ENDOR data suggest strongly out-of-plane hydrogen bonding in the  $Q_H$  site,<sup>219</sup> and it is possible that our structures do not capture this completely. However, still more pronounced out-of-plane hydrogen bonds would lead to a) slightly larger and not lower  $\Delta g_x$  values (see below),<sup>51</sup> and b) probably to only minor effects on  $^{13}\text{C}(\text{CO})$  and  $^1\text{H}(\text{CH}_3)$  hyperfine tensors. In the absence of more detailed structural information, we regard the chosen models as reasonable. Notably, we have computed EPR parameters for i) naked  $\text{UQ-E}^{\bullet-}$  radical anion, ii) systems with single-sided hydrogen bonding either to  $\text{O}_1$  or to  $\text{O}_4$ , and iii) symmetric or asymmetric double-sided hydrogen bonding. We have found several minimum structures for our most promising 2/1 1HO-1HN-4HO model. They are all within  $3\text{ kJ mol}^{-1}$  of each other and give relatively similar EPR parameters (see below). It is clear that a more complete treatment would have to include extensive molecular dynamics,<sup>159,160</sup> but this is outside the scope of the present study.

In the presence of only one contact to a carbonyl oxygen, the computed hydrogen bond lengths (Table 4.2.1) are similar to those in benzosemiquinone complexes. As soon as we have more than one hydrogen bond, some of the contacts become appreciably longer than found for the parent system,<sup>51</sup> in particular when we force three hydrogen bonds to the same oxygen atom. This is due to the steric influence of the substituents in ubisemiquinones, which is also responsible for the out-of-plane character of the hydrogen bonds. In several of the 2/2, 3/2, 3/1, or 3/0 models, one of the hydrogen bonds to a given oxygen is noticeably longer ( $> 2.0\text{ \AA}$ ) than the other(s), provided more than one water molecule is involved at this site (Table 4.2.1). In previous calculations on a  $\text{UQ-M}^{\bullet-}$  model (dimethoxydimethylsemiquinone) with four (or six) water or alcohol molecules, this behavior

was not observed.<sup>51</sup> Closer analysis indicates that the hydrogen bond preferences are strongly coupled to the conformations of the methoxy substituents (dihedral angle  $\theta$  in Table 4.2.1, see definition in Figure 4.2.2a), and the previous calculations did not represent optimum conformations (computed energies for the present structures are somewhat lower). In the majority of cases, where both methoxy substituents are on the same side of the ring,  $\theta_1$  is near 130-140<sup>0</sup> and  $\theta_2$  near -55<sup>0</sup> to -60<sup>0</sup> (see ref 229 for other DFT calculations on models without hydrogen bonding). This corresponds to both methoxy groups being tilted in the direction of the same carbonyl group (Figure 4.2.2). There are a few exceptions, e.g. for the 1/0 HO model (Figure 4.2.2f) or for both 2/2 models with four water molecules (the 2/2-a model is shown in Figure 4.2.2k), where an opposite orientation is preferred. Obviously, our static optimizations, although carried out from many different starting points, cannot guarantee that we have in all cases found the global minimum. We are currently carrying out ab initio molecular dynamics simulations for aqueous ubisemiquinone<sup>158</sup> (cf. refs 159 and 160 for related work on benzosemiquinone) to obtain further insight into the conformational preferences.

The experimental evidence for the QOX Q<sub>H</sub> site does not seem to suggest hydrogen bonding to the methoxy-substituents<sup>236</sup> (in contrast to protic solution<sup>51</sup>). Therefore we prefer in Table 4.2.1 structures in which the water molecules do not bridge between carbonyl oxygen and methoxy groups. The 3/1-a structure is a notable exception. A wide range of hydrogen-bond out-of-plane angles is found for the more sophisticated Q<sub>A</sub><sup>•-</sup>, Q<sub>B</sub><sup>•-</sup>, and A<sub>1</sub><sup>•-</sup> models (cf. Chapter 4.1<sup>153</sup>). The largest (experimental)  $\gamma$  value is 87° for Q<sub>B</sub><sup>•-</sup>, the smallest 13° for A<sub>1</sub><sup>•-</sup>. The partial reoptimization carried out for all three models resulted in moderate to appreciable reduction of the out-of-plane angles for the Q<sub>A</sub><sup>•-</sup> and Q<sub>B</sub><sup>•-</sup> models but in a slight increase for the A<sub>1</sub><sup>•-</sup> model. Additionally, a contraction of the hydrogen bonds was observed.<sup>155</sup>

Table 4.2.1 Hydrogen bond lengths, hydrogen-bond dihedral angles,<sup>a</sup> and methoxy-group out-of-plane dihedral angles.<sup>a</sup>

Model	d (H $\cdots$ O) in Å; absolute dihedral angle $\gamma$ in deg						Dihedral angles $\theta$ of methoxy groups
	O <sub>1</sub> $\cdots$ HO; $\gamma$	O <sub>1</sub> $\cdots$ HO; $\gamma$	O <sub>1</sub> $\cdots$ HN; $\gamma$	O <sub>4</sub> $\cdots$ HO; $\gamma$	O <sub>4</sub> $\cdots$ HN; $\gamma$	O <sub>4</sub> $\cdots$ HO; $\gamma$	
0/1 4HO				1.76; 51			132; -58
0/1 4HN					1.75; 2		137; -61
1/0 1HN			1.76; 18				138; -58
1/0 1HO	1.76; 21						62; -57
2/0 1HO-1HN	1.79; 58		1.82; 22				139; -58
3/0 1HO-1HO-1HN	1.81; 30	2.08; 63	1.89; 62				130; -55
1/1 1HN-4HN			1.81; 3			1.78; 27	136; -59
3/1-a 1HO-1HO-1HN-4HO	1.80; 29	2.11; 61	1.92; 61	1.88; 40			135; -64
3/1-b 1HO-1HO-1HN-4HO	1.82; 78	2.06; 20	1.95; 11	1.81; 43			140; -59
2/2-a 1HO-1HO-4HO-4HO	1.76; 3	2.10; 24		1.75; 18		2.11; 22	68; -69
2/2-b 1HO-1HO-4HO-4HO	1.75; 0	2.12; 27		1.77; 20		2.11; 55	-82; 63
2/1-a 1HO-1HN-4HO	1.78; 17		1.89; 3	1.79; 32			132; -57
2/1-b 1HO-1HN-4HO	1.78; 17		1.91; 9	1.80; 33			110; -51
2/1-c 1HO-1HN-4HO	1.78; 13		1.90; 8	1.80; 31			106; 60
2/1-d 1HO-1HN-4HO	1.76; 32		1.89; 25	1.79; 38			-92; -60
2/1 1HN-1HN-4HN			1.85; 16 1.93; 2		1.80; 27		137; -59
1/2 1HO-4HO-4HN	1.80; 18			1.79; 14	1.88; 36		58; -66
3/2 1HO-1HO-1HN-4HO-4HN	1.84; 75	2.08; 25	1.97; 11	1.81; 19	1.90; 41		144; -66
2/2 1HO-1HN-4HO-4HN	1.80; 9		1.91; 1	1.80; 24	1.87; 42		142; -65
2/3 1HO-1HN-4HO-4HO-4HN	1.81; 6		1.92; 1	1.88; 78	1.93; 37	1.87; 40	146; -69

<sup>a</sup>Cf. Figures 4.2.2a and 4.2.2b for definition of dihedral angles.

### 4.2.3.2 $g$ -Tensors

Table 4.2.2 compares computed  $g$ -shift tensors for various models with experimental data in a variety of environments, including data for the QOX  $Q_H$  site<sup>209</sup>. Notably, the  $\Delta g_x$  value for the  $Q_H$  site is lower than data for the  $Q_A$  and  $Q_B$  sites in bacterial photosynthetic reaction centers, or even than for isotropic 2-propanol solution. As these reference systems feature extensive (double-sided) hydrogen bonding and a low  $\Delta g_x$  is representative of strong hydrogen bonding, we must conclude that the low  $\Delta g_x$  can only be explained by strong hydrogen bonding.

The computed  $\Delta g_x$  values for the models are significantly too large, and they remain too large even after scaling by 0.88 to account for systematic deficiencies of the DFT method used (cf. 4.2.2 Computational Details). Most notably, the values remain much closer to the large gas-phase value in all models that exhibit single-sided hydrogen bonding to only one carbonyl oxygen atom. This is due to a polarization of the spin density towards the “non-coordinated” oxygen atom. Spin-orbit (SO) contributions from this oxygen atom will partly compensate for the loss of  $\Delta g_{SO/OZ}$  contributions to the  $g_x$  component caused by hydrogen bonding on the other side.<sup>51</sup> Once we add a hydrogen bond to the second carbonyl oxygen atom, we observe immediately an appreciable lowering of  $\Delta g_x$  (cf. ref 51), as now the SO contributions from both oxygen atoms decrease. However, even with the most promising (asymmetric) double-sided 2/1 hydrogen-bond models (e.g. 1HO-1HN-4HO, Figure 4.2.2b), the scaled  $\Delta g_x$  is still about 500 ppm too large. This may be attributed to further factors, e.g. a change of the conformation of the methoxy substituents. It is known that conformational changes of the two methoxy groups may alter  $\Delta g_x$  by up to 600 ppm.<sup>51</sup> Indeed, Table 4.2.2 shows that going from the optimized structure parameters of the 1HO-1HN-4HO model (with  $\theta_1 = 132^\circ$ ,  $\theta_2 = -57^\circ$ ) to those of a fully optimized gas-phase model (with  $\theta_1 = 61^\circ$ ,  $\theta_2 = -57^\circ$ ) reduces  $\Delta g_x$  by about 600 ppm for the free radical (first two rows in Table 4.2.2, scaled values in parentheses). The overall effect in the presence of hydrogen bonding is probably somewhat smaller, due to the general reduction of  $\Delta g_x$ .<sup>51</sup>



Table 4.2.2 g-Shift tensors (ppm) for ubisemiquinone radical anion models.

Model <sup>a</sup>	$\Delta g_x$ <sup>b</sup>	$\Delta g_y$	$\Delta g_z$
0/0 optimized	5466 (4810)	3282	-46
0/0 //2/1 1HO-1HN-4HO	6194 (5451)	3389	-33
0/1 4HO	5481 (4823)	3256	-56
0/1 4HN	5433 (4781)	3193	-50
1/0 1HN	5276 (4642)	3233	-44
1/0 1HO	5254 (4623)	3193	-70
2/0 1HO-1HN	4989 (4390)	3174	-59
3/0 1HO-1HO-1HN	5083 (4473)	3223	-68
1/1 1HN-4HN	4966 (4370)	3090	-71
3/1-a 1HO-1HO-1HN-4HO	4825 (4246)	3203	-121
3/1-b 1HO-1HO-1HN-4HO	4710 (4145)	3124	-36
2/2-a 1HO-1HO-4HO-4HO	4642 (4084)	2961	-129
2/2-b 1HO-1HO-4HO-4HO	4695 (4132)	3001	-88
2/1-a 1HO-1HN-4HO	4660 (4101)	3031	-105
2/1-b 1HO-1HN-4HO	4766 (4194)	3019	-92
2/1-c 1HO-1HN-4HO	4804 (4228)	3018	-84
2/1-d 1HO-1HN-4HO	4786 (4212)	3020	-58
2/1 1HN-1HN-4HN	4691 (4128)	3008	-85
1/2 1HO-4HO-4HN	4672 (4111)	3013	-81
3/2 1HO-1HO-1HN-4HO-4HN	4464 (3928)	3073	-53
2/2 1HO-1HN-4HO-4HN	4444 (3911)	3007	-80
2/3 1HO-1HN-4HO-4HO-4HN	4345 (3824)	3111	-105
<i>Models from Chapter 4.1</i> <sup>153</sup>			
$Q_A^{\bullet-}$ (UQ-EM <sup>•-</sup> -nmf-imd-ind) <sup>c</sup>	5095 (4484)	3052	11
$Q_A^{\bullet-}$ (UQ-EM <sup>•-</sup> -nmf-imd) <sup>c</sup>	5004 (4404)	3003	26
$Q_A^{\bullet-}$ (UQ-EM <sup>•-</sup> -nmf-imd),reopt1 <sup>c</sup>	4569 (4021)	3052	-44
$Q_A^{\bullet-}$ (UQ-EM <sup>•-</sup> -nmf-imd), reopt2 <sup>c</sup>	4693 (4130)	3037	-50
$Q_B^{\bullet-}$ (UQ-EM <sup>•-</sup> -ind-SIG) <sup>c</sup>	4563 (4015)	2890	48
$Q_B^{\bullet-}$ (UQ-EM <sup>•-</sup> -ind-SIG), reopt1 <sup>c</sup>	4352 (3830)	2941	-82
UQ-EM <sup>•-</sup> (iPrOH) <sub>6</sub> <sup>c</sup>	4602 (4050)	2927	85
$A_1^{\bullet-}$ (EMNQ <sup>•-</sup> -nmf-ind) <sup>c</sup>	4428 (3897)	2675	1
$A_1^{\bullet-}$ (EMNQ <sup>•-</sup> -nmf-ind), reopt3 <sup>c</sup>	4366 (3842)	2630	23

Model <sup>a</sup>	$\Delta g_x$ <sup>b</sup>	$\Delta g_y$	$\Delta g_z$
exp. $Q_H^{\bullet-}$ in $bo_3$ -QOX <sup>d</sup>	3611	3111	-119
exp. $Q_A^{\bullet-}$ in Zn-bRCs <sup>e</sup>	4300	3100	-100
exp. $Q_A^{\bullet-}$ in Zn-bRCs <sup>f</sup>	4170	3000	-220
exp. $Q_B^{\bullet-}$ in Zn-bRCs <sup>f</sup>	3940	2950	-220
exp. UQ-10 $^{\bullet-}$ in <i>i</i> PrOH <sup>g</sup>	4140	3100	-100
exp. UQ-3 $^{\bullet-}$ in <i>i</i> PrOH <sup>h</sup>	3900	2940	-220
exp. UQ-3 $^{\bullet-}$ in DME/MTHF <sup>h</sup>	4680	3050	-300
exp. $A_1^{\bullet-}$ in PS-I <sup>i</sup>	3900	2750	-140
exp. $A_1^{\bullet-}$ in PS-I <sup>j</sup>	3930	2710	-49

<sup>a</sup> Cf. Figure 4.2.2. <sup>b</sup> Values scaled by 0.88 in parentheses. <sup>c</sup> Supermolecular model structures adopted from Chapter 4.1 <sup>153</sup>: UQ-EM $^{\bullet-}$  = 5-ethyl-2,3-dimethoxy-6-methyl-1,4-benzosemiquinone; EMNQ $^{\bullet-}$  = 2-ethyl-3-methyl-1,4-naphthosemiquinone; nmf = N-methylformamide; imd = imidazole; ind = indole; reopt1: structure was reoptimized with the positions of all heavier atoms of hydrogen-bond donors frozen; reopt2: the same as reopt1 but with dihedral angles of methoxy groups also kept frozen; reopt3: the position of nmf was reoptimized with coordinates of all other atoms fixed; small differences of  $g$ -tensors with values of ref 153 are due to a slightly different computational level of the  $g$ -tensor calculations. <sup>d</sup> W-band EPR in  $bo_3$ -QOX. <sup>209</sup> <sup>e</sup> W-band EPR for zinc-substituted bRC. <sup>168</sup> <sup>f</sup> Q-band EPR in zinc substituted bRC of *Rb. shaeroides* R-26, with fully deuterated UQ-10 $^{\bullet-}$ . <sup>173</sup> <sup>g</sup> W-band EPR in frozen 2-propanol. <sup>168,173</sup> <sup>h</sup> Q-band EPR in 2-propanol- $d_8$  or DME/MTHF mixtures, respectively. <sup>192</sup> <sup>i</sup> Transient spin-polarized W-band EPR on  $P_{700}^{\bullet+}A_1^{\bullet-}$  in a PS-I single crystal. <sup>170</sup> <sup>j</sup> Photoaccumulated  $A_1^{\bullet-}$  at 283 GHz. <sup>172</sup>

Placing a +2 point charge at one of the presumed positions of the iron atom of *heme a*<sup>20</sup> changes the  $\Delta g_x$  component at most by 50 ppm and the  $\Delta g_y$  component by less than 10 ppm. This suggests that electrostatic contributions from this site should not affect our conclusions. The calculations confirm clearly that the very low  $\Delta g_x$  observed for the  $Q_H$  site is incompatible with single-sided hydrogen bonding. What would happen, if the hydrogen bond on the  $O_4$  site is present but very weak? Figure 4.2.3 shows that an increase of the  $O\cdots H$  distance increases  $\Delta g_x$  essentially linearly but only moderately. In going from optimized 1.80 Å to about 2.20 Å,  $\Delta g_x$  (scaled) for the 2/1 model changes from ca. 4100 ppm to ca. 4250 ppm and thus remains appreciably below the 4514 ppm computed for the single-sided case (cf. Table 4.2.2), with the hydrogen bond to  $O_4$  removed completely.

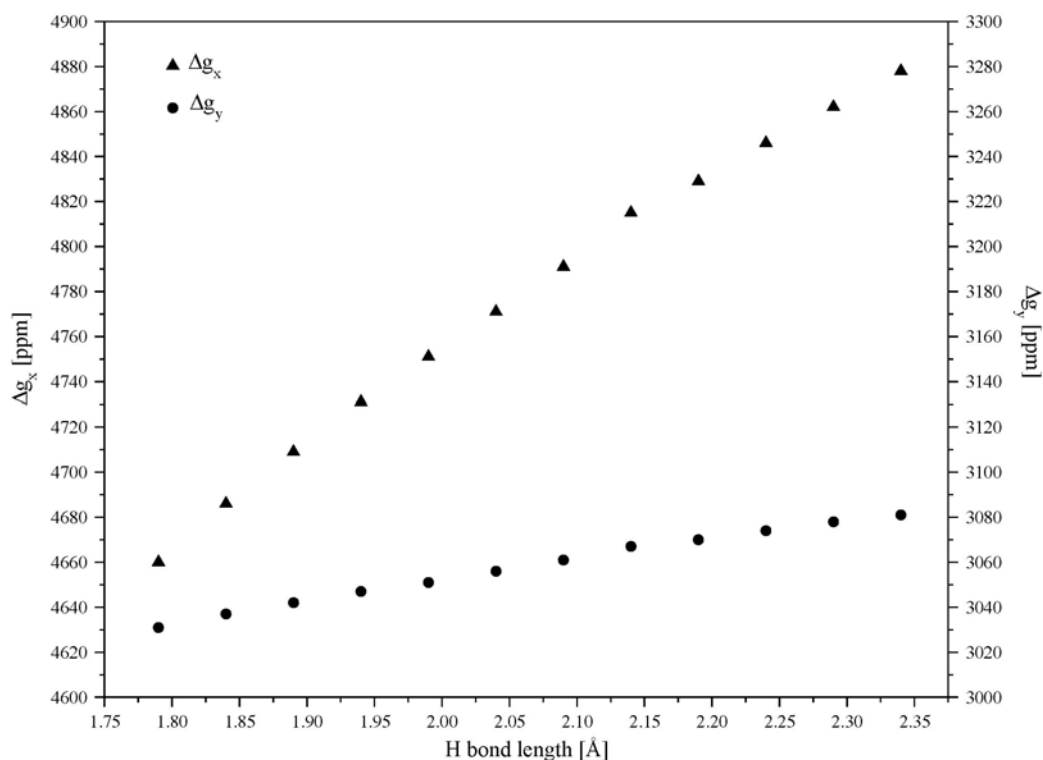


Figure 4.2.3 Variation of  $\Delta g_x$  and  $\Delta g_y$  with the hydrogen-bond distance to  $O_4$  for the 2/1-a 1HO-1HN-4HO model (cf. Figure 4.2.2b).

Systems with even more hydrogen bonding would allow a further reduction of  $\Delta g_x$  by about 200 ppm. Of these models, the 3/2 model 1HO-1HO-1HN-4HO-4HN (Table 4.2.2) is still expected to provide significant asymmetry in the  $^{13}\text{C}$  hyperfine couplings (see below). An artificial shortening of some or all hydrogen bonds to 1.60 Å in the 2/1a 1HO-1HN-4HO model reduces  $\Delta g_x$  maximally by 300 ppm (results not shown), when all hydrogen bonds are short. However, this is already a very unlikely bonding situation.

Previous  $g$ -tensor calculations on more specific supermolecular model complexes for the  $Q_A^{\bullet-}$ ,  $Q_B^{\bullet-}$ , and  $A_1^{\bullet-}$  sites, and for ubisemiquinone in frozen isopropanol (Chapter 4.1<sup>153</sup> and ref 51) provided excellent agreement with experiment after appropriate scaling of the  $\Delta g_x$  component to account for systematic errors of the DFT approach used. This is confirmed by the corresponding values in Table 4.2.2 (which differ slightly from those from Chapter 4.1<sup>153</sup>). Structural reoptimization provided somewhat stronger intermolecular interactions compared to the initial

structures. Consequently, the  $g_x$  components are also lowered slightly more. This is most pronounced for the  $Q_A^{\bullet-}$  model (Table 4.2.2); the scaled  $\Delta g_x$  component for the “reopt1” structure is now somewhat below experiment. It is possible that this model overestimates the strength of the hydrogen bonds now compared to the situation in the protein. The effect is smaller for the  $Q_B^{\bullet-}$  model. While the  $g$ -tensor for this model agrees excellently with experiment, the hyperfine tensors do not (see discussion below). The  $g$ -tensor of the  $A_1^{\bullet-}$  model is affected only slightly by the reoptimization of the single hydrogen bond (which shortens by 10 pm).

#### 4.2.3.3 $^{13}\text{C}$ -Carbonyl Hyperfine Tensors

It was the strongly different  $A_z$  components of the carbonyl  $^{13}\text{C}$  hyperfine tensors for the  $C_1$  and  $C_4$  positions, and in particular the very low value for the  $C_4$  position, that led authors of ref 209 to favor a single-sided hydrogen bonding model. In view of the above results for the  $g$ -tensors, it is thus of great interest to evaluate the compatibility of the hyperfine tensors for different models with this experimental observation. Computed  $^{13}\text{C}$  hyperfine tensors are shown in Table 4.2.3, in comparison with experimental data for a variety of environments.

As  $A_x$  and  $A_y$  are determined less accurately by the measurements,<sup>209</sup> we concentrate in particular on the better defined  $A_z$  values. Comparison of the data for the  $Q_H$  site with frozen protic solution demonstrates the pronounced asymmetry for the two carbonyl sites. The  $A_z$  value at  $C_4$  is indeed comparable to measurements in aprotic solvent mixtures (DME/mTHF; Table 4.2.3), where hydrogen bonding must be presumed absent.

Table 4.2.3  $^{13}\text{C}$  Hyperfine coupling tensors (in MHz) for the C1 and C4 carbonyl positions in ubisemiquinone radical anion models.

Model <sup>a</sup>	$^{13}\text{C}$ -HFC at C <sub>1</sub>			$^{13}\text{C}$ -HFC at C <sub>4</sub>		
	$A_x$	$A_y$	$A_z$	$A_x$	$A_y$	$A_z$
0/0 optimized	-12.8	-16.3	14.0	-12.9	-16.4	14.1
0/0 //2/1 1HO-1HN-4HO	-15.0	-18.8	6.4	-11.3	-14.6	16.8
0/1 4HO	-16.4	-20.5	1.5	-8.5	-11.2	31.0
0/1 4HN	-16.8	-20.9	0.9	-8.3	-10.9	32.3
1/0 1HN	-11.4	-14.4	24.3	-13.7	-17.4	10.1
1/0 1HO	-10.5	-13.4	25.6	-14.4	-18.1	9.4
2/0 1HO-1HN	-9.0	-11.4	37.0	-14.9	-18.6	6.6
3/0 1HO-1HO-1HN	-7.3	-9.5	41.5	-15.9	-19.9	3.5
1/1 1HN-4HN	-14.0	-17.3	15.8	-10.5	-13.3	25.9
3/1-a 1HO-1HO-1HN-4HO	-9.4	-11.7	37.0	-13.7	-17.0	12.9
3/1-b 1HO-1HO-1HN-4HO	-9.0	-11.3	38.6	-13.6	-16.9	15.2
2/2-a 1HO-1HO-4HO-4HO	-11.7	-14.6	24.7	-11.8	-14.7	24.6
2/2-b 1HO-1HO-4HO-4HO	-12.6	-15.5	20.8	-11.6	-14.4	26.5
2/1-a 1HO-1HN-4HO	-11.2	-14.0	27.9	-12.0	-15.0	20.8
2/1-b 1HO-1HN-4HO	-11.1	-13.9	26.1	-12.6	-15.7	20.8
2/1-c 1HO-1HN-4HO	-11.0	-13.8	26.7	-13.1	-16.4	18.5
2/1-d 1HO-1HN-4HO	-10.8	-13.4	27.9	-13.5	-16.7	18.5
2/1 1HN-1HN-4HN	-11.6	-14.4	27.9	-12.0	-15.0	20.8
1/2 1HO-4HO-4HN	-13.4	-16.7	18.2	-10.0	-12.6	30.3
3/2 1HO-1HO-1HN-4HO-4HN	-11.3	-13.8	33.6	-11.3	-14.0	25.3
2/2 1HO-1HN-4HO-4HN	-13.6	-16.5	23.1	-10.3	-12.8	29.7
2/3 1HO-1HN-4HO-4HO-4HN	-14.6	-17.7	19.4	-7.6	-9.6	40.1

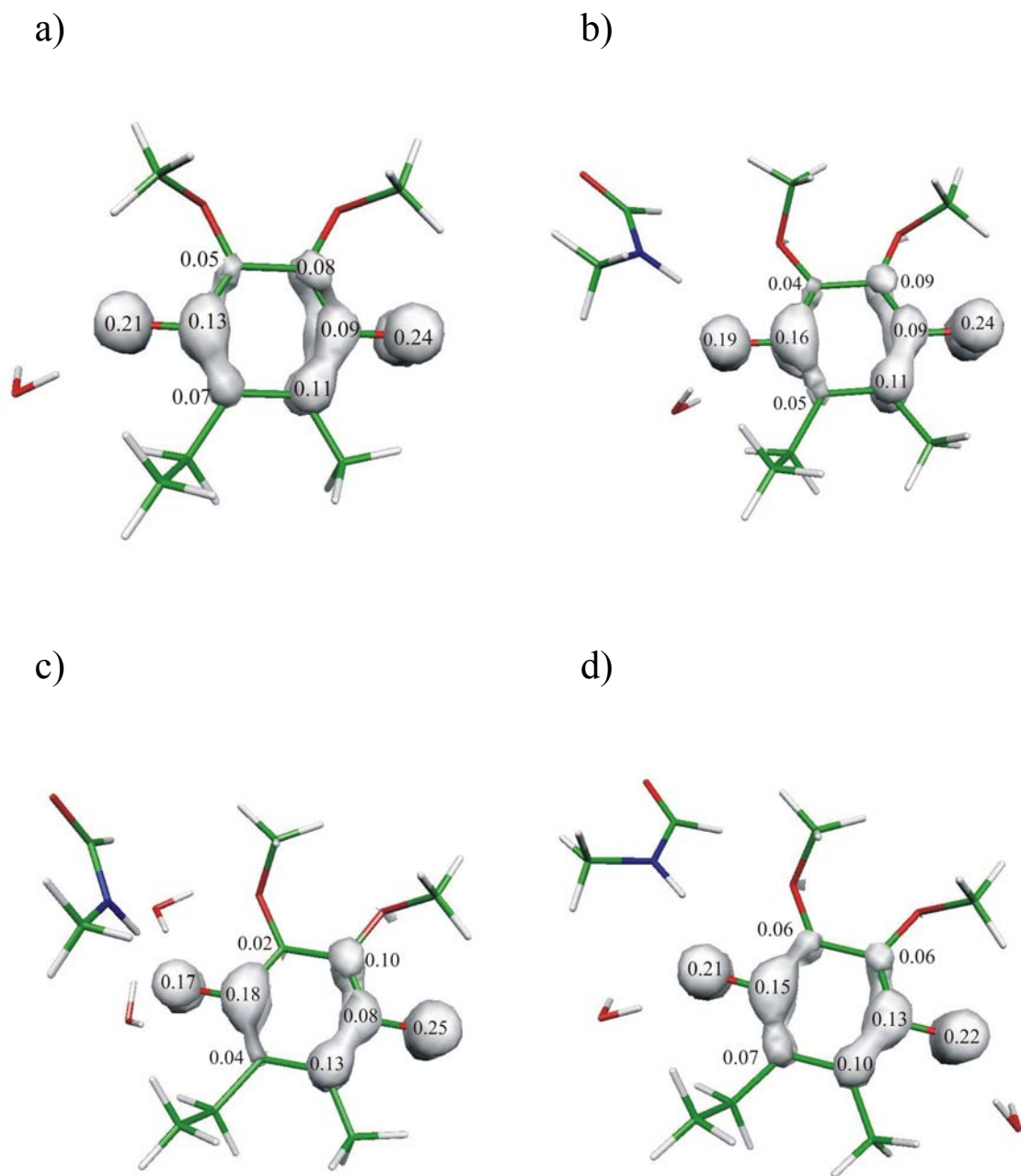
Model <sup>a</sup>	<sup>13</sup> C-HFC at C <sub>1</sub>			<sup>13</sup> C-HFC at C <sub>4</sub>		
	A <sub>x</sub>	A <sub>y</sub>	A <sub>z</sub>	A <sub>x</sub>	A <sub>y</sub>	A <sub>z</sub>
<i>Models from Chapter 4.1</i> <sup>153</sup>						
Q <sub>A</sub> <sup>•-</sup> (UQ-EM <sup>•-</sup> -nmf-imd-ind) <sup>b</sup>	-13.7	-17.1	16.3	-10.7	-13.7	23.0
Q <sub>A</sub> <sup>•-</sup> (UQ-EM <sup>•-</sup> -nmf-imd) <sup>b</sup>	-13.6	-17.1	16.6	-11.1	-14.1	22.6
Q <sub>A</sub> <sup>•-</sup> (UQ-EM <sup>•-</sup> -nmf-imd), reopt1 <sup>b</sup>	-14.5	-17.9	16.0	-10.0	-12.6	28.0
Q <sub>A</sub> <sup>•-</sup> (UQ-EM <sup>•-</sup> -nmf-imd), reopt2 <sup>b</sup>	-13.6	-17.0	15.5	-10.2	-13.1	26.4
Q <sub>B</sub> <sup>•-</sup> (UQ-EM <sup>•-</sup> -ind-SIG) <sup>b</sup>	-11.0	-13.9	26.5	-13.4	-16.7	18.8
Q <sub>B</sub> <sup>•-</sup> (UQ-EM <sup>•-</sup> -ind-SIG), reopt1 <sup>b</sup>	-11.4	-14.2	28.6	-12.1	-15.1	21.6
UQ-EM <sup>•-</sup> (iPrOH) <sub>6</sub> <sup>b</sup>	-11.7	-14.4	26.9	-12.1	-14.9	26.4
A <sub>1</sub> <sup>•-</sup> (EMNQ <sup>•-</sup> -nmf-ind) <sup>b</sup>	-11.3	-14.3	21.3	-13.0	-16.4	11.0
A <sub>1</sub> <sup>•-</sup> (EMNQ <sup>•-</sup> -nmf-ind), reopt3 <sup>b</sup>	-10.5	-13.3	26.0	-13.4	-16.8	9.9
exp. $Q_H^{\bullet-}$ in bo <sub>3</sub> -QOX <sup>c</sup>	-4.2 (14)	-12.6 (14)	30.8 (8)	-7.0(14)	-10.4(14)	20.2 (8)
exp. Q <sub>A</sub> <sup>•-</sup> in Zn-bRCs <sup>d</sup>	-12.6(17)	-14.6(17)	22.7 (6)	-9.2 (17)	-9.8(17)	35.0 (6)
exp. Q <sub>A</sub> <sup>•-</sup> in Zn-bRCs <sup>e</sup>	15.4 (14)	18.2 (14)	22.4 (8)	<7.0 (14)	<7.0(14)	35.6 (8)
exp. Q <sub>B</sub> <sup>•-</sup> in Zn-bRCs <sup>d</sup>	-10.9 (17)	-13.2 (17)	27.7 (6)	-10.1 (17)	-10.4(17)	32.2 (6)
exp. UQ-3 <sup>•-</sup> in iPrOH <sup>d</sup>	-12.1 (17)	-10.4 (17)	30.6 (6)	-11.2 (17)	-9.8(17)	32.2 (6)
exp. UQ-10 <sup>•-</sup> in iPrOH <sup>e</sup>	n.d.	n.d.	31.7 (8)	n.d.	n.d.	30.8 (8)
exp. UQ-3 <sup>•-</sup> in DME/MTHF <sup>f</sup>	-12.1 (22)	-15.1 (22)	20.5 (6)	-13.2 (22)	-15.4 (22)	20.5 (6)
exp. 2-methyl-NQ <sup>•-</sup> in PS-I <sup>g</sup>	-10.5 (15)	-10.5 (15)	44.0 (20)	n.d.	n.d.	n.d.
calc. VK <sub>1</sub> <sup>•-</sup> <sup>h</sup>	-12.2	-15.1	22.2	-16.6	-20.4	1.5

<sup>a</sup> Cf. Figure 4.2.2. Atom labels for A<sub>1</sub> converted in analogy to the numbering used for ubisemiquinone models. <sup>b</sup> Structures adapted from Chapter 4.1<sup>153</sup>; see footnote c of Table 4.2.2. <sup>c</sup> Native UQ-8 substituted with <sup>13</sup>C selectively labelled UQ-2.<sup>209</sup> <sup>d</sup> Native UQ-10 substituted with selectively <sup>13</sup>C labelled UQ-3 (cf. ref 237). <sup>e</sup> With selectively <sup>13</sup>C-labelled UQ-10.<sup>238</sup> <sup>f</sup> Ref 192. <sup>g</sup> From simulations of Q- and X-band transient radical pair spectra for 2-methyl-naphthoquinone in the A<sub>1</sub> binding site.<sup>239</sup> <sup>h</sup> B3LYP/EPR-II calculations on an A<sub>1</sub> model made from vitamin K<sub>1</sub> and a methyl-imidazole molecule hydrogen-bonded to O<sub>4</sub>.<sup>145</sup>

However, our computations show that single-sided hydrogen bonding would cause an even much larger asymmetry than observed for the  $Q_H$  site, and in particular an even much lower  $A_z$  for the C<sub>4</sub> position. This may be understood from the strongly asymmetric and alternating spin density distribution in the single-sided case, which places relatively large positive spin density on O<sub>4</sub> but very low spin density on C<sub>4</sub>. In contrast, unsymmetrical double-sided models provide much better agreement with the measured data for the  $Q_H$  site. This holds in particular for the 2/1 models 1HO-1HN-4HO or 1HN-1HN-4HN, which agree rather well with experimental data for the  $Q_H$  site. 3/1 models appear to provide too asymmetrical hyperfine couplings. Thus, the

computations provide not only better agreement with experimental  $g$ -tensors of  $Q_H$  when allowing double-sided yet asymmetrical hydrogen bonding, but even the characteristic carbonyl  $^{13}\text{C}$  hyperfine tensors are reproduced more faithfully by 2/1 models. Notably, the 3/2 model does provide somewhat too large  $A_z$  components but also a reasonable asymmetry between  $C_1$  and  $C_4$ .

Turning to the  $A_x$  and  $A_y$  components in the  $Q_H$  site, we note that due to inherent inaccuracies in their experimental determination, the observed differences between  $A_x$  and  $A_y$  may indeed not be reliable, and even the absolute values may vary somewhat upon varying the simulation parameters (without affecting the overall quality of the spectral simulation).<sup>209</sup> Based on knowledge from other semiquinone spectra and computations, one would expect more negative  $A_x$  and  $A_y$  components for that *ipso*-carbon atom with the lower spin density (that is, the one bonded to the oxygen atom that experiences less hydrogen bonding). This is due to accumulation of spin density on the neighboring oxygen and *ortho*-carbon atoms (as demonstrated by spin density distributions for various model complexes provided in Figure 4.2.4). A lower  $A_z$  component should thus be accompanied by more negative  $A_x$  and  $A_y$  components. This can be observed, e.g., in the experimental data for the  $Q_A$  and  $Q_B$  sites (Table 4.2.3). It is thus conceivable that the  $A_x$  and  $A_y$  components in the  $Q_H$  site should be significantly more negative at  $C_4$  than at  $C_1$ . Notably, calculations for single-sided models provide not only unrealistically small  $A_z$  values but also unrealistically large absolute  $A_x$  and  $A_y$  values at the position of low spin density. Indeed, this effect becomes more pronounced when going from, e.g., the 1/0 to 2/0 and 3/0 models (Table 4.2.3). The 2/1 or 3/2 models perform better also in this respect.





e)

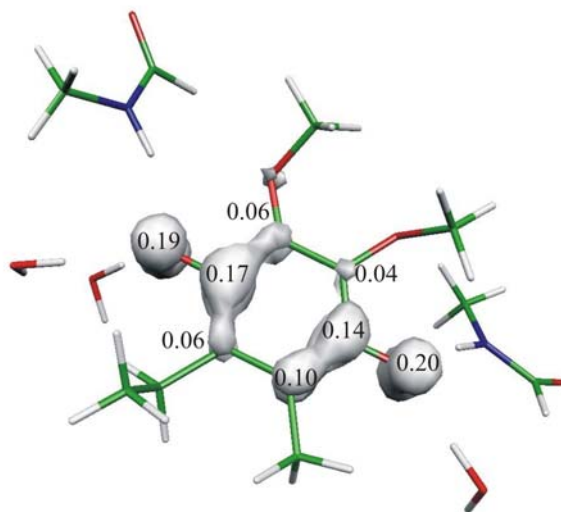


Figure 4.2.4 Spin-density isosurface plots ( $\pm 0.005$  a.u.; BP86/DZVP results) and Mulliken atomic spin density values for a number of model complexes: a) 1/0 1HO, b) 2/0 1HO-1HN, c) 3/0 1HO-1HO-1HN, d) 2/1-a 1HO-1HN-4HO, e) 3/2 1HO-1HO-1HN-4HO-4HN.

We have again evaluated the effect of a successive lengthening of the hydrogen bond to  $O_4$  in the double-sided 2/1 model 1HO-1HN-4HO (Figure 4.2.5). Going from a hydrogen bond distance of 1.80 Å to 2.20 Å,  $A_z$  in  $C_1$  position increases slightly towards the experimental value of 30.8 MHz, but in  $C_4$  position it decreases below the observed 20.2 MHz. These calculations provide thus no indications for or against a somewhat weakened hydrogen bond on the  $O_4$  side.

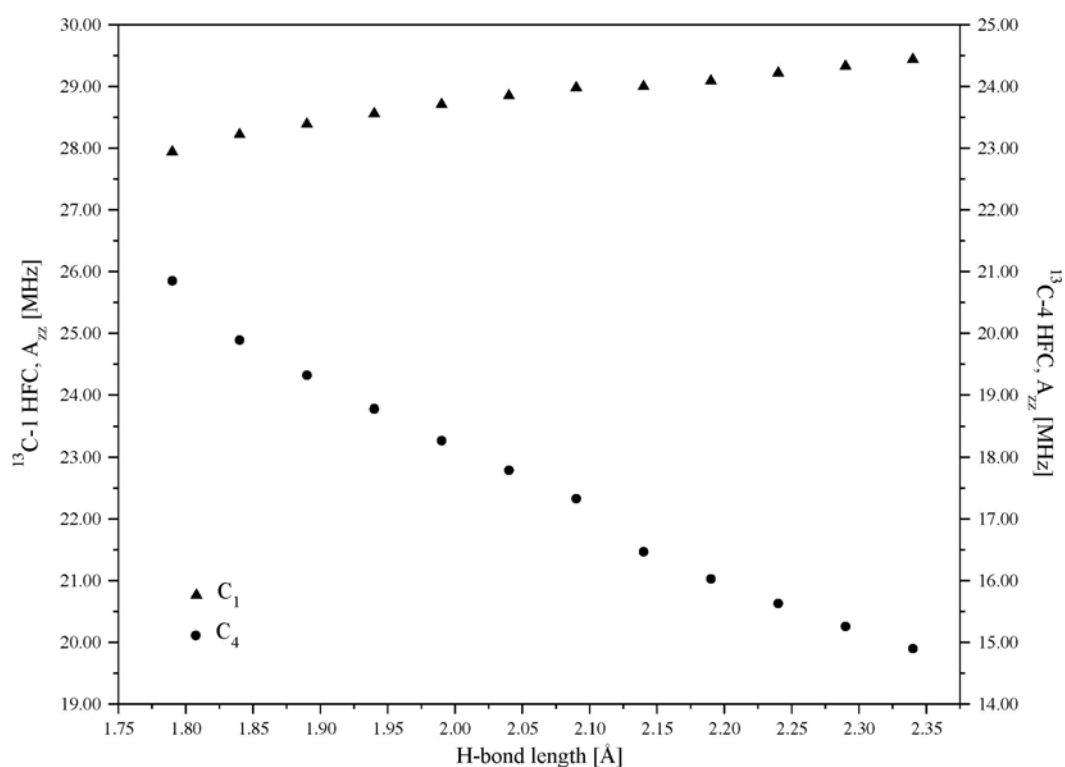


Figure 4.2.5 Variation of  $^{13}\text{C}$ (carbonyl)  $A_z$  hyperfine components ( $C_1$  and  $C_4$  positions) with the hydrogen-bond distance to  $O_4$  for the 2/1-a 1HO-1HN-4HO model (cf. Figure 4.2.2b).

We have also performed calculations for the 2/1 model 1HO-1HN-4HO with +2 point charge at the *heme-a* iron position. Depending on the orientation of the semiquinone in the putative binding site, slightly different relative arrangements of the point charges and the semiquinone arise.<sup>155</sup> For different orientations chosen, the  $A_z$  values of  $C_1$  vary between 27.7 and 29.7 MHz, and those for  $C_4$  between 17.7 and 18.0 MHz. There is thus an electrostatic influence on these carbonyl  $^{13}\text{C}$  couplings. However, it is not large enough to favor any of the other models for the hydrogen-bonding environment. Models with artificially *shortened* hydrogen bonds provide generally too high values for  $A_z$  of  $C_1$  and too low ones for  $C_4$ .<sup>155</sup> An exception is due to the model where only one  $\text{O}_1\cdots\text{OH}$  bond is shortened. This model provides good agreement with the experimental values.

We may also compare our computed hyperfine values to experimental values from other, structurally better characterized protein sites (Table 4.2.3). In comparison with the bacterial  $Q_A$  site, a 1/1 model provides overall too low  $A_z$  values but gives the right type of asymmetry. A 2/3 model exhibits a somewhat larger asymmetry in  $A_z$  than measured, as well as rather reasonable  $A_x$  and  $A_y$  components. While the 2/3 complex is far from the experimentally observed structure,<sup>181,201</sup> it does thus seem to model the spin-density distribution in the  $Q_A$  site well. In fact, it appears to be generally accepted that of the two hydrogen bonds to  $\text{O}_1$  and  $\text{O}_4$ , the  $\text{O}_4\cdots$ histidine one is stronger.<sup>166,240</sup> The  $Q_A^{\bullet-}$  model from Chapter 4.1<sup>153</sup>, with or without  $\pi$ -stacked indole (to model a tryptophan residue), gives a lower asymmetry. The asymmetry is better reproduced after reoptimization of the structure (cf. entries reopt 1 and reopt 2 in Table 4.2.3), but both  $A_z$  components remain too low (absolute  $A_x$  and  $A_y$  values tend in turn to be overestimated, in agreement with the discussion above).

Experimental data for the  $Q_B$  site are also best reproduced by the 2/3 model. The supermolecular model for  $Q_B^{\bullet-}$  model from Chapter 4.1<sup>153</sup> was based on an X-ray structure for the charge-separated  $\text{P}^+Q_B^{\bullet-}$  state at 2.6 Å resolution.<sup>181</sup> It reproduces well the  $g$ -tensor (see above). However, the asymmetry in the carbonyl  $^{13}\text{C}$   $A_z$  components has the wrong sign (albeit reasonable magnitude, cf. Table 4.2.3). Reoptimization of the structure increases both  $A_z$  components slightly but does not reverse the asymmetry. We suspect that the very hydrophilic environment within the  $Q_B$  site provides a highly dynamical hydrogen-bonding situation that is not adequately described by the static model from Chapter 4.1.<sup>153</sup>

The phyllosemiquinone  $A_1$  site in PS-I has only been studied so far using 2-methyl-naphthoquinone  $^{13}\text{C}$ -labelled at the  $C_1$  position (Table 4.2.3). The authors state that this molecule is bound with the same orientation as the native phylloquinone and thus can be used as a model system. Spectral simulation of the transient radical pair spectra at two microwave frequencies are used to determine the observed HFCs. While it is clear that the magnitude of  $A_z$  is about 40 MHz (see Table 4.2.3), the other two components of the hyperfine tensor are quite difficult to determine with much degree of accuracy from such spectra. Moreover, it is unclear to what extent the missing extended side chain might affect the hydrogen-bonding framework and thus the spin-density distribution. The results obtained with the  $A_1^{\bullet-}$  model from Chapter 4.1<sup>153</sup> provide an appreciable asymmetry but a significantly too low  $A_z$  value for  $C_1$ . Other supermolecular model DFT calculations by O'Malley<sup>145</sup> on a complex between vitamin  $K_1$  (i.e. the phytyl side chain of phylloquinone was replaced by a propene moiety) hydrogen-bonded at  $O_1$  (when using analogous atom labelling as shown for ubisemiquinone in Figure 4.2.2) to a methylimidazole molecule (Table 4.2.3) provide similar  $A_z$  for  $C_1$  but still lower  $A_z$  at  $C_4$  (and a more negative  $A_{iso}$  at that position). While no structural data were provided in ref 145, the otherwise almost identical computational level makes us suspect that a very short hydrogen bond had been chosen to provide such a large asymmetry (see discussion below for  $^1\text{H}$  and  $^{17}\text{O}$  HFCs).

In comparison with isotropic protic solution results, computed data for symmetrical 2/2 models depend also sensitively on the particular minimum structure used (cf. entries 2/2-a and 2/2-b in Table 4.2.3). They may provide symmetrical HFCs or unsymmetrical ones, in the latter case with  $A_z(C_4) > A_z(C_1)$ . The UQ-EM $^{\bullet-}$  (iPrOH)<sub>6</sub> model from Chapter 4.1<sup>153</sup> provides symmetrical HFCs, somewhat below the experimental values. It is clear that the identical values observed for the two positions in frozen solution reflect dynamical or statistical averaging. Another interesting result is the almost vanishing  $A_z$  at  $C_1$  for 0/1 models. A general conclusion is, that one may not use measurements in a completely symmetrical situation (e.g. in protic or aprotic solvents) to estimate the carbonyl HFCs in unsymmetrical situations. The asymmetric spin density distribution in the latter case may lead to very different hyperfine data.

#### 4.2.3.4 $^1\text{H}(\text{CH}_3)$ Hyperfine Tensors

Table 4.2.4 shows the  $^1\text{H}$  HFC tensors of the methyl group in  $C_5$ -position, averaged over all three hydrogen atoms.<sup>241</sup> As expected and found experimentally,<sup>166,242</sup> the largest component,  $A_y$ , is oriented roughly along the  $C_5$ -C(methyl) bond, and the tensor is almost but not quite axial, consistent with the structure of the radical (cf. Figure 4.2.1). These  $^1\text{H}$  HFC tensors are the only quantity that appears to be slightly better described by a single-sided 2/0 than by double-sided 2/1 models (Table 4.2.4). In the latter case, all three components (and thus the isotropic value) are about 2-3 MHz too low relative to the observed value, whereas the 2/0 model is slightly closer to experiment. A 3/1 model (Table 4.2.4) also provides somewhat larger values. Interestingly, also the 3/2 model provides slightly better agreement with experiment than the 2/1 models. Lengthening of the hydrogen bond to  $O_4$  to about 2.20 Å in the 2/1-a 1HO-1HN-4HO model increases the three values by only about 0.3 MHz. Introduction of the +2 point charge at the suspected position of the *heme-a* iron atom changes the tensor components by at most 0.5 MHz and thus cannot account for the discrepancies between the 2/1 models and experiment. Shortening of the hydrogen bonds to 1.60 increases of the HFC tensor components by up to 1MHz.<sup>155</sup>

We may again also compare results from the more sophisticated X-ray structure-based models from Chapter 4.1<sup>153</sup> with the corresponding experimental HFC tensors (Table 4.2.4). The  $Q_A^{\bullet-}$  model without reoptimization provides excellent agreement with experiment. Removal of the indole residue increases all components by about 0.8 MHz. Full reoptimization of this reduced model (“reopt1”) has little effect, whereas reoptimization under freezing of the methoxy conformation (“reopt2”) decreases the results somewhat. The  $Q_B^{\bullet-}$  binding site model from Chapter 4.1<sup>153</sup> provides results slightly above experiment, whereas structure reoptimization leads to unrealistically low values (this confirms our above conclusion that the X-ray structure for the charge-separated  $P^+Q_B^{\bullet-}$  state<sup>181</sup> may not reflect well the dynamical hydrogen-bonding situation in this hydrophilic site; see discussion above). An underestimate by ca. 2 MHz for all three components is found for the  $A_1^{\bullet-}$  model, but reoptimization increases the HFCs slightly towards experiment. Here the vitamin  $K_1$ /methyl-

imidazole model of O'Malley<sup>145</sup> provides larger values (at the same computational level). As discussed above for the  $^{13}\text{C}$  HFCs, this may reflect a choice of a very short hydrogen bond length and thus a more asymmetric spin-density distribution than our best optimized models provide. The UQ-EM $^{\bullet-}$  (iPrOH)<sub>6</sub> model underestimates experimental values for ubisemiquinone in frozen isopropanol also by about 1-2 MHz.

Table 4.2.4 5-Methyl  $^1\text{H}$  hyperfine coupling tensors HFC (in MHz).<sup>a</sup>

Model <sup>b</sup>	$^1\text{H}$ -HFC		
	$A_x$	$A_y$	$A_z$
0/0 opt	4.9	8.3	3.9
0/0 from best model	4.7	8.1	3.8
0/1 4HO	2.8	5.9	1.8
0/1 4HN	2.6	5.8	1.7
1/0 1HN	6.4	10.2	5.5
1/0 1HO	6.2	9.9	5.3
2/0 1HO-1HN	7.8	11.5	6.8
3/0 1HO-1HO-1HN	8.0	11.9	7.1
1/1 1HN-4HN	4.3	7.7	3.5
3/1-a 1HO-1HO-1HN-4HO	7.1	10.8	6.2
3/1-b 1HO-1HO-1HN-4HO	7.7	11.5	6.8
2/2-a 1HO-1HO-4HO-4HO	5.0	8.5	4.2
2/2-b 1HO-1HO-4HO-4HO	3.7	7.1	2.9
2/1-a 1HO-1HN-4HO	5.9	9.5	5.1
2/1-b 1HO-1HN-4HO	5.1	8.6	4.2
2/1-c 1HO-1HN-4HO	5.2	8.8	4.3
2/1-d 1HO-1HN-4HO	5.3	8.8	4.4
2/1 1HN-1HN-4HN	6.0	9.7	5.2
1/2 1HO-4HO-4HN	3.9	7.2	3.0
3/2 1HO-1HO-1HN-4HO-4HN	6.4	10.0	5.6
2/2 1HO-1HN-4HO-4HN	4.8	8.2	4.0
2/3 1HO-1HN-4HO-4HO-4HN	4.0	7.3	3.2

Model <sup>b</sup>	<sup>1</sup> H-HFC		
	$A_x$	$A_y$	$A_z$
<i>Models from Chapter 4.1</i> <sup>153</sup>			
$Q_A^{\bullet-}$ (UQ-EM <sup>•-</sup> -nmf-imd-ind) <sup>c</sup>	3.9	7.0	3.0
$Q_A^{\bullet-}$ (UQ-EM <sup>•-</sup> -nmf-imd) <sup>c</sup>	4.6	7.9	3.7
$Q_A^{\bullet-}$ (UQ-EM <sup>•-</sup> -nmf-imd), reopt1 <sup>c</sup>	4.8	8.2	3.8
$Q_A^{\bullet-}$ (UQ-EM <sup>•-</sup> -nmf-imd), reopt2 <sup>c</sup>	4.0	7.3	3.1
$Q_B^{\bullet-}$ (UQ-EM <sup>•-</sup> -ind-SIG) <sup>c</sup>	5.3	8.9	4.4
$Q_B^{\bullet-}$ (UQ-EM <sup>•-</sup> -ind-SIG), reopt1 <sup>c</sup>	0.0	2.1	-0.4
UQ-EM <sup>•-</sup> + (iPrOH) <sub>6</sub> <sup>c</sup>	4.0	7.3	3.2
$A_1^{\bullet-}$ (EMNQ <sup>•-</sup> -nmf-imd) <sup>c</sup>	6.9	10.5	6.0
$A_1^{\bullet-}$ (EMNQ <sup>•-</sup> -nmf-imd), reopt3 <sup>c</sup>	7.6	11.3	6.7
exp. $Q_H^{\bullet-}$ in $bo_3$ -QOX <sup>d</sup>	8.40	12.78	7.85
exp. $Q_A^{\bullet-}$ in Zn-bRCs <sup>e</sup>	3.8(1)	6.9(1)	3.2(1)
exp. $Q_B^{\bullet-}$ in Zn-bRCs <sup>e</sup>	4.4(1)	7.8(1)	3.9(1)
exp. UQ-0 <sup>•-</sup> in iPrOH <sup>f</sup>	4.8 (3)	9.0 (3)	4.8 (3)
exp. UQ-3 <sup>•-</sup> in iPrOH <sup>f</sup>	5.3 (3)	8.4 (3)	5.0 (3)
exp. UQ-10 <sup>•-</sup> in iPrOH <sup>g</sup>	4.8	8.5	4.8
exp. UQ-0 <sup>•-</sup> in DME/mTHF <sup>f</sup>	5.0 (3)	8.4 (3)	5.0 (3)
exp. UQ-3 <sup>•-</sup> in DME/mTHF <sup>f</sup>	5.0 (3)	8.1 (3)	5.0 (3)
exp. UQ-10 <sup>•-</sup> in DME/mTHF <sup>h</sup>	5.2 (3)	8.4 (3)	5.2 (3)
exp. $A^{\bullet-}$ in PS-I <sup>i</sup>	9.0	12.6	9.0
exp. $A_1^{\bullet-}$ in PS I <sup>j</sup>	8.9(1)	12.5(1)	8.9(1)
calc. VK <sub>1</sub> <sup>•-</sup> <sup>k</sup>	9.2	12.6	8.2

<sup>a</sup>Cf. Figure 4.2.1 for atom labels. Atom labels for  $A_1$  converted in analogy to the numbering used for ubisemiquinone models. Average HFCs for the three hydrogen atoms. <sup>b</sup>Cf. Figure 4.2.2. <sup>c</sup>Structures adapted from Chapter 4.1<sup>153</sup>, see footnote c of Table 4.2.2. <sup>d</sup>Ref 221; <sup>e</sup>Ref 166. <sup>f</sup>X-band ENDOR and X- and Q-band EPR simulations.<sup>192</sup> <sup>g</sup>Ref 230. <sup>h</sup>Ref 243. <sup>i</sup>Ref 194. <sup>j</sup>Transient spin-polarized ENDOR.<sup>244</sup> <sup>k</sup>B3LYP/EPR-II calculations on an  $A_1$  model made from vitamin K<sub>1</sub> and a methyl-imidazole molecule hydrogen-bonded to O<sub>4</sub>.<sup>145</sup>

It seems easy to be off by a few MHz in either direction for these  $^1\text{H}$  HFCs, even with relatively realistic models. It appears that these  $^1\text{H}(\text{CH}_3)$  couplings are generally more sensitive to small (unsymmetrical) changes in the wider environment of the semiquinone than, e.g.,  $^{13}\text{C}$  HFCs or  $g$ -tensors. For example, the experimental  $^1\text{H}(\text{CH}_3)$  HFCs for the  $Q_H$  site in Table 4.2.4 are for a pH of 6 but increase by about 2 MHz upon going to pH 8 (for all components).<sup>243</sup> In view of the results for other binding sites and other model complexes, and based on the relatively modest differences between models, we do not think that the  $^1\text{H}(\text{CH}_3)$  HFCs provide strong evidence for a single-sided model either.

#### 4.2.3.5 $^1\text{H}$ Hyperfine Tensors for Hydrogen-Bonded Protons

Table 4.2.5 provides  $^1\text{H}$  HFCs for the hydrogen-bonded protons, together with some experimental values for semiquinones in different environments. A few general trends related to the structures in Table 4.2.1 may be noted from the computed values. a) Larger  $A_{33}$  values ( $> 6$  MHz) are associated with short hydrogen bonds, whereas the hydrogen bonds above  $2 \text{ \AA}$  tend to exhibit values around 4-5 MHz. The particularly large  $A_{33}$  values in some of the quoted experimental cases (in particular  $Q_A^{\bullet-}$  in bacterial reaction centers, but also the  $A_1^{\bullet-}$  site in photosystem I) suggest thus a rather short and strong hydrogen bond, in agreement with observation. b) As one might expect, essentially dipolar tensors (with  $A_{iso} < 1$  MHz) are found in particular for hydrogen bonds close to the ring plane (or in one case for an extremely out-of-plane hydrogen bond, cf. 3/1-b model), whereas the hydrogen bonds with  $\gamma$  values between ca.  $20\text{-}60^\circ$  tend to exhibit larger isotropic contributions. This is well known from ENDOR measurements.<sup>166,230,242,245</sup> Among the experimental examples included, isotropic contributions are particularly notable for UQ-10 $^{\bullet-}$  in 2-propanol, where they suggest a substantial out-of-plane orientation of the measured proton.



Table 4.2.5  $^1\text{H}$  hyperfine couplings (in MHz) for exchangeable hydrogens.

Model <sup>a</sup>	H-bond <sup>a</sup>	$^1\text{H}$ -HFC (MHz)		
		$A_{11}$	$A_{22}$	$A_{33}$
0/1 4HO	4HO	-5.6	-5.3	7.2
0/1 4HN	4HN	-3.0	-2.4	6.0
1/0 1HN	1HN	-3.5	-3.4	6.5
1/0 1HO	1HO	-3.6	-3.2	6.5
2/0 1HO-1HN	1HO	-6.1	-5.7	7.2
	1HN	-3.2	-3.1	5.8
3/0 1HO-1HO-1HN	1HO	-3.6	-3.5	4.3
	1HO	-3.7	-3.3	5.7
	1HN	-4.9	-4.3	6.4
1/1 1HN-4HN	1HN	-3.0	-2.9	6.4
	4HN	-3.4	-3.0	6.6
3/1-a 1HO-1HO-1HN-4HO	1HO	-3.6	-3.5	4.4
	1HO	-4.1	-3.6	6.0
	1HN	-5.0	-4.5	6.3
	4HO	-4.9	-4.4	6.4
3/1-b 1HO-1HO-1HN-4HO	1HO	-2.1	-2.0	4.4
	1HO	-6.5	-6.0	7.8
	1HN	-2.3	-2.1	4.8
	4HO	-5.0	-4.8	7.0
2/2-a 1HO-1HO-4HO-4HO	1HO	-3.2	-3.7	6.5
	1HO	-2.4	-2.3	4.5
	4HO	-2.2	-2.2	4.5
	4HO	-3.8	-3.3	6.8
2/2-b 1HO-1HO-4HO-4HO	1HO	-3.8	-3.7	6.4
	1HO	-3.3	-3.2	4.6
	4HO	-2.3	-2.2	4.5
	4HO	-3.3	-2.8	6.6
2/1-a 1HO-1HN-4HO	1HO	-3.4	-3.1	6.3
	1HN	-2.5	-2.4	5.4
	4HO	-4.3	-4.1	6.7
2/1-b 1HO-1HN-4HO	1HO	-3.4	-3.1	6.3
	1HN	-2.5	-2.4	5.2
	4HO	-4.4	-4.2	6.9
2/1-c 1HO-1HN-4HO	1HO	-3.3	-2.9	6.2
	1HN	-2.5	-2.4	5.3
	4HO	-4.4	-4.2	6.8
2/1-d 1HO-1HN-4HO	1HO	-4.1	-3.9	6.5
	1HN	-3.0	-2.8	5.5
	4HO	-5.0	-4.9	7.1

Model <sup>a</sup>	H-bond <sup>a</sup>	<sup>1</sup> H-HFC (MHz)		
		$A_{11}$	$A_{22}$	$A_{33}$
2/1 1HN-1HN-4HN	1HN	-2.9	-2.6	6.0
	1HN	-2.4	-2.2	5.2
	4HN	-3.4	-3.0	6.6
1/2 1HO-4HO-4HN	1HO	-2.1	-1.0	4.5
	4HO	-2.9	-2.6	6.0
	4HN	-3.6	-3.4	5.8
	1HO	-6.8	-6.4	7.8
3/2 1HO-1HO-1HN-4HO-4HN	1HO	-2.4	-2.3	4.6
	1HN	-2.4	-2.1	4.9
	4HO	-3.1	-2.8	6.1
	4HN	-4.1	-3.8	5.9
	1HO	-3.3	-2.9	6.6
2/2 1HO-1HN-4HO-4HN	1HN	-2.6	-2.4	5.7
	4HO	-3.1	-2.9	6.1
	4HN	-4.1	-3.8	6.0
	1HO	-3.2	-2.8	6.7
2/3 1HO-1HN-4HO-4HO-4HN	1HN	-2.6	-2.4	5.7
	4HO	-4.0	-3.7	5.2
	4HO	-5.9	-4.8	6.3
	4HN	-3.3	-2.9	5.0
<i>Models from Chapter 4.1<sup>153</sup></i>				
$Q_A^{\bullet-}$ (UQ-EM <sup>•-</sup> -nmf-imd-ind) <sup>b</sup>	1HN	-6.5	-6.2	8.2
	4HN	-5.4	-5.2	8.0
$Q_A^{\bullet-}$ (UQ-EM <sup>•-</sup> -nmf-imd) <sup>b</sup>	1HN	-6.4	-6.1	8.2
	4HN	-5.4	-5.2	8.0
$Q_A^{\bullet-}$ (UQ-EM <sup>•-</sup> -nmf-imd), reopt1 <sup>b</sup>	1HN	-4.5	-4.3	6.9
	4HN	-4.7	-4.5	7.3
$Q_A^{\bullet-}$ (UQ-EM <sup>•-</sup> -nmf-imd), reopt2 <sup>b</sup>	1HN	-4.7	-4.7	7.2
	4HN	-4.9	-4.7	7.6
$Q_B^{\bullet-}$ (UQ-EM <sup>•-</sup> -ind-SIG) <sup>b</sup>	1HO	-2.2	-2.1	3.8
	1HN	-4.2	-4.0	5.8
	1HN	-2.0	-1.4	3.3
	4HN	-4.5	-4.2	7.3
$Q_B^{\bullet-}$ (UQ-EM <sup>•-</sup> -ind-SIG), reopt1 <sup>b</sup>	1HO	-2.6	-2.2	4.8
	1HN	-4.3	-4.1	5.7
	1HN	-1.9	-1.3	3.3
	4HN	-3.4	-3.0	6.5

Model <sup>a</sup>	H-bond <sup>a</sup>	<sup>1</sup> H-HFC (MHz)		
		$A_{11}$	$A_{22}$	$A_{33}$
UQ-EM <sup>•-</sup> (iPrOH) <sub>6</sub> <sup>b</sup>	1HO	-5.7	-5.6	7.0
	1HO	-3.4	-3.1	6.5
	4HO	-7.2	-6.8	7.1
	4HO	-4.0	-3.7	6.7
A <sub>1</sub> <sup>•-</sup> (EMNQ <sup>•-</sup> -nmf-ind) <sup>b</sup>	1HN	-2.5	-2.2	5.9
A <sub>1</sub> <sup>•-</sup> (EMNQ <sup>•-</sup> -nmf-ind), reopt3 <sup>b</sup>	1HN	-3.4	-2.9	6.4
exp. UQ-10 <sup>•-</sup> in iPrOH <sup>c</sup>	HO	-1.33	-1.33	6.00
exp. BQ <sup>•-</sup> in iPrOH <sup>d</sup>	HO	-2.8	-2.8	5.9
exp. BQ <sup>•-</sup> in H <sub>2</sub> O <sup>e</sup>	HO	-2.66	-2.67	6.36
exp. Q <sub>A</sub> <sup>•-</sup> in Zn-bRCC <sup>f</sup>	HN	(-)4.6	(-)4.6	8.9
exp. deuterated 2-methyl-NQ in PS-I <sup>g</sup>	HN	-4.9	-4.9	7.7

<sup>a</sup>Cf. Figure 4.2.2. <sup>b</sup>Structures adapted from Chapter 4.1<sup>153</sup>; see footnote c of Table 4.2.2. <sup>c</sup>From ENDOR difference spectra (protonated minus deuterated 2-propanol).<sup>230</sup> <sup>d</sup>Ref 246. <sup>e</sup>Ref 247. <sup>f</sup>Ref 166. <sup>g</sup>Ref 245.

In the context of the  $Q_H$  site, it is notable that the 3/2 model exhibits one distinctly larger hyperfine anisotropy (1OH position) than any of the 2/1 models, combined with an appreciably negative isotropic value. From H<sub>2</sub>O/D<sub>2</sub>O exchange ENDOR experiments, Hasting et al.<sup>220</sup> indicated exchangeable proton hyperfine features of  $A_{\perp} = -5.1$  MHz and  $A_{\parallel} = 11.7$  MHz and suggested strongly out-of-plane hydrogen bonding. This would be consistent with three hydrogen bonds to O<sub>1</sub>. An improved identification of the hydrogen-bonding environment might be obtained from orientation-selective ENDOR, possibly at higher frequencies or using 2-dimensional pulsed EPR (HYSCORE).

#### 4.2.3.6 <sup>17</sup>O Hyperfine Tensors

No <sup>17</sup>O carbonyl hyperfine couplings have as yet been measured for semiquinones in QOX. Table 4.2.6 provides predicted values for the different supermolecular model complexes. Assuming a 2/1 double-sided model, the difference between O<sub>1</sub> vs. O<sub>4</sub> position is only about 1.5-2.0 MHz for all three components, with the value for O<sub>1</sub> being lower. That is, mainly the isotropic HFC differs between the two oxygen centers. The single-sided 2/0 model provides a much larger difference of about 20 MHz for  $A_z$ , whereas the  $A_x$  and  $A_y$  components are about 6 MHz more

negative on  $O_4$  than on  $O_1$  (Table 4.2.6). 3/1 models give about 15 MHz more negative  $A_z$  and about 4 MHz more negative  $A_x$  and  $A_y$  values on  $O_4$ . The addition of a double point charge at the presumed *heme-a* iron position in the 2/1 1HO-1HN-4HO model reduces  $A_z(O_1)$  by about 2 MHz and increases  $A_z(O_4)$  by about the same amount. The asymmetry is thus potentially increased by the electrostatic effect of the *heme-a* group maximally from about 2 MHz to about 6 MHz. It seems that the  $^{17}\text{O}$  HFCs (of suitably labelled samples) reflect the hydrogen-bonding situation less than the corresponding  $^{13}\text{C}$  HFCs (see above and ref 240). Whether they may be of diagnostic value will depend on the experimental resolution available (see below).

When turning to ubisemiquinone sites with experimentally known  $^{17}\text{O}$  HFCs (Table 4.2.6), we note that the ca. 18 MHz larger  $A_z$  for  $O_1$  for  $Q_A^{\bullet-}$  is somewhat underestimated (ca. 11 MHz) by a 1/1 model (which is close to the actually observed structure), as the  $A_z$  value of  $O_4$  is too negative. The more sophisticated  $Q_A^{\bullet-}$  model from Chapter 4.1<sup>153</sup> provides a similar asymmetry (12-13 MHz) but even slightly larger absolute values. Reoptimization of this model enhances the asymmetry and provides thus better agreement with experiment (with somewhat too large absolute values, cf. entry “reopt1”). On the other hand, the resolution of the experimental asymmetry is somewhat uncertain anyway (and the assignment to the two positions was based on the related  $^{13}\text{C}$  data).<sup>166</sup>

Experimental uncertainties are even more pronounced for the  $Q_B$  site, where the asymmetry has been obtained from the simulation of a single peak that was about 30% broader than for  $Q_A$  at the same experimental conditions. None of the models studied appears to reproduce the smaller asymmetry for  $Q_B^{\bullet-}$  particularly well. The  $Q_B^{\bullet-}$  model from Chapter 4.1<sup>153</sup> exhibits the wrong sign of the asymmetry, and reoptimization worsens matters. Apart from the experimental uncertainties, it is also possible that the spin density distribution in the very flexible  $Q_B$  site is not well represented by the particular static model used (see discussion above).

Table 4.2.6 Computed  $^{17}\text{O}$  hyperfine coupling tensors HFC (in MHz) for the  $\text{O}_1$  and  $\text{O}_4$  positions.

Model <sup>a</sup>	$^{17}\text{O}$ -HFC at $\text{O}_1$			$^{17}\text{O}$ -HFC at $\text{O}_4$		
	$A_x$	$A_y$	$A_z$	$A_x$	$A_y$	$A_z$
0/0 optimized <sup>b</sup>	19.3	18.6	-96.6	19.1	18.5	-96.2
0/0 from best model <sup>c</sup>	22.2	21.5	-107.8	18.0	17.3	-91.9
0/1 4HO	22.3	21.7	-106.9	14.9	14.2	-82.2
0/1 4HN	22.8	22.2	-108.4	14.3	13.5	-79.8
1/0 1HN	17.1	16.3	-90.0	20.0	19.3	-99.3
1/0 1HO	15.9	15.2	-87.5	20.6	19.9	-102.6
2/0 1HO-1HN	15.0	14.2	-82.7	20.5	20.0	-98.5
3/0 1HO-1HO-1HN	13.5	12.6	-74.5	22.1	21.5	-105.5
1/1 1HN-4HN	18.9	18.2	-97.6	16.0	15.3	-86.4
3/1-a 1HO-1HO-1HN-4HO	14.7	13.9	-80.8	19.4	18.9	-95.6
3/1-b 1HO-1HO-1HN-4HO	14.4	13.7	-78.3	18.6	18.0	-95.0
2/2-a 1HO-1HO-4HO-4HO	16.3	15.5	-89.4	16.4	15.6	-91.2
2/2-b 1HO-1HO-4HO-4HO	16.8	16.0	-91.1	16.4	15.6	-90.0
2/1-a 1HO-1HN-4HO	16.3	15.5	-88.2	17.8	17.1	-91.2
2/1-b 1HO-1HN-4HO	15.5	14.8	-87.4	18.3	17.6	-94.6
2/1-c 1HO-1HN-4HO	15.6	14.8	-87.6	18.4	17.7	-95.4
2/1-d 1HO-1HN-4HO	15.1	14.4	-85.5	18.5	17.9	-95.6
2/1 1HN-1HN-4HN	16.2	15.4	-89.2	17.0	16.4	-90.0
1/2 1HO-4HO-4HN	18.6	18.0	-97.9	14.7	14.0	-82.6
3/2 1HO-1HO-1HN-4HO-4HN	15.7	15.0	-84.9	15.2	14.6	-85.0
2/2 1HO-1HN-4HO-4HN	17.2	16.5	-95.8	14.3	13.7	-81.4
2/3 1HO-1HN-4HO-4HO-4HN	18.2	17.5	-98.5	12.7	12.0	-71.0

Model <sup>a</sup>	<sup>17</sup> O-HFC at O <sub>1</sub>			<sup>17</sup> O-HFC at O <sub>4</sub>		
	A <sub>x</sub>	A <sub>y</sub>	A <sub>z</sub>	A <sub>x</sub>	A <sub>y</sub>	A <sub>z</sub>
<i>Models from Chapter 4.1</i> <sup>153</sup>						
Q <sub>A</sub> <sup>•-</sup> (UQ-EM <sup>•-</sup> -nmf-imd) <sup>d</sup>	18.8	18.2	-94.8	14.7	14.1	-82.4
Q <sub>A</sub> <sup>•-</sup> (UQ-EM <sup>•-</sup> -nmf-imd) <sup>d</sup>	18.4	17.8	-95.3	14.7	14.1	-83.1
Q <sub>A</sub> <sup>•-</sup> (UQ-EM <sup>•-</sup> -nmf-imd), reopt1 <sup>d</sup>	19.2	18.6	-98.0	14.6	13.9	-79.6
Q <sub>A</sub> <sup>•-</sup> (UQ-EM <sup>•-</sup> -nmf-imd), reopt2 <sup>d</sup>	18.9	18.3	-96.6	15.3	14.7	-83.1
Q <sub>B</sub> <sup>•-</sup> (UQ-EM <sup>•-</sup> -ind-SIG) <sup>d</sup>	15.0	14.3	-81.7	17.3	16.6	-93.5
Q <sub>B</sub> <sup>•-</sup> (UQ-EM <sup>•-</sup> -ind-SIG), reopt1 <sup>d</sup>	16.2	15.3	-85.5	16.4	15.8	-87.9
UQ-EM <sup>•-</sup> + (iPrOH) <sub>6</sub> <sup>d</sup>	15.2	14.6	-84.8	15.8	15.2	-87.1
A <sub>1</sub> <sup>•-</sup> (EMNQ <sup>•-</sup> -nmf-imd) <sup>d</sup>	15.6	14.8	-83.3	17.5	16.8	-86.9
A <sub>1</sub> <sup>•-</sup> (EMNQ <sup>•-</sup> -nmf-imd), reopt3 <sup>d</sup>	14.5	13.8	-79.7	17.7	17.0	-87.3
exp. Q <sub>A</sub> <sup>•-</sup> in Zn-bRC <sub>m</sub> <sup>e</sup>			(-)94			(-)75
exp. Q <sub>B</sub> <sup>•-</sup> in Zn-bRC <sub>m</sub> <sup>e</sup>			(-)88			(-)82
exp. BQ <sup>•-</sup> in iPrOH <sup>f</sup>			-91.6			-91.6
exp. DQ <sup>•-</sup> in iPrOH <sup>g</sup>			-81.4			-81.4
exp. 2-methyl-NQ <sup>•-</sup> in iPrOH <sup>h</sup>			(-)78			n.d.
exp. 2-methyl-NQ <sup>•-</sup> in PS I <sup>i</sup>	4.5	4.5	(-)77	4.5	4.5	(-)84
calc. VK <sub>1</sub> <sup>•-</sup> <sup>j</sup>	13.4	14.0	-83.1	19.6	20.1	-97.3

<sup>a</sup>Cf. Figure 4.2.2. Atom labels for A<sub>1</sub> converted in analogy to the numbering used for ubisemiquinone models. <sup>b</sup>Fully optimized gas-phase radical. <sup>c</sup>Isolated radical but with structure taken from the 2/1 1HO-1HN-4HO model. <sup>d</sup>Structures adapted from Chapter 4.1<sup>153</sup>; see footnote c of Table 4.2.2. <sup>e</sup>Cf. ref 166. <sup>f</sup>From W-band EPR in frozen deuterated 2-propanol.<sup>[230]</sup> <sup>g</sup>From Q-band EPR in frozen deuterated 2-propanol.<sup>[230]</sup> <sup>h</sup>Ref 243. <sup>i</sup>Ref 240. <sup>j</sup>B3LYP/EPR-II calculations on an A<sub>1</sub> model made from vitamin K<sub>1</sub> and a methyl-imidazole molecule hydrogen-bonded to O<sub>4</sub>.<sup>145</sup>

In the case of 2-methyl-naphthosemiquinone in the A<sub>1</sub><sup>•-</sup> site of PS-I (Table 4.2.6), the A<sub>1</sub> models from Chapter 4.1<sup>153</sup> gives reasonable asymmetry, particularly after reoptimization (“reopt3”). The vitamin K<sub>1</sub>/methyl-imidazole model of O’Malley<sup>145</sup> for A<sub>1</sub><sup>•-</sup> gives a more pronounced asymmetry (larger A<sub>z</sub> for O<sub>4</sub>). Again (see discussion above for <sup>13</sup>C and <sup>1</sup>H HFCs) this may reflect a choice of a very short hydrogen bond length and thus a very asymmetric spin density.

#### 4.2.3.7 A Model for Cofactor-Protein Interactions in the $Q_H$ Binding site

Taking all available data into account that is available from a) crystallography,<sup>216</sup> b) functional studies of site-directed mutants,<sup>216</sup> c) various EPR, ENDOR and ESEEM studies,<sup>209,217-221</sup> and d) our present quantum chemical calculations, we may propose a refined model for the binding mode of the semiquinone state in the  $Q_H$  site of  $bo_3$  QOX. Based on the model of Abramson et al. for the binding site,<sup>216</sup> and accepting a double-sided 2/1 hydrogen-bonding environment with the single hydrogen bond on the  $O_4$  side, we arrive at the tentative model shown in Figure 4.2.6, in which Asp75 and Arg71 hydrogen-bond to  $O_1$  of the semiquinone and X represents the single hydrogen bond to  $O_4$ . In this case, His98 and Gln101 would not be involved in hydrogen bonding to the semiquinone. This choice rests on the ESEEM data,<sup>221</sup> coupling to a single nitrogen nucleus, assigned to a backbone peptide nitrogen,<sup>209</sup> while no indications for a coupling to histidine have been found. The experimental data are sufficiently specific to exclude a strong interaction to histidine, whereas a backbone peptide nitrogen and an arginine nitrogen could not be distinguished so easily. Thus, the model in Figure 4.2.6 is consistent with the available ESEEM data,<sup>221</sup> with the general model of the binding site by Abramson et al.,<sup>216</sup> and with the  $g$ -tensor and hyperfine data.<sup>209</sup> On the other hand, we cannot exclude that more hydrogen bonding is present on both sides, in a situation that would be better described by a 3/2 model (see above). Both 2/1 and 3/2 models share an asymmetric yet not single-sided arrangement with one more hydrogen bond to  $O_1$  than to  $O_4$ .

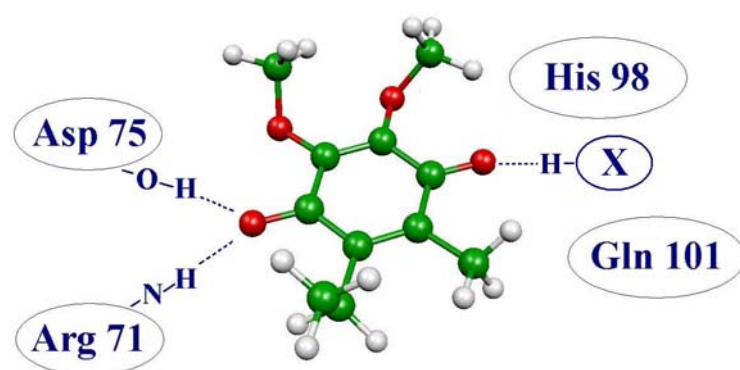


Figure 4.2.6 Binding-site model derived for cofactor-protein interactions in the  $Q_H$  site of  $bo_3$  quinol oxidase.

#### 4.2.4 Conclusions

Our calculations suggest that the hydrogen-bonding environment in the high-affinity ( $Q_H$ ) binding site of  $bo_3$  quinol oxidase is asymmetrical to the two carbonyl oxygen atoms  $O_1$  and  $O_4$  of the ubisemiquinone, but not single-sided to  $O_1$  alone. The single-sided model would not be consistent with the rather low  $g_x$  component of the  $g$ -tensor, and it would also give a far too large asymmetry of the two carbonyl  $^{13}\text{C}$  hyperfine couplings. Our best models suggest two hydrogen bonds to  $O_1$  and one to  $O_4$ , and we have provided a tentative assignment of the protein residues involved, based on the suggested binding site from X-ray crystallography.<sup>216</sup> A 3/2 model with more extensive hydrogen bonding is equally possible. Both of these hydrogen-bond patterns appear to be consistent with the high affinity of the  $Q_H$  site for the semiquinone state.

The present quantum chemical calculations of hyperfine and  $g$ -tensors for a large variety of supermolecular models of ubisemiquinones in different environments have provided appreciable general insight into the interrelationships between hydrogen-bond environment and EPR parameters. While our main goal was to better understand the  $Q_H$  binding site of  $bo_3$  quinol oxidase, the data provided may be used also in other cases, where accurate structural data for the semiquinone state are lacking. While the  $g$ -tensor is a very compact representation of the spin-density



distribution, we may at least rely on the sensitivity of the  $g_x$  component for the strength of hydrogen bonding in general and on the larger reduction of  $g_x$  by double-sided relative to single-sided hydrogen bonding. The asymmetry of  $^{13}\text{C}$  hyperfine couplings of the carbonyl groups reflects the asymmetry of the hydrogen-bonding framework characteristically, if one keeps in mind that one may not straightforwardly transfer HFC values from symmetrical to asymmetrical environments. The  $^1\text{H}$  HFCs of the methyl group appear to be difficult to reproduce computationally, as small structural inaccuracies or environmental effects may cause relatively large deviations. Determination of exchangeable proton hyperfine couplings will provide additional useful information, and experiments are currently being performed to determine them.



## 4.3 Molecular Mechanical Devices Based on Quinone-Pyrrole and Quinone-Indole Dyads<sup>154</sup>

### 4.3.1 Introduction

The conversion of chemical, electrical or light energy into mechanical motion on a molecular scale is of great current interest, partly due to nature's abounding examples in biological systems. The artificial design of rotational "molecular motors" is a particularly intense area of research, and a number of successes on the way to systems of practical interest have been obtained.<sup>248</sup> The control of the direction of the motion is one of the greatest challenges that has to be met.<sup>249-255</sup>

In this chapter we report on some first steps in the theoretical design, based on quantum chemical calculations, of relatively small rotational molecular motors made up from an intramolecularly connected dyad of a quinone and a pyrrole or indole. We show computationally that several of these systems will exhibit a reorientation of the pyrrole/indole moiety relative to the quinone upon chemical or electrochemical reduction of the latter to the semiquinone anion or quinolate dianion state. The proposed models are related to recently reported systems involving quinone and benzene units,<sup>256</sup> but the present molecules should exhibit a number of important advantages over the previously reported ones, which exhibited significant reorientation only in the dianionic state.

Indeed, the impetus for the present study came from an entirely different area of research, namely computational studies related to the mechanism of electron transfer in photosystem I (PS I).<sup>174</sup> We had been intrigued by a high-field/high-frequency EPR (HF-EPR) study of Stehlik and coworkers on so-called "reconstituted" variants of PS I.<sup>179,180</sup> In the latter, the phylloquinone (vitamin K<sub>1</sub>) secondary electron acceptor had been extracted from its A<sub>1</sub> active site by certain solvent mixtures and was replaced by smaller quinones like duroquinone (2,3,5,6-tetramethyl-benzoquinone) or naphthoquinone. The HF-EPR spectra of the semiquinone states exhibited unusually high  $g_x$  and  $g_y$  components of the  $g$ -tensor and were interpreted in terms of a reorientation of the semiquinone relative to its position in the neutral ground state by

ca. 90°. The quantum-chemical modeling of semiquinone-tryptophan interactions in these systems suggested that a neutral quinone and an indole (which was used to model tryptophan) will prefer a  $\pi$ -stacked parallel arrangement relative to each other. However, the indole will preferentially reorient in the reduced semiquinone anion state and will create a T-stacked hydrogen bond of its N-H function to the semiquinone  $\pi$ -system.<sup>174</sup> The even more stable complex with a hydrogen bond to a semiquinone oxygen atom apparently is sterically unfavorable in the particular surroundings of the active site of the reconstituted PS I reaction centers. Indeed, it appears that the bulky nature of the phylloquinone in the native PS I reaction centers will prohibit even the T-stacked arrangement, and the particular experimental conditions of the extraction/reconstitution experiments may have facilitated the observation of the reoriented structures. In any case, the calculations indicated clearly an appreciable driving force for reorientation to a T-stacked arrangement of a quinone/tryptophan (or quinone/indole) complex upon reduction to the semiquinone state.<sup>174</sup> This has prompted us to investigate here intramolecular versions of such complexes. In the course of this study, we became aware of recent experimental and theoretical investigations of related, intramolecularly linked quinone-benzene complexes,<sup>256</sup> and we will compare our results to those data. We note in passing that recent ab initio molecular dynamics simulations provided appreciable evidence for T-stacked hydrogen bonding for aqueous benzosemiquinone but not for the neutral quinone.<sup>160</sup>

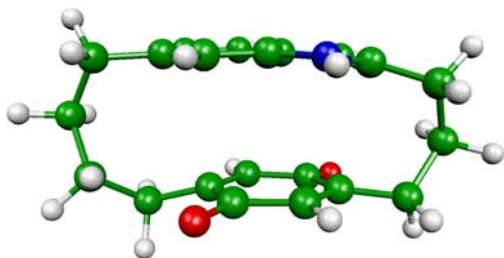
## 4.3.2 Computational Details

### 4.3.2.1 Choice of Model Systems

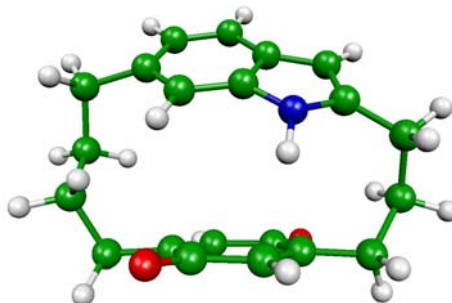
The selected model systems are various complexes between quinone and indole or pyrrole moieties interconnected by two aliphatic “handles” or „linkers“ in a cyclophane-type manner (see Figure 4.3.1 for the optimized structures). Apart from the choice of pyrrole vs. indole, the complexes differ in the length and type of the linkers, and also in their connection points on the quinone side. Several specific systems have linkers with either three or four CH<sub>2</sub> groups (the number of CH<sub>2</sub> groups in both linkers is indicated by numbers in brackets, e.g. as [4,4]). Alternatively, we

have studied systems with a CH<sub>2</sub>-S-CH<sub>2</sub>-CH<sub>2</sub> chain as linker (with the ethylene moiety connected to pyrrole; these systems are designated by an [S,S] label).

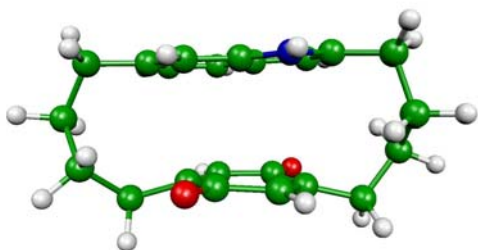
a)



b)



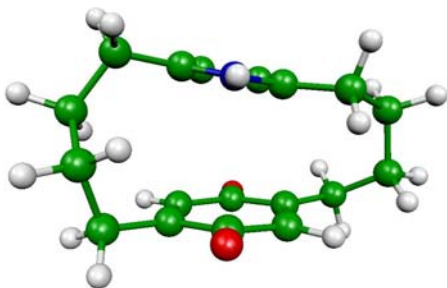
c)



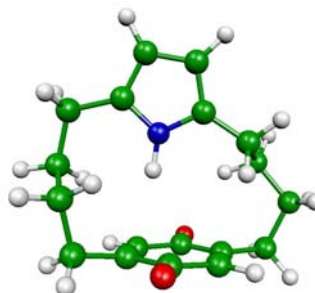
d)



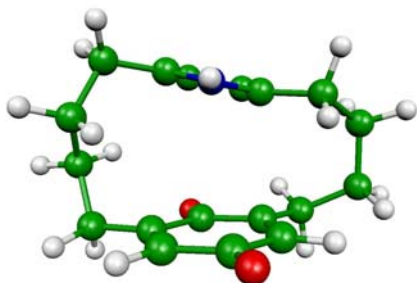
e)



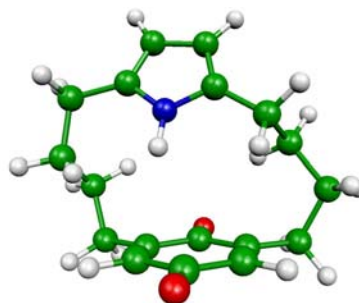
f)



g)



h)



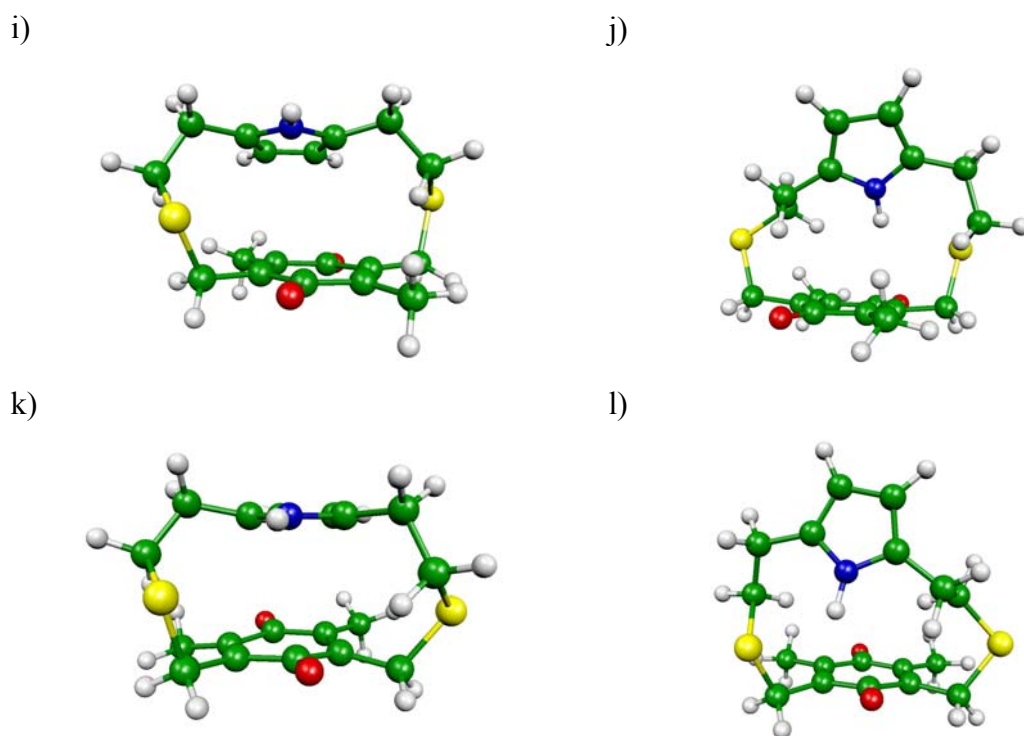


Figure 4.3.1 MP2-Optimized structures of model systems in neutral and monoanionic states (RI-MP2/SVP except for the indole systems, where MP2/ECP-DZP structures are shown): a) [4,3] 2,5-Q-Ind, b) [4,3] 2,5-Q-Ind<sup>•-</sup>, c) [4,4] 2,5-Q-Ind, d) [4,4] 2,5-Q-Ind<sup>•-</sup>, e) [4,4] 2,5-Q-Pyr, f) [4,4] 2,5-Q-Pyr<sup>•-</sup>, g) [4,4] 2,6-Q-Pyr, h) [4,4] 2,6-Q-Pyr<sup>•-</sup>, i) [S,S] 2,5-Q-Pyr, j) [S,S] 2,5-Q-Pyr<sup>•-</sup>, k) [S,S] 2,6-Q-Pyr, l) [S,S] 2,6-Q-Pyr<sup>•-</sup>.

The latter systems are closely related to the quinone-benzene complexes in ref 256. For consistency with that work, the two remaining hydrogen atoms on the quinone ring were replaced by methyl groups in these systems. The choice of a thioether linkage was made for relatively straightforward synthetic access. In several cases, we have compared attachments of the linker to the quinone at C2 and C5 position or at C2 and C6 position (see additional labels in Figure 4.3.1). Both the variable chain length and the different attachment points provide us with a range of different flexibilities of the corresponding complexes for redox-induced rearrangement. For comparison of redox potentials and EPR parameters, we have also carried out calculations for simpler quinone, semiquinone, and quinolate reference systems with appropriate substitution patterns (cf. Figure 4.3.2).

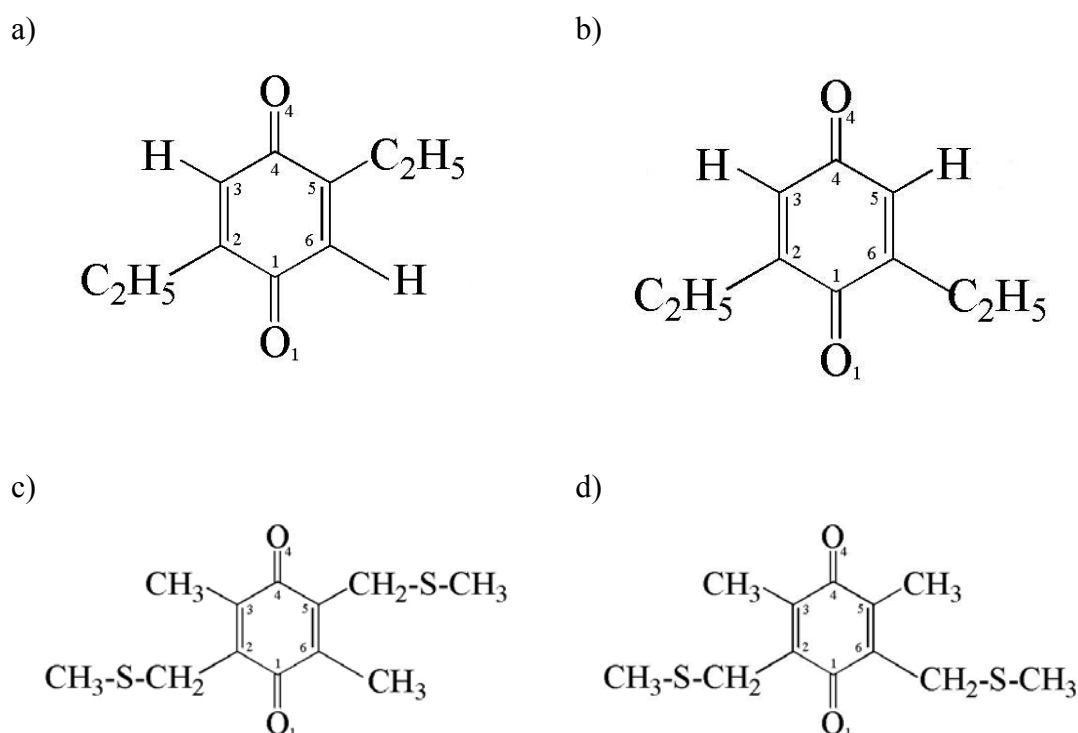


Figure 4.3.2 Reference molecules for  $g$ -tensor and reduction-energy calculations: a) 2,5-DEBQ (2,5-diethyl-1,4-benzoquinone), b) 2,6-DEBQ (2,6-diethyl-1,4-benzoquinone), c) 2,5-DTQ (3,6-dimethyl-2,5-bis(methylthio)methyl-1,4-benzoquinone), d) 2,6-DTQ (3,5-dimethyl-2,6-bis(methylthio)methyl-1,4-benzoquinone).

#### 4.3.2.2 Structure Optimizations and Energy Calculations

All structures have been fully optimized at the second-order Møller-Plesset perturbation (MP2) level of theory. This choice of level was based on the need to describe dispersion-type interactions between the  $\pi$ -systems and the inabilities of currently used density functionals to describe these interactions adequately. The major part of the calculations was carried out with the RI-MP2 method<sup>257,258</sup> with SVP orbital and auxiliary basis sets,<sup>258,259</sup> using the TURBOMOLE 5.6 program suite.<sup>232,233</sup> Due to convergence problems of the optimizations for two systems, [4,3] 2,5-Q-Ind and [4,4] 2,5-Q-Ind, these were optimized with the Gaussian 98 program at the conventional MP2 level.<sup>186</sup> In the latter, computationally very demanding calculations

we used effective core potentials and DZP valence basis sets<sup>187</sup> for C, O, and N, and a DZV valence basis set for hydrogen.<sup>188</sup>

Calculations of relative energies posed a dilemma. On one hand, MP2 is the lowest level at which we could expect to recover dispersion contributions to the reduction energies (due to  $\pi$ -stacking in the neutral state). On the other hand, it is known that MP2 underestimates the first adiabatic electron affinities of quinones dramatically, whereas DFT methods perform reasonably well (as indicated, e.g., by comparison to SAC-CI calculations on benzoquinone/benzoquinone<sup>260-262</sup>). This is probably due to differential effects of non-dynamical electron correlation, which are not described well at the leading order of many-body perturbation theory. More sophisticated multi-reference configuration interaction or related approaches with large active orbital spaces would be needed to incorporate both dispersion and non-dynamical correlation contributions at the same time. Unfortunately, such methods are currently unpractical for systems of the sizes considered here. The reduction energies were therefore calculated and compared at two different levels of theory: a) B3LYP hybrid DFT<sup>83,86,87,263</sup> with TZVP basis sets,<sup>264</sup> at the corresponding MP2-optimized structures, b) RI-MP2/SVP. In addition to gas-phase calculations, B3LYP/TZVP single point calculations have also been carried out for most systems (except for [4,3] 2,5-Q-Ind and [4,4] 2,5-Q-Ind) in a continuum solvent model. The conductor-like screening model (COSMO)<sup>265</sup> was used, as implemented in TURBOMOLE,<sup>232,233</sup> with the parameters for CHCl<sub>3</sub> solvent ( $\epsilon=4.90$ ). Both  $Q \rightarrow Q^{\bullet-}$  and  $Q^{\bullet-}/Q^{2-}$  reduction energies will be reported as adiabatic electron affinities, that is for optimized structures of oxidized and reduced state, but without vibrational or entropic corrections (we are mainly interested in changes of the energies due to intramolecular contacts). Electrostatic potentials (ESP) were computed at BP86<sup>77,78,80,266</sup>/SVP<sup>259</sup> level and were mapped onto electron-density isosurfaces ( $\rho=0.01$  au) calculated at the same level of theory. All energy and ESP calculations were carried out with TURBOMOLE. The ESP visualization was done with the Molekel program.<sup>267</sup>



### 4.3.2.3 *g*-Tensor Calculations

The electronic *g*-tensors of the semiquinone radical anionic states were computed at the MP2-optimized structures, using a second-order perturbation theory density functional (DFT) approach.<sup>45,106</sup> All the details of the calculations are as described in refs 106,159, and 160 and in Chapter 3. Here we only summarize the main features. The electronic structure calculations were done with TURBOMOLE 5.6<sup>232,233</sup> at the uncoupled RI-DFT level, using the BP86 functional<sup>77,78,80,266</sup> and a DZVP basis set<sup>188</sup> (SVP auxiliary basis sets<sup>231,268</sup> were used to fit the electron density). The Kohn-Sham molecular orbital information from these calculations was then transferred by appropriate interface routines<sup>106</sup> to the MAG (magnetic resonance) property module of the in-house program ReSpect.<sup>50</sup> In the second-order perturbation approach<sup>45</sup> we employed the all-electron atomic mean-field approximation (AMFI)<sup>115,116</sup> to compute the spin-orbit matrix elements. The common gauge origin for the external magnetic vector potential was placed at the midpoint between the two carbonyl oxygen atoms of the benzosemiquinone ring. This is expected to be close to the center of spin density. As discussed in Chapter 3, the *g*-tensor is defined as  $\mathbf{g} = g_e \mathbf{1} + \Delta\mathbf{g}$ , where the free-electron value  $g_e = 2.002319$ . We present and discuss *g*-shift components ( $\Delta\mathbf{g}$ ) defined as corrections to  $g_e$  in ppm (that is, in units of  $10^{-6}$ ). As for the thermochemical calculations (see above), *g*-tensors for a number of semiquinone radical anions have been computed not only in the gas phase but also with a polarizable continuum solvent model added (again for CHCl<sub>3</sub>,  $\epsilon=4.90$ , using COSMO).

## 4.3.3 Results and Discussion

### 4.3.3.1 Structures of Model Complexes

Figure 4.3.1 shows the RI-MP2 optimized structures of neutral and monoanionic systems (regular MP2 for the indole systems, cf. 4.3.2 Computational Details). For the pyrrole-containing systems, the structures of the dianionic systems were also optimized (structures for the thioether-linked systems are shown in Figure 4.3.3) and will be discussed below with the corresponding monoanions.

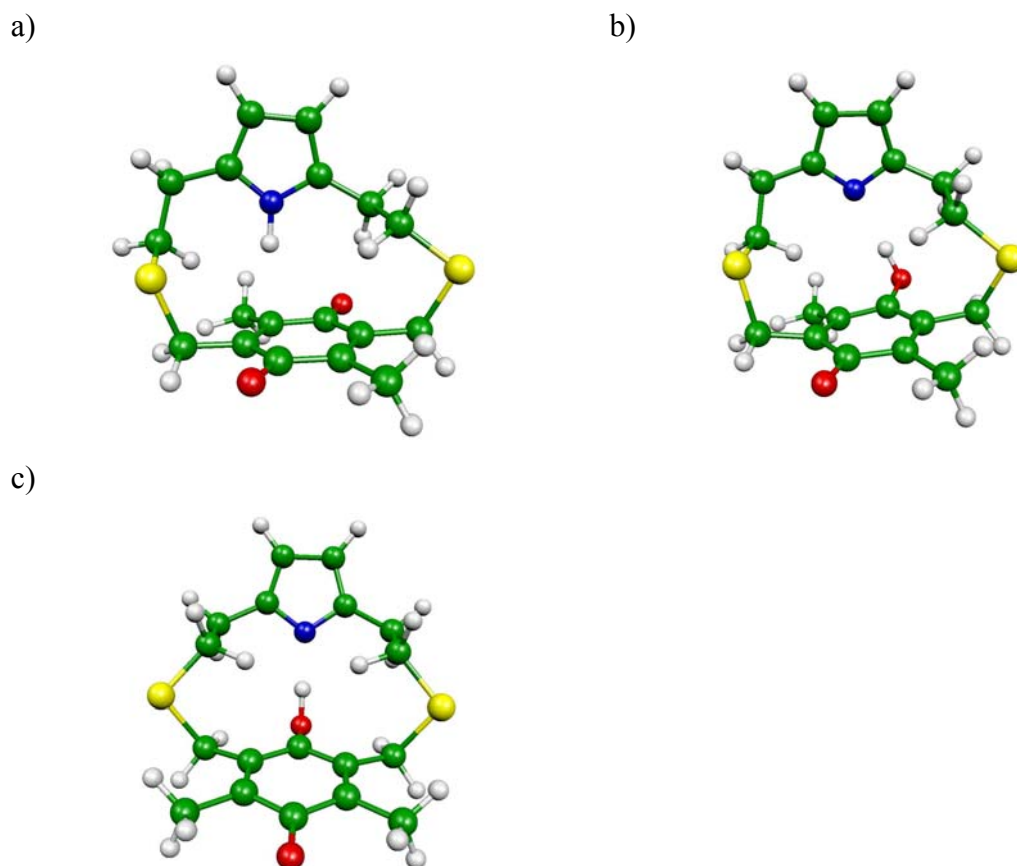


Figure 4.3.3 RI-MP2/SVP-optimized structures of the dianionic thioether-linked systems: [S,S] 2,5-Q-Pyr<sup>2-</sup> a) without, and b) with proton transfer from pyrrole to the quinolate oxygen atom; c) [S,S] 2,6-Q-Pyr<sup>2-</sup>.

**Quinone-indole models.** The optimized structures of quinone-indole complexes with either two four-carbon linkers or with one four-carbon and one three-carbon linker in their neutral and monoanionic states are shown in Figure 4.3.1a-d. Both systems exhibit a 2,5 connection pattern (for this particular set of large systems, we have not investigated alternative structures with a 2,6 connection). For the indole unit, the C3 and C7 positions are the natural attachment points for the two linkers (Figure 4.3.1d provides the atom numbering within the indole).

The neutral complexes (Figure 4.3.1a,c) have essentially coplanar,  $\pi$ -stacked quinone and indole moieties, at an average plane-to-plane distance of 3.01 Å, which agrees excellently with the MP2-optimized structures of unconnected, bimolecular quinone-indole model complexes,<sup>174</sup> and also with the dimensions of the quinone-

tryptophan  $\pi$ -stacking in the X-ray structure of photosystem I,<sup>182</sup> or in the structure of the Q<sub>A</sub> site of purple bacteria photosynthetic reaction centers.<sup>181</sup> The N-H vector is directed roughly parallel to the bisector of the quinone C2-C3 bond. In contrast, the two semiquinone states (Figure 4.3.1b,d) exhibit different stages of reorientation towards a T-stacked structure. The [4,3] system apparently does not provide sufficient flexibility for a complete 90° reorientation, and the semiquinone and indole planes are inclined only by ca. 40° with respect to each other (Figure 4.3.1b). The N-H $\cdots\pi$  hydrogen bond points towards C6 of the quinone (H $\cdots$ C distance 2.2Å), and the C2-H bond of indole points into the direction of O1 (H $\cdots$ O distance 3.0Å), allowing additional weak C-H $\cdots$ O interactions. On the other hand, the reduced [4,4] system exhibits ideal T-stacking, with an inclination angle of exactly 90° and a H $\cdots$ ring distance of 2.24 Å (Figure 4.3.1d). This indicates the need for sufficient chain length. Clearly, the [4,4] system is already a viable candidate for a potential molecular motor.

**Quinone-pyrrole models with hydrocarbon linkers.** The structures of the quinone-pyrrole complexes studied are divided in two subgroups (see 4.3.2 Computational Details), one with pure hydrocarbon linkers and two C-H units within the quinone and the other with a thioether linker and two methyl substituents (Figure 4.3.1), discussed below. The natural attachment points of the linkages on the pyrrole side are the positions adjacent to the ring nitrogen atom. Starting with the hydrocarbon-linked systems, we see that both the 2,5 and 2,6 attachments on the quinone side provide more or less parallel  $\pi$ -stacked structures for the neutral systems (Figure 4.3.1e,g), with average interplanar distances of 3.09 Å and 3.01 Å, respectively. In the 2,5 case, the pyrrole ring eclipses the quinone ring, with the N-H bond above the quinone C=O bond. In the 2,6 case, the pyrrole ring is somewhat displaced towards the quinone C1 atom and lies above the C1=O bond.

Upon reduction to the semiquinone state, the 2,5-linked system provides ideal T-stacking with an essentially exact perpendicular orientation of quinone and pyrrole rings (Figure 4.3.1f), with the hydrogen bond pointing towards the center of the C2-C3 bond with a relatively short distance to the quinone plane of only 2.34 Å. The 2,6-linked system appears to be sterically more restricted and reorients only to an interplanar angle of 56° (Figure 4.3.1h), with the hydrogen bond directed towards C3 (H $\cdots$ C3 distance 2.67Å).

Upon reduction to the dianionic quinolate state, the 2,6-linked system exhibits stronger T-stacked interactions (the  $H\cdots\pi$  distance is shortened to 2.17Å), and the interplanar angle of the quinone and pyrrole rings increases to 70°. Strengthening of the T-stacked interaction is also observed for the dianionic 2,5-linked system (the  $H\cdots\pi$  distance is shortened to 2.16Å), although the interplanar angle of the quinone and pyrrole rings decrease slightly to 82°.

**Quinone-pyrrole models with thioether linkers.** For the neutral thioether-linked systems (Figure 4.3.1i,k), reasonably parallel  $\pi$ -stacked structures are again found. The optimized average interplanar distances are longer than in the previous cases, 3.50 Å for the 2,5 system and 3.20 Å for the 2,6 case. Apparently the thioether linkage keeps the two rings at a larger distance. In the 2,5 case, the pyrrole ring is somewhat displaced so that the ring center is above the quinone C3 atom, and the N-H bond is roughly parallel to the C1=O bond (Figure 4.3.1i), but pointed slightly away from the quinone. In the 2,6-linked case (Figure 4.3.1k), the nitrogen atom of the pyrrole is essentially above C1 of the quinone.

Upon reduction to the semiquinone anion, the 2,5 system reorients to an approximately T-stacked arrangement but with an interplanar angle of only ca. 57° (Figure 4.3.1j). The hydrogen bond is directed towards the intersection of the quinone C1-C2 bond. In the 2,6 case, the interplanar angle of 75° is closer to perpendicular, but now the hydrogen bond is to a significant extent directed towards the semiquinone carbonyl oxygen atom (but with a very long N-H $\cdots$ O distance of 3.85 Å).

As with the hydrocarbon-linked systems above, further reduction of the 2,5 system to the dianion leads to a strengthening of the T-stacked hydrogen bond (cf. Figure 4.3.3a; the shortest H $\cdots$ ring distance is only 2.12Å, interplanar angle 91°). The optimization for the dianion of the 2,6 system led to the transfer of the N-H proton to the nearest quinolate oxygen (Figure 4.3.3c), and no minimum without transfer of the proton was located. We have then performed an optimization for the 2,5 system in which the proton was also put onto the nearest quinolate oxygen atom, and it stayed there (Figure 4.3.3b). The energy of this second minimum is almost degenerate with the first one (at RI-MP2 level it was about 5 kJ mol<sup>-1</sup> lower, a B3LYP/TZVP single point placed it about 9 kJ mol<sup>-1</sup> higher in energy). We have not attempted to locate the barrier for the proton transfer. The O-H $\cdots$ N hydrogen bond in the proton-transferred

structures is shorter for the much better suited 2,6 system (Figure 4.3.3c; 1.63 Å) than for the more strained 2,5 system (Figure 4.3.3b; 2.15 Å), consistent with the larger driving force for the proton transfer.

#### 4.3.3.2 Influence of the Interactions on Reduction Energies

The previous computational studies of “unlinked” complexes between various quinones or semiquinones with indole have provided estimates (counterpoise-corrected MP2 data) of the interaction energies involved.<sup>174</sup> That is, the  $\pi$ -stacked interactions between neutral quinone and indole ranged from about 15 kJ mol<sup>-1</sup> for benzoquinone to about 30-35 kJ mol<sup>-1</sup> for substituted quinones (apparently, van-der-Waals interactions with the substituents contribute to the interactions). The T-stacked monoanionic (semiquinone) complexes exhibited remarkably large interaction energies of about 50 kJ mol<sup>-1</sup>, which we may take as upper limit for the interactions in the present, sterically more restricted intramolecular complexes. In view of these data, it may be presumed that the overall interactions between quinone/semiquinone and indole will stabilize the radical anionic state relative to the neutral state and thereby render the Q $\rightarrow$ Q<sup>-</sup> reduction energies more negative. This may be of interest also with respect to quinone/tryptophan interactions in redox proteins. We note in passing that calculations suggest somewhat lower interactions to water molecules T-stacked to benzosemiquinone. “Normal” hydrogen bonds to the semiquinone oxygen atoms are expected to provide a stabilization that is about 10-20 kJ mol<sup>-1</sup> larger than even in the optimum T-stacked arrangement. In a sterically unconstrained situation, this will thus be the most stable configuration for the anionic semiquinone-indole or semiquinone-pyrrole complexes. But as we have seen above, the choice of linker length and of attachment point may be used to control the preferred structures.

As an estimate of the changes in reduction energies effected by the “weak” interactions between quinone/semiquinone and indole/pyrrole moieties, we report in Table 4.3.1 energies for addition of an electron to the neutral or singly reduced quinone system, in comparison with appropriately substituted simpler quinones (cf. Figure 4.3.2), which we use as reference systems lacking these interactions. Unless stated otherwise, the energy changes refer generally to an adiabatic process. That is, they include the structural relaxation in the reduced state. We report static gas-phase

data, which neglect any environmental and vibrational effects. For most complexes we provide in addition B3LYP/TZVP results in a continuum solvent model (COSMO for CHCl<sub>3</sub>, ε=4.90).

Table 4.3.1 Computed reduction energies (Q→Q<sup>•-</sup> and Q<sup>•-</sup>→Q<sup>2-</sup>) of linked quinone model systems and reference molecules in gas phase and in the solution (cosmo solvation model).<sup>a</sup>

Model <sup>b</sup>	ΔE in kJ mol <sup>-1</sup>			
	Q→Q <sup>•-</sup>		Q <sup>•-</sup> →Q <sup>2-</sup>	
	gas phase	cosmo	gas phase	cosmo
2,6-DEBQ	-177.7 (-100.7)	-315.9	315.1 (336.6)	-95.1
[4,4] 2,6-Q-Pyr	-208.4 (-125.1)	-328.3	255.7 (259.6)	-111.3
2,6-DTQ	-187.5 (-115.2)	-311.7	265.2 <sup>c</sup> (294.2 <sup>c</sup> ) 233.0 <sup>d</sup> (240.6 <sup>d</sup> )	-103.9 <sup>c</sup> -119.4 <sup>d</sup>
[S,S] 2,6-Q-Pyr	-236.3 (-135.5)	-346.1	141.6 (142.0)	-171.1
2,5-DEBQ	-181.4 <sup>e</sup> (-108.7 <sup>e</sup> )	-320.2	316.8 (343.4)	-95.3
[4,4] 2,5-Q-Pyr	-212.4 (-122.2)	-332.6	260.0 (269.3)	-109.2
2,5-DEBQ	-179.5 <sup>e</sup> (-108.2 <sup>e</sup> )			
[4,3] 2,5-Q-Ind	-214.8 (-103.7)			
[4,4] 2,5-Q-Ind	-218.8 (-113.3)			
2,5-DTQ	-186.2 (-117.5)	-311.5	263.6 <sup>c</sup> (294.7 <sup>c</sup> ) 228.8 <sup>d</sup> (239.5 <sup>d</sup> )	-105.9 <sup>c</sup> -119.8 <sup>d</sup>
[S,S] 2,5-Q-Pyr	-228.9 (-146.5)	-336.3	218.1 (224.2) 222.5 <sup>f</sup> (217.8 <sup>f</sup> )	-125.2 -94.8 <sup>f</sup>

<sup>a</sup>B3LYP/TZVP results with RI-MP2/SVP data in parentheses. Cosmo calculations for CHCl<sub>3</sub> solvent (ε=4.9). <sup>b</sup>Cf. Figures 4.3.1, 4.3.2 and 4.3.3 for structures. <sup>c</sup>Conformations of the methylthio-methyl substituents were fixed to those in the linked complex. <sup>d</sup>Full structure optimization with reorientation of the methylthio-methyl substituents, see text. <sup>e</sup>Reference molecules optimized at the same level as corresponding complexes, that is RI-MP2/SVP for pyrrole-based complexes, MP2/ECP-DZP for indole-based complexes; see Computational Details. <sup>f</sup>Energy for dianion after proton transfer to quinolate oxygen; see text.

Starting with the gas-phase data, we report both B3LYP/TZVP and RI-MP2/SVP energies. As discussed in Computational Details above, we expect that the MP2 level recovers the dispersion-type interactions due to  $\pi$ -stacking in the neutral state. On the other hand, the overall reduction energies should be much better reproduced at the hybrid DFT level. This is confirmed by the computed values for the  $Q \rightarrow Q^{\bullet-}$  reduction energies. They should be in the range of about 2 eV (200 kJ mol<sup>-1</sup>; gas-phase data).<sup>260-262</sup> The B3LYP results agree with this, whereas the RI-MP2 data are appreciably lower. We are interested mainly in the changes due to the intramolecular interactions ( $\pi$ - or T-stacking, regular hydrogen bonds), relative to the reference molecules lacking such interactions. And indeed, here the RI-MP2 values provide smaller differences than the B3LYP calculations, as one might expect.

While MP2 and B3LYP should both recover the stabilization of the semiquinone radical anion by T-stacked or regular hydrogen bonds, the stabilization by  $\pi$ -stacking in the neutral state is only included at MP2 level. On the other hand, the  $Q^{\bullet-} \rightarrow Q^{2-}$  reduction energies differ much less between B3LYP and RI-MP2 results, suggesting that differential non-dynamical electron correlation effects (cf. Computational Details section) are less pronounced in this case.

Starting with the  $Q \rightarrow Q^{\bullet-}$  redox couples, we see that the additional weak interactions stabilize overall the semiquinone state and thereby render the adiabatic electron affinities more negative. The magnitude of the effect should reflect both the stability of the  $\pi$ -stacked interactions in the neutral state and the degree of flexibility for reorientation in the anionic state. The differences are generally smaller at RI-MP2 than at B3LYP level. The largest stabilization of the semiquinone radical anion state, on the order of 40-50 kJ mol<sup>-1</sup> at B3LYP level and of 20-30 kJ mol<sup>-1</sup> at RI-MP2 level, is found for the [S,S]-linked pyrrole systems. This holds also for the 2,6-linked system (Table 4.3.1, cf. Figure 4.3.1k,l), which exhibits a regular hydrogen-bond to the semiquinone oxygen atom in the monoanionic state (as discussed above, this interaction is expected to slightly exceed the T-stacked interaction). Somewhat lower, but still significant stabilization is found for other systems (the relatively unfavorable [4,3] 2,5-Q-Ind system - cf. Figure 4.3.1a,b - is an exception, as it exhibits no extra stabilization of the reduced state at RI-MP2 level). It is thus clear that the reduction energies for the quinone/semiquinone couple in intramolecular complexes with a

favorable reorientation upon reduction will be more negative than those for the reference molecules.

Reduction to the dianionic state ( $Q^{\bullet-} \rightarrow Q^{2-}$ ) is generally very endothermic in the gas phase, as one might have expected. Depending on solvent, this further reduction may turn into an exothermic process in solution (see below). We note again a stabilization of the more negatively charged states by the additional interactions in the complexes compared to the reference systems (Table 4.3.1). The RI-MP2 values are about 10-30 kJ mol<sup>-1</sup> more positive than the B3LYP results for the reference systems, but less so for the complexes. The stabilization of the reduced states by intramolecular hydrogen-bond interactions in the complexes is thus slightly larger at RI-MP2 level. Focusing on the probably more reliable B3LYP data in the following (dispersion-type interactions should not be very important for the  $Q^{\bullet-} \rightarrow Q^{2-}$  reduction), the additional stabilization is about 50-60 kJ mol<sup>-1</sup> for most cases but appears to be even larger for the [S,S] 2,6-Q-Pyr system. For the [S,S] 2,5-Q-Pyr system, the energies depend of course also somewhat on whether we use the proton-transferred minimum or not (cf. above). In case of both [S,S]-linked systems, full optimization of the reference molecules led to conformations of the methylthio-methyl substituents (towards the quinolate oxygen atoms) that differed substantially from the conformations of the corresponding linkers in the complex. As this affects the reduction energies, the table provides also values for the case where the conformation in the reference molecule was fixed to that in the complex.

When moving from the gas-phase calculations to calculations in a continuum solvent model, the semiquinone monoanions are stabilized relative to the neutral quinones, and the quinolate dianions are stabilized even more. This renders the  $Q \rightarrow Q^{\bullet-}$  reduction energies about 110-140 kJ mol<sup>-1</sup> and the  $Q^{\bullet-} \rightarrow Q^{2-}$  reduction energies even by about 300-400 kJ mol<sup>-1</sup> more negative (the latter process is thus turned exothermic). When comparing the linked complexes to the smaller reference systems, the effects of the extra intramolecular T-stacking or regular hydrogen bonding interactions are damped nonnegligibly. In case of the  $Q \rightarrow Q^{\bullet-}$  reductions, the extra stabilization is reduced by about 15-20 kJ mol<sup>-1</sup>. The resulting differential effects are thus already rather small. Further test calculations with different dielectric constants of the continuum solvent (data not shown) indicate that the damping effect increases for polar solvents. It therefore appears likely that the differential



intramolecular stabilization effects may still be notable in nonpolar solvents but might be undetectable in polar solvents (note that the effects may be even slightly smaller at MP2 level, see above). In case of the  $Q^{\bullet-} \rightarrow Q^{2-}$  reduction energies, the differential effects are also notably damped (by about 30-50 kJ mol<sup>-1</sup>) but remain visible in the energies reported.

#### 4.3.3.3 $g$ -Tensor Results

It is well known that hydrogen bonds to the semiquinone carbonyl oxygen atoms lower particularly the  $g_x$  and more moderately the  $g_y$  component of the semiquinone  $g$ -tensor. This has become an extremely important spectroscopic probe in the study of the environment of semiquinone radical anions in proteins (and also for related  $\pi$ -radicals).<sup>166-169,173,175,180,222,223,269</sup> In contrast, recent calculations have demonstrated that T-stacked hydrogen bonds to the  $\pi$ -system effect a somewhat more moderate *enhancement* of both  $g_x$  and  $g_y$ .<sup>174</sup>  $g$ -Tensors computed for the semiquinone states of the present linked models are compared to those for the corresponding reference compounds in Table 4.3.2. We report gas-phase data for all systems and results in continuum solvent for most of them. The results are essentially consistent with the expectations but show a somewhat more subtle behavior.

In those cases where the structural results point to a true T-stacking, the  $\Delta g_x$  and  $\Delta g_y$  components are increased by about 3-8% and 1-3%, respectively. However, for [S,S] 2,5-Q-Pyr<sup>•-</sup> only the  $g_x$  component is enhanced, whereas  $g_y$  is slightly lowered. For the [S,S] 2,6-Q-Pyr<sup>•-</sup> anion, where the hydrogen bonding is preferentially to the semiquinone oxygen atom, both  $\Delta g_x$  and  $\Delta g_y$  are reduced compared to the reference compound 2,6-DTQ<sup>•-</sup>, consistent with expectations. For the sterically restricted model [4,3] 2,5-Q-Ind<sup>•-</sup> with incomplete reorientation of the indole,  $\Delta g_x$  is lowered and  $\Delta g_y$  is somewhat increased. The by far largest enhancement of both  $g_x$  and  $g_y$  is found for the almost ideally T-stacked [4,4] 2,5-Q-Pyr<sup>•-</sup> system (cf. Figure 4.3.1h). Including the CHCl<sub>3</sub> continuum solvent model reduces  $\Delta g_x$  by ca. 350-500 ppm and  $\Delta g_y$  by ca. 120-150 ppm (Table 4.3.2) but does not alter the relevant differential effects notably. Measurement of electronic  $g$ -tensors by HF-EPR methods may thus provide a good method to establish the structure of the semiquinone state of the linked systems, provided that reference data for the corresponding unconnected systems are available.

Of course the flexibility of the relative orientation of the two  $\pi$ -systems may play a role, and potentially molecular dynamics may have to be considered.

Table 4.3.2 Calculated  $g$ -shift tensors (in ppm) for linked semiquinone complexes and reference molecules.<sup>a</sup>

Model	gas phase			cosmo		
	$\Delta g_z$	$\Delta g_y$	$\Delta g_x$	$\Delta g_z$	$\Delta g_y$	$\Delta g_x$
2,6-DEBQ <sup>•-</sup>	-1	2911	5533	-13	2783	5030
[4,4] 2,6-Q-Pyr <sup>•-</sup>	28	2954	5782	-8	2818	5223
2,6-DTQ <sup>•-</sup>	338	2933	4824	350	2816	4468
[S,S] 2,6-DMBQ-Pyr <sup>•-</sup>	569	2874	4637	442	2794	4194
2,5-DEBQ <sup>•-</sup>	5	2917	5709	4	2792	5347
[4,3] 2,5-Q-Ind <sup>•-</sup>	58	2952	5582			
[4,4] 2,5-Q-Ind <sup>•-</sup>	29	2947	5880			
[4,4] 2,5-Q-Pyr <sup>•-</sup>	19	2994	6064	14	2848	5540
2,5-DTQ <sup>•-</sup>	340	2833	4812	367	2682	4462
[S,S] 2,5-DMBQ-Pyr <sup>•-</sup>	354	2729	5198	416	2607	4818

<sup>a</sup>BP86/DZVP results with AMFI spin-orbit operators at MP2-optimized structures. Calculations with COSMO continuum solvent for CHCl<sub>3</sub> solvent ( $\epsilon = 4.9$ ).

In case of the diamagnetic neutral and dianionic systems, NMR spectroscopy might be used for structural characterization. For related quinone-benzene complexes, high-field shifts of the T-stacked benzene proton due to ring currents of the hydroquinone turned out to be characteristic.<sup>256</sup> Provided the <sup>1</sup>H shifts of the N-H protons may be determined, these may provide some additional information, in particular for the dianions.

#### 4.3.3.4 Nature of the Interaction and Comparison to Related Systems

$\pi$ -Stacked interactions are of particular interest, for example in the context of base-base interactions in DNA, tertiary structure formation in proteins, protein stability, molecular assembly or molecular recognition. The competition between  $\pi$ -

stacked (parallel displaced) and T-stacked arrangements has been studied extensively by quantum chemical calculations for the weakly interacting prototypical benzene dimer. Both structures are nearly isoenergetic with energy differences smaller than 1 kJ mol<sup>-1</sup>, and the interaction energies in the order of only 10 kJ mol<sup>-1</sup>.<sup>270-272</sup> Other molecular complexes studied in this context were, e.g., toluene-toluene,<sup>273</sup> indole-benzene,<sup>274</sup> indole-indole,<sup>275,276</sup> pyrrole-pyrrole,<sup>277</sup> or phenol-phenol.<sup>278</sup> In many cases, the relatively weak interactions and shallow energy landscapes for rearrangements made the theoretical study of these intermolecular complexes a challenge.

The much larger charge-dependent preferences for one particular arrangement in the present study are expected to derive from more pronounced electrostatic interactions. In previous calculations on benzoquinone/benzene models, a change of structural preference was also found from a (parallel displaced)  $\pi$ -stacked arrangement for the neutral quinone towards T-stacked arrangements upon reduction to the semiquinone radical anion and quinol dianion states.<sup>256,279</sup> However, the preference for T-stacking in the monoanionic state was very weak, and only reduction to the dianion established a clearly T-stacked system. This was then confirmed experimentally<sup>256,279</sup> for complexes that are closely related to the thioether-linked models in Figure 4.3.1i-l. These were indicated to act as flipper-like nanomechanical molecular motors. The much larger preference for the T-stacked structure in the present case with indole or pyrrole donors reflects probably the larger dipole moment of the N-H bond compared to a C-H bond in benzene.

Why does the system change its preference from  $\pi$ -stacked towards T-stacked upon addition of an electron? Figure 4.3.4 shows plots of the electrostatic potential (ESP) for one particular quinone and its monoanion and dianion.

Obviously, the additional electrons render the ESP above and below the ring  $\pi$ -system dramatically more negative. With addition of electrons, the  $\pi$ -system becomes a more and more potent acceptor for hydrogen bonds (of course, the acceptor character of the oxygen atoms is also enhanced, and hydrogen-bonding to oxygen remains the most stable interaction). At the same time, we expect repulsive interactions between a negatively charged  $\pi$ -system and another  $\pi$ -stacked ring. The

change of structural preferences with addition of electrons is thus largely controlled by the electrostatics of the system.

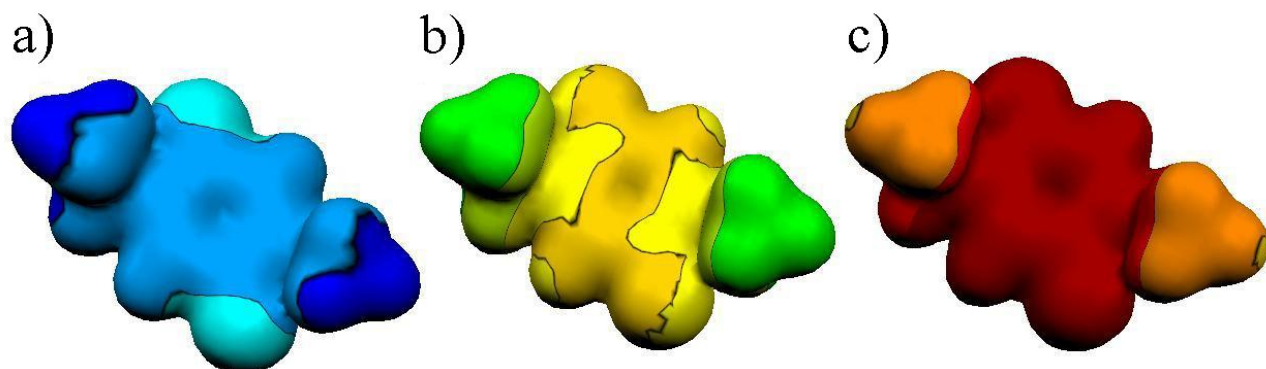


Figure 4.3.4 Computed electrostatic potentials of different states of 2,5-DEBQ (2,5-diethyl-1,4-benzoquinone) plotted as colour scale on a  $\rho = 0.01$  a.u. isodensity surface (BP86/SVP results). The colour scale ranges from -0.30 a.u. (red) to 0.05 a.u. (blue). a) Neutral quinone, b) semiquinone radical anion, c) quinolate dianion.

#### 4.3.4 Conclusions

Motivated by recent computational results for models of the quinone binding site of reconstituted variants of photosystem I,<sup>174</sup> we have designed theoretically a number of promising intramolecular mechanical devices. They are based on the charge-dependent change of orientational preferences of a complex between a quinone and a pyrrole or indole. Compared to recent theoretical and experimental work on related quinone-benzene complexes,<sup>256</sup> the present systems have the advantage of exhibiting a more pronounced orientational change already for one-electron reduction of the quinone to the semiquinone radical anion. This avoids a problem encountered for the dianions in ref 256, where protonation by the solvent appears to destroy partly the orientational preferences. Additionally, characteristic effects of the semiquinone-pyrrole or semiquinone-indole interactions on electronic  $g$ -tensors may make HF-EPR spectroscopy the method of choice for the structural characterization of the monoanionic complexes. We have initiated preparative and

spectroscopic studies aimed at establishing these systems as viable molecular mechanical devices. Quinone-based systems are attractive also in view of the straightforward synthetic access to larger aggregates, e.g. in so-called calix-quinone assemblies.<sup>280</sup> In addition, the present results may also bear on the question how intermolecular interactions in a protein framework may alter redox potentials and function of quinone redox systems in proteins.



## 4.4 Understanding the EPR Parameters of Glycine-Derived Radicals. The case of N-Acetylglycyl in the N-Acetylglycine Single-Crystal Environment<sup>157</sup>

### 4.4.1 Introduction

Since the seminal experiment of Sjöberg et al., which showed a tyrosyl radical to be essential for the function of ribonucleotide reductase (RNR) in *E. coli*,<sup>281</sup> it is known that protein radicals may play important roles in the enzymatic activity of proteins. Most of the protein radicals discovered to date are produced by one-electron oxidation of the protein side chains, e.g. thiyl, tryptophanyl, tyrosyl.<sup>52</sup> The only exception is glycyl radical which has its unpaired spin density almost entirely located on the protein back-bone. So far glycyl radicals were found unambiguously in three different enzymes: anaerobic class III ribonucleotide reductase (RNR),<sup>282-284</sup> pyruvate formate-lyase (PFL),<sup>285</sup> and benzylsuccinate synthase (BSS).<sup>286</sup> Many other enzymes are very likely to require glycyl radicals for their activity.<sup>287-290</sup>

In X-band EPR spectra, a doublet due to hyperfine splitting of the  $\alpha$ -hydrogen is observed for all of the studied glycyl radicals at  $g = 2.0034$ - $2.0039$ . Further information about structure and environment could be expected from the  $g$ -tensor. However, the extremely small  $g$ -anisotropy did not allow the  $g$ -tensor to be resolved until a very recent study at extremely high magnetic fields.<sup>291</sup> These high-field high-frequency EPR (HF-EPR) studies provided very similar  $g$ -tensors for glycyl radicals in BSS and PFL proteins, but somewhat different tensor components (at the given resolution) for the RNR of *E. coli*. While three-dimensional structure information for the RNR and PFL cases shows the presence of a glycyl radical and its involvement in the function of the enzymes, for none of these systems is the precise environment of the radical known. In this situation, it is desirable to relate the EPR parameters in

more detail to the structure and protein environment of glycyl radicals by carrying out quantum chemical calculations.

Before attempting to extract structural information by applying quantum chemical methods to models for protein-bound glycyl in a Chapter 4.5,<sup>156</sup> we calibrate carefully in this chapter our state-of-the-art computational methodology for a structurally better characterized, closely related system: the N-acetylglycyl (NAG<sup>•</sup>) radical generated by irradiation of a single crystal of N-acetylglycine (NAGH). X-ray crystal structure information is also available for NAGH.<sup>292</sup> The NAGH molecules adopt a nearly planar conformation in the crystal structure and remain planar upon formation of the NAG<sup>•</sup> radical. The molecular plane is created by the C<sub>α</sub>, N, O and H<sub>α</sub> atoms.<sup>293,294</sup> Two slightly different sets of EPR parameters are found in the literature for NAG<sup>•</sup>.<sup>293,294</sup> The reported *g*-tensors differ in the magnitude of the tensor components but agree in the orientation of the principal axes. The *g*-anisotropies reported for NAG<sup>•</sup> resemble those obtained recently for glycyl radical enzymes,<sup>291</sup> suggesting that we may use NAG<sup>•</sup> as an excellent analogue to evaluate methods to be applied to the protein-bound glycyl radical. We consider the dataset of Saxebøl et al.<sup>293</sup> more reliable, given in particular the appreciably positive  $\Delta g_z$  in the older dataset<sup>294</sup> ( $\Delta g_x=1881$ ,  $\Delta g_y=881$ ,  $\Delta g_z=381$ ). Limited information on <sup>1</sup>H<sub>α</sub> hyperfine couplings (<sup>1</sup>H<sub>α</sub>-HFC) is also available for NAG<sup>•</sup>.

A number of theoretical studies of glycyl radical and its dipeptide analogue have been performed, most of them investigating the conformational behavior and hyperfine properties of the radical.<sup>150,151,295</sup> A strong preference for planar or quasi-planar conformations was found, allowing effective delocalization of the  $\pi$ -electrons across the whole radical. Similar values of isotropic hyperfine splittings were found for various conformers. Very limited spin transfer between free radical and solvent (water) molecules indicated the solvent effect to be largely due to a redistribution of spin density within the radical.<sup>150,295</sup> Himo et al. suggested a non-planar structure of the glycyl radical in bacteriophage T<sub>4</sub> RNR to explain its somewhat different <sup>13</sup>C<sub>α</sub> HFCs compared to the PFL and *E. coli* RNR enzymes.<sup>296</sup>

Two recent studies using density functional theory (DFT) have also dealt with the *g*-tensor of N-formylglycyl<sup>161,162</sup> forms of the glycyl radical. Focusing each only on one conformer (different ones in the two studies), both works tried to establish the



validity of their respective DFT protocols. Basis sets, density functional, vibrational averaging (of the out-of-plane displacement of  $H_\alpha$ ) and solvent effects were evaluated in ref 161. Very limited modeling of environment, the lack of conformational studies, and the restriction to semi-empirical spin-orbit operators leave a number of open questions to be answered. For the NAG $\bullet$  radical, only early INDO MO-calculations of isotropic hyperfine coupling constants are available.<sup>293</sup>

In this chapter we report the first systematic computational study of  $g$ -tensor and HFCs for the NAG $\bullet$  radical. As the accurate computation of  $g$ -tensors for this radical, as well as for the protein-bound glycy radical (see Chapter 4.5<sup>156</sup>), turn out to be a more pronounced challenge to current DFT methods than for any other organic radical we have studied before,<sup>51,105,125,153,174</sup> this chapter includes detailed evaluations of various computational parameters. These range from the methods used for structure optimization via basis-set effects to the choice of spin-orbit operators and gauge-origin of the magnetic vector potential. Environmental effects are investigated by various supermolecular models, and conformational effects on the EPR parameters are also studied in detail. In view of the known structure and environment, the results of this study serve as the primary basis for calibrating parallel computational investigations (see Chapter 4.5<sup>156</sup>) of protein-bound glycy radicals, for which less structural information is available.

## 4.4.2 Computational Details

### 4.4.2.1 Structure Optimizations

The X-ray single-crystal structure of N-acetylglycine<sup>292</sup> provides information on the local environment of the NAG $\bullet$  radical. Nearly planar layers of N-acetylglycine molecules are joined together by a two-dimensional network of hydrogen bonds, with each molecule having four hydrogen bonds to its closest neighbors. EPR studies on the irradiated crystal indicated that the radical preserves the planar structure.<sup>293,294</sup>

Initially, we have evaluated various structures for the isolated radical. Four energetically low-lying conformers of NAG $\bullet$  were investigated (cf. Figure 4.4.1), the cis-cis (CC-NAG $\bullet$ ), cis-trans (CT-NAG $\bullet$ ), trans-cis (TC-NAG $\bullet$ ), and trans-trans (TT-NAG $\bullet$ ) forms, where cis and trans conformations are defined by the  $\phi$  and  $\psi$  dihedral

angles as shown in Figure 4.4.1a. Environmental effects were subsequently evaluated by two types of supermolecular models (based on the CC-NAG<sup>•</sup> form): a) hydrogen bonding modeled by up to four water molecules (models 1-5 in Figure 4.4.2), and b) a model of CC-NAG<sup>•</sup> cut out of the single-crystal environment (model 6 in Figure 4.4.3).

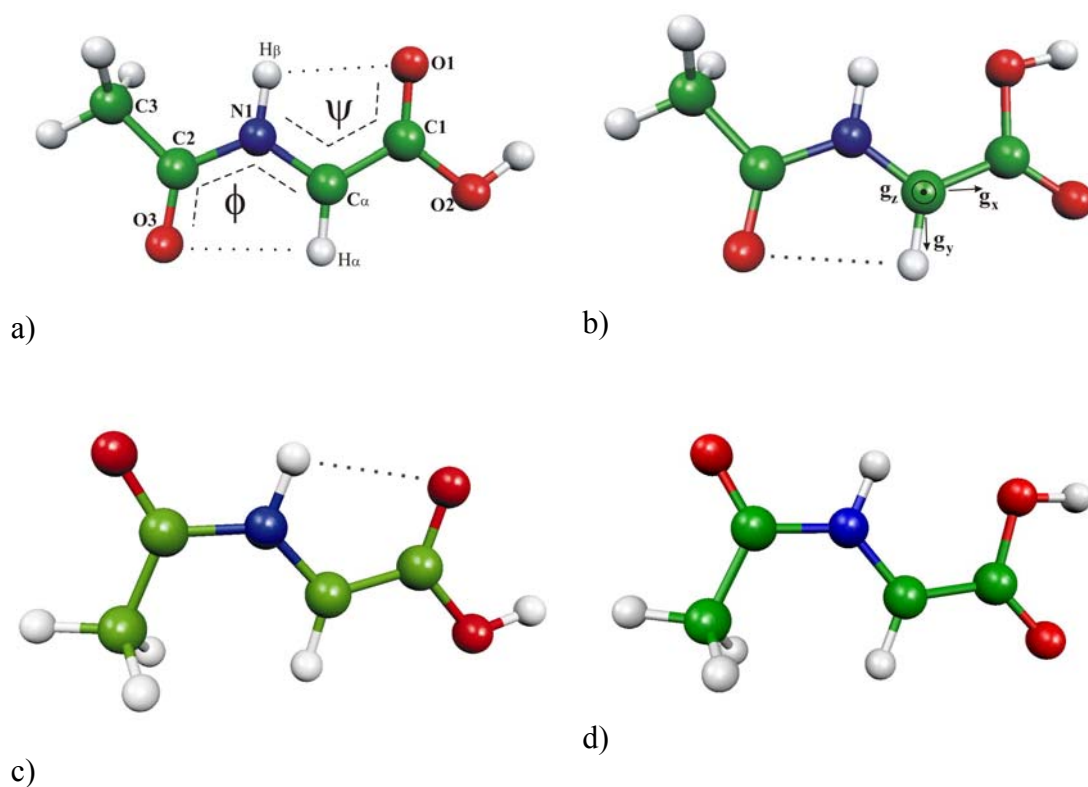


Figure 4.4.1 Conformers of the NAG<sup>•</sup> radical: a) cis-cis (CC-NAG<sup>•</sup>); atom numbering and definition of  $\phi$  and  $\psi$  dihedral angles. b) cis-trans (CT-NAG<sup>•</sup>); principal axes of g-tensor. c) trans-cis (TC-NAG<sup>•</sup>). d) trans-trans (TT-NAG<sup>•</sup>). The dotted lines indicate intramolecular hydrogen bonds.

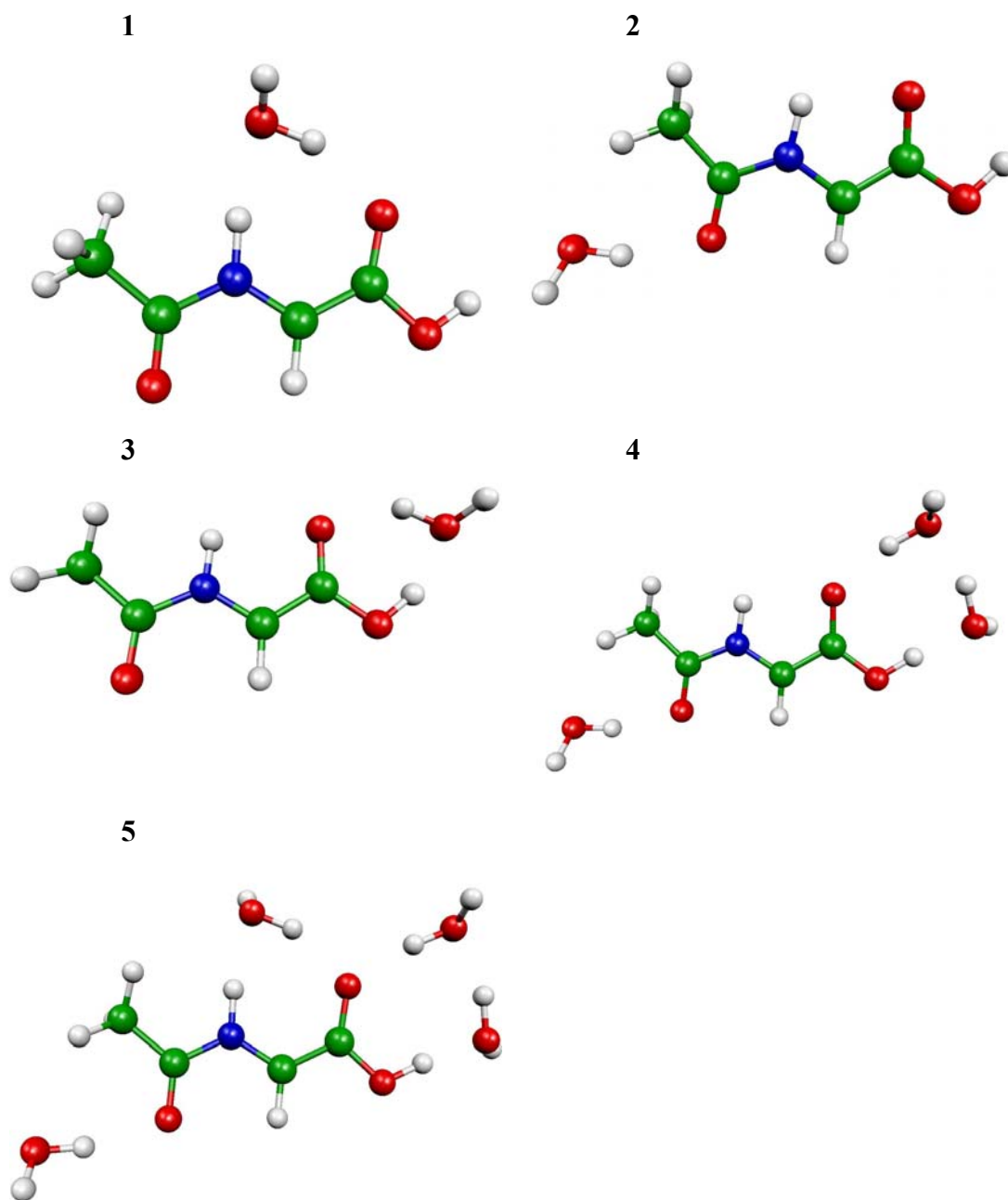


Figure 4.4.2 Optimized structures of the CC-NAG<sup>•</sup> radical in different hydrogen bonding frameworks modeled by water molecules.

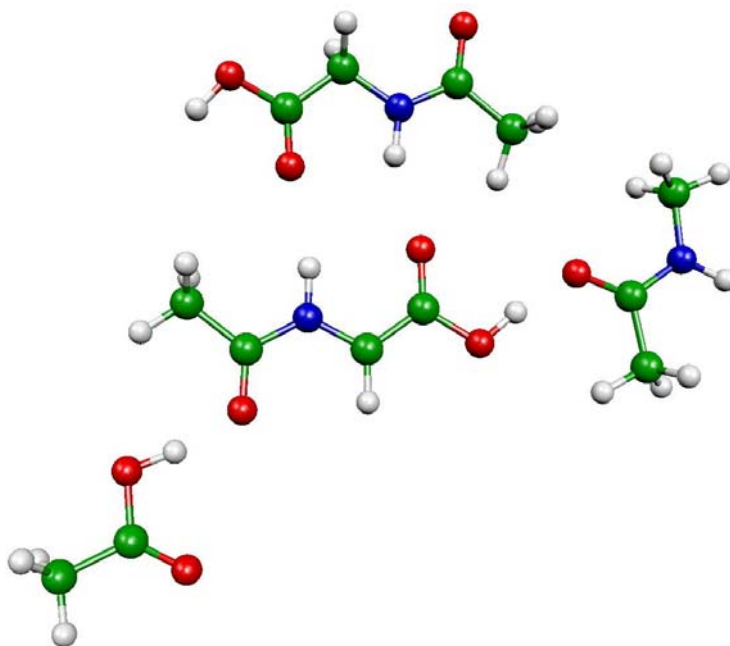


Figure 4.4.3 Model of CC-NAG<sup>•</sup> in the single-crystal environment.

The model 6 of CC-NAG<sup>•</sup> was built on the basis of the intermolecular arrangement given by the X-ray structure<sup>292</sup> (the NAGH molecules in the crystal are in CC conformation, and structure optimizations favor the CC form also for the radical – see below). To include accurately all hydrogen-bonding interactions, fragments representing three neighboring NAGH molecules, hydrogen-bonded to a central NAG<sup>•</sup> radical, were constructed. Both the NAG<sup>•</sup> radical and the hydrogen-bonded neighbor fragments were DFT-optimized (see below). The fragments were a) NAGH, b) acetic acid (AcOH), and c) N-methylacetamide (NMA) (see Figure 4.4.3). In a subsequent partial optimization of the whole supermolecular model, the positions of all atoms of the radical and of all hydrogens of the neighboring molecules were relaxed while the positions of all the heavier atoms on the neighbor fragments were kept fixed.

This partial optimization of model 6 was performed with the Gaussian03 program.<sup>234</sup> All other structure optimizations used the TURBOMOLE (v.5.6) program.<sup>232,233</sup> Unless stated otherwise, all structure optimizations were done with the hybrid B3LYP functional<sup>83,86,87</sup> and DZVP basis sets.<sup>188</sup> As we found the *g*-tensor of NAG<sup>•</sup> radical to be unusually sensitive to small structural changes, different

computational levels of structure optimization have been compared for the isolated CC-NAG<sup>•</sup> radical: i) the B3LYP and BP86<sup>78,80</sup> DFT levels with either DZVP or TZVP<sup>264</sup> basis sets (for BP86 the RI approximation was used with the corresponding auxiliary basis sets<sup>231,268</sup>); ii) the RI-MP2 level with either SVP or TZVP basis sets (and corresponding auxiliary basis sets).<sup>257,258</sup>

#### 4.4.2.2 *g*-Tensor Calculations

The *g*-tensor calculations used the DFT approach of refs 45 and 106, introduced also in Chapter 3. Specifically, the unrestricted Kohn-Sham orbitals obtained from the TURBOMOLE (v.5.6) program<sup>232,233</sup> were transferred by appropriate routines to the MAG (magnetic resonance) property module of the in-house program ReSpect.<sup>50</sup> Specifics about spin-orbit operators and choice of gauge origin are discussed below. The extensive experience for computations of *g*-tensors of organic radicals<sup>51,105,125,153,155,190</sup> has indicated the RI-BP86/DZVP<sup>78,80,188,231,268</sup> level of theory to be an excellent compromise between accuracy and computational effort. As a somewhat different basis-set level has been favored in a recent study of glycyl radical *g*-tensors,<sup>161</sup> and as very small *g*-anisotropies are studied, we have performed an extensive basis-set study for CC-NAG<sup>•</sup> with basis sets including EPR-II,<sup>235</sup> EPR-III,<sup>235</sup> 6311++G(3df,3dp),<sup>297-300</sup> and cc-pVQZ.<sup>301</sup>

Usually, the *g*-tensor is much less dependent on the choice of the gauge origin of the magnetic vector potential than other second-order properties depending on an external magnetic field (as, e.g., NMR chemical shifts or magnetic susceptibilities; cf., e.g., various chapters in ref 49). In the past, a common gauge origin in *g*-tensor calculations was often used, e.g. at the center of nuclear charges (this renders the calculations computationally less expensive than when using more sophisticated gauge methods like GIAO). As matters turn out to be more complicated in the present case (see below), we have compared, again for the isolated CC-NAG<sup>•</sup> radical, gauge origins at different nuclei in the system, and also distributed gauges with gauge-including atomic orbitals (GIAO<sup>119,120</sup>). Our preferred choice of approximations to the full one- and two-electron Breit-Pauli spin-orbit operator in the past has been the very efficient one-electron one-center atomic mean-field approximation (AMFI).<sup>115,116</sup> As the one-center approximation is not strictly compatible with calculations using GIAOs

(but see discussion below), we have in addition employed two further spin-orbit operators: (a) an exact, explicit treatment of all one- and two-electron Breit-Pauli spin-orbit integrals (FULL), and (b) semi-empirical one-electron SO operators with adjusted effective nuclear charges ( $Z_{\text{eff}}$ ).<sup>117</sup> The latter choice appears to be the basis of the  $g$ -tensor implementation in the G03 program that was used in the two recent  $g$ -tensor studies of glycylic radicals.<sup>161,162</sup> Following our detailed benchmark studies below, we chose for the remainder of the calculations in this chapter an exact treatment of the SO integrals (FULL), together with the GIAO method.

As discussed in Chapter 3, we report and discuss  $g$ -shift tensors ( $\Delta g$ ), defined as the correction to the free-electron value as  $\Delta g = \mathbf{g} - g_e(\mathbf{1})$  ( $g_e = 2.002319$ ) in ppm (i.e., in units of  $10^{-6}$ ).

### 4.4.2.3 Hyperfine Tensor Calculations

All hyperfine coupling tensors were computed in the usual non-relativistic first-order framework (see Chapter 3), using the MAG-ReSpect<sup>50</sup> code based on unrestricted Kohn-Sham wave functions obtained with the TURBOMOLE (v.5.6)<sup>232,233</sup> program. These calculations used the B3LYP<sup>83,86,87</sup> hybrid functional in combination with the EPR-II<sup>235</sup> basis set.

## 4.4.3 Results and Discussion

### 4.4.3.1 Optimized Structures

Figure 4.4.1 shows optimized structures of the four conformers of NAG<sup>•</sup> radical. All four structures are minima on the potential energy surface. The CC-NAG<sup>•</sup> conformer is the lowest in energy. It is analogous to the conformation of the NAGH molecules in the single-crystal structure.<sup>292</sup> At B3LYP/DZVP level the three other conformers are only slightly higher, by 7.6 kJ mol<sup>-1</sup> (CT-NAG<sup>•</sup>), 6.0 kJ mol<sup>-1</sup> (TC-NAG<sup>•</sup>), and 10.9 kJ mol<sup>-1</sup> (TT-NAG<sup>•</sup>).

All conformers except TT-NAG<sup>•</sup> contain weak intramolecular hydrogen bonds (marked with dotted lines in Figure 4.4.1) which influence the calculated molecular energies, and also spin densities and EPR parameters (cf. below). Two such hydrogen-

bonds are present in CC-NAG<sup>•</sup> with the respective distances 234.6 pm (O1<sup>•••</sup>H<sub>β</sub>) and 254.0 pm (O3<sup>•••</sup>H<sub>α</sub>). One is present in CT-NAG<sup>•</sup> with distance 251.4 pm (O3<sup>•••</sup>H<sub>α</sub>), and one in TC-NAG<sup>•</sup> with distance 238.1 pm (O1<sup>•••</sup>H<sub>β</sub>). The covalent primary bond lengths vary by only up to 2 pm between the conformers, but the spin densities change significantly.

Relevant Mulliken atomic spin densities are summarized in Table 4.4.1. The O1<sup>•••</sup>H<sub>β</sub> and O3<sup>•••</sup>H<sub>α</sub> interactions reduce the spin densities on the O1 and O3 atoms, respectively. The spin density on O1 depends thus mainly on  $\psi$  and that on O3 on  $\phi$  (cf. Figure 4.4.1a). The spin density on O2 depends somewhat on  $\psi$ , possibly due to a weak O2<sup>•••</sup>H<sub>β</sub> interaction. The spin density on the N1 atom is largest for both of those conformers (TC and TT) where the O3<sup>•••</sup>H<sub>α</sub> interaction is missing and is thus most dependent on  $\phi$ . The spin density on C<sub>α</sub> depends on  $\phi$  as well. It is well known for organic  $\pi$ -radicals like semiquinones, tyrosyls, nitroxides, etc., that hydrogen bonds to oxygen tend to lower the spin densities on the oxygen atoms and redistribute it to the neighboring atoms.<sup>51,125,153,174</sup> The influence of intramolecular hydrogen-bonds in the isolated NAG<sup>•</sup> radicals on spin density and EPR parameters will be partly replaced by the effects of intermolecular hydrogen bonding with the environment (see below).

Table 4.4.1 Selected Mulliken atomic spin densities<sup>a</sup> for different conformers of NAG<sup>•</sup> radical.

Spin Densities	Conformer			
	CC-NAG <sup>•</sup>	CT-NAG <sup>•</sup>	TC-NAG <sup>•</sup>	TT-NAG <sup>•</sup>
C <sub>α</sub>	0.621	0.619	0.598	0.594
O1	0.132	0.169	0.128	0.165
O3	0.086	0.084	0.117	0.115
O2	0.034	0.018	0.033	0.018
N1	0.104	0.098	0.124	0.118

<sup>a</sup> RI-BP86/DZVP//B3LYP/DZVP results.

#### 4.4.3.2 Influence of the Level of Structure Optimization on Computed *g*-Tensors

In our initial test calculations, we noted an appreciable dependence of the computed *g*-tensors on the details of the structure optimization. Table 4.4.2 lists *g*-tensors (RI-BP86/DZVP level) for the free CC-NAG<sup>•</sup> radical calculated at structures optimized with different computational methods.

Table 4.4.2  $\Delta g$ -Tensor components (in ppm) computed for CC-NAG<sup>•</sup> at structures optimized with different computational levels.<sup>a</sup>

Structure (Method/Basis)	$\Delta g_z$	$\Delta g_y$	$\Delta g_x$
RI-BP86/DZVP	-127	1443	2677
RI-BP86/TZVP	-127	1424	2628
B3LYP/DZVP	-126	1426	2641
B3LYP/TZVP	-126	1400	2592
RI-MP2/SVP	-127	1281	2420
RI-MP2/TZVP	-127	1325	2497

<sup>a</sup> RI-BP86/DZVP results, with GIAOs and FULL treatment of spin-orbit integrals.

Overall, the DFT-optimized structures give larger *g*-anisotropies than the RI-MP2-optimized ones. Variations reach up to 250 ppm and 160 ppm for  $\Delta g_x$  and  $\Delta g_y$ , respectively. In view of the very small *g*-anisotropies in question, this corresponds to nonnegligible differences of about 10% of the total *g*-shifts. The values computed for different DFT-based structures differ only relatively little. Going from DZVP to TZVP basis sets in the DFT-optimizations reduces the *g*-anisotropies slightly, by ca. 50 ppm for  $\Delta g_x$  and by ca. 25 ppm for  $\Delta g_y$ . In contrast, improvement of the basis set for RI-MP2-optimizations increases both components somewhat, by ca. 80 ppm for  $\Delta g_x$  and by ca. 50 ppm for  $\Delta g_y$ . In case of the related dipeptide analog of the glycyl radical, the smaller size of the most basic model radical has allowed us to carry out coupled-cluster (CCSD) structure optimizations (see Chapter 4.5<sup>156</sup>). The *g*-tensor components for the CCSD reference structures were between DFT- and RI-MP2-



based results. In view of the close structural analogies between the two radicals, we assume that this will hold in the present case as well. For computations on larger supermolecular model complexes we have decided to use the B3LYP/DZVP method, which is known to give reasonable structural parameters. Given the structural dependence indicated by the values in Table 4.4.2, we expect a systematic overestimate of  $\Delta g_x$  and  $\Delta g_y$  on the order of 40-120 ppm (compared to CCSD/TZVP as a reference level, Chapter 4.5<sup>156</sup>), due to the chosen level of structure optimization.

While the underlying differences in the optimized structures are actually rather modest (always below 3 pm; see Table 4.4.3), we may nevertheless identify the major parameters that affect the  $g$ -tensors: the RI-MP2 optimizations afford generally shorter C-O bonds (in particular for C1-O1 and C2-O3; Table 4.4.3) than the DFT optimizations. An increase of the basis set for a given DFT level also shortens these C-O bonds slightly, whereas the basis-set effects are less clear-cut at RI-MP2 level. As is known for other  $\pi$ -radicals like semiquinones or tyrosyl,<sup>39,159,160</sup> an expansion of relevant C-O bonds shifts spin density from carbon to oxygen (in the present case in particular in the C1-O1 bond; cf. the Mulliken spin densities in Table 4.4.3). Due to the smaller spin-orbit coupling constant of carbon compared to oxygen, and augmented by a reduced energy denominator in the perturbation expression,<sup>159</sup> the spin-orbit/orbital-Zeeman contributions to the  $g$ -shifts are thus increased and larger  $\Delta g_x$  and  $\Delta g_y$  components result for DFT compared to RI-MP2-based structures (and slightly lower  $g$ -shifts for TZVP than for DZVP basis sets in the DFT optimizations).

Table 4.4.3 Selected bond lengths (in pm) and Mulliken atomic spin densities for CC-NAG<sup>•</sup> radical, when optimized at different computational levels.<sup>a</sup>

	Computational Level (Method/Basis)					
	RI-BP86 /DZVP	RI-BP86 /TZVP	B3LYP /DZVP	B3LYP /TZVP	RI-MP2 /SVP	RI-MP2 /TZVP
<i>bond lengths</i>						
C1 – O1	124.6	123.6	123.4	122.4	121.9	122.1
C2 – O3	123.4	122.4	122.3	121.3	121.5	121.6
C1 – C <sub>α</sub>	144.6	144.0	144.1	143.5	145.1	144.2
C <sub>α</sub> – N1	136.9	136.2	136.7	136.0	136.2	135.9
N1 – C2	140.8	140.5	139.9	139.5	139.3	139.4
C2 – C3	151.9	151.5	151.7	151.2	151.0	150.7
C1 – O2	137.6	137.1	136.4	135.9	134.4	135.2
O1···H <sub>β</sub>	233.3	232.5	234.6	234.4	231.4	232.7
O3···H <sub>α</sub>	254.9	253.9	254.0	253.1	251.4	250.9
<i>spin densities</i>						
C <sub>α</sub>	0.613	0.613	0.621	0.621	0.635	0.627
O1	0.133	0.132	0.132	0.129	0.118	0.123
O3	0.087	0.087	0.086	0.085	0.084	0.085
O2	0.035	0.035	0.034	0.034	0.034	0.035
N1	0.104	0.106	0.104	0.105	0.102	0.104

<sup>a</sup>BP86/DZVP Mulliken spin densities. See Figure 4.4.1a for atom labels.

#### 4.4.3.3 Dependence of *g*-Tensors on Gauge Origin and Spin-Orbit Operator

Our recent DFT approach<sup>45,106</sup> for *g*-tensor calculations has been shown to provide accurate *g*-tensors for a large variety of radicals including semiquinone radical anions,<sup>51,153,174,105</sup> a number of phenoxyl<sup>45</sup> and tyrosyl radicals,<sup>125</sup> and

nitroxides.<sup>302</sup> Most of these calculations employed the inexpensive atomic mean-field approximation to the respective (Breit-Pauli or Douglas-Kroll) spin-orbit operator (AMFI). The AMFI approximation was shown to provide excellent results when used with a common gauge origin for the magnetic vector potential at the center of nuclear charges.<sup>51,125,153,174</sup> A significant dependence on gauge origin has up to now only been found for models of the *ortho*-thioether-substituted tyrosyl radical in *Galactose Oxidase*.<sup>125</sup> While the *g*-tensor components changed only moderately with different positions of the common gauge, the tensor orientation showed a marked dependence.

Due to low symmetry, the strong delocalization of spin density onto different atoms with comparable spin-orbit (SO) coupling constants, and the extremely low *g*-anisotropy of the NAG<sup>•</sup> radical and of glycyl, the choice of the gauge origin is more critical than for any other example studied up to now (the studies of refs 161 and 162 were done exclusively with GIAOs), and we have decided to compare different choices of gauge. As the use of our preferred AMFI SO-operators with GIAOs is not straightforward, we tested also different choices of SO operators in this context (cf. Computational Details above). The results of the detailed evaluations for the CC-NAG<sup>•</sup> radical are summarized in Table 4.4.4.

Table 4.4.4 Dependence of computed *g*-shift components (in ppm) and *g*-tensor orientation for CC-NAG<sup>•</sup> on the choice of gauge origin and SO operators.<sup>a</sup>

Gauge Origin	$\Delta g_z$	$\Delta g_y$	$\Delta g_x$	Angle <sup>b</sup>
AMFI SO operator				
C <sub>1</sub>	-89	1348	2482	40.5
C <sub>2</sub>	-77	1063	2608	42.0
C <sub>3</sub>	-55	1039	2713	40.1
C <sub>α</sub>	-93	1223	2494	42.5
N <sub>1</sub>	-76	1182	2583	40.8
O <sub>1</sub>	-71	1412	2554	37.0
O <sub>2</sub>	-108	1382	2390	42.9
O <sub>3</sub>	-94	982	2552	44.5
GIAO	-124	1393	2624	46.6

Gauge Origin	$\Delta g_z$	$\Delta g_y$	$\Delta g_x$	Angle <sup>b</sup>
FULL SO operator				
C <sub>1</sub>	84	1524	2672	44.6
C <sub>2</sub>	84	1425	2754	46.0
C <sub>3</sub>	91	1420	2815	45.1
C <sub>α</sub>	81	1480	2683	45.8
N <sub>1</sub>	86	1468	2736	45.2
O <sub>1</sub>	90	1550	2709	43.0
O <sub>2</sub>	79	1534	2618	45.3
O <sub>3</sub>	78	1394	2723	47.4
GIAO	-126	1426	2641	46.5
Z <sub>eff</sub> SO operator				
C <sub>1</sub>	-174	1546	2792	42.3
C <sub>2</sub>	-183	1445	2878	44.1
C <sub>3</sub>	-181	1438	2946	43.3
C <sub>α</sub>	-179	1501	2801	43.6
N <sub>1</sub>	-178	1488	2860	43.1
O <sub>1</sub>	-170	1571	2835	40.8
O <sub>2</sub>	-175	1558	2732	42.9
O <sub>3</sub>	-187	1415	2843	45.5
GIAO	-176	1573	2908	46.1

<sup>a</sup>See Figure 4.4.1a for atom labels and Figure 4.4.1b for the tensor axis system. RI-BP86/DZVP//B3LYP/DZVP results. Cf. Computational details for explanations of the different SO operators. <sup>b</sup>Angles of  $g_y$  with the C<sub>α</sub>-H bond.

Comparisons of calculations with a common gauge at various atoms of the radical indicate an unusually pronounced gauge dependence of both  $\Delta g_x$  and  $\Delta g_y$  when using the AMFI approximation for the SO matrix elements (variations reach up to 10% for  $\Delta g_x$  and up to ca. 30% for  $\Delta g_y$ !). The gauge dependence is smaller but still significant with FULL (exact) and Z<sub>eff</sub> (effective nuclear-charge one-electron) SO operators (on the order of about 10% for both components with FULL SO operators and similar amounts with Z<sub>eff</sub>). Using GIAOs, the AMFI results agree quite well with the FULL reference data (while from a fundamental theoretical point of view, AMFI SO operators are incompatible with the GIAO approach, our experience suggests that

with the moderate DZVP basis sets used here, this problem is not pronounced), much better than in single-gauge calculations. In contrast, the effective one-electron SO operators (“ $Z_{\text{eff}}$ ”) that have been used in the two previous studies of glycy radical  $g$ -tensors,<sup>161,162</sup> provide appreciably larger  $\Delta g_x$  and  $\Delta g_y$  components. Given the fact that the computed  $g$ -shift components tend to be generally too large compared with experiment (see below), use of the semi-empirical  $Z_{\text{eff}}$  SO operators increases the computational errors. Given the unusual gauge dependence of the  $g$ -tensor in the present case, and in view of the deficiencies of both AMFI and  $Z_{\text{eff}}$  approximations to the SO matrix elements, we have decided to use the GIAO approach with FULL SO operators in the remainder of this chapter. While the calculation of the full one- and two-electron SO integrals is computationally much more demanding than the approximate AMFI or  $Z_{\text{eff}}$  integrals, the efficient implementation within the MAG-ReSpect code allows us to use this more reliable method also for the larger supermolecular models to be discussed below. We note that differences between AMFI results with common gauge at  $C_\alpha$  and our best FULL-GIAO data are on the order of about 150-200 ppm. While this is still appreciable, it allows us to use the AMFI calculations with a common gauge to carry out a breakdown of the  $g$ -tensor components into atomic SO contributions for closer interpretation (see below; this type of analysis would be more difficult with the FULL SO operators).

#### 4.4.3.4 Basis-Set effects on $g$ -Tensors

$g$ -Tensors tend to be less basis-set dependent than, e.g., hyperfine couplings, and our previous experience suggests that a moderate-sized DZVP basis provides good agreement with much larger basis sets (partly due to some error compensation).<sup>45,105,160,190</sup> In their recent study of the dipeptide analog of glycy radical,<sup>161</sup> Ciofini et al. favored the somewhat larger EPR-II basis, based on comparison with  $6\text{-}311^{++}\text{G}(3df,3pd)$  results (and partly in order to have a common computational protocol for hyperfine and  $g$ -tensor calculations). Our own initial test calculations suggested that the DZVP results are actually somewhat closer to the basis-set limit results (again probably due to error compensation). This is illustrated by the results for  $\text{CC-NAG}^\bullet$  in Table 4.4.5. As we did not consider the  $6\text{-}311^{++}\text{G}(3df,3pd)$  basis to be superior to the also investigated EPR-III basis, we carried out additional calculations with a cc-pVQZ basis, which is better balanced in

the sp-function space (and has almost the same number of polarization functions as the 6-311<sup>++</sup>G(3df,3pd) basis). Addition of the diffuse sp-set (“++”) from the Pople 6-311<sup>++</sup>G(3df,3pd) basis – to give cc-pVQZ<sup>++</sup> - does not affect the results, whereas removal of the diffuse functions from the Pople basis appears to be more notable, probably due to the less complete valence sp-set. We confirm the result of Ciofini et al.<sup>161</sup> that the EPR-II results agree well with the 6-311<sup>++</sup>G(3df,3pd) results. However, both of them are further from our cc-pVQZ (and cc-pVQZ<sup>++</sup>) reference data than the EPR-III results. Results with the modest DZVP basis agree excellently with both EPR-III and cc-pVQZ data and differ by about 100 ppm from the EPR-II results. While the differences are generally not very large, the very small overall *g*-anisotropy of the glycyl radicals under study lets us thus adhere to our previous strategy of using the DZVP basis for *g*-tensor calculations of organic radicals.

Table 4.4.5 Basis-set effects on *g*-shift tensors (in ppm) of the CC-NAG<sup>•</sup> radical.<sup>a</sup>

Basis set	$\Delta g_z$	$\Delta g_y$	$\Delta g_x$
DZVP	-126	1426	2641
EPR-II	-123	1348	2522
EPR-III	-122	1461	2664
6-311G(3df,3dp)	-157	1414	2624
6-311 <sup>++</sup> G(3df,3dp)	-177	1357	2559
cc-pVQZ	-115	1430	2659
cc-pVQZ <sup>++ b</sup>	-110	1422	2655

<sup>a</sup> BP86 results with DZVP basis set, GIAO gauge, and exact treatment of spin orbit integrals, using the B3LYP/DZVP-optimized structure. <sup>b</sup>Diffuse functions from 6-311<sup>++</sup>G(3df,3dp) set added.

#### 4.4.3.5 Atomic Analyses of the *g*-Shift Tensor of CC-NAG<sup>•</sup>

As a basis to better understand the conformational and environmental effects on the *g*-tensor discussed below, we provide in Table 4.4.6 a breakdown of the dominant  $\Delta g_{SO/OZ}$  contribution to the *g*-shift components into atomic contributions. This is possible with SO operators that are composed of effective atomic SO operators, as the

AMFI or  $Z_{\text{eff}}$  approximations (here we chose AMFI SO operators and a common gauge at  $C_{\alpha}$ , to avoid couplings between occupied MOs, which occur within the GIAO framework).

As expected, the  $\Delta g_{SO/OZ}$  contributions to both  $\Delta g_x$  and  $\Delta g_y$  of the CC-NAG $\bullet$  radical are dominated by spin-orbit coupling at the carbonyl oxygen atoms. While the spin density is largest on  $C_{\alpha}$  (cf. spin densities in Table 4.4.1), the larger SO coupling constant of oxygen renders the O1 contribution the largest individual atomic term, followed by that from O3. The carboxyl O2 atom and the amide N1 contribute still more than 400 ppm to  $\Delta g_x$ , followed by less than 200 ppm from  $C_{\alpha}$ . It is thus in particular changes in the spin densities on the oxygen atoms, and partly on nitrogen, that will determine the  $g$ -tensor components.

Table 4.4.6 Breakdown of the dominant  $\Delta g_{SO/OZ}$  contribution to the  $g$ -shift-tensors into atomic contributions (in ppm) for CC-NAG $\bullet$  radical.<sup>a</sup>

Atom	$\Delta g_z$	$\Delta g_y$	$\Delta g_x$
C <sub>1</sub>	-1	-95	45
C <sub>2</sub>	-1	-39	18
C <sub>3</sub>	-2	2	3
C <sub><math>\alpha</math></sub>	-1	29	177
N <sub>1</sub>	-6	-22	404
O <sub>1</sub>	-7	749	884
O <sub>2</sub>	4	69	426
O <sub>3</sub>	-5	530	545
$\Sigma$	-18	1224	2502

<sup>a</sup> BP86/DZVP//B3LYP/DZVP results with AMFI SO operators and common gauge origin at  $C_{\alpha}$ . Contributions from hydrogen atoms are generally negligible.

#### 4.4.3.6 Structural Results and Spin Densities for Supermolecular Models

We employ two types of supermolecular models for treating environmental effects: in models 1-5 (Figure 4.4.2), water molecules are used as hydrogen-bond donors/acceptors; in model 6 (Figure 4.4.3), neighboring fragments from the crystal structure of NAGH<sup>292</sup> are included, modeling more realistically the true situation (see 4.4.2 Computational Details chapter for more information). The shortcomings of water molecules to model hydrogen-bonding arise from the fact that they tend to hydrogen-bond to more than one site of the CC-NAG<sup>•</sup> radical, and the directions of the hydrogen-bonds do not match those found in the crystal. The water-based models provide, however, further insight into the influence of individual direct and indirect interactions. These turn out to be made up from various contributions that add up in a complicated way, and it has not been possible to fully analyze in every detail the way in which the environmental interactions modify the spin density of the radical.

Effects on primary bond lengths are relatively small, below ca. 3 pm. More pronounced effects pertain to the hydrogen bonds (this affects also some bond angles). Some trends are apparent: the water molecule hydrogen-bonded to the amide hydrogen (Figure 4.4.2, model 1) interacts simultaneously with carbonyl oxygen O1. This weakens the intramolecular hydrogen bond (H<sub>β</sub>···O1), which is lengthened by 20 pm. As a result, the spin density on O1 decreases. A hydrogen bond to O3 (model 2) affects the O3···H<sub>α</sub> distance negligibly, but the H<sub>β</sub>···O1 distance is reduced by 20 pm, accompanied by appreciable reduction of the spin density on O1. A water molecule hydrogen-bonded to the carboxyl group (model 3) polarizes spin density away from O1 without affecting the length of intramolecular hydrogen bonds. In models 4 and 5 the effects from individual water molecules add up. The redistribution of spin density due to environmental interactions affects indirectly the *g*-tensors, as will be analyzed below.

In the crystal structure of NAGH,<sup>292</sup> each molecule donates two hydrogen-bonds to and accepts two from its closest neighbors: two to carbonyl oxygens, one from the amide hydrogen, and one from the hydroxyl hydrogen. The structural parameters of the central “radical” moiety of model 6 (Figure 4.4.3) differ relatively little from the



gas-phase values. The most pronounced difference is found for the O3 $\cdots$ H $_{\alpha}$  distance, which is shortened by ca.14 pm. Compared to models 1-5 (cf. Figure 4.4.2), there are significant differences in computed intermolecular hydrogen-bond distances. The H $_{\beta}$  $\cdots$ O bond is elongated by 10 pm and the O3 $\cdots$ H-O bond is shortened by ca. 30 pm. The O1 $\cdots$ H bond distance compares well with model 3 but is longer by ca. 20 pm than in model 5. The O2-H $\cdots$ O distance is quite short and very similar in all models.

#### 4.4.3.7 Conformational and Environmental Effects on $g$ -Tensors

Table 4.4.7 provides computed  $g$ -shift tensors for different conformers of the free NAG $\bullet$  radical and for CC-NAG $\bullet$  in different hydrogen-bonding frameworks, in comparison with experimental data for NAG $\bullet$  in the NAGH single-crystal environment. Starting with the free radicals, the computed  $g$ -tensors for the gas-phase radicals correlate well with the presence or absence of intramolecular hydrogen bonds (cf. Figure 4.4.1) in the four conformers. The CC conformer with two such hydrogen-bonds exhibits the lowest  $g$ -anisotropies. The highest  $\Delta g_x$  and  $\Delta g_y$  values are computed for the TT conformer which lacks intramolecular hydrogen-bonds. The CT and TC conformers (each with one intramolecular hydrogen-bond) provide intermediate values. The overall variations amount to 900 ppm for  $\Delta g_x$  and to 670 ppm for  $\Delta g_y$  (Table 4.4.7). The differences may be traced back mainly to the redistribution of spin density due to the intramolecular hydrogen bonds. (cf. Table 4.4.1, see discussion above). In particular, hydrogen-bonds to O1 or O3 oxygens reduce the oxygen spin densities and thereby the spin-orbit contributions of oxygen to the  $g$ -shifts. In the CT and TT conformers, there is also a weak hydrogen-bond from H $_{\beta}$  to O2 (not indicated in Figure 4.4.1). This explains why both  $\Delta g_x$  and  $\Delta g_y$  are somewhat lower in the CT compared to the TC conformer.

Table 4.4.7 Computed *g*-shift components (in ppm) for different conformations of free NAG• and for supermolecular model complexes of CC- NAG• compared to experimental data of NAG• in the NAGH single crystal environment.<sup>a</sup>

Model	$\Delta g_z$	$\Delta g_y$	$\Delta g_x$
<i>Conformations of free radical</i>			
CC-NAG•	-126	1426	2641
CT-NAG•	-126	1976	2811
TC-NAG•	-134	2087	2863
TT-NAG•	-135	2101	3552
<i>Supermolecular model complexes<sup>b</sup></i>			
1	-128	1433	2799
2	-116	1260	2665
3	-132	1431	2572
4	-133	1329	2478
5	-139	1354	2632
6	-197	1393	2502
Exp. <sup>c</sup>	-319	781	2181

<sup>a</sup> BP86/DZVP//B3LYP/DZVP results with GIAO gauge and exact (“FULL”) treatment of SO integrals. <sup>b</sup>Cf. Figures 4.4.2 and 3. <sup>c</sup>Ref 293.

Turning to the effects of intermolecular hydrogen bonding, as obtained from the supermolecular complexes (Figures 4.4.2 and 4.4.3; Table 4.4.7), we note that the overall effects on both  $\Delta g_x$  and  $\Delta g_y$ , compared to free CC-NAG• are rather modest. In fact, models 1 and 2 provide actually an *increased*  $\Delta g_x$  (and models 1 and 3 a slightly increased  $\Delta g_y$ ). The overall reduction for the largest model 6 is only ca. 140 ppm for  $\Delta g_x$  and ca. 30 ppm for  $\Delta g_y$ . These are extremely small effects compared to typical reductions of the in-plane *g*-tensor components for other  $\pi$ -radicals.<sup>51,125,153,174</sup> This must obviously arise from a partial compensation between the effects of intramolecular and intermolecular hydrogen bonding in the present case (and from the generally lower oxygen spin densities compared to other  $\pi$ -radicals).

It is known that hydrogen-bonding affects the  $g$ -shifts both directly (by polarization of the spin density at a given structure) and indirectly (by slight structural modifications).<sup>105</sup> In model 1, the  $H_{\beta}\cdots O1$  intramolecular hydrogen-bond is broken and replaced by an hydrogen-bond from the water molecule to O1 and by one from  $H_{\beta}$  to the water oxygen. The consequence is an *increase* of  $\Delta g_x$  by 150 ppm, suggesting that the intermolecular hydrogen-bond to O1 reduces the spin density on O1 less than the intramolecular one in the gas-phase radical. The intermolecular hydrogen-bond to O3 in model 2 affects the molecular bond distances insignificantly but changes the charge distribution and thereby indirectly enhances the  $N1-H_{\beta}\cdots O1$  hydrogen bond. The final redistribution of spin density results in a small increase of spin density on O3 and N1, and a decrease on O1 (cf. Table 4.4.8). As these atoms contribute differently to  $\Delta g_x$  and  $\Delta g_y$  (cf. Table 4.4.6), the final effect is negligible for  $\Delta g_x$  but a reduction by 170 ppm for  $\Delta g_y$ . Optimization of a single water molecule hydrogen-bonded to the carboxyl group converges always to the structure shown for model 3 in Figure 4.4.2, with an hydrogen-bond to O1 and one from the hydroxyl group to the water oxygen, irrespective of the starting structure. The  $\Delta g_x$  component is reduced only by ca. 60 ppm, and  $\Delta g_y$  is left unchanged. This small effect is the joint result of reduced spin density on O1 and increased spin densities on O2 and N1. Model 4 combines the hydrogen-bonding situation of model 2 with two water molecules near the carboxyl group (Table 4.4.8).  $\Delta g_x$  and  $\Delta g_y$  are reduced by 160 ppm and by ca. 100 ppm, respectively. In model 5, a fourth water molecule interacts with  $H_{\beta}$  and O1. This weakens the  $H_{\beta}\cdots O1$  bond and increases  $\Delta g_x$  by ca. 150 ppm in comparison to model 4, whereas  $\Delta g_y$  remains nearly unchanged. The  $g$ -tensor of model 6 is remarkably close to that of the gas-phase radical, with  $\Delta g_y$  slightly reduced (by ca. 30 ppm), and  $\Delta g_x$  reduced by 140 ppm. The differences relative to models like 4 or 5 arise from different arrangements and lengths of hydrogen bonds.

Overall, these various effects are subtle and complicated, due to the strongly delocalized spin-density distribution, which is affected in various ways by intra- and intermolecular hydrogen bonds. It is clear, however, that the overall environmental effects in the NAGH single-crystal environment on the spin-density distribution and  $g$ -tensor of the  $NAG^{\bullet}$  radical are only moderate.

Table 4.4.8 Selected bond lengths (in pm) and Mulliken atomic spin densities for model complexes.<sup>a</sup>

	Model						
	Gas phase (CC-NAG <sup>*</sup> )	1	2	3	4	5	6
<i>bond lengths<sup>b</sup></i>							
C1 - O1	123.4	124.2	122.1	124.7	124.9	125.8	123.9
C2 - O3	122.3	122.4	123.1	122.4	123.2	123.2	123.7
C1 - C <sub>α</sub>	144.1	143.7	141.1	144.3	144.7	144.3	144.2
C <sub>α</sub> - N1	136.7	136.4	135.5	136.7	136.8	136.5	136.7
N1 - C2	139.9	140.2	138.2	139.7	138.9	139.3	137.6
C2 - C3	151.7	151.5	151.0	151.7	151.3	151.2	151.1
C1 - O2	136.4	136.4	133.6	134.6	133.3	133.3	134.0
O1 <sup>⋯</sup> H <sub>β</sub>	234.6	258.6	213.8	232.0	230.2	257.7	237.6
O3 <sup>⋯</sup> H <sub>α</sub>	254.0	246.3	255.8	254.0	253.1	244.4	240.7
N1-H <sup>⋯</sup> O		188.6				188.0	197.8
O1 <sup>⋯</sup> H-O		190.2				190.0	
O1 <sup>⋯</sup> H-O/H-N				201.4	182.9	182.7	203.1
O2-H <sup>⋯</sup> O					166.9	167.2	164.9
O3 <sup>⋯</sup> H-O			195.1		195.2	193.7	166.6
<i>spin densities</i>							
C <sub>α</sub>	0.621	0.577	0.581	0.624	0.638	0.596	0.639
O1	0.132	0.125	0.108	0.115	0.104	0.099	0.114
O3	0.086	0.086	0.091	0.087	0.084	0.083	0.082
O2	0.034	0.041	0.050	0.045	0.050	0.059	0.042
N1	0.104	0.122	0.125	0.097	0.083	0.101	0.064

<sup>a</sup> BP86/DZVP//B3LYP/DZVP results. <sup>b</sup> See Figure 4.4.1a for atom labels.

As a result, the conformation of the radical has the overall largest influence on the  $g$ -tensor. All models provide computed  $g$ -anisotropies that are significantly larger than experiment. Even for model 6, which is expected to provide a realistic description of the single-crystal environment,  $\Delta g_x$  is overestimated by ca. 300 ppm and  $\Delta g_y$  by ca. 600 ppm. Slightly reduced deviations of ca. 200 ppm and ca. 500 ppm, respectively, are found if we compare our results with the experimentally more reliable relative values<sup>293</sup>  $\Delta(g_x-g_z)$  and  $\Delta(g_y-g_z)$ .

This arises from a combination of reasons. Recall that very small inaccuracies of the structures obtained at B3LYP/DZYP level do already lead to an overestimate of  $\Delta g_x$  and  $\Delta g_y$  by ca. 50-100 ppm (see above). Next we have to account for deficiencies in the underlying gradient-corrected exchange-correlation functionals. In related calculations on  $\pi$ -radicals like semiquinones, it has been shown that  $\Delta g_x$  was systematically overestimated by about 10%, whereas  $\Delta g_y$  was reproduced well.<sup>153,160,174</sup> A corresponding reduction of the computed  $\Delta g_x$  for model 6 would give 2200 ppm, which is already in the range of experimental values. However, we see that  $\Delta g_y$  is also overestimated in the present case, likely due to the more mixed contributions from different MOs to the perturbation expressions for both in-plane components. Vibrational effects on the  $g$ -tensor of glycyl have been found to be small by Ciofini et al.<sup>161</sup> There is, however, another potential error source in the calculations that we cannot exclude completely. In a recent theoretical analysis, Patchkovskii et al. came to the conclusion that gauge-correction terms arising from the spin-other-orbit interaction may be larger than hitherto assumed.<sup>303</sup> These are not included in the present calculations (irrespective of the actual choice of field-independent SO operators), as we account only for the one-electron gauge corrections.<sup>45,105,106</sup> However, as the reliability of the approximations used to estimate the two-electron gauge corrections in ref 303 is uncertain, the question of the importance of such terms will require further study. Finally, possible inaccuracies of the experimental data have to be considered. Considering the single-crystal data of ref 293, we expect these to be relatively low when differences like  $\Delta(g_x-g_z)$  or  $\Delta(g_y-g_z)$  are considered. It is clear that the very small  $g$ -anisotropies and the delocalized spin density make the  $g$ -tensor of glycyl-derived radicals a challenge to both theory and experiment. In any case, we consider the deviations of our best calculations on model 6 (Table 4.4.7) as representative of the inherent deficiencies of the computational

method. We may thus expect a similar overestimate of both  $\Delta g_x$  and  $\Delta g_y$  for the structurally less well characterized case of protein glycy radical.<sup>156</sup>

#### 4.4.3.8 $^1\text{H}_\alpha$ and $^{13}\text{C}_\alpha$ Hyperfine Tensors

Table 4.4.9 lists isotropic and anisotropic components of the  $^1\text{H}_\alpha$  and  $^{13}\text{C}_\alpha$  hyperfine tensors computed for different models of NAG $\bullet$ . Previous computational studies of the  $^1\text{H}_\alpha$  hyperfine tensor for different minima of glycy radical<sup>150</sup> showed negligible dependence on the conformation. This is confirmed here largely for the free NAG $\bullet$  radical. The intramolecular hydrogen bonds render the absolute  $A_{iso}$  values largest (for both  $\text{C}_\alpha$  and  $\text{H}_\alpha$ ) for the CC-NAG $\bullet$  conformer, but the differences are less than 1 G.

Environmental effects are slightly larger but do not exceed 2 G either (environmental effects on the largest  $A_x$  component for  $\text{C}_\alpha$  range from -5 G for model 1 to +3 G for model 6). These variations are probably too small to be of much diagnostic value for establishing spectroscopically the environment of glycy-based radicals. The largest absolute  $A_{iso}$  values are found for the most realistic model 6. Agreement with the available experimental data for  $\text{H}_\alpha$  is reasonable (we have to consider that the effect of the out-of-plane vibration of  $\text{H}_\alpha$  on  $A_{iso}(^1\text{H})$  has been estimated to be +3.4 G<sup>161</sup>).

Table 4.4.9  $^1\text{H}_\alpha$  and  $^{13}\text{C}_\alpha$  hyperfine coupling constants (in Gauss) for gas-phase and solvated models of NAG $^\bullet$  radical.<sup>a</sup>

Model	$^1\text{H}_\alpha$				$^{13}\text{C}_\alpha$			
	$A_{iso}$	$A_x$	$A_y$	$A_z$	$A_{iso}$	$A_x$	$A_y$	$A_z$
<i>Conformations of free radical</i>								
CC-NAG $^\bullet$	-16.5	-25.3	-6.9	-17.3	16.1	-1.5	-2.1	52.0
CT-NAG $^\bullet$	-16.4	-24.9	-7.0	-17.4	16.6	-1.2	-1.6	52.5
TC-NAG $^\bullet$	-15.8	-24.6	-6.3	-16.4	15.4	-1.8	-2.2	50.4
TT-NAG $^\bullet$	-15.7	-24.3	-6.4	-16.5	15.9	-1.5	-1.8	50.9
<i>Supramolecular models complexes</i>								
1	-15.0	-23.1	-6.1	-15.9	13.6	-2.7	-3.2	46.6
2	-16.5	-25.1	-7.1	-17.4	15.3	-2.2	-2.8	51.0
3	-16.4	-25.2	-6.8	-17.2	16.0	-1.7	-2.3	52.1
4	-16.8	-25.7	-7.0	-17.6	16.8	-1.4	-2.0	53.7
5	-15.5	-23.7	-6.3	-16.4	14.5	-2.4	-3.0	48.9
6	-17.1	-26.1	-7.3	-17.9	17.4	-1.0	-1.6	54.7
Exp. <sup>b</sup>	-17.6	-26.9	-8.4	-17.4				
Exp. <sup>c</sup>	-17.4	-27.2	-8.1	-16.8				
Exp. <sup>d</sup>	-18.2	-27.1	-10.0	-17.1				

<sup>a</sup>B3LYP/EPR-II//B3LYP/DZVP results. For both nuclei,  $A_z$  is perpendicular to the molecular plane and collinear with the  $g_z$  vector.  $A_x$  and  $A_y$  lie in the molecular plane.  $A_y$  ( $^1\text{H}_\alpha$ ) is parallel to the  $\text{C}_\alpha\text{-H}_\alpha$  bond and  $A_x$  ( $^1\text{H}_\alpha$ ) is perpendicular to it.  $A_y$  and  $A_x$  for  $^{13}\text{C}_\alpha$  are almost aligned with the  $g_x$  and  $g_y$  principal components (cf. Figure 4.4.1 for  $g$ -tensor axes). <sup>b</sup>Ref 304. <sup>c</sup>Ref 293. <sup>d</sup>Ref 294.

#### 4.4.4 Conclusions

The  $g$ -tensor of glycyll-based radicals is a true challenge to both computation and experiment. Unless one has access to a single crystal, like in the present case of the N-acetylglycyl radical, the small  $g$ -anisotropy requires very high-frequency/high-field EPR for its resolution.<sup>291</sup> Together with the unsymmetrical structure and delocalized spin density, the small  $g$ -shift values put also extremely high demands on the computational methodology. If we want to be able to use such calculations to

assist EPR studies in deriving structure and environment of protein glycy radical in biological systems, we have to carefully control all possible error sources. The present work provides an initial step into this direction by applying various computational protocols based on density functional theory, and detailed analyses of bonding and EPR parameters, to the N-acetylglycyl radical in the structurally well-characterized environment of an N-acetylglycine single crystal. In particular, our best results on model 6 suggest that the chosen computational protocol will overestimate the spectroscopically better defined differences between spectral lines,  $\Delta(g_x-g_z)$  and  $\Delta(g_y-g_z)$ , of glycy radical by a margin of about 200-500 ppm. This careful calibration turns out to be crucial for the interesting structural conclusions obtained in study of protein glycy radical presented in Chapter 4.5.<sup>156</sup>

We noted already that the computational level used for structure optimization has a nonnegligible effect on the computed  $g$ -tensor. Basis-set effects in the  $g$ -tensor calculation are less pronounced, and a moderate-sized DZVP basis provides a reasonable description. However, the choice of approximate spin-orbit operators and of the gauge origin of the magnetic vector potential turned out to be far more critical here than for any other system studied up to now. We finally settled for a GIAO treatment with a full explicit description of all one- and two-electron Breit-Pauli spin-orbit integrals.

Hydrogen-bonding effects on the  $g$ - and hyperfine-tensors were studied by various supermolecular models. The environmental effects turned out to be overall moderate and subtle, due to various partly counteracting effects of intra- and intermolecular hydrogen bonds on structure and spin-density distribution. As a result, the conformation of the free radical was found to provide the largest overall structural effect on the  $g$ -tensors, due to different intramolecular hydrogen bonds in the different conformers. This is of interest also for structure determination of protein-based glycy radical, see next chapter (Chapter 4.5<sup>156</sup>), as the conformations are less well known in the protein environment than in the present single-crystal environment of N-acetylglycine.



## 4.5 Understanding the EPR Parameters of Protein-Bound Glycyl Radicals<sup>156</sup>

### 4.5.1 Introduction

In the previous chapter (Chapter 4.4<sup>157</sup>), we have systematically validated density functional theory (DFT) methods for reproducing the experimental  $g$ - and hyperfine tensors of N-acetylglycyl radical (NAG $\bullet$ ) created by irradiation of a single crystal of N-acetylglycine. The aim was to establish for a structurally<sup>292</sup> and spectroscopically<sup>293,294</sup> well-characterized example the dependence of the computed EPR properties, in particular of the electronic  $g$ -tensor, on the computational protocol to be applied then to protein  $C_\alpha$ -based radicals. It turned out (cf. Chapter 4.4<sup>157</sup>) that the small  $g$ -anisotropy combined with a delocalized spin-density distribution make the NAG $\bullet$   $g$ -tensor a true challenge for quantum-chemical calculations.

In this chapter we extend the investigations to realistic molecular models for protein  $C_\alpha$  radicals, which have recently received increased attention. Protein-bound glycyl radical may be considered the simplest redox-active amino-acid radical, and up to now the only one with the unpaired electron predominantly localized on the protein backbone (in  $C_\alpha$  position). While the glycyl radical has been established experimentally as an intermediate beyond doubt only for three enzymes (anaerobic class III ribonucleotide reductase (RNR),<sup>282-284</sup> pyruvate formate lyase (PFL),<sup>285</sup> and benzylsuccinate synthase (BSS)<sup>286</sup>), there are clear indications that an appreciable number of other anaerobic redox enzymes require a glycyl radical for their activity.<sup>287-290</sup> While X-band spectra had provided a characteristic doublet splitting due to hyperfine coupling to the hydrogen bound to  $C_\alpha$ , as well as some other hyperfine features,<sup>282,283,285,286</sup> the extremely small  $g$ -anisotropy could not be resolved at X-band. This was only possible very recently at much higher frequencies and magnetic fields.<sup>291</sup> Very similar  $g$ -tensors were found for BSS and PFL, somewhat different parameters (at the given resolution) for anaerobic RNR of *E. coli*.<sup>291</sup> It would be desirable to correlate these spectroscopic parameters to structural features of the

radical and its environment. While three-dimensional structure information for *E. coli* PFL<sup>305,306</sup> and RNR (the G580A mutant of bacteriophage T<sub>4</sub> NrdG<sup>307</sup>) together with biochemical and sequence information suggest the most likely position of a glycyl radical and its involvement in the function of the enzymes, for none of these systems the precise environment of the radical is known. This is a situation in which quantum chemical calculations may provide important additional information.

Indeed, a number of theoretical studies for glycyl radical and its dipeptide analogue have been carried out, most of them concentrating on the conformational behavior and hyperfine properties of the radical.<sup>150,151,295,308</sup> While the non-radical form of a protein glycyl residue has access to a number of conformers, the conformational space of the radical was found to be restricted only to planar or quasi-planar conformations. This is due to substantial delocalization of the unpaired  $\pi$ -electron over the whole structure. The fully extended conformer was proposed to be the best dipeptide model based on computed energies. Solvent effects were investigated for the free radical<sup>150,295</sup> and for the dipeptide analogue<sup>161</sup> in the aqueous solution. The very limited transfer between radical and solvent (water) molecules indicated that the solvent caused predominantly a redistribution of spin density within the radical. Himo et al. have investigated the local structure of the protein bound radical and suggested a non-planar structure of the glycyl radical in bacteriophage T<sub>4</sub> ARNR to explain its somewhat larger <sup>13</sup>C <sub>$\alpha$</sub> -HFC ( $A_{zz}$ ) compared to the PFL and *E. coli* ARNR enzymes.<sup>296</sup>

During the course of the study presented in this chapter, two DFT studies were reported that dealt also with the  $g$ -tensor of N-formylglycyl<sup>161,162</sup> forms of glycyl radical. In both cases, the emphasis was on the validation of a given computational protocol, using semi-empirical spin-orbit (SO) operators. Each of the two studies focused only on one conformer: in ref 161 the fully extended model (further below defined as CC-Gly<sup>•</sup>, cf. Figure 4.5.1) was used, while the model from ref 162 was prepared based on the X-ray structure of the non-radical form of the enzymes (below termed ext.CT-Gly<sup>•</sup> (N-CH<sub>3</sub>)). Very limited modeling of environment effect was done in ref 162 (one water molecule hydrogen bonded to the O1 carbonyl oxygen). More extensive studies of environmental effects on hyperfine couplings and  $g$ -tensor are provided in ref 161, where the first solvation shell has been considered directly (water cluster), and bulk solvent effects were included by a continuum solvent model.

Here we go beyond these two studies in several aspects: a) we investigate in detail the simultaneous effects of conformation *and* environment on spin-density distribution and *g*-tensors (and hyperfine couplings); b) we use refined spin-orbit operators together with GIAOs; c) we show that the method used for structure optimization also has an unusually large influence on the computed *g*-tensors. As found also for NAG• radical (Chapter 4.4<sup>157</sup>), the *g*-tensor of glycyl radicals places thus high demands on the computational methodology. However, based on the results of our calibration study on NAG• (Chapter 4.4<sup>157</sup>), we have been able to identify different conformations as the origin of different *g*-tensors measured<sup>291</sup> for different enzyme sites.

## 4.5.2 Computational Details

### 4.5.2.1 Structure Optimizations

Among the “glycyl-radical enzymes” studied here, only two three-dimensional structures, in their non-radical forms, are available: a) pyruvate formate lyase (PFL)<sup>306</sup> from *E. coli* and the G580A mutant of bacteriophage T<sub>4</sub> anaerobic ribonucleotide reductase (ARNR)<sup>307</sup> (cf. ref 288 for a related structure). In both structures the parent amino acid (glycine in PFL and alanine in the RNR mutant) occurs in what we will in the following call the cis-trans (CT) conformation (see Figure 4.5.1 for definition of the conformation). Given that the cis-cis (CC) conformer (“fully extended conformer” or  $\beta$ -sheet conformer<sup>150,151,161,308</sup>) of the radical is lower in energy and separated by an appreciable barrier from other conformers,<sup>150,151,161</sup> the actual conformation of the protein-bound radical is an open question. It may be determined alternatively by the kinetics of the abstraction of a hydrogen atom from the protein, leading to the CT form, or by thermochemical stability, preferring the CC form. As mentioned above, one of the two prior computational *g*-tensor studies<sup>161</sup> (and most studies of hyperfine tensors<sup>150,151,296,309</sup>) employed the CC conformation, whereas the other was performed for the CT conformation.<sup>162</sup>

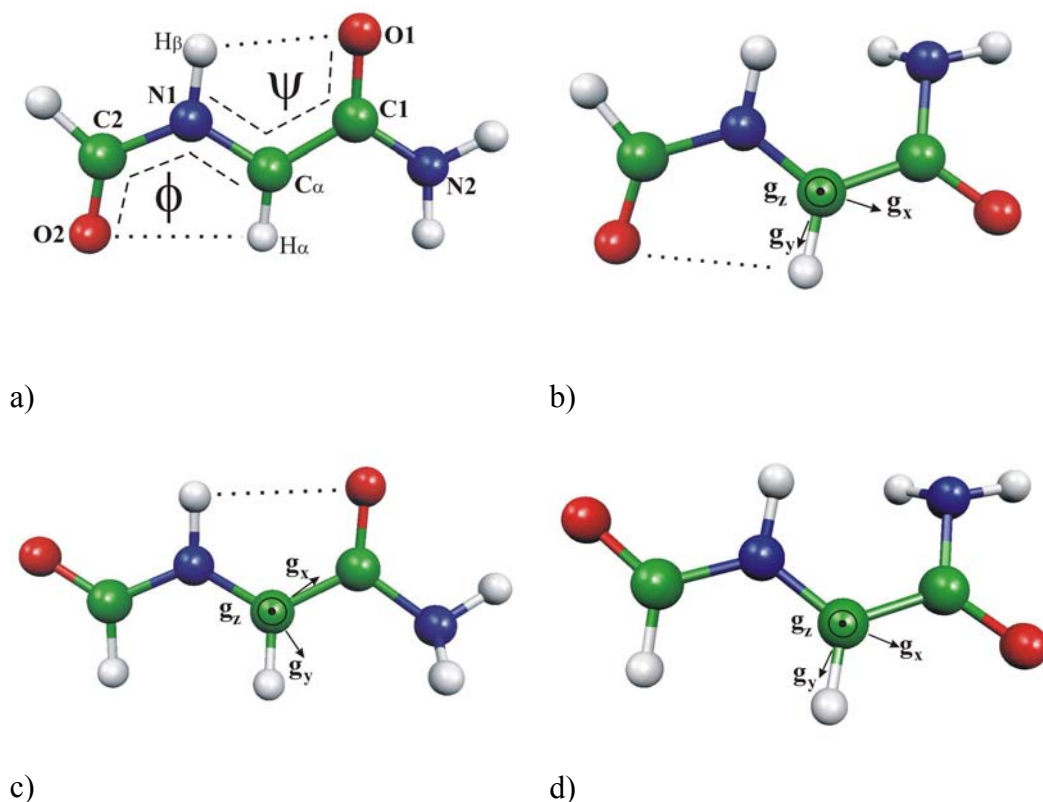


Figure 4.5.1 Conformers of the dipeptide analog of glycyl radical: a) cis-cis (CC-Gly<sup>•</sup>), with atom numbering and definition of  $\phi$  and  $\psi$  dihedral angles; b) cis-trans (CT-Gly<sup>•</sup>); c) trans-cis (TC-Gly<sup>•</sup>); d) trans-trans (TT-Gly<sup>•</sup>). The dotted lines indicate intramolecular hydrogen bonds. Directions of  $g$ -tensor components are shown for CT, TC and TT conformers. The directions of  $g$ -tensor components for CC conformer are similar to these for the TC.

Most previous computational studies<sup>151,161,162,296,309,310</sup> modeled the protein-bound glycyl radical as a so-called dipeptide analog model, HCO-HN-HC<sup>•</sup>-CO-NH<sub>2</sub>, hereafter referred to as Gly<sup>•</sup>. The adequacy of formyl and amino terminal groups was validated in various conformational and HFCs studies.<sup>151,161,311</sup> Larger models with acetyl and methylamino terminal groups were considered to change matters negligibly. As will be shown below, this does not hold anymore for  $g$ -tensor calculations.

Initially, we have investigated four energetically close-lying conformers of the gas-phase Gly<sup>•</sup> radical (cf. Figure 4.5.1), cis-cis (CC-Gly<sup>•</sup>), cis-trans (CT-Gly<sup>•</sup>), trans-

cis (TC-Gly<sup>•</sup>) and trans-trans (TT-Gly<sup>•</sup>) structures, with cis and trans defined by  $\phi$  and  $\psi$  dihedral angles (Figure 4.5.1a). Due to the restrictions of the single-crystal environment, we have been able to concentrate exclusively on the CC conformer in our detailed studies of environmental effects for the NAG<sup>•</sup> radical in Chapter 4.4.<sup>157</sup> In view of the less clear situation for protein-bound glycyl radicals, two of the conformers, CC and CT, were investigated further. The effect of the size of the radical model on the *g*-tensor was evaluated by extending the CC- and CT-Gly<sup>•</sup> models; the formyl and amino terminal groups were substituted individually or simultaneously by acetyl and methylamino groups, respectively (the doubly-extended models are shown in Figure 4.5.2).

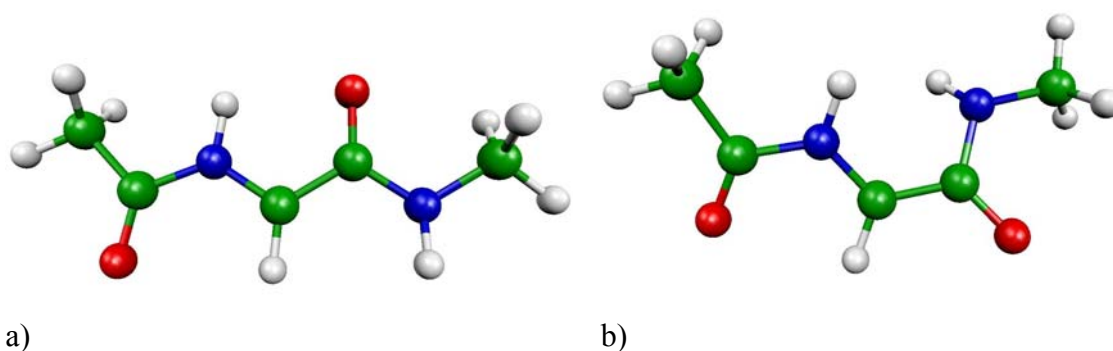
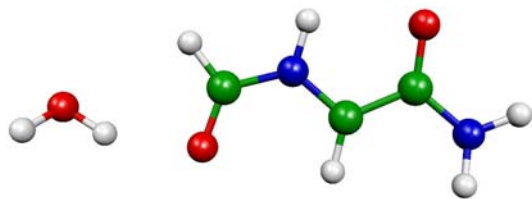


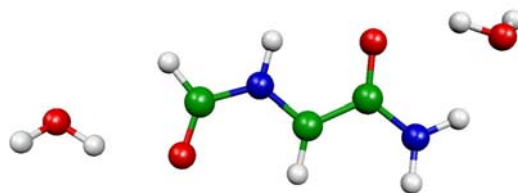
Figure 4.5.2 Doubly extended structures of CC-Gly<sup>•</sup> (a) and CT-Gly<sup>•</sup> (b) models.

For all structures (basic and extended models), the amide group at the C-terminus pyramidalized during optimization. As this does affect the spin-density distribution and is relatively unlikely in the protein environment, we have carried out additional computations with the amide group forced to be planar. An additional type of non-planarity was found in the structures of CT- and TT-Gly<sup>•</sup>, where the C-terminus twisted out of the molecular plane by ca. 10-20° (N1-C<sub>α</sub>-C1-O1 and N1-C<sub>α</sub>-C1-N2 dihedral angles). Our supermolecular models consist of the central Gly<sup>•</sup> radical (CT or CC conformer) forming hydrogen bonds with up to five water molecules (Figure 4.5.3 and Figure 4.5.4). In a few cases, the doubly-extended models were used (CC10, CC11, CT10, CT11).

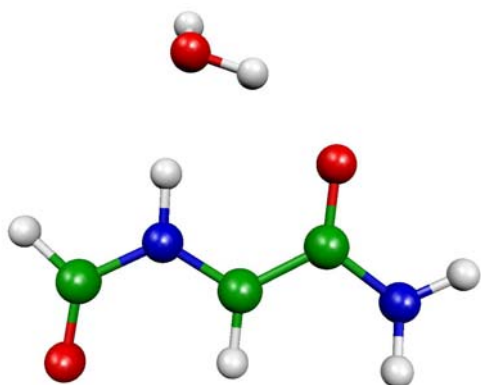
CC 1



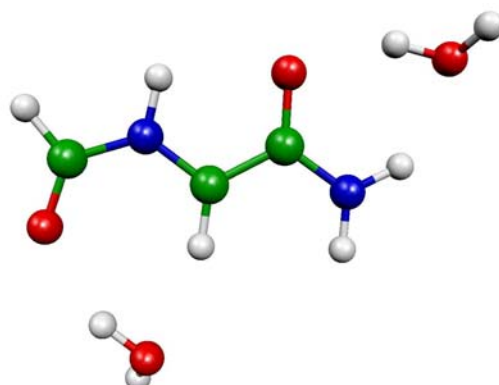
CC 2



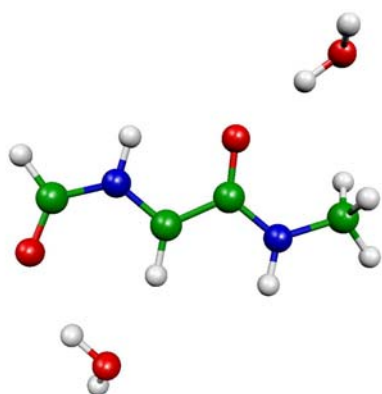
CC 3



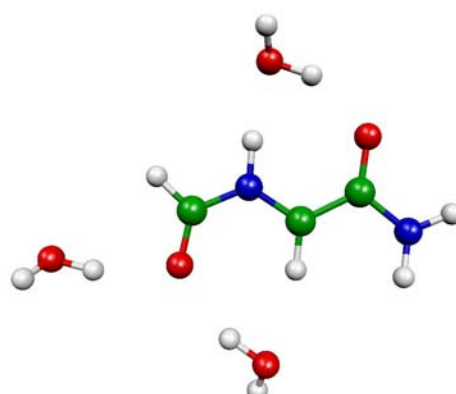
CC 4



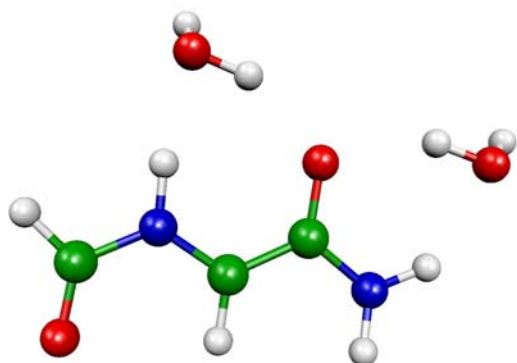
CC 5



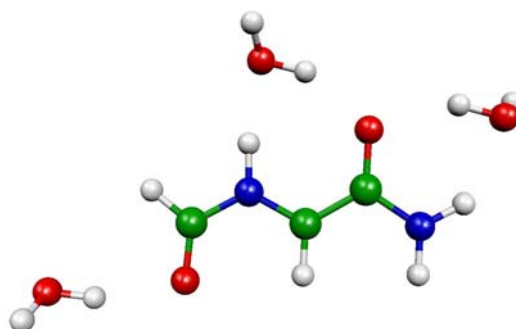
CC 6



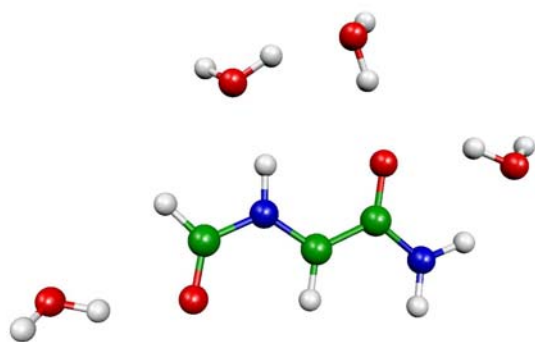
CC 7



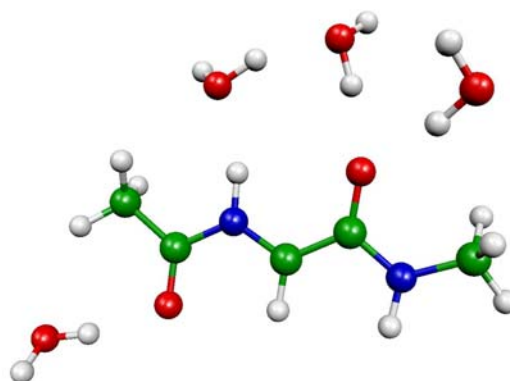
CC 8



CC 9



CC 10



CC 11

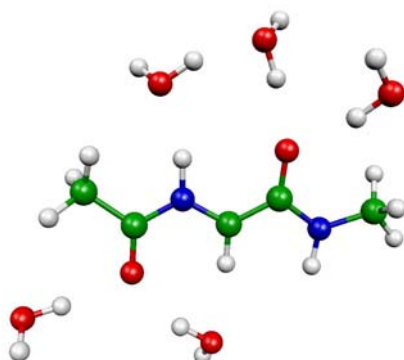
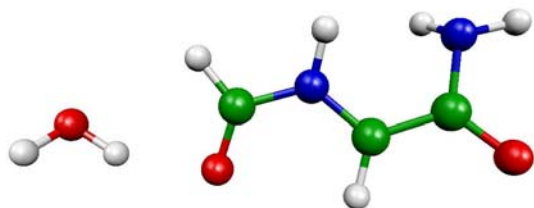
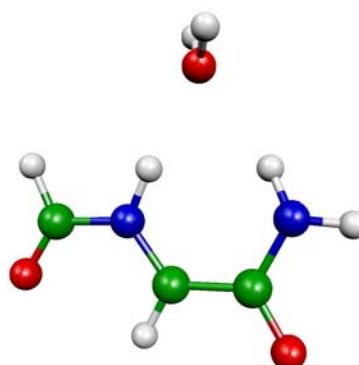


Figure 4.5.3 Optimized structures of supermolecular models of CC-Gly<sup>•</sup> radical in water environment (models CC 1 through CC 11).

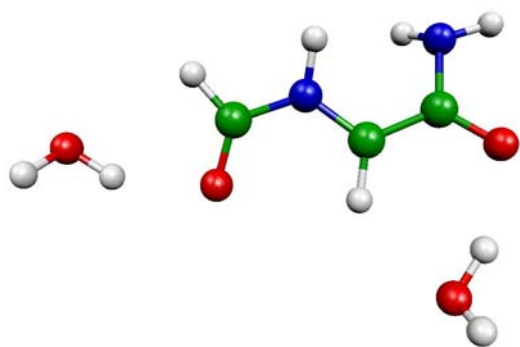
CT 1



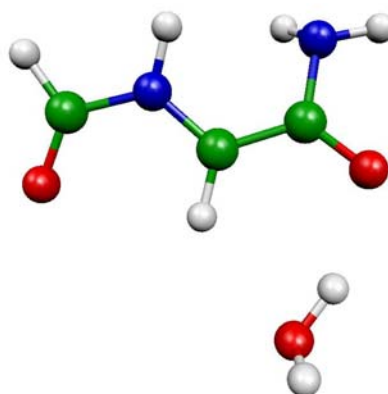
CT 2



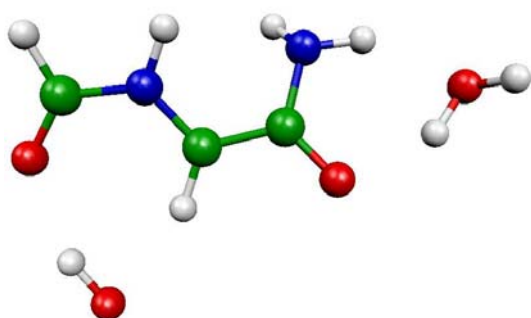
CT 3



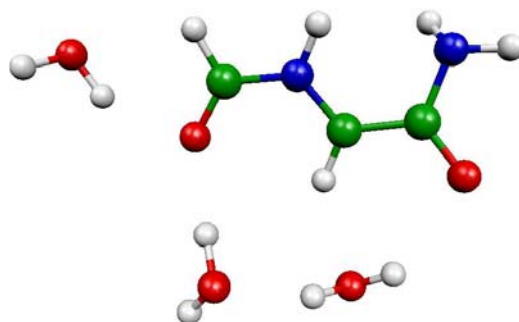
CT 4



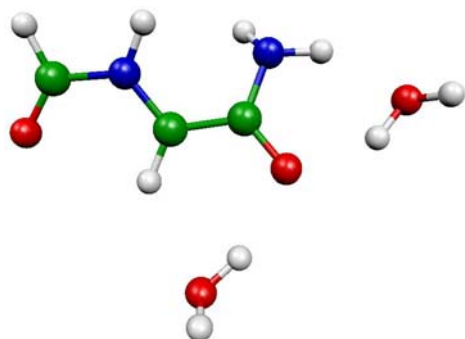
CT 5



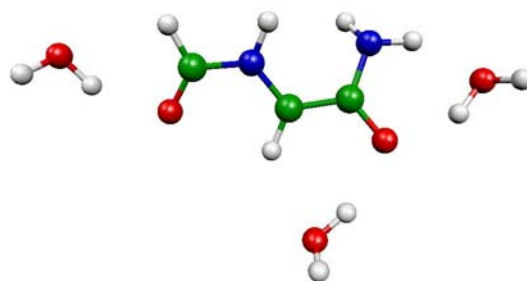
CT 6



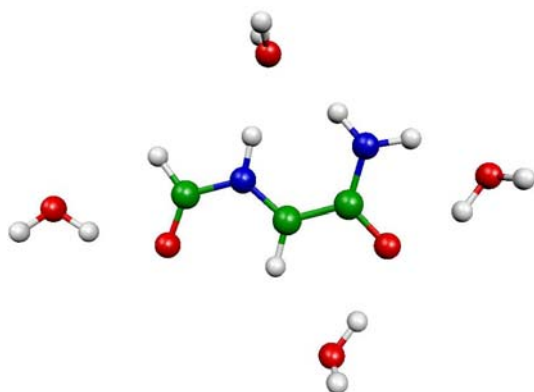
CT 7



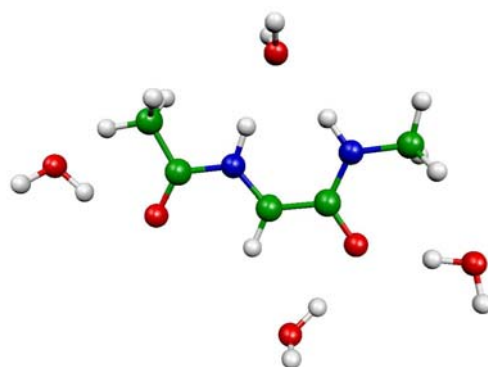
CT 8



CT 9



CT 10





CT 11

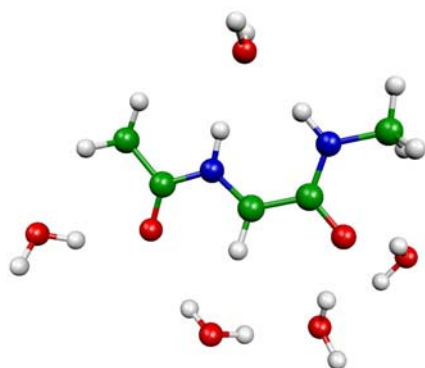


Figure 4.5.4 Optimized structures of supermolecular models of CT-Gly<sup>•</sup> radical in water environment (models CT 1 through CT 11).

Unless stated otherwise, structure optimizations have been performed with the TURBOMOLE (v.5.6) program<sup>232,233</sup> at the B3LYP<sup>83,86,87</sup>/DZVP<sup>188</sup> level. As we identified an unusually large dependence of computed *g*-tensors on the level of structure optimization in Chapter 4.4 for the NAG<sup>•</sup> radical,<sup>157</sup> we studied the influence of the optimization level also for the gas-phase CC-Gly<sup>•</sup> and CT-Gly<sup>•</sup> models. While the size of the NAG<sup>•</sup> radical model precluded levels beyond MP2, the slightly smaller size of Gly<sup>•</sup> has allowed levels up to coupled-cluster singles-doubles (CCSD). *g*-Tensors at RI-BP86 level were thus compared for structures obtained at the following levels: i) the B3LYP and RI-BP86<sup>78,80</sup> DFT levels with either DZVP or TZVP<sup>264</sup> basis sets (RI-BP86 with corresponding auxiliary basis sets<sup>231,268</sup> were used to fit the charge density); ii) the RI-MP2 level with either SVP or TZVP basis sets (and corresponding auxiliary basis sets),<sup>257,258</sup> iii) the CCSD level with TZVP basis sets. The CCSD optimizations were done with the Gaussian 03 program.<sup>234</sup>

#### 4.5.2.2 *g*-Tensor Calculations

The *g*-tensor calculations employed the second-order perturbation DFT approach of refs 45 and 106, introduced also in Chapter 3. Briefly, the unrestricted Kohn-Sham orbitals were obtained at the RI-BP86/DZVP<sup>78,80,188,231,268</sup> level from the TURBOMOLE (v.5.6) program.<sup>232,233</sup> The molecular-orbital information was transferred by appropriate routines to the MAG (magnetic resonance) property

module of the in-house program ReSpect.<sup>50</sup> The extensive experience for computation of  $g$ -tensors for organic radicals<sup>51,105,125,153,155,190</sup> indicate the chosen level of theory to be suited very well. In particular, the moderate-sized DZVP basis set has turned out to provide excellent agreement with much larger basis sets for CC-NAG<sup>•</sup> (cf. Chapter 4.4.<sup>157</sup>). The high spin delocalization and low symmetry of the structure together with small  $g$ -anisotropy increased the requirements for the choice of spin-orbit operator and gauge origin of the magnetic vector potential (see Chapter 4.4<sup>157</sup>). Based on detailed test calculations (not shown), similar to those discussed in Chapter 4.4 for NAG<sup>•</sup>,<sup>157</sup> an explicit description of all one- and two-electron Breit-Pauli spin-orbit integrals (FULL) and distributed gauges with gauge-including atomic orbitals (GIAO<sup>119,120</sup>) were used.

As discussed in Chapter 3, we report and discuss the  $g$ -shift tensor ( $\Delta g$ ), which is defined as the correction to the free electron value i.e.:  $\Delta g = \mathbf{g} - g_e(\mathbf{1})$  ( $g_e = 2.002319$ ) in ppm (i.e., in units of  $10^{-6}$ ).

We note in passing that the out-of-plane vibration of  $H_\alpha$  has been previously found to affect nonnegligibly the  $C_\alpha$  and  $H_\alpha$  hyperfine couplings but not the  $g$ -tensor of model systems,<sup>161</sup> and we thus consider static computations adequate.

### 4.5.2.3 Hyperfine Tensor Calculations

All hyperfine coupling parameters were computed in the usual non-relativistic first-order approach (see Chapter 3), using the MAG-ReSpect<sup>50</sup> code based on unrestricted Kohn-Sham wave functions obtained with the TURBOMOLE (v.5.6)<sup>232,233</sup> program. These calculations used the B3LYP<sup>83,86,87</sup> hybrid functional in combination with the EPR-II<sup>235</sup> basis set.

## 4.5.3 Results and Discussion

### 4.5.3.1 Influence of the Level of Structure Optimization on Computed $g$ -Tensors

We have found an unexpectedly pronounced dependence of the computed  $g$ -tensors on the details of structure optimization for NAG<sup>•</sup> (cf. Chapter 4.4<sup>157</sup>).

Different DFT and RI-MP2 levels were compared in that case. As the basic gas-phase Gly<sup>•</sup> model is somewhat smaller than that of NAG<sup>•</sup>, we have been able in the present case to include also benchmark CCSD structures (cf. Table 4.5.1). Table 4.5.2 lists *g*-tensors (RI-BP86/DZVP level) calculated for the structures of the free CC- and CT-Gly<sup>•</sup> radicals optimized at different computational levels. While the structural differences between the different optimization methods are rather modest in all cases (cf. Table 4.5.1 and Chapter 4.4<sup>157</sup>), the effects on the *g<sub>x</sub>* and *g<sub>y</sub>* components of the *g*-tensor are nonnegligible. Interestingly, the variations are much more pronounced for CT-Gly<sup>•</sup> than for CC-Gly<sup>•</sup> (Table 4.5.2). As for NAG<sup>•</sup> (Chapter 4.4<sup>157</sup>), the largest *g*-shift components are obtained at DFT levels and the lowest at RI-MP2 level.

Table 4.5.1 Selected bond lengths (in pm) and dihedral angles (in deg) for CC-Gly<sup>•</sup> and CT-Gly<sup>•</sup> radicals optimized at different computational levels. <sup>a</sup>

	Level of Structure Optimization (Method/Basis)						
	RI-BP86 /DZVP	RI-BP86 /TZVP	B3LYP /DZVP	B3LYP /TZVP	RI-MP2 /SVP	RI-MP2 /TZVP	CCSD /TZVP
CC-Gly <sup>•</sup>							
<i>bond lengths</i>							
C1 – O1	125.4	124.5	124.2	123.3	123.0	123.2	122.8
C2 – O2	123.3	122.3	122.2	121.2	121.2	121.4	121.0
C1 – C <sub>α</sub>	146.1	145.6	145.6	145.2	146.5	145.6	145.7
C <sub>α</sub> – N1	136.9	136.2	136.8	136.1	136.5	136.2	136.8
N1 – C2	139.3	138.8	138.4	137.8	137.8	137.8	137.5
C1 – N2	138.9	137.6	138.2	136.9	136.2	136.8	136.4
O2··H <sub>α</sub>	260.8	259.6	259.1	258.3	254.7	254.6	255.1
O1··H <sub>β</sub>	223.6	223.6	226.4	226.0	224.4	225.6	228.4
CT-Gly <sup>•</sup>							
<i>bond lengths</i>							
C1 – O1	124.6	123.7	123.5	122.6	121.2	121.5	122.4
C2 – O2	122.9	121.9	121.8	120.8	120.9	121.1	120.6
C1 – C <sub>α</sub>	145.5	145.0	145.0	144.6	147.2	146.5	145.4
C <sub>α</sub> – N1	137.9	137.2	137.8	137.1	137.6	137.5	138.0
N1 – C2	140.1	139.6	139.1	138.6	138.5	138.4	138.3
C1 – N2	141.9	140.9	141.3	140.1	138.7	138.6	137.6
O1··H <sub>β</sub>	260.1	259.2	259.0	257.8	254.8	255.2	250.7
<i>dihedral angles</i>							
N1-C <sub>α</sub> -C1-O1	160.7	160.1	162.3	162.0	157.2	154.6	180.0
N1-C <sub>α</sub> -C1-N2	-14.8	-15.6	-13.8	-14.2	-20.0	-22.2	0.0

<sup>a</sup>See Figure 4.5.1a for atom labels.

The CCSD-structure based results are clearly intermediate between DFT and MP2 for CT-Gly<sup>•</sup>. For CC-Gly<sup>•</sup> the situation is more complicated, as the CCSD/TZVP-structure based results are intermediate between those based on RI-MP2/SVP and RI-MP2/TZVP structures. However, the CCSD-optimized structures may not be compared straightforwardly to the others, due to the enforced C<sub>s</sub> symmetry of the radical in the CCSD optimizations (full optimizations provide a pyramidal NH<sub>2</sub> terminal group in both conformers and an out-of-plane twist of the C-terminus for CT-Gly<sup>•</sup>; see Chapter 4.5.2 Computational Details). The *g*-tensors computed for CC-Gly<sup>•</sup> vary by maximally 180 ppm for Δ*g*<sub>y</sub> and 240 ppm for Δ*g*<sub>x</sub> (Table 4.5.2). Larger variations are computed for CT-Gly<sup>•</sup>, ca. 500 ppm for Δ*g*<sub>y</sub> and ca. 600 ppm for Δ*g*<sub>x</sub>. The effect of the basis set used in the optimization is also larger for CT-Gly<sup>•</sup> than for CC-Gly<sup>•</sup>. The major structural parameters affecting the *g*-tensor for the Gly<sup>•</sup> are the same as found for NAG<sup>•</sup> (cf. Chapter 4.4<sup>157</sup>): shorter C-O bonds (due to either optimization method or basis-set effect) shift spin density from oxygen to carbon (Table 4.5.3 shows relevant Mulliken spin densities).

Table 4.5.2 Δ*g*-Tensor components (in ppm) computed for CC-Gly<sup>•</sup> and CT-Gly<sup>•</sup> radicals optimized at different computational levels.

Structure (Method/Basis)	Δ <i>g</i> <sub>z</sub> <sup>a</sup>	Δ <i>g</i> <sub>y</sub>	Δ <i>g</i> <sub>x</sub>
<b>CC-Gly<sup>•</sup></b>			
RI-BP86/DZVP	-136	1499	2295
RI-BP86/TZVP	-135	1442	2201
B3LYP/DZVP	-135	1469	2275
B3LYP/TZVP	-134	1417	2186
RI-MP2/SVP	-134	1321	2056
RI-MP2/TZVP	-134	1382	2159
CCSD/TZVP	-134	1352	2118

<b>Structure (Method/Basis)</b>	$\Delta g_z$	$\Delta g_y$	$\Delta g_x$
<b>CT-Gly<sup>•</sup></b>			
RI-BP86/DZVP	-28	2025	2954
RI-BP86/TZVP	-63	1966	2799
B3LYP/DZVP	-64	2016	2894
B3LYP/TZVP	-66	1933	2744
RI-MP2/SVP	-34	1550	2272
RI-MP2/TZVP	12	1516	2308
CCSD/TZVP	-139	1909	2536

<sup>a</sup> RI-BP86/DZVP results, with GIAOs and FULL treatment of spin-orbit integrals.

Table 4.5.3 Selected Mulliken atomic spin densities for CC-Gly<sup>•</sup> and CT-Gly<sup>•</sup> radicals, when optimized at different computational levels.<sup>a</sup>

	<b>Computational Level (Method/Basis)</b>						
	RI-BP86 /DZVP	RI-BP86 /TZVP	B3LYP /DZVP	B3LYP /TZVP	RI-MP2 /SVP	RI-MP2 /TZVP	CCSD /TZVP
<b>CC-Gly<sup>•</sup></b>							
C <sub>α</sub>	0.642	0.647	0.651	0.654	0.667	0.657	0.670
O1	0.108	0.100	0.106	0.099	0.091	0.099	0.094
O2	0.110	0.110	0.107	0.107	0.105	0.105	0.104
N1	0.075	0.075	0.057	0.075	0.073	0.075	0.072
N2	0.058	0.061	0.075	0.060	0.059	0.057	0.060
<b>CT-Gly<sup>•</sup></b>							
C <sub>α</sub>	0.649	0.651	0.653	0.661	0.698	0.697	0.691
O1	0.168	0.163	0.168	0.159	0.129	0.128	0.142
O2	0.100	0.101	0.099	0.098	0.094	0.095	0.094
N1	0.060	0.061	0.062	0.061	0.054	0.055	0.052
N2	0.021	0.021	0.020	0.022	0.025	0.024	0.031

<sup>a</sup>BP86/DZVP Mulliken spin densities. See Figure 4.5.1a for atom labels.

This effect is moderate for the oxygens incorporated in intramolecular hydrogen-bonds and larger for those lacking this interaction (e.g. O1 in CT-Gly<sup>•</sup>). As the *g*-tensors are dominated by the spin-orbit contributions from oxygen (see below and Chapter 4.4<sup>157</sup>), this explains the larger variations of *g*-tensor with optimization level for CT-Gly<sup>•</sup>.

### 4.5.3.2 Optimized Structures and Spin Densities of Gas-Phase Conformers

Four different, more or less planar conformers of Gly<sup>•</sup> are shown in Figure 4.5.1, all of which were found to be minima on the potential energy surface (as confirmed by harmonic vibrational frequency analyses). The CC-Gly<sup>•</sup> conformer is lowest in energy, as for the NAG<sup>•</sup> radical (see Chapter 4.4<sup>157</sup>). At B3LYP/DZVP level the three other conformers are higher in energy, by 27.2 kJ mol<sup>-1</sup> (CT-Gly<sup>•</sup>), 7.4 kJ mol<sup>-1</sup> (TC-Gly<sup>•</sup>), and 26.4 kJ mol<sup>-1</sup> (TT-Gly<sup>•</sup>). This is a larger spread than found for the NAG<sup>•</sup> conformers, where the least stable TT conformer was only 10.9 kJ mol<sup>-1</sup> above the lowest-lying CC minimum (see Chapter 4.4<sup>157</sup>). Interestingly, in the present case, the CT conformer is the least stable one. This is notable, as CT-Gly<sup>•</sup> is the radical that would be obtained by straightforward abstraction of a hydrogen atom from the non-radical form of the structurally characterized enzymes,<sup>306,307</sup> provided no rearrangement takes place. All conformers but TT-Gly<sup>•</sup> contain weak intramolecular hydrogen bonds (marked with dotted lines in Figure 4.5.1) which influence the spin density distribution and thereby the EPR parameters (cf. below). The fact that the CT conformer is actually highest in energy here, may be due to repulsive interaction of two amino groups (this interaction is not present in NAG<sup>•</sup>), which results in an out-of-plane twist of the C-terminus (see, e.g., N1-C<sub>α</sub>-C1-O1 dihedral angle in Table 4.5.1). Additionally, in all conformers a more or less pyramidalized amide group was found. When this amide group was forced to be non-pyramidal during optimization, a negligible increase of the energy by 0.7 kJ mol<sup>-1</sup> was calculated for the CC conformer, while for the CT conformer the energy increased by 11.3 kJ mol<sup>-1</sup>.

Two intramolecular hydrogen-bonds are present in CC-Gly<sup>•</sup>, with the respective distances 226.4 pm (O1<sup>•••</sup>H<sub>β</sub>) and 259.1 pm (O2<sup>•••</sup>H<sub>α</sub>). One hydrogen-bond is present in CT-Gly<sup>•</sup>, with distance 259.0 pm (O2<sup>•••</sup>H<sub>α</sub>), and one in TC-Gly<sup>•</sup>, with distance 230.4 pm (O1<sup>•••</sup>H<sub>β</sub>). Covalent regular bond lengths vary only by up to 2 pm between the conformers,<sup>156</sup> while the spin densities change significantly.

Selected Mulliken atomic spin densities for different conformers of Gly<sup>•</sup> are summarized in Table 4.5.4. The O1<sup>•••</sup>H<sub>β</sub> and O2<sup>•••</sup>H<sub>α</sub> interactions influence mainly the

spin density localized on the O1 and O2 atoms. The presence and strength of the O1 $\cdots$ H $\beta$  interaction correlates well with the amount of spin density on O1.

Table 4.5.4 Selected Mulliken atomic spin densities<sup>a</sup> for different conformers of Gly $\bullet$  in basic or extended form.

Spin Densities	Conformer					
	CC-Gly $\bullet$	ext.CC-Gly $\bullet$	CT-Gly $\bullet$	ext.CT-Gly $\bullet$	TC-Gly $\bullet$	TT-Gly $\bullet$
C $\alpha$	0.651	0.650	0.652	0.677	0.634	0.641
O1	0.106	0.089	0.168	0.149	0.112	0.169
O2	0.107	0.088	0.099	0.080	0.115	0.105
N1	0.075	0.084	0.062	0.068	0.099	0.082
N2	0.057	0.076	0.020	0.033	0.056	0.023

<sup>a</sup> RI-BP86/DZVP//B3LYP/DZVP results.

No such straightforward dependence is found for O2 for which the spin density in the presence of the O2 $\cdots$ H $\alpha$  interaction (CC-Gly $\bullet$ ) appears to be even slightly higher than for TT-Gly $\bullet$ , where this interaction is absent. Overall the changes of the spin density due to intramolecular hydrogen-bonding are much smaller for O2 than for O1. The spin density on N1 is largest for TC and TT conformers, for which the O1 $\cdots$ H $\beta$  interaction is missing. On the other hand the spin density on N2 is lowest for the CT and TT conformers. This is due to non-planarity of the C-terminus of the radical (the  $\psi$  dihedral angle is ca. 160° in both structures) and pyramidalization of the NH<sub>2</sub> group. This prevents redistribution of spin density to the N2 atom. As mentioned above, the CT and TT conformers converge to slightly twisted structures due to repulsion between partially positively charged amino hydrogen atoms (H $\beta$  and H of the NH<sub>2</sub> group). Extension of the models modifies further the spin density for both CC and CT conformers. (see Table 4.5.4 for the spin densities of the doubly extended models). The significant reduction of spin densities on O1 and O2, accompanied by an increase of spin density on all other atoms, suggests nonnegligible effects on g-tensors (see below). The extension of the model did not reduce the pyramidalization of the NH<sub>2</sub> terminal group or the out-of-plane twist of the C-terminus in the CT conformer.

Compared to results for the NAG $\bullet$  radical (Chapter 4.4<sup>157</sup>), the Mulliken spin densities for Gly $\bullet$  in Table 4.5.4 suggest somewhat less pronounced delocalization of

the spin density (larger spin density on C $\alpha$ ). Moreover, the spin densities on O1 and O2 in the present case appear somewhat more similar for CC and CT conformers but somewhat more divergent for the TC and TT conformers. This is of course expected to affect the *g*-tensors of the two systems, as well as the influence of external hydrogen bonding (see below).

#### 4.5.3.3 Conformational Effects on *g*-Tensors for Gas-Phase Radicals

Table 4.5.5 provides computed *g*-shift tensors for different conformers of the free Gly $\bullet$  radical (including extended gas-phase models) and for various solvated models of the CC- and CT-Gly $\bullet$  conformers. The computed *g*-tensors for the gas-phase radicals correlate well with the presence or absence of intramolecular hydrogen bonds (cf. Figure 4.5.1) for all four conformers. CC-Gly $\bullet$  (two hydrogen-bonds) and TT-Gly $\bullet$  (no hydrogen-bond) exhibit the lowest and highest *g*-anisotropies, respectively. However, the largest  $\Delta g_y$  component (above 2000 ppm) is computed for CT-Gly $\bullet$  ( $\Delta g_y$  for TT-Gly $\bullet$  is negligibly smaller). CT-Gly $\bullet$  and TC-Gly $\bullet$  (each with one intramolecular hydrogen-bond) give both intermediate values of *g*-anisotropies but markedly different tensors (due to unequal contributions from the two oxygen atoms, see below). The overall variations with conformation amount to more than 1250 ppm for  $\Delta g_y$  and to 550 ppm for  $\Delta g_x$ , and they are accompanied by changes in the orientations of both components: the CC and TC conformers exhibit similar *g*-tensor orientations, and so do the CT and TT conformers, albeit different from the former two conformers (see Figure 4.5.1b for the computed tensor orientation of the CT, TC and TT conformers, tensor orientation for CC conformer is very similar to that of the TC conformer).



Table 4.5.5 Computed  $\Delta g$ -shift-tensor components (in ppm) for different conformations of the gas-phase Gly $\cdot$  radical, and for various supermolecular models of CC-Gly $\cdot$  and CT-Gly $\cdot$ .<sup>a</sup>

<b>Gas-phase model<sup>b</sup></b>	$\Delta g_z$	$\Delta g_y$	$\Delta g_x$
CC-Gly $\cdot$	-135	1469	2275
<i>ext. CC-Gly<math>\cdot</math></i>	-142	1349	2144
CT-Gly $\cdot$	-64	2016	2894
<i>ext. CT-Gly<math>\cdot</math></i>	-44	1789	2681
<i>ext. CT-Gly<math>\cdot</math><sup>c</sup></i>	-63	1661	2425
TC-Gly $\cdot$	-150	1873	2531
TT-Gly $\cdot$	-102	2001	3550
<b>Supermolecular model<sup>d</sup></b>	$\Delta g_z$	$\Delta g_y$	$\Delta g_x$
CC 1	-123	1435	2202
CC 2	-126	1288	2074
CC 3	-142	1387	2440
CC 4	-129	1292	2004
CC 5	-147	1327	2012
CC 6	-118	1278	2200
CC 7	-151	1277	2300
CC 8	-131	1221	2208
CC 9	-118	1226	2236
CC 10	-123	1146	2161
CC 11	-104	1116	2063
CT 1	-59	1947	2887
CT 2	-146	2124	2825
CT 3	-32	1867	2616
CT 4	-58	1984	2638
CT 5	-52	1734	2604
CT 6	-84	1870	2526
CT 7	-54	1783	2374
CT 8	-32	1698	2362
CT 9	-135	1813	2253
CT 10	-137	1705	2158
CT 11	-57	1700	2110
<i>E.coli</i> PFL <sup>e</sup>	181	1581	2381
<i>Azoarcus</i> sp. BSS <sup>e</sup>	-119	1281	2181
<i>E.coli</i> ARNR <sup>e</sup>	-19	981	1881

<sup>a</sup> BP86/DZVP//B3LYP/DZVP results with GIAO gauge and exact FULL treatment of spin orbit integrals; <sup>b</sup>Figures 4.5.1 and 4.5.2. <sup>c</sup>Planarity of the C-terminal peptide bond was enforced. <sup>d</sup>Figures 4.5.3 and 4.5.4. <sup>e</sup>Experimental data for protein glycyl radicals, ref 291.

It appears thus, that the tensor depends mostly on the value of dihedral angle  $\psi$ . Notably, however, the orientations of the tensors are almost invariant to either extension of the models or to external hydrogen-bonding interactions.

In view of the delocalized nature of the spin density (Table 4.5.4), one might expect that further extension of the model along the peptide chain may lead to further changes of the  $g$ -tensor (even though no significant effects were obtained for hyperfine couplings<sup>151,311</sup>). This is confirmed by the  $g$ -shifts computed for the doubly-extended models (Table 4.5.5), which exhibit a reduction of both  $\Delta g_x$  and  $\Delta g_y$  by 120-130 ppm for ext.CC-Gly $\cdot$  vs. CC-Gly $\cdot$  and by 200-230 ppm for ext.CT-Gly $\cdot$  vs. CT-Gly $\cdot$ . An additional reduction by 260 ppm and 130 ppm for  $\Delta g_x$  and  $\Delta g_y$ , respectively, is obtained for ext.CT-Gly $\cdot$  when planarity of the C-terminal peptide bond ( $\psi = 180^\circ$ ) is enforced (full optimization of the CC-conformer does not result in twisting, cf. discussion above). A planar unit is expected in the protein, and planarity is also restored by a suitable bridging hydrogen-bond acceptor (see below).

#### 4.5.3.4 Analyses of Gas-Phase $g$ -Tensors in Terms of Atomic Spin-Orbit Contributions

To understand better the conformational effects on the  $g$ -tensor, and to provide a basis upon which to discuss environmental effects, a breakdown of the dominant  $\Delta g_{SO/OZ}$  contribution to the  $g$ -shift components into atomic contributions is provided in Table 4.5.6. For this analysis, we have used the atomic mean-field approximation (AMFI) to the spin-orbit operator<sup>115,116</sup> and a common gauge on  $C_\alpha$  (the computed  $g$ -shifts differ by less than 215 ppm from the FULL-GIAO data used otherwise; cf. Table 4.5.5, see also Chapter 4.4<sup>157</sup>). While most of the spin density is concentrated at  $C_\alpha$  (cf. Table 4.5.4), due to the larger spin-orbit coupling at oxygen the carbonyl oxygen atoms dominate the  $\Delta g_{SO/OZ}$  contributions to  $\Delta g_x$  and  $\Delta g_y$  in all four conformers of Gly $\cdot$  ( $C_\alpha$  contributions amount to only 4-9% or 100-200 ppm, of the total  $\Delta g_x$ ; Table 4.5.6). In CC-Gly $\cdot$  the spin densities on O1 and O2 are almost identical (both oxygen atoms are incorporated in intramolecular hydrogen-bonds), and almost equal contributions from these oxygen atoms to  $\Delta g_x$  and  $\Delta g_y$  are found. In CT-

Gly<sup>•</sup>, on the other hand, more of the spin density is located on O1 (which does not take part in an intramolecular hydrogen-bond).

Table 4.5.6 Breakdown of the dominant  $\Delta g_{SO/OZ}$  contribution to the  $g$ -shift-tensors into atomic contributions (in ppm) for the four conformers of gas-phase Gly<sup>•</sup>.<sup>a</sup>

Atom	CC-Gly <sup>•</sup>			CT-Gly <sup>•</sup>			TC-Gly <sup>•</sup>			TT-Gly <sup>•</sup>		
	$\Delta g_z$	$\Delta g_y$	$\Delta g_x$	$\Delta g_z$	$\Delta g_y$	$\Delta g_x$	$\Delta g_z$	$\Delta g_y$	$\Delta g_x$	$\Delta g_z$	$\Delta g_y$	$\Delta g_x$
O1	-13	737	701	-36	1113	1861	-13	798	728	-35	1147	1932
O2	-3	630	693	66	655	559	-6	947	878	30	545	1162
C $_{\alpha}$	-1	29	157	4	26	102	-1	7	213	6	36	141
N1	-5	-22	325	-17	106	110	-4	-47	467	-10	291	30
N2	-2	80	143	20	-22	99	-2	109	127	21	-17	106
C1	-4	-74	37	0	-4	-23	-4	-73	47	-1	2	-18
C2	0	-25	7	-4	-37	37	1	-61	47	0	3	-1
$\Sigma$	-27	1355	2062	34	1838	2744	-29	1680	2507	11	2008	3352

<sup>a</sup> BP86/DZVP//B3LYP/DZVP results with AMFI SO operators and common gauge origin at the C $_{\alpha}$ . Contributions from hydrogen atoms are generally negligible.

Consequently, the contribution from O1 is larger, but in a non-uniform manner, 1860 ppm to  $\Delta g_x$  and 1100 ppm to  $\Delta g_y$  (cf. the similar contributions in TT-Gly<sup>•</sup>). In TT-Gly<sup>•</sup>, the O2 contribution to  $\Delta g_x$  is also enhanced. This leads to a particularly pronounced  $g$ -anisotropy for this conformer.

The two nitrogen atoms contribute very differently and have to be discussed separately. The spin density on N1 is strongly dependent on the presence of an intramolecular O1 $\cdots$ H $_{\beta}$  hydrogen bond. In CC- and TC-Gly<sup>•</sup>, the presence of this hydrogen-bond interaction increases the spin density on N1 (Table 4.5.4), which contributes appreciably to  $\Delta g_x$  (325 and 467 ppm for the CC- and TC-conformers, respectively; Table 4.5.6). In CT- and TT-Gly<sup>•</sup> the spin density on N1 decreases (compared to CC and TC, respectively) due to the lack of an hydrogen-bond interaction. The contribution to  $\Delta g_x$  decreases significantly, but the contribution to  $\Delta g_y$  increases. The spin density on N2 is overall smaller than on N1 (especially for CT and TT conformers in which the NH $_2$  group is twisted out of plane) and contributes

positively to  $\Delta g_x$ , ca. 100-150 ppm. The contribution to  $\Delta g_y$  is also small and either positive (80-100 ppm for CC and TC conformers) or negative (for CT and TT conformers).

The lower  $\Delta g_x$  and  $\Delta g_y$  values of the doubly extended CC and CT models, compared to the corresponding smaller models, may be explained similarly: in particular, the methyl substituent on the C-terminal amide group redistributes some of the spin density from O1 to N2 (cf. Table 4.5.3), and the methyl group on the other side decreases the spin density on O2 (and enhances it on N1). Both effects reduce the  $\Delta g_x$  and  $\Delta g_y$  components. Similarly, forced planarity of the peptide bond (the O1-C1-N2-H dihedral angle) on the C-terminus enhances the redistribution of spin density from O1 towards N2 and thus reduces the  $g$ -anisotropy further.

Compared to computations at corresponding levels (either FULL-GIAO or AMFI with common gauge on  $C_\alpha$ ) for the CC conformer of NAG $\cdot$  (see Chapter 4.4<sup>157</sup>) the results for gas-phase CC-Gly $\cdot$  exhibit about 400-500 ppm lower  $\Delta g_x$  but similar (slightly increased)  $\Delta g_y$ . This is in particular due to a lower contribution from N2 compared to the carboxyl oxygen (O3) in NAG $\cdot$  (see Chapter 4.4<sup>157</sup>), and to somewhat different O1 and O2 contributions. Thus, while the NAG $\cdot$  radical is a reasonable model for the electronic structure of the protein-bound glycyl radical, replacement of a hydroxyl by an amide group causes subtle differences that may lead to somewhat different effects of conformation and environment on  $g$ -tensors (see also below).

#### 4.5.3.5 Structural Results and Spin Densities for Supermolecular Models

In view of the uncertainty regarding the preferred conformation of protein-bound glycyl radicals (see above), two sets of supermolecular structures were employed to model environmental effects, based either on CC-Gly $\cdot$  or CT-Gly $\cdot$ , and using water molecules as hydrogen-bond donors and acceptors. Optimized structures of all models are shown in Figures 4.5.3 and 4.5.4 (Table 4.5.7 presents Mulliken atomic spin densities for all supermolecular models studied). The information on the radical structure in glycyl radical enzymes is very limited, and no information on the

interaction with environment is available. It is thus desirable to correlate conformation and intermolecular interactions to computed  $g$ -tensors, in the hope of relating measured  $g$ -anisotropies to the situation in the protein environment. We may distinguish direct environmental effects due to spin polarization at a given structure and indirect effects due to alteration of the structural parameters of the radical by hydrogen bonding. While we will point out the main effects of spin-density changes due to individual hydrogen bonds, these effects sum up in a complex manner for the larger supermolecular models, rendering detailed analysis difficult.

Table 4.5.7 Selected Mulliken atomic spin densities<sup>a</sup> for supermolecular structures of CC-Gly<sup>•</sup> and CT-Gly<sup>•</sup>.

<b>Model</b>	<b>C<sub>α</sub></b>	<b>O1</b>	<b>O2</b>	<b>N1</b>	<b>N2</b>
CC-Gly <sup>•</sup>	0.651	0.106	0.107	0.075	0.057
CC 1	0.661	0.105	0.104	0.061	0.057
CC 2	0.656	0.083	0.104	0.062	0.078
CC 3	0.614	0.099	0.107	0.092	0.068
CC 4	0.661	0.081	0.106	0.046	0.081
CC 5	0.653	0.071	0.105	0.044	0.092
CC 6	0.647	0.089	0.101	0.043	0.075
CC 7	0.608	0.078	0.106	0.093	0.093
CC 8	0.623	0.075	0.104	0.075	0.094
CC 9	0.609	0.078	0.104	0.081	0.093
CC 10	0.601	0.070	0.080	0.095	0.105
CC 11	0.621	0.066	0.078	0.062	0.111
CT-Gly <sup>•</sup>	0.652	0.168	0.099	0.062	0.020
CT 1	0.659	0.167	0.097	0.051	0.019
CT 2	0.660	0.156	0.102	0.054	0.028
CT 3	0.642	0.155	0.096	0.057	0.028
CT 4	0.633	0.158	0.098	0.068	0.027
CT 5	0.655	0.145	0.099	0.039	0.030
CT 6	0.662	0.158	0.094	0.032	0.020
CT 7	0.635	0.134	0.098	0.069	0.043
CT 8	0.644	0.133	0.096	0.058	0.043
CT 9	0.650	0.117	0.100	0.052	0.057
CT 10	0.653	0.108	0.078	0.062	0.069
CT 11	0.661	0.107	0.075	0.051	0.069

<sup>a</sup>BP86/DZVP Mulliken spin densities. See Figure 4.5.1a for atom labels.

Structural effects of hydrogen bonding relate mostly to the breaking of intramolecular hydrogen bonds when the somewhat stronger intermolecular hydrogen bonds are formed. This affects also somewhat the bond angles around the fragments

in question. Changes in regular covalent bond lengths are relatively small, below 1 pm for the bond lengths in the proximity of  $C_\alpha$  and 1-4 pm for all others.

Starting with complexes of CC-Gly $\bullet$ , we note that a water molecule interacting with O2 lengthens the C2-O2 bond slightly and typically shortens somewhat the O2 $\cdots$ H $_\alpha$  distance (models CC1, CC2). When a water molecule hydrogen-bonds simultaneously to O2 and H $_\alpha$  (models CC4 and CC5), the O2 $\cdots$ H $_\alpha$  is lengthened by ca. 10 pm. However, the spin density on O2 is affected relatively little (Table 4.5.7). A water molecule interacting simultaneously with H $_\beta$  and O1 breaks the intramolecular hydrogen-bond (the N1 $\cdots$ H $_\beta$  distance expands by ca. 30 pm) and reduces the spin density on O1 (model CC3). At the same time some of the spin density shifts from  $C_\alpha$  to N1, and the O2 $\cdots$ H $_\alpha$  distance is reduced. A water molecule hydrogen-bonded to O2 and H $_\alpha$  compensates these effects (model CC6). As some of the influences of different hydrogen bonds counteract each other, a relatively complicated pattern of spin-density redistribution is found for the model with four water molecules (CC9): compared to the gas-phase model, the spin density on  $C_\alpha$ , O1 and O2 is reduced while the spin density on both nitrogen atoms is enhanced. Using the extended model of the CC-Gly $\bullet$  radical (model CC10), further reduction of spin density is observed for O1, O2 and  $C_\alpha$  (the spin densities on N1 and N2 increase slightly; Table 4.5.7). This reflects the increased delocalization of spin density along the backbone (cf. Table 4.5.4 for spin densities of the corresponding gas-phase radicals). Addition of one more water molecule to the CC10 model reduces O1, O2 and N1 spin densities and increases spin densities on  $C_\alpha$  and N2 (CC11).

The gas-phase CT-Gly $\bullet$  radical lacks the intramolecular hydrogen-bond to O1 and thus exhibits rather different spin densities on O1 and O2 (0.168 and 0.099, respectively, Table 4.5.4). External hydrogen-bonds to O2 affect the O2 spin density relatively little. The O2 $\cdots$ H $_\alpha$  intramolecular bond is not affected by interaction of O2 with water molecules unless the water molecule simultaneously interacts with H $_\alpha$  (O2 $\cdots$ H $_\alpha$  expands then by ca. 10 pm, CT5). Distinct structural changes are found if a water molecule accepts hydrogen-bonds simultaneously from both amide groups (CT2, CT9, CT10, CT11). This removes the repulsive interaction between the amide groups and the out-of-plane twist of the C-terminus (but pyramidalicity of the amide group is reduced only slightly). The almost planar structure induces a redistribution of

spin density (decrease on O1 and N1, increase on O2 and N2). Additionally, the charge distribution is altered, and the hydrogen-bonds to both carbonyl oxygens are strengthened (model CT9). The spin density on O1 is very sensitive to hydrogen-bond interactions: one water molecule (model CT5) reduces the O1 spin density by 14%, two water molecules (model CT7) by 20%.

Comparing the spin-density distribution of the largest CT9 model (Table 4.5.7) to the gas-phase radical, one finds negligible changes for  $C_\alpha$  and O2, a reduction by 30% on O1, a small reduction on N1, and an increase on N2. As for CC-Gly<sup>•</sup> (see above), additional reduction of spin densities on the oxygen atoms and on N1 (and enhancement on N2 and  $C_\alpha$ ) is observed upon extension of the model (CT10), and even more when a further water molecule is added (CT11).

#### 4.5.3.6 Environmental Effects on $g$ -Tensors

Table 4.5.5 provides the  $g$ -shift tensors for all supermolecular complexes with water molecules derived from the CC and CT conformers (cf. Figures 4.5.3 and 4.5.4). Interestingly, the environmental effects turn out to be rather different for the two conformers.

Starting with CC-Gly<sup>•</sup>, we find the influence of hydrogen bonding, compared to the gas-phase radical, to be overall relatively modest.  $\Delta g_x$  is reduced at most by 260 ppm (CC5), but the largest complex derived from the basic CC-Gly<sup>•</sup> model (CC9) exhibits a value only ca. 40 ppm below the gas-phase result (models CC3 and CC7 provide even an increase). Changes are somewhat more pronounced for  $\Delta g_y$ , and generally provide a reduction compared to the gas-phase model, 240 ppm for CC9, the model with the most extensive hydrogen bonding. As in the gas phase (see above), extension of the radical along the backbone (CC10 vs. CC9) reduces both components further, by about 70-80 ppm. Addition of a fifth water molecule reduces  $\Delta g_x$  and  $\Delta g_y$  by another ca. 100 ppm and 30 ppm, respectively (CC11). These rather moderate effects of external hydrogen bonding on  $g$ -tensors disagree with the much larger effects of hydrogen bonding for related  $\pi$ -radicals like semiquinones or tyrosyl,<sup>45,51,153,174</sup> but they are consistent with the results for the corresponding conformer of the NAG<sup>•</sup> radical presented in Chapter 4.4.<sup>157</sup> Obviously, for the CC

conformer, there exists a pronounced compensation between the effects of intra- and intermolecular hydrogen bonding on the oxygen spin densities.

Larger effects of hydrogen bonding are computed for CT-Gly<sup>•</sup>, in particular for the  $\Delta g_x$  component. Here the basic model with the most extensive hydrogen bonding (CT9) exhibits a value 640 ppm below the gas-phase result (with a smaller reduction of  $\Delta g_y$  by ca. 200 ppm, Table 4.5.5). A further reduction is again obtained upon extending the basic radical model (CT10 vs. CT9).

As a result, the largest models with the most extensive hydrogen bonding, CC11 and CT11, exhibit rather similar  $\Delta g_x$  values, whereas the  $\Delta g_y$  value of the CT conformer is still almost 600 ppm larger than for the CC conformer (in the gas-phase models, both components differed appreciably, depending somewhat on the twist of the peptide bond of the C-terminus in the CT conformer, cf. Table 4.5.5).

We may further analyze the larger effects of intermolecular hydrogen bonding on the  $\Delta g_x$  component of the CT conformer (and the moderate effects on  $\Delta g_y$ ) by looking at the individual models, keeping in mind the computed differences in the spin densities (cf. Table 4.5.2 for the gas phase and Table 4.5.7 for the supermolecular complexes), and the atomic spin-orbit analyses carried out above for the gas-phase radicals (Table 4.5.6). A single hydrogen bond to O2 has very little effect on  $\Delta g_x$  and reduces  $\Delta g_y$  by less than 100 ppm (CT1, cf. also CT8 vs. CT7). This is consistent with the very moderate effect on the oxygen spin densities (cf. Table 4.5.7), due to a compensation of the effects of inter- and intramolecular hydrogen bonds to O2. The effect of a hydrogen bond to O1 (which is not present in the gas-phase CT conformer) is a more pronounced reduction of  $\Delta g_x$  but not  $\Delta g_y$  (see, e.g. CT4), consistent with a reduction of spin density on O1 (Table 4.5.7). A hydrogen-bond acceptor bridging the two amide groups has a special effect, as it planarizes the C-terminus (see above), and the hydrogen bonds to both carbonyl oxygen atoms tend to get stronger. The spin density is thereby reduced on O1 and N1 but enhanced on O2 and N2 (Table 4.5.7). A reduction of  $\Delta g_x$  is thus accompanied by an increase of  $\Delta g_y$  (see, e.g., CT2 vs. gas-phase model, or CT9 vs. CT8). Overall, the effects of the various external hydrogen bonds apparently add up to a pronounced reduction of  $\Delta g_x$  but partly compensate for  $\Delta g_y$  (as they do for both components of the CC conformer, Table 4.5.5).



Summarizing the  $g$ -tensor data in Table 4.5.5, we note that the property of the radical determining most strongly the  $\Delta g_y$  and  $\Delta g_x$  components is the conformation. Among the conformers expected most likely in the protein environment, the CT conformer has the larger  $g$ -shift components than the CC conformer, due to the lack of an intramolecular hydrogen bond between  $H_\beta$  and O1. Intermolecular hydrogen bonds to and from the radical have more moderate effects, which may mutually cancel, depending on the actual environment of the radical. While extensively hydrogen-bonded complexes of the CC conformer exhibit only moderate reductions of  $\Delta g_y$  and  $\Delta g_x$  compared to the corresponding gas-phase models, the  $\Delta g_x$  component of the CT conformer is reduced more significantly (to values resembling those of the CC models). The  $\Delta g_y$  component of the CT models remains appreciably larger. Extension of the radical model along the peptide chain reduces both components somewhat.

#### 4.5.3.7 Comparison with Experimental $g$ -Tensors

For the NAG $\bullet$  radical (Chapter 4.4<sup>157</sup>), calculations on the presumably best supermolecular model complexes overestimated the  $\Delta g_x$  and  $\Delta g_y$  components measured<sup>293,294</sup> in an N-acetylglycine single crystal systematically (see below). A similar overestimation of the largest  $g$ -tensor component at the given computational level (gradient-corrected BP86 functional, DZVP basis, full or atomic mean-field Breit-Pauli spin-orbit operators) by typically 10% is found for related  $\pi$ -radicals like semiquinones, tyrosyl or nitroxide radicals (due to the higher local symmetry in those systems, only the  $\Delta g_x$  component is typically controlled predominantly by one low-lying excited state).<sup>45,51,153,160</sup> It is thus interesting to note that our best results for the CC conformer tend to be already appreciably below experiment for both components when compared to the PFL data, and even somewhat below the BSS data, albeit still above the *E. coli* ARNR values (Table 4.5.5). In contrast, the larger  $\Delta g_y$  component for the CT conformer (cf., e.g. CT11 results in Table 4.5.5) is still above the PFL result.

How significant are both computational and experimental data in view of the very small  $g$ -anisotropies, and can we derive any useful information on structure and environment of protein-bound glycyl radicals from the comparison? To analyze this question, we need to discuss errors in both the experimental and computational

studies. Starting with experiment, we note that the error margins provided in the very-high-field EPR study of ref 291 are  $\pm 400$  ppm for the absolute  $g$ -values (due to problems with the calibration of the magnetic field) and  $\pm 200$  ppm for the difference  $\Delta(g_x-g_z)$ . While the former value appears realistic, the latter is presumed to be a very conservative estimate,<sup>312</sup> and the differences between the three tensor components may be as accurate as  $\pm 100$  ppm (notably, line broadening due to  $g$ -strain appears to be essentially absent<sup>291</sup>).

That is, we may consider the differences between  $g_x$  and  $g_z$ , and between  $g_y$  and  $g_z$  (and of course between  $g_x$  and  $g_y$ ) as reasonably reliable measures (cf. Figures 4.5.5 and 4.5.6). The  $\Delta(g_y-g_z)$  differences for PFL, BSS, and ARNR amount to 1400 ppm, 1400 ppm, and 1000 ppm, respectively. The  $\Delta(g_x-g_z)$  differences for the same enzymes amount to 2200 ppm, 2300 ppm, and 1900 ppm, respectively ( $\Delta(g_x-g_y)$  values are 800 ppm, 900 ppm, and 900 ppm, respectively). Thus, while the PFL and BSS  $g$ -tensors have to be considered equal within experimental error, the deviations of the ARNR data from those for the two other systems appear to be significant.

On the computational side, the analysis of potential errors sources is somewhat more complicated, as the only closely similar benchmark system studied is indeed the NAG<sup>•</sup> radical in an N-acetylglycine single crystal (Chapter 4.4<sup>157</sup>). Compared to the most reliable experimental data,<sup>293</sup> the “best” computed  $\Delta(g_x-g_z)$  of ca. 2700 ppm was too large by ca. 200 ppm, and the  $\Delta(g_y-g_z)$  difference of ca. 1600 ppm was too large by ca. 500 ppm (Figures 4.5.5 and 4.5.6, see Chapter 4.4<sup>157</sup>). Possible error sources of the calculations include deficiencies in the gradient-corrected functional, potentially incomplete modeling of the interactions in the extended solid (although we expect these errors to be small), and the fact that the two-electron gauge-corrections were not included in the calculations. In view of recent work by Patchkovskii et al.,<sup>303</sup> the role of the latter omission is currently unclear. We expect that the employed spin-orbit Hamiltonian (full calculation of all one- and two-electron Breit-Pauli integrals, combined with GIAOs) itself is rather accurate (for the NAG<sup>•</sup> radical, the semiempirical one-electron spin-orbit operators used in the two previous computational  $g$ -tensor studies of glycyl models<sup>161,162</sup> provided still ca. 10% larger  $\Delta g_x$  and  $\Delta g_y$  values than the full treatment, Chapter 4.4<sup>157</sup>).

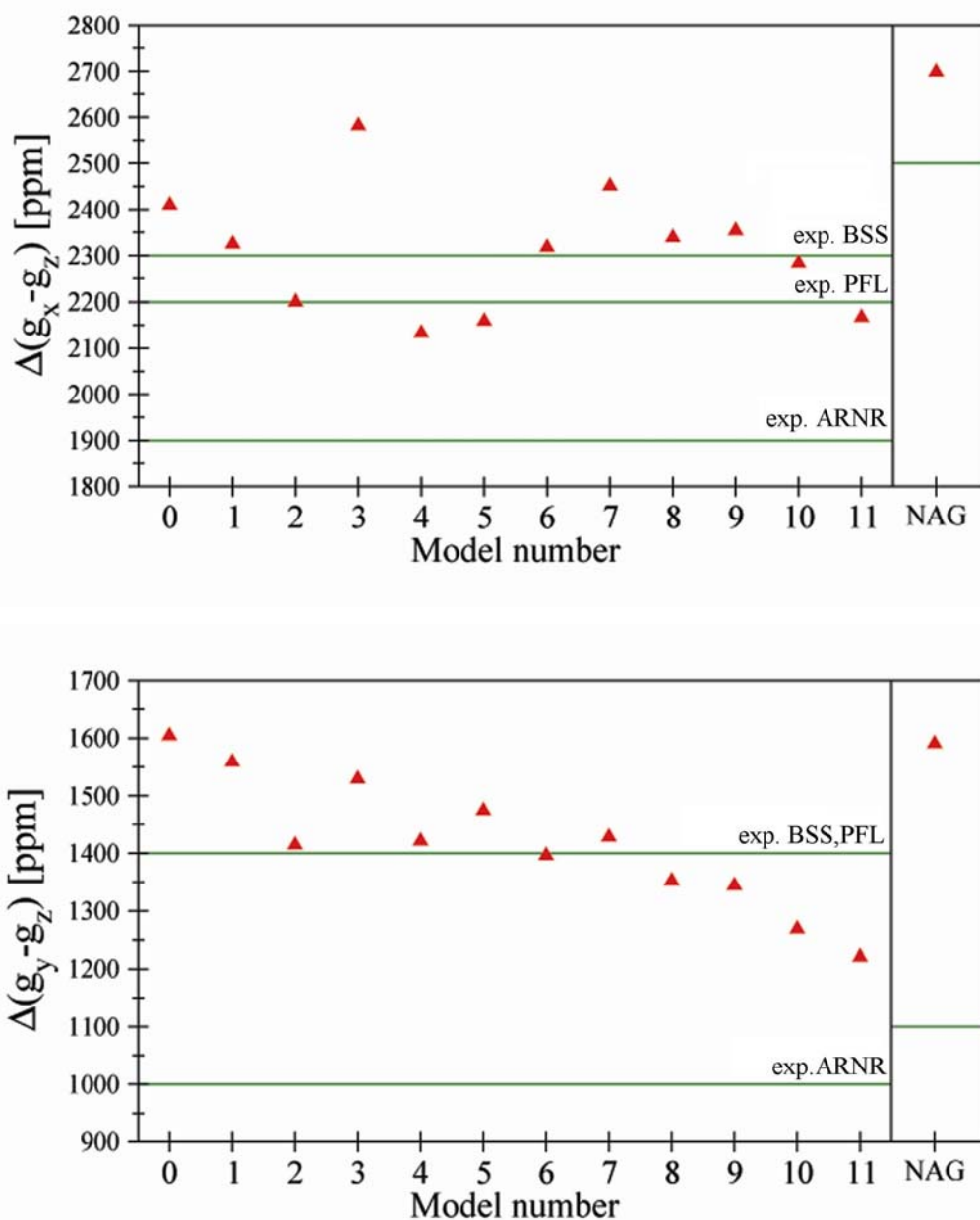


Figure 4.5.5 Comparison of computed and experimental differences between  $g$ -tensor components (in ppm) for various models of the CC conformer. a)  $\Delta(g_x - g_z)$ . b)  $\Delta(g_y - g_z)$ . In both cases, comparison of results for the best model for the CC-NAG $^{\bullet}$  radical in an N-acetylglycine single crystal (taken from Chapter 4.4<sup>157</sup>) with the corresponding experimental results is shown on the right side.

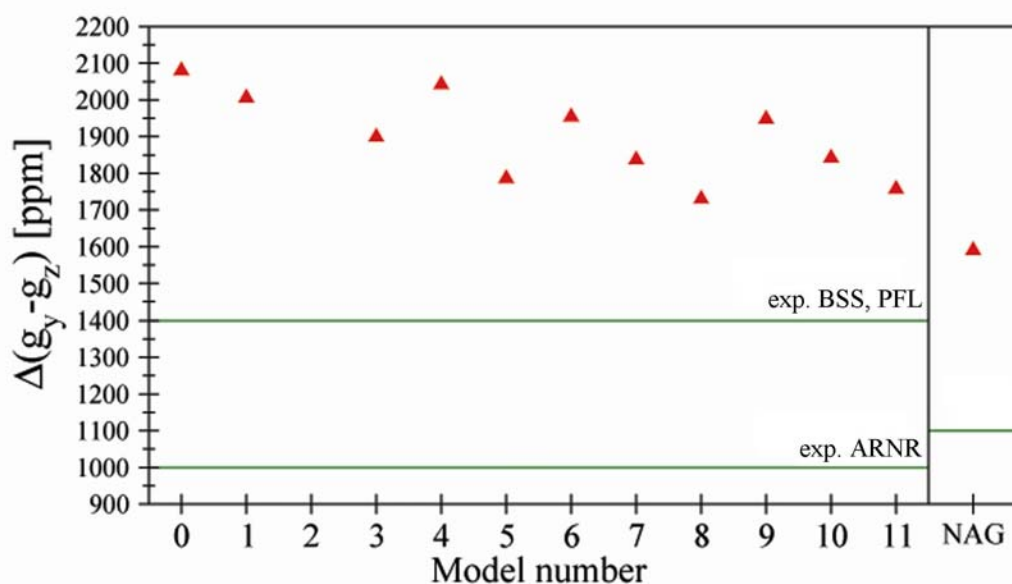
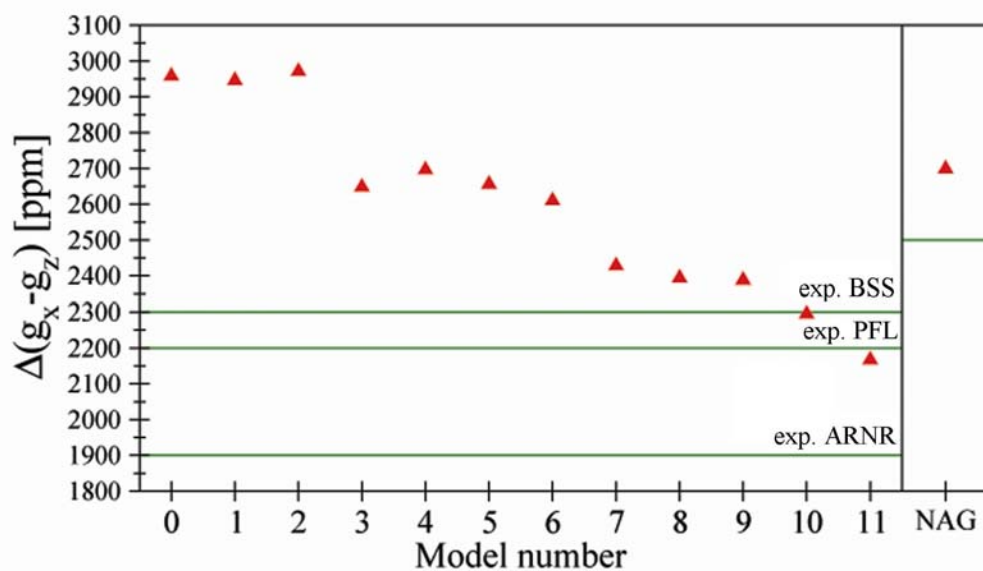


Figure 4.5.6 Comparison of computed and experimental differences between  $g$ -tensor components (in ppm) for various models of the CT conformer. a)  $\Delta(g_x - g_z)$ . b)  $\Delta(g_y - g_z)$ . In both cases, comparison of results for the best model for the CC-NAG $\cdot$  radical in an N-acetylglycine single crystal (taken from Chapter 4.4<sup>157</sup>) to experimental results is shown on the right side.

Keeping the overestimate of both  $g_x$  and  $g_y$  for NAG<sup>•</sup> at identical computational level in mind, we may compare the  $\Delta(g_x-g_z)$  and  $\Delta(g_y-g_z)$  differences in the protein sites to those obtained for the supermolecular model complexes (Figures 4.5.5 and 4.5.6). For example, considering the extended models with most pronounced hydrogen bonding, we arrive at  $\Delta(g_y-g_z)$  values of 1270 ppm and 1840 ppm for CC11 and CT11, respectively, and at  $\Delta(g_x-g_z)$  values of 2070 ppm for CC11 and 2170 ppm for CT11. Both differences for the CC11 model are thus already below the experimental values for PFL and BSS but still above ARNR (Figure 4.5.5). The same holds for the  $\Delta(g_x-g_z)$  difference computed for the CT11 model (it is very slightly below the PFL value, Figure 4.5.6a), whereas the computed  $\Delta(g_y-g_z)$  value for this most extensive model with CT conformation is safely above the “large” experimental values for PFL and BSS (Figure 4.5.6b).

It is tempting to attribute the differences between the *E. coli* ARNR data on one side and the PFL and BSS data on the other side to conformational effects. The glycyl radical in *E. coli* ARNR would thus be considered to have the most stable CC conformation, whereas the PFL and BSS data might be interpreted as arising from the CT conformation observed<sup>306,307</sup> also for the non-radical forms of the protein. A counter-argument is provided by the fact that even the computed  $\Delta(g_x-g_z)$  difference for the CT11 model is lower than the PFL and BSS data (Figure 4.5.6a). However, given the fact that this is the difference that is most affected by hydrogen bonding, it appears possible that the CT11 model exhibits too extensive hydrogen bonding to O1 compared to the protein environment. Models with less hydrogen bonding to O1 exhibit appreciably larger  $g_x$  values, whereas  $g_y$  is relatively unaffected (e.g. models CT7-CT9, Figure 4.5.6, Table 4.5.5). If we thus assume that the experimental differences between the  $g$ -tensors of the glycyl radical in *E. coli* ARNR on one side and in PFL or BSS on the other side are significant,<sup>291,312</sup> and that our present computational errors are similar as those found in the benchmark study on the structurally well-characterized N-acetylglycine single crystal (see Chapter 4.4<sup>157</sup>), we do indeed arrive at the conclusion that the radical in *E. coli* ARNR is in the CC conformation, and the radicals in PFL and BSS exist in the CT conformation. Such conformational differences are potentially significant also with respect to the mechanisms of these enzymes. In this context, it is particularly notable that  $H_\alpha$  in PFL

exchanges rapidly, whereas that in *E.coli* ARNR does not.<sup>284,285</sup> Moreover, the PFL radical exhibits more complex substructure in the EPR spectrum than the ARNR radical.<sup>284,285</sup> It will be interesting to see, if these differences arise indeed from a different conformation of the radical.

#### 4.5.3.8 $^1\text{H}_\alpha$ and $^{13}\text{C}_\alpha$ Hyperfine Tensors

Table 4.5.8 provides computed  $^1\text{H}_\alpha$  and  $^{13}\text{C}_\alpha$  hyperfine (HFC) tensors for all considered models of Gly $\bullet$ , together with available experimental hyperfine information for these nuclei in the three protein glycyl radicals. Earlier computational studies of the  $^1\text{H}_\alpha$ -HFC for different minima of the glycyl radical,<sup>150</sup> and our results for  $^1\text{H}_\alpha$ -HFC and  $^{13}\text{C}_\alpha$ -HFC of different minima of the NAG $\bullet$  radical (Chapter 4.4<sup>157</sup>), indicated negligible dependence on conformation. This is confirmed by the data in Table 4.5.8. Conformational effects on the isotropic HFCs are at most 1.1 G. In agreement with previous results,<sup>150</sup> extension of the peptide radical model has no effect on the isotropic HFCs for CC-Gly $\bullet$ , and only a relatively small one for CT-Gly $\bullet$  (ca. 0.5G). Slightly larger effects (ca. 1-2G) are computed for the extended model of CT-Gly $\bullet$  if the C-terminal peptide bond is kept planar. This is due to an increase of spin density on  $\text{C}_\alpha$ . Environmental effects on the HFCs depend characteristically on the conformer (Table 4.5.8): for CC-Gly $\bullet$ -based models, extensive intermolecular hydrogen bonding reduces the absolute values of the isotropic  $^1\text{H}_\alpha$  and  $^{13}\text{C}_\alpha$  HFCs by up to 1.3 G and 2.4 G, respectively. This reflects a reduction of spin density at  $\text{C}_\alpha$  by external hydrogen bonding (cf. Table 4.5.7). In CT-Gly $\bullet$ -based models, the spin density on  $\text{C}_\alpha$  varies much less with external hydrogen bonding (Table 4.5.7), and the changes in the HFCs are correspondingly less pronounced and less uniform. For CT-Gly $\bullet$ , the absolute  $^{13}\text{C}_\alpha$ -HFC in the more strongly hydrogen-bonded models tends to be lowered, whereas the  $^1\text{H}_\alpha$ -HFCs vary relatively little around the corresponding gas-phase models (Table 4.5.8). Variations in the largest components of both HFC-tensors may be from -3.5 G to +0.4 G. Given the experimental error bars (Table 4.5.8), this is not enough to provide detailed insight into structure or environment of the radical. Computed isotropic  $^{13}\text{C}_\alpha$ - and  $^1\text{H}_\alpha$ -HFCs tend to be in the range of experimental data for the protein glycyl radicals, once we consider also that out-of-plane vibration of  $\text{H}_\alpha$

is expected to decrease the  $^{13}\text{C}_\alpha\text{-HFC}$  by ca. 5 G and to increase the  $^1\text{H}_\alpha\text{-HFC}$  by about 3.4 G. The computed  $^{13}\text{C}_\alpha A_z$  components are also in the range of experimental data. Here the difference between the data for *E. coli* PFL and *E. coli* ARNR on one side and the larger value found for the bacteriophage T<sub>4</sub> ARNR on the other side appears to be significant. This has been addressed previously by conformational studies,<sup>296</sup> as will be discussed below.

Table 4.5.8  $^1\text{H}_\alpha$  and  $^{13}\text{C}_\alpha$  hyperfine coupling tensors (in Gauss) for gas-phase and supermolecular models of protein glycyl radical compared to experiment.<sup>a</sup>

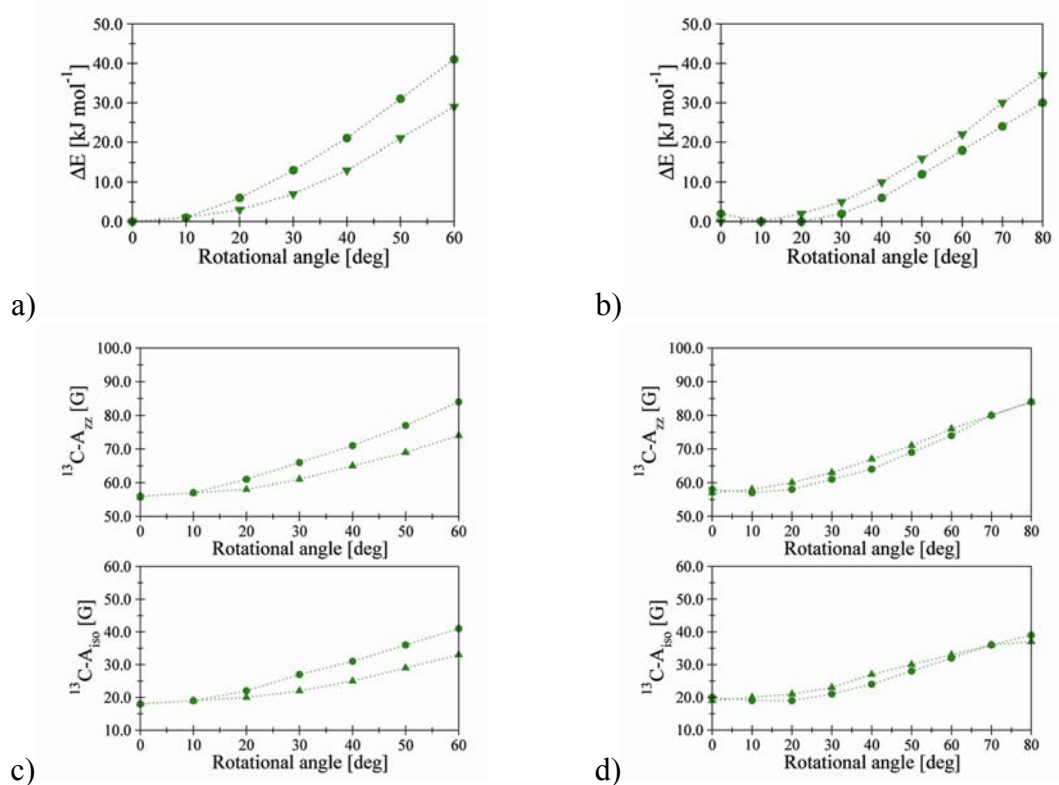
Model	$^1\text{H}_\alpha$				$^{13}\text{C}_\alpha$			
	$A_{iso}$	$A_x$	$A_y$	$A_z$	$A_{iso}$	$A_x$	$A_y$	$A_z$
CC-Gly $\bullet$	-17.1	-26.3	-7.2	-17.8	18.7	-0.5	0.1	56.5
CT-Gly $\bullet$	-16.6	-25.6	-6.7	-17.6	19.5	0.1	0.7	57.8
TC-Gly $\bullet$	-16.5	-25.9	-6.4	-17.2	18.4	-0.8	-0.3	56.2
TT-Gly $\bullet$	-16.0	-25.3	-5.8	-17.0	19.3	-0.2	0.3	57.9
ext. CC-Gly $\bullet$	-17.1	-26.4	-7.2	-17.8	18.6	-0.6	-0.1	56.0
ext. CT-Gly $\bullet$ (N-CH <sub>3</sub> )	-17.8	-27.5	-7.2	-18.7	22.1	1.1	1.8	63.4
ext. CT-Gly $\bullet$ (C-CH <sub>3</sub> )	-16.4	-25.3	-6.6	-17.3	18.8	-0.4	0.2	56.5
ext. CT-Gly $\bullet$	-17.0	-26.2	-6.8	-17.8	20.0	0.1	0.7	59.1
ext. CT-Gly $\bullet$ <sup>b</sup>	-17.8	-27.6	-7.2	-18.7	21.6	0.8	1.4	62.5
CC 1	-17.4	-26.7	-7.4	-18.1	19.4	-0.2	0.5	57.9
CC 2	-17.3	-26.6	-7.3	-18.1	19.2	-0.4	0.3	57.6
CC 3	-16.0	-24.5	-6.6	-16.8	16.7	-1.4	-0.8	52.3
CC 4	-17.6	-26.9	-7.6	-18.4	19.4	-0.4	0.3	58.1
CC 5	-17.5	-26.7	-7.6	-18.2	19.4	-0.3	0.4	58.0
CC 6	-16.9	-25.8	-7.1	-17.7	18.5	-0.7	-0.0	56.3
CC 7	-15.8	-24.3	-6.5	-16.7	16.4	-1.6	-1.1	51.9
CC 8	-16.2	-24.8	-6.7	-17.0	17.3	-1.2	-0.7	53.7
CC 9	-15.8	-24.3	-6.49	-16.7	16.6	-1.6	-1.0	52.3
CC 10	-15.7	-24.2	-6.47	-16.6	16.2	-1.7	-1.2	51.6
CC 11	-16.5	-25.0	-6.8	-17.1	17.9	-1.4	-0.8	53.8
CT 1	-17.0	-26.1	-7.0	-17.9	20.1	0.4	1.0	58.9
CT 2	-17.4	-26.4	-7.6	-18.3	19.9	0.3	0.9	58.3
CT 3	-16.6	-25.4	-6.7	-17.6	18.8	-0.4	0.2	56.8
CT 4	-16.4	-25.1	-6.8	-17.5	18.3	-0.7	-0.1	55.6
CT 5	-17.2	-26.3	-7.2	-18.2	20.3	0.4	1.0	59.4
CT 6	-17.4	-26.4	-7.4	-18.4	20.3	0.4	1.1	59.3
CT 7	-16.5	-25.3	-6.7	-17.6	18.2	-0.8	-0.2	55.7
CT 8	-16.6	-25.5	-6.7	-17.6	18.6	-0.7	-0.1	56.7
CT 9	-17.4	-26.3	-7.6	-18.4	19.0	-0.5	0.1	57.2
CT 10	-17.6	-26.6	-7.6	-18.5	19.2	-0.4	0.2	57.8
CT 11	-17.6	-26.7	-7.6	-18.6	19.5	-0.3	0.3	58.4
<i>E.coli</i> PFL <sup>c</sup>	15				16-21	ca. 1	ca. 2	49
<i>E.coli</i> RNR <sup>d</sup>	14-15				15-21	0-5	0-5	46-50
<i>T4</i> RNR <sup>e</sup>	14.4				-	-	-	ca. 66

<sup>a</sup> B3LYP/EPR-II/B3LYP/DZVP results. Cf. Figures 4.5.1-4.5.4 for the molecular models, and Table 4.5. 1 for structural data. The labels N-CH<sub>3</sub> and C-CH<sub>3</sub> correspond to addition of a methyl group on the N- and C-terminus, respectively. <sup>b</sup>The planarity of the N-terminal peptide moiety was enforced during optimization. <sup>c</sup>Ref 285. <sup>d</sup>Ref 282. <sup>e</sup>Ref 283.



## 4.5.3.9 Effects of Out-of-Plane Twisting

Based on DFT calculations of energy and hyperfine profiles for rotation around the  $C_\alpha$ - $C_1$  and  $C_\alpha$ - $N_1$  bonds, Himo et al.<sup>296</sup> suggested non-planarity of the radical unit as possible explanation for the much larger  $A_z(^{13}C_\alpha)$  value (see above and Table 4.5.8) of bacteriophage T<sub>4</sub> ARNR compared to *E. coli* RNR and PFL. A scan of the two relevant dihedral angles in steps of 10° was carried out for the CC-Gly<sup>•</sup> model (without reoptimization of the molecule), and the dependencies of energies and HFC constants ( $A_z(^{13}C_\alpha)$ ,  $A_{iso}(H_\alpha)$ ) were plotted.<sup>296</sup> We have performed similar scans, albeit with full reoptimization of the system at each step and not only for the CC conformer of Gly<sup>•</sup> but also for the CT conformer, and we have additionally studied the dependence of  $\Delta g_x$  and  $\Delta g_y$  on the rotations (Figure 4.5.7). We concentrate only on the conformational space within 60° from the CC and CT conformers. This corresponds to an energy window of about 30-40 kJ mol<sup>-1</sup> above the respective minima.



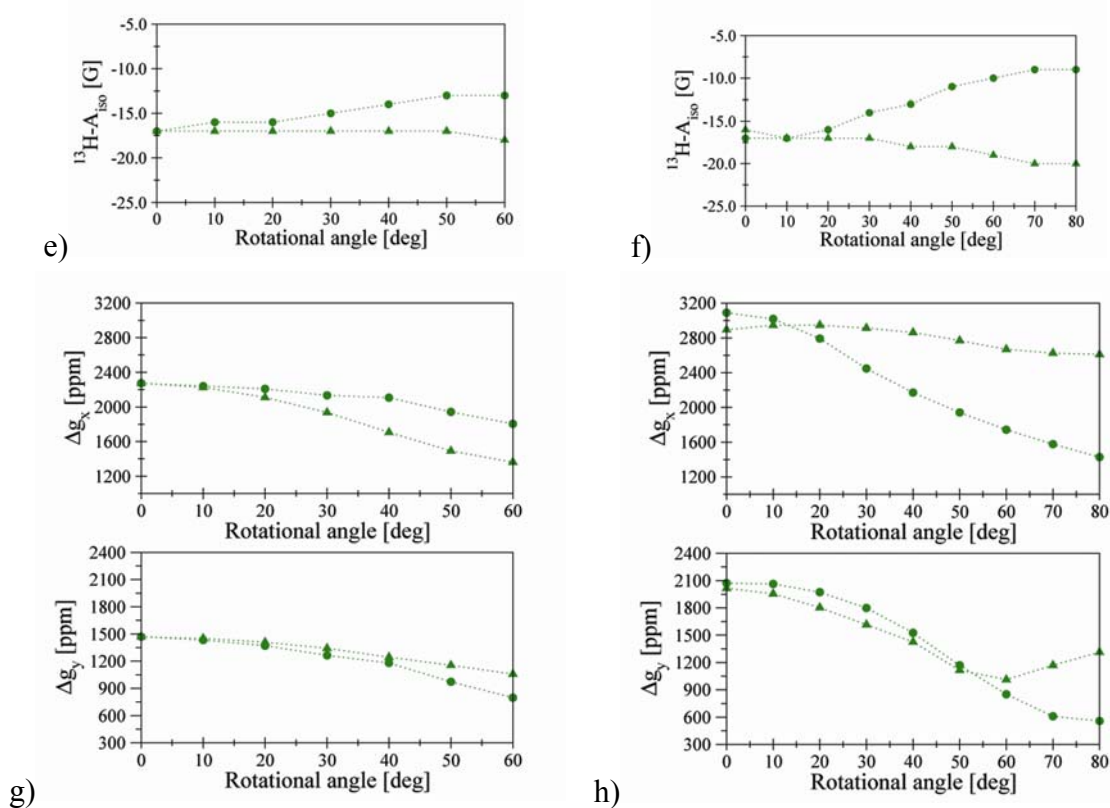


Figure 4.5.7 Dependence of  $\Delta g_x$  and  $\Delta g_y$  on rotations around  $C_\alpha$ -C1 (●) and around  $C_\alpha$ -N1 (▲). a)  $\Delta E$  - CC-Gly•, b)  $\Delta E$  - CT-Gly•, c)  $A_{zz}(^{13}C_\alpha)$  and  $A_{iso}(^{13}C_\alpha)$  - CC-Gly•, d)  $A_{zz}(^{13}C_\alpha)$  and  $A_{iso}(^{13}C_\alpha)$  - CT-Gly•, e)  $A_{iso}(^{13}H_\alpha)$  - CC-Gly•, f)  $A_{iso}(^{13}H_\alpha)$  - CT-Gly•, g) CC-Gly• and h) CT-Gly•.

Out-of-plane rotation interrupts the delocalization of the unpaired spin throughout the radical and thus enhances the spin density on  $C_\alpha$ . This increases the HFC on  $C_\alpha$ , in particular the  $A_z$  component, as found already by Himo and Eriksson.<sup>296</sup> Our own calculations, using the B3LYP/EPR-II//B3LYP/DZVP level (cf. Figure 4.5.7c,d), confirm their results and agree that an out-of-plane rotation might explain the larger  $A_z(^{13}C_\alpha)$  value for the T<sub>4</sub> ARNR radical compared to the other spectra, while affecting the  $^1H_\alpha$  HFC much more moderately (Figure 4.5.7e,f).

At the same time, the spin density on the carbonyl oxygen atoms decreases, and so do the in-plane g-shift components (Figure 4.5.7g,h). This holds for rotations about

both relevant dihedral angles. The decrease is more pronounced for the CT conformer (which lacks the  $H_{\beta} \cdots O1$  hydrogen bond, see above) than for the CC conformer, especially for rotation around the  $C_{\alpha}$ - $C_1$  bond.

#### 4.5.4 Conclusions

The study presented in this chapter provides an unprecedentedly detailed picture of the interrelations between structure and environment of protein glycyl radicals and their spin density and EPR parameters. In particular, the appreciable challenge of accurately predicting electronic  $g$ -tensors for glycyl radicals by DFT methods has been met. This was made possible by a benchmark study for the structurally well-characterized case of an N-acetylglycyl radical (NAG $\bullet$ ) presented in Chapter 4.4.<sup>157</sup> The latter provides an important anchor point to judge the accuracy of our computed  $g$ -tensors for protein-based glycyl radicals. In both cases, we have studied in detail the challenging dependence of the computed very small  $g$ -anisotropies on the level of structure optimization, on spin-orbit operators and gauge of magnetic vector potential, and on conformation and intermolecular interactions.

Due to the presence of weak intramolecular hydrogen bonds, the single most important aspect determining the  $g$ -tensor of a glycyl radical is its conformation, followed by more moderate effects of external hydrogen bonds. Except for the notion of an essentially planar radical for most of the experimentally observed protein glycyl radicals (except for the  $T_4$  ARNR,<sup>296</sup> see above), both the conformation and the protein environment of the radicals have been essentially unknown. The detailed analysis of computed  $g$ -tensors for various conformations and for a large variety of hydrogen-bonded supermolecular model complexes (cf. ref 155 for a similar study of supermolecular models to unravel the protein environment for a ubisemiquinone radical anion in the  $Q_H$  site of quinol oxidase) lets us suggest that the different  $g$ -tensors for the glycyl radicals in *E.coli* ARNR on one side and of PFL and BSS on the other side may be due to a different conformation: cis-cis for the former case and cis-trans for the two latter cases (combined with only moderate hydrogen bonding to oxygen O1). This conclusion is based to a great extent on the calibration of the computational model for the N-acetylglycine single crystal presented in Chapter 4.4.<sup>157</sup> Our observation may be significant in the context of enzymatic mechanisms,

and of differences between chemical and spectroscopical characteristics found for the PFL and ARNR radicals (see above). Detailed analyses of spin-density distributions and of atomic spin-orbit contributions to the  $g$ -tensors have provided further insight that improved our understanding of the various subtle aspects that affect the small  $g$ -anisotropy of a glycyl radical.

## 5 Summary and Outlook

Electron paramagnetic resonance (EPR) techniques are probably the most important analytical tools for investigations of the structures and properties of organic  $\pi$ -radicals in biological systems. The spectral parameters obtainable from experiment, the  $g$ -tensor and the hyperfine coupling constants ( $A$ -tensors), provide indirect knowledge on the structure of radicals. However, the information held by them can be quite complex and difficult to infer directly from the experimental spectra. For difficult cases, the detailed theoretical analysis can determine the electronic and geometric structure of radicals starting from their spectral properties and additionally can provide detailed descriptions of various effects determining the observed spectral parameters.

In this work we present several application studies which show the accuracy and capability of density functional (DFT) method for the calculation of EPR parameters, as implemented into our ReSpect-MAG computer program,<sup>50</sup> in addressing problems of biological relevance. Primarily we have focused on calculations of  $g$ -tensors, but the hyperfine-tensor calculations were crucial for the final conclusions of Chapter 4.2 and relevant for studies reported in Chapter 4.5.

In earlier reported studies, our DFT method provided remarkably accurate  $g$ -tensors for a number of organic  $\pi$ -radicals: (i) semiquinone radical anions *in vitro*,<sup>51</sup> and (ii) tyrosyl<sup>45</sup> and modified tyrosyl radicals.<sup>125</sup> In this work we have studied  $g$ - and  $A$ -tensors of two different types of bioradicals in their protein environments: (i) cofactor-based semiquinone radicals and (ii) amino-acid-based glycy radical. Firstly, we validated the methodology for each type of radicals on structurally- and spectroscopically-well characterized cases: (i) semiquinone anion radicals in the  $Q_A$  and  $Q_B$  binding sites of the photosynthetic reaction centers of purple bacteria and in the  $A_1$  ( $Q_K$ ) binding site of PS-I (Chapter 4.1); and (ii) N-acetylglycyl radical in the environment of a single crystal of N-acetylglycine (Chapter 4.3). In the former calculations, accurate  $g$ -tensors were obtained using the efficient one-electron mean-field approximation (AMFI) to the spin-orbit (SO) matrix elements. The latter

calculations turned out to be much more demanding and required the expensive exact treatment of SO matrix elements, increasing the costs of the calculations. Secondly, we have applied the well-established methodology to specific problems of biological relevance. In Chapter 4.2 we have studied  $g$ - and  $A$ -tensors for a number of model structures of ubisemiquinone anion radicals in hydrogen-bonding frameworks. Based on the detailed comparison of the computed and experimental data a model with two hydrogen bonds to O<sub>1</sub> and one hydrogen bond to O<sub>4</sub> was suggested for the Q<sub>H</sub> binding site of ubiquinol oxidase (QOX). In Chapter 4.5 systematic studies of various models of protein-derived glycy radical have been reported. Environmental effects due to hydrogen bonding were shown to be complicated and to depend in a subtle fashion on the different intramolecular hydrogen bonding for different conformations of the radical. The conformation was calculated to have the largest overall effect on the computed  $g$ -tensors (less so on the hyperfine tensors). The comparison of calculated  $g$ -tensors and these obtained in recent high-field EPR measurements suggested that the glycy radical observed in *E.coli* anaerobic ribonucleotide reductase (RNR) has a fully extended conformation, which differs from those of the corresponding radicals in pyruvate formate-lyase (PFL) or benzylsuccinate synthase (BSS). A project inspired by studies on intramolecular interactions between semiquinone radical anions and a tryptophane residue in the A<sub>1</sub> binding site of PS-I<sup>174</sup> is reported in Chapter 4.3. Based on quantum-chemical calculations we have designed small rotational molecular motors made up from intramolecularly connected dyads consisting of a quinone unit and a pyrrole or indole moiety. A reduction of the quinone to the semiquinone radical anion or quinolate dianion states leads to a reversible intramolecular reorientation from a  $\pi$ -stacked to a T-stacked arrangement. EPR spectroscopy is proposed as the technique of choice for confirming the structure of newly-designed molecular devices once these will be synthesized.

The studies presented in this work emphasize the accuracy and efficiency of our DFT methods for calculations of  $g$ - and  $A$ -tensors. The ability of the method to treat relatively large radical systems allows future applications to systems like, e.g.: flavins, pyrroloquinolino quinones or bacteriopheophytin radical anions.

All the calculations presented in this thesis were carried out for static structural models. The close investigation of the influence of motional effects on the EPR parameters should be considered in addition. Recently in our laboratory, the Car-

Parrinello molecular dynamics method has been used for studies of benzoquinone in aqueous solution; *g*- and *A*-tensor calculations were performed at selected snapshots from molecular dynamics trajectories.<sup>159,160</sup>





## 6 Bibliography

- (1) Weltner, W., Jr. *Magnetic Atoms and Molecules*; Von Nostrand: New York, 1983; 422 pp.
- (2) Weil, J. A.; Bolton, J. R.; Wertz, J. E. *Electron Paramagnetic Resonance: Elementary Theory and Practical Applications*; Wiley&Sons: New York, 1994.
- (3) Harriman, J. E. *Theoretical Foundations of Electron Spin Resonance*; Academic Press: New York, 1978.
- (4) Feller, D.; Davidson, E. R., *J. Chem. Phys.* **1984**, *80*, 1006-1017.
- (5) Feller, D.; Davidson, E. R., *J. Chem. Phys.* **1988**, *88*, 7580-7587.
- (6) Feller, D.; Davidson, E. R., *Theor. Chim. Acta* **1985**, *68*, 57-67.
- (7) Feller, D.; Davidson, E. R., *Theoretical approaches to ESR spectroscopy*; In *Theoretical Models of Chemical Bonding*; Maksic, Z. B., Ed.; Springer: Berlin, Germany, 1991; Vol. 3, pp 429-455.
- (8) Chipman, D. M., *Theor. Chim. Acta* **1992**, *82*, 93-115.
- (9) Chipman, D. M., *J. Chem. Phys.* **1983**, *78*, 3112-3132.
- (10) Carmichael, I., *J. Phys. Chem.* **1989**, *93*, 190-193.
- (11) Carmichael, I., *J. Phys. Chem.* **1990**, *94*, 5734-5740.
- (12) Lunell, S.; Eriksson, L. A.; Huang, M. B., *THEOCHEM* **1991**, *76*, 263-286.
- (13) Lunell, S.; Eriksson, L. A.; Worstbrock, L., *J. Am. Chem. Soc.* **1991**, *113*, 7508-7512.
- (14) Lunell, S.; Huang, M., *J. Chem. Soc., Chem. Commun.* **1989**, 1031-1033.
- (15) Huang, M. B.; Lunell, S., *Chem. Phys.* **1990**, *147*, 85-90.
- (16) Lunell, S.; Eriksson, L. A.; Faengstroem, T.; Maruani, J.; Sjoqvist, L.; Lund, A., *Chem. Phys.* **1993**, *171*, 119-131.
- (17) Chipman, D. M., *Theor. Chim. Acta* **1989**, *76*, 73-84.
- (18) Engels, B., *Chem. Phys. Lett.* **1991**, *179*, 398-404.
- (19) Engels, B.; Peyerimhoff, S. D., *Mol. Phys.* **1989**, *67*, 583-600.
- (20) Karna, S. P.; Grein, F.; Engels, B.; Peyerimhoff, S. D., *Int. J. Quantum Chem.* **1989**, *36*, 255-263.
- (21) Karna, S. P.; Grein, F.; Engels, B.; Peyerimhoff, S. D., *Mol. Phys.* **1990**, *69*, 549-557.
- (22) Engels, B.; Eriksson, L. A.; Lunell, S., *Adv. Quantum Chem.* **1996**, *27*, 297-369.
- (23) Sekino, H.; Bartlett, R. J., *J. Chem. Phys.* **1985**, *82*, 4225-4229.
- (24) Perera, S. A.; Watts, J. D.; Bartlett, R. J., *J. Chem. Phys.* **1994**, *100*, 1425-1434.
- (25) Ishii, N.; Shimizu, T., *Physical Review A: Atomic, Molecular, and Optical Physics* **1993**, *48*, 1691-1694.
- (26) Barone, V.; Adamo, C.; Russo, N., *Chem. Phys. Lett.* **1993**, *212*, 5-11.
- (27) Malkin, V. G.; Malkina, O. L.; Eriksson, L. A.; Salahub, D. R., *The calculation of NMR and ESR spectroscopy parameters using density functional theory*; In *Theoretical and Computational Chemistry*; Seminario, J. M., Politzer, P., Eds.; Elsevier: Amsterdam, 1995; Vol. 2, pp 273-347.
- (28) Stone, A. J., *Mol. Phys.* **1963**, *6*, 509-515.
- (29) Stone, A. J., *Proc. Roy. Soc. A* **1963**, *271*, 424-434.

- (30) Moores, W. H.; McWeeny, R., *Proc. R. Soc. London, Ser. A* **1973**, 332, 365-384.
- (31) Case, D. A.; Karplus, M., *J. Am. Chem. Soc.* **1977**, 99, 6182-6194.
- (32) Geurts, P. J. M.; Bouten, P. C. P.; Van der Avoird, A., *J. Chem. Phys.* **1980**, 73, 1306-1312.
- (33) Lushington, G. H.; Grein, F., *Theor. Chim. Acta* **1996**, 93, 259-267.
- (34) Bruna, P. J.; Lushington, G. H.; Grein, F., *Chem. Phys.* **1997**, 225, 1-15.
- (35) Lushington, G. H.; Grein, F., *Int. J. Quantum Chem.* **1996**, 60, 467-472.
- (36) Lushington, G. H.; Grein, F., *J. Chem. Phys.* **1997**, 106, 3292-3300.
- (37) Vahtras, O.; Minaev, B.; Ågren, H., *Chem. Phys. Lett.* **1997**, 281, 186-192.
- (38) Engström, M.; Minaev, B.; Vahtras, O.; Ågren, H., *Chem. Phys.* **1998**, 237, 149-158.
- (39) Engström, M.; Vahtras, O.; Ågren, H., *Chem. Phys.* **1999**, 243, 263-271.
- (40) Engström, M.; Himo, F.; Ågren, H., *Chem. Phys. Lett.* **2000**, 319, 191-196.
- (41) Engström, M.; Owenius, R.; Vahtras, O., *Chem. Phys. Lett.* **2001**, 338, 407-413.
- (42) Schreckenbach, G.; Ziegler, T., *J. Phys. Chem. A* **1997**, 101, 3388-3399.
- (43) Schreckenbach, G.; Ziegler, T., *Theor. Chem. Acc.* **1998**, 99, 71-82.
- (44) Patchkovskii, S.; Ziegler, T., *J. Phys. Chem. A* **2001**, 105, 5490-5497.
- (45) Malkina, O. L.; Vaara, J.; Schimmelpfennig, B.; Munzarova, M.; Malkin, V. G.; Kaupp, M., *J. Am. Chem. Soc.* **2000**, 122, 9206-9218.
- (46) Neese, F., *J. Chem. Phys.* **2001**, 115, 11080-11096.
- (47) van Lenthe, E.; Wormer, P. E. S.; van der Avoird, A., *J. Chem. Phys.* **1997**, 107, 2488-2498.
- (48) Neyman, K. M.; Ganyushin, D. I.; Matveev, A. V.; Nasluzov, V. A., *J. Phys. Chem. A* **2002**, 106, 5022-5030.
- (49) Kaupp, M.; Bühl, M.; Malkin, V. G.; Editors *Calculation of NMR and EPR Parameters: Theory and Applications*; Wiley-VCH: Weinheim, Germany, 2004; 603 pp.
- (50) Malkin, V. G.; Malkina, O. L.; Reviakine, R.; Arbuznikov, A. V.; Kaupp, M.; Schimmelpfennig, B.; Malkin, I.; Helgaker, T.; Ruud, K. *MAG-ReSpect*, "version 1.1"; 2003.
- (51) Kaupp, M.; Remenyi, C.; Vaara, J.; Malkina, O. L.; Malkin, V. G., *J. Am. Chem. Soc.* **2002**, 124, 2709-2722.
- (52) Stubbe, J.; van der Donk, W. A., *Chemical Reviews (Washington, D. C.)* **1998**, 98, 705-762.
- (53) Deisenhofer, J.; Norris, J. R. *The Photosynthetic Reaction Center*; Academic Press: San Diego, 1993.
- (54) Möbius, K., *High-field EPR and ENDOR on bioorganic systems*; In *Biological Magnetic Resonance*; Berliner, L. J., Reuben, J., Eds.; Plenum Press: New York, 1993; Vol. 13, pp 253-274.
- (55) Prisner, T. F., *Pulsed high-frequency/high-field EPR*; In *Advances in Magnetic and Optical Resonance*; Warren, W., Ed.; Academic Press: New York, 1997; Vol. 20, pp 245-299.
- (56) Blankenship, R. E. *Molecular Mechanisms of Photosynthesis*; Blackwell Science: Oxford, UK, 2002.
- (57) Szabo, A.; Ostlund, N. S. *Modern Quantum Chemistry: Introduction to Advanced Electronic Structure Theory.*; Dover Publications: New York, 1996; 466 pp.

- (58) Jensen, F. *Introduction to Computational Chemistry*; Wiley & Sons Ltd.: Chichester, 1999.
- (59) Cramer, C. J. *Essentials of Computational Chemistry: Theories and Models*; John Wiley & Sons: 2002; 562 pp.
- (60) Koch, W.; Holthausen, M. C. *A Chemist's Guide to Density Functional Theory, 2nd Edition*; John Wiley & Sons: Chichester, UK, 2001; 528 pp.
- (61) Pyykkö, P., *Chem. Rev.* **1988**, *88*, 563-594.
- (62) Kobus, J., *Adv. Quantum Chem.* **1997**, *28*, 1-14.
- (63) Cizek, J., *J. Chem. Phys.* **1966**, *45*, 4256-4266.
- (64) Purvis, G. D.; Bartlett, R. J., *J. Chem. Phys.* **1982**, *76*, 1910-1918.
- (65) Watts, J. D.; Bartlett, R. J., *International Journal of Quantum Chemistry, Quantum Chemistry Symposium* **1993**, *27*, 51-66.
- (66) Raghavachari, K.; Trucks, G. W.; Pople, J. A.; Head-Gordon, M., *Chem. Phys. Lett.* **1989**, *157*, 479-483.
- (67) Møller, C.; Plesset, M. S., *Phys. Rev.* **1934**, *46*, 618-622.
- (68) Bartlett, R. J., *Annu. Rev. Phys. Chem.* **1981**, *32*, 359-401.
- (69) Parr, R. G.; Yang, W. *Density-functional Theory of Atoms and Molecules*; Oxford University Press: Oxford, 1989; 333 pp.
- (70) Parr, R. G.; Yang, W., *Annu. Rev. Phys. Chem.* **1995**, *46*, 701-728.
- (71) Hohenberg, P.; Kohn, W., *Phys. Rev.* **1964**, *136*, 864.
- (72) Kohn, W.; Sham, L. J., *Phys. Rev.* **1965**, *140*, 1133A.
- (73) Perdew, J. P.; Burke, K., *Int. J. Quantum Chem.* **1996**, *57*, 309-319.
- (74) Adamo, C.; Di Matteo, A.; Barone, V., *Adv. Quantum Chem.* **1999**, *36*, 45-75.
- (75) Slater, J. C., *Phys. Rev.* **1951**, *81*, 385-390.
- (76) Ceperley, D. M.; Alder, B. J., *Phys. Rev. Lett.* **1980**, *45*, 566-569.
- (77) Vosko, S. H.; Wilk, L.; Nusair, M., *Can. J. Phys.* **1980**, *58*, 1200-1211.
- (78) Becke, A. D., *Phys. Rev. A* **1988**, *38*, 3098-3100.
- (79) Becke, A. D., *J. Chem. Phys.* **1986**, *84*, 4524-4529.
- (80) Perdew, J. P., *Phys. Rev. B* **1986**, *33*, 8822-8824.
- (81) Perdew, J. P.; Burke, K.; Ernzerhof, M., *Phys. Rev. Lett.* **1996**, *77*, 3865-3868.
- (82) Perdew, J. P.; Chevary, J. A.; Vosko, S. H.; Jackson, K. A.; Pederson, M. R.; Singh, D. J.; Fiolhais, C., *Phys. Rev. B* **1992**, *46*, 6671-6687.
- (83) Lee, C.; Yang, W.; Parr, R. G., *Phys. Rev. B* **1988**, *37*, 785-789.
- (84) Perdew, J. P.; Ruzsinszky, A.; Tao, J.; Staroverov, V. N.; Scuseria, G. E.; Csonka, G. I., *J. Chem. Phys.* **2005**, *123*, 062201-062209.
- (85) Becke, A. D., *J. Chem. Phys.* **1993**, *98*, 1372-1377.
- (86) Becke, A. D., *J. Chem. Phys.* **1993**, *98*, 5648-5652.
- (87) Miehlich, B.; Savin, A.; Stoll, H.; Preuss, H., *Chem. Phys. Lett.* **1989**, *157*, 200-206.
- (88) Arbuznikov, A. V.; Kaupp, M., *Chem. Phys. Lett.* **2004**, *386*, 8-16.
- (89) Arbuznikov, A. V.; Kaupp, M., *Chem. Phys. Lett.* **2004**, *391*, 16-21.
- (90) Hieringer, W.; Della Sala, F.; Gorling, A., *Chem. Phys. Lett.* **2004**, *383*, 115-121.
- (91) Teale, A. M.; Tozer, D. J., *Chem. Phys. Lett.* **2004**, *383*, 109-114.
- (92) Della Sala, F.; Gorling, A., *J. Chem. Phys.* **2001**, *115*, 5718-5732.
- (93) Gritsenko, O. V.; Baerends, E. J., *Phys. Rev. A* **2001**, *64*, 0425061-04250612.
- (94) Sharp, R. T.; Horton, G. K., *Phys. Rev.* **1953**, *90*, 317.
- (95) Talman, J. D.; Shadwick, W. F., *Phys. Rev. A* **1976**, *14*, 36-40.

- (96) Neese, F.; Munzarova, M. L., *Historical aspects of EPR parameter calculations*; In *Calculation of NMR and EPR Parameters*; Kaupp, M., Bühl, M., Malkin, V. G., Eds.; Wiley-VCH: Weinheim, Germany, 2004; pp 21-32.
- (97) Meyer, W., *J. Chem. Phys.* **1969**, *51*, 5149-5162.
- (98) Weber, J.; Goursot, A.; Penigault, E.; Ammeter, J. H.; Bachmann, J., *J. Am. Chem. Soc.* **1982**, *104*, 1491-1506.
- (99) Salahub, D. R.; Fournier, R.; Mlynarski, P.; Papai, I.; St-Amant, A.; Ushio, J. *Density Functional Methods in Chemistry*; Labanowski, J., Andzelm, J., Eds.; Springer: New York, 1991.
- (100) McWeeny, R. *Methods of Molecular Quantum Mechanics*; Academic Press: London, 1996.
- (101) Moos, R. E. *Advanced molecular quantum mechanics; an introduction to relativistic quantum mechanics and the quantum theory of radiation*; Chapman and Hall: London, 1973.
- (102) Pyykkö, P., *Chem. Phys.* **1977**, *22*, 289-296.
- (103) Pyykkö, P.; Wiesenfeld, L., *Mol. Phys.* **1981**, *43*, 557-580.
- (104) Pyykkö, P.; Görling, A.; Rösch, N., *Mol. Phys.* **1987**, *61*, 195-205.
- (105) Kaupp, M., *Ab Initio and Density Functional Calculations of Electronic g-Tensors for Organic Radicals*; In *EPR Spectroscopy of Free Radicals in Solids. Trends in Methods and Applications.*; Lund, A., Shiotani, M., Eds.; Kluwer: Dordrecht, 2003; pp 267-302.
- (106) Kaupp, M.; Reviakine, R.; Malkina, O. L.; Arbuznikov, A.; Schimmelpfennig, B.; Malkin, V. G., *J. Comput. Chem.* **2002**, *23*, 794-803.
- (107) Patchkovskii, S.; Ziegler, T., *J. Chem. Phys.* **1999**, *111*, 5730-5740.
- (108) Arbuznikov, A. V.; Kaupp, M.; Malkin, V. G.; Reviakine, R.; Malkina, O. L., *Phys. Chem. Chem. Phys.* **2002**, *4*, 5467-5474.
- (109) Eriksson, L. A.; Himo, F., *Trends in Physical Chemistry* **1997**, *6*, 153-170.
- (110) Adamo, C.; Barone, V.; Fortunelli, A., *J. Chem. Phys.* **1995**, *102*, 384-393.
- (111) Eriksson, L. A. *Density-functional Methods in Chemistry and Materials Science*; Springborg, M., Ed.; Wiley&Sons: New York, 1997; 125.
- (112) Colwell, S. M.; Handy, N. C., *Chem. Phys. Lett.* **1993**, *217*, 271-278.
- (113) Vignale, G.; Rasolt, M., *Phys. Rev. Lett.* **1987**, *59*, 2360-2363.
- (114) Rajagopal, A. K.; Callaway, J., *Physical Review B: Solid State* **1973**, *7*, 1912-1919.
- (115) Hess, B. A.; Marian, C. M.; Wahlgren, U.; Gropen, O., *Chem. Phys. Lett.* **1996**, *251*, 365-371.
- (116) Schimmelpfennig, B. *Atomic Spin-Orbit Mean-Field Integral Program*, Stockholms Universitet, Stockholm, Sweden, 1996.
- (117) Koseki, S.; Schmidt, M. W.; Gordon, M. S., *J. Phys. Chem.* **1992**, *96*, 10768-10772.
- (118) Vaara, J.; Malkina, O. L.; Stoll, H.; Malkin, V. G.; Kaupp, M., *J. Chem. Phys.* **2001**, *114*, 61-71.
- (119) Ditchfield, R., *Mol. Phys.* **1974**, *27*, 789-807.
- (120) Wolinski, K.; Hinton, J. F.; Pulay, P., *J. Am. Chem. Soc.* **1990**, *112*, 8251-8260.
- (121) Kutzelnigg, W.; Fleischer, U.; Schindler, M., In *NMR-Basic Principles and Progress*; Springer: Hedelberg, 1990; Vol. 23, pp 165-262.
- (122) Lushington, G. H.; Bündgen, P.; Grein, F., *Int. J. Quantum Chem.* **1995**, *55*, 377-392.
- (123) Lushington, G. H., *J. Phys. Chem. A* **2000**, *104*, 2969-2974.

- (124) Jayatilaka, D., *J. Chem. Phys.* **1998**, *108*, 7587-7594.
- (125) Kaupp, M.; Gress, T.; Reviakine, R.; Malkina, O. L.; Malkin, V. G., *J. Phys. Chem. B* **2003**, *107*, 331-337.
- (126) *CRC handbook of EPR spectra from quinones and quinols*; Jens A. Pedersen CRC Press, Boca Raton: Florida, 1985.
- (127) Ortiz de Montellano, P. R. *Cytochrome P-450: Structure, Mechanism, and Biochemistry*; Ortiz de Montellano, P. R., Ed.; Plenum Press: New York, 1986; 556.
- (128) Davidson, V. L. *Principles and Applications of Quinoproteins*; Davidson, V. L., Ed.; M. Dekker: New York, 1993; 453.
- (129) Eichhorn, G. L.; Marzilli, L. G. *Advances in Inorganic Biochemistry, Heme Proteins*; Eichhorn, G. L., Marzilli, L. G., Eds.; Elsevier: New York, 1988; 271 pp.
- (130) *Advances in Photosynthesis, Oxygenic Photosynthesis: The Light Reactions*; Ort, D. R., Yocum, C. F., Eds.; Kluwer Academic Publishers: Dordrecht, 1996.
- (131) Hoff, A. J.; Deisenhofer, J., *Phys. Rep.* **1997**, *287*, 1-247.
- (132) *Coenzyme Q: Biochemistry, Bioenergetics, and Clinical Applications of Ubiquinone*, Lenaz, G., Ed.; John Wiley & Sons: New York, 1985.
- (133) Gilbert, B. C.; Davies, M. J.; Murphy, D. M. *Electron Paramagnetic Resonance, Volume 19*; Royal Society of Chemistry: Cambridge, UK, 2004.
- (134) *Advanced EPR. Applications in Biology and Biochemistry*; Hoff, A. J., Ed.; Elsevier: Amsterdam, 1989.
- (135) Möbius, K.; Savitsky, A.; Wegener, C.; Plato, M.; Fuchs, M.; Schnegg, A.; Dubinskii, A. A.; Grishin, Y. A.; Grigor'ev, I. A.; Kuehn, M.; Duche, D.; Zimmermann, H.; Steinhoff, H. J., *Magn. Reson. Chem.* **2005**, *43*, S4-S19.
- (136) McConnell, H. M., *J. Chem. Phys.* **1956**, *24*, 764-766.
- (137) McConnell, H. M., *J. Chem. Phys.* **1958**, *28*, 1188-1192.
- (138) McConnell, H. M.; Chesnut, D. B., *J. Chem. Phys.* **1958**, *28*, 107-117.
- (139) Heller, C.; McConnell, H. M., *J. Chem. Phys.* **1960**, *32*, 1535-1539.
- (140) Babcock, G. T.; Espe, M.; Hoganson, C.; Lydakis-Simantiris, N.; McCracken, J.; Shi, W.; Styring, S.; Tommos, C.; Warncke, K., *Acta Chem. Scand.* **1997**, *51*, 533-540.
- (141) O'Malley, P. J., *J. Phys. Chem. A* **1997**, *101*, 6334-6338.
- (142) O'Malley, P. J., *Chem. Phys. Lett.* **1998**, *285*, 99-104.
- (143) O'Malley, P. J., *J. Phys. Chem. A* **1998**, *102*, 248-253.
- (144) O'Malley, P. J., *J. Am. Chem. Soc.* **1998**, *120*, 5093-5097.
- (145) O'Malley, P. J., *Biochim. Biophys. Acta* **1999**, *1411*, 101-113.
- (146) Langgard, M.; Spanget-Larsen, J., *THEOCHEM* **1998**, *431*, 173-180.
- (147) Chipman, D. M., *J. Phys. Chem. A* **2000**, *104*, 11816-11821.
- (148) Eriksson, L. A.; Himo, F.; Siegbahn, P. E. M.; Babcock, G. T., *J. Phys. Chem. A* **1997**, *101*, 9496-9504.
- (149) Sinnecker, S.; Reijerse, E.; Neese, F.; Lubitz, W., *J. Am. Chem. Soc.* **2004**, *126*, 3280-3290.
- (150) Barone, V.; Adamo, C.; Grand, A.; Jolibois, F.; Brunel, Y.; Subra, R., *J. Am. Chem. Soc.* **1995**, *117*, 12618-12624.
- (151) Barone, V.; Adamo, C.; Grand, A.; Brunel, Y.; Fontecave, M.; Subra, R., *J. Am. Chem. Soc.* **1995**, *117*, 1083-1089.
- (152) Improta, R.; Barone, V., *Chemical Reviews (Washington, DC, United States)* **2004**, *104*, 1231-1253.
- (153) Kacprzak, S.; Kaupp, M., *J. Phys. Chem. B* **2004**, *108*, 2464-2469.

- (154) Kacprzak, S.; Kaupp, M., *J. Phys. Chem. B* **2006**, *110*, 8158-8165.
- (155) Kacprzak, S.; Kaupp, M.; MacMillan, F., *J. Am. Chem. Soc.* **2006**, *128*, 5659-5671.
- (156) Kacprzak, S.; Reviakine, R.; Kaupp, M., **2006**, submitted to *J. Am. Chem. Soc.*
- (157) Kacprzak, S.; Reviakine, R.; Kaupp, M., **2006**, submitted to *J. Am. Chem. Soc.*
- (158) Asher, J. R.; Kaupp, M., **2006**, submitted to *Chem. Phys. Chem.*
- (159) Asher, J. R.; Doltsinis, N. L.; Kaupp, M., *Magn. Reson. Chem.* **2005**, *43*, S237-S247.
- (160) Asher, J. R.; Doltsinis, N. L.; Kaupp, M., *J. Am. Chem. Soc.* **2004**, *126*, 9854-9861.
- (161) Ciofini, I.; Adamo, C.; Barone, V., *J. Chem. Phys.* **2004**, *121*, 6710-6718.
- (162) Un, S., *Magn. Reson. Chem.* **2005**, *43*, S229-S236.
- (163) Benisvy, L.; Bittl, R.; Bothe, E.; Garner, C. D.; McMaster, J.; Ross, S.; Teutloff, C.; Neese, F., *Angew. Chem. Int. Ed.* **2005**, *44*, 5314-5317.
- (164) Fuchs, M. R.; Schleicher, E.; Schnegg, A.; Kay, C. W. M.; Toerring, J. T.; Bittl, R.; Bacher, A.; Richter, G.; Möbius, K.; Weber, S., *J. Phys. Chem. B* **2002**, *106*, 8885-8890.
- (165) Möbius, K., *Biological Magnetic Resonance*; Berliner, L. J., Reuben, J., Eds.; Plenum Press: New York, 1993; Vol. 13, pp 253-274.
- (166) Lubitz, W.; Feher, G., *Applied Magnetic Resonance* **1999**, *17*, 1-48.
- (167) Levanon, H.; Möbius, K., *Annual Review of Biophysics and Biomolecular Structure* **1997**, *26*, 495-540.
- (168) Burghaus, O.; Plato, M.; Rohrer, M.; Möbius, K.; MacMillan, F.; Lubitz, W., *J. Phys. Chem.* **1993**, *97*, 7639-7647.
- (169) Rohrer, M.; Plato, M.; MacMillan, F.; Grishin, Y.; Lubitz, W.; Möbius, K., *J. Magn. Reson.* **1995**, *116*, 59-66.
- (170) Zech, S. G.; Hofbauer, W.; Kamlowski, A.; Fromme, P.; Stehlik, D.; Lubitz, W.; Bittl, R., *J. Phys. Chem. B* **2000**, *104*, 9728-9739.
- (171) Van der Est, A.; Prisner, T.; Bittl, R.; Fromme, P.; Lubitz, W.; Möbius, K.; Stehlik, D., *J. Phys. Chem. B* **1997**, *101*, 1437-1443.
- (172) MacMillan, F.; Hanley, J.; van der Weerd, L.; Knüpling, M.; Un, S.; Rutherford, A. W., *Biochemistry* **1997**, *36*, 9297-9303.
- (173) Isaacson, R. A.; Lendzian, F.; Abresch, E. C.; Lubitz, W.; Feher, G., *Biophys. J.* **1995**, *69*, 311-322.
- (174) Kaupp, M., *Biochemistry* **2002**, *41*, 2895-2900.
- (175) Knüpling, M.; Törring, J. T.; Un, S., *Chem. Phys.* **1997**, *219*, 291-304.
- (176) Törring, J. T.; Un, S.; Knüpling, M.; Plato, M.; Möbius, K., *J. Chem. Phys.* **1997**, *107*, 3905-3913.
- (177) Teutloff, C.; Hofbauer, W.; Zech, S. G.; Stein, M.; Bittl, R.; Lubitz, W., *Applied Magnetic Resonance* **2001**, *21*, 363-379.
- (178) Neyman, K. M.; Ganyushin, D. I.; Rinkevicius, Z.; Rösch, N., *Int. J. Quantum Chem.* **2002**, *90*, 1404-1413.
- (179) Sieckman, I.; Van der Est, A.; Bottin, H.; Sétif, P.; Stehlik, D., *FEBS Lett.* **1991**, *284*, 98-102.
- (180) Van der Est, A.; Sieckmann, I.; Lubitz, W.; Stehlik, D., *Chem. Phys.* **1995**, *194*, 349-359.
- (181) Stowell, M. H. B.; McPhillips, T. M.; Rees, D. C.; Solitis, S. M.; Abresch, E.; Feher, G., *Science* **1997**, *276*, 812-816.
- (182) Jordan, P.; Fromme, P.; Witt, H. T.; Klukas, O.; Saenger, W.; Krauss, N., *Nature* **2001**, *411*, 909-917.

- (183) Deligiannakis, Y.; Rutherford, A. W., *Biochimica et Biophysica Acta, Bioenergetics* **2001**, 1507, 226-246.
- (184) Xu, W.; Chitnis, P.; Valieva, A.; van der Est, A.; Pushkar, Y. N.; Krzystyniak, M.; Teutloff, C.; Zech, S. G.; Bittl, R.; Stehlik, D.; Zybailov, B.; Shen, G.; Golbeck, J. H., *J. Biol. Chem.* **2003**, 278, 27864-27875.
- (185) Xu, W.; Chitnis Parag, R.; Valieva, A.; van der Est, A.; Brettel, K.; Guergova-Kuras, M.; Pushkar Yulia, N.; Zech Stephan, G.; Stehlik, D.; Shen, G.; Zybailov, B.; Golbeck John, H., *J. Biol. Chem.* **2003**, 278, 27876-27887.
- (186) Frisch, M. J.; Trucks, G. W.; Schlegel, H. B.; Scuseria, G. E.; Robb, M. A.; Cheeseman, J. R.; Zakryewski, V. G.; Montgomery, J. A.; Stratmann, R. E.; Burant, J. C.; Dapprich, S.; Millam, J. M.; Daniels, A. D.; Kudin, K. N.; Strain, M. C.; Farkas, O.; Tomasi, J.; Barone, V.; Cossi, M.; Cammi, R.; Mennucci, B.; Pomelli, C.; Adamo, C.; Clifford, S.; Ochterski, J.; Petersson, G. A.; Ayala, P. Y.; Cui, Q.; Morokuma, K.; Malick, D. K.; Rabuck, A. D.; Raghavachari, K.; Foresman, J. B.; Cioslowski, J.; Ortiz, J. V.; Baboul, A. G.; Stefanov, B. B.; Liu, G.; Liashenko, A.; Piskory, P.; Komaromi, I.; Gomperts, R.; Martin, R. L.; Fox, D. J.; Keith, T.; Al-Laham, M. A.; Peng, C. Y.; Nanayakkara, A.; Gonzalez, C.; Challacombe, M.; Gill, P. M.; Johnson, B.; Chen, W.; Wong, M. W.; Andres, J. L.; Head-Gordon, M.; Replogle, E. S.; Pople, J. A. *Gaussian 98, Revision A.7, A.9*, Gaussian, Inc.: Pittsburgh PA, 1998.
- (187) Bergner, A.; Dolg, M.; Küchle, W.; Stoll, H.; Preuss, H., *Mol. Phys.* **1993**, 80, 1431-1441, d-functions were taken from: *Gaussian Basis Sets for Molecular Calculations*; Huzinaga, S., Ed.; Elsevier: New York, 1984.
- (188) Godbout, N.; Salahub, D. R.; Andzelm, J.; Wimmer, E., *Can. J. Chem.* **1992**, 70, 560-571.
- (189) Burke, K.; Perdew, J. P.; Wang, Y., *Derivation of a Generalized Gradient Approximation: The PW91 Density Functional*; In *Electronic Density Functional Theory. Recent Progress and New Directions*; Dobson, J. F., Vignale, G., Das, M. P., Eds.; Plenum Press: New York, 1998.
- (190) Ciofini, I.; Reviakine, R.; Arbuznikov, A.; Kaupp, M., *Theor. Chem. Acc.* **2004**, 111, 132-140.
- (191) Similar results have also been obtained for most other main group radicals (see refs 45 and 106), and also in uncoupled DFT calculations of NMR chemical shifts for main group systems with multiple bonds (cf.: Bühl, M.; Kaupp, M.; Malkin, V. G.; Malkina, O. L., *J. Comput. Chem.* **1999**, 20, 91, and references therein). The overestimate of the most "paramagnetic" component of the tensors by uncoupled DFT calculations appears in all cases to be related to the fact that these large components tend to be dominated by one specific low-energy excitation in the second-order perturbation expression. As the corresponding energy denominator is underestimated by gradient-corrected functionals, the observed overestimation of the tensor component arises. As the "smaller" components are not so much dependent on one excitation but feature contributions from several couplings with larger energy denominator, they tend to be less sensitive to these deficiencies of the currently available functionals.
- (192) Nimz, O.; Lendzian, F.; Boullais, C.; Lubitz, W., *Applied Magnetic Resonance* **1998**, 14, 255-274.
- (193) Nonella, M., *Photosynthesis Research* **1998**, 55, 253-259.
- (194) Rigby, S. E.; Evans, M. C.; Heathcote, P., *Biochemistry* **1996**, 35, 6651-6656.

- (195) Kamlowski, A.; Altenberg-Greulich, B.; Van der Est, A.; Zech, S. G.; Bittl, R.; Fromme, P.; Lubitz, W.; Stehlik, D., *J. Phys. Chem. B* **1998**, *102*, 8278-8287.
- (196) *The Chemistry of the Quinonoid Compounds, Pt. I and II*, Patai, S., Ed.; Wiley, Interscience: New York, 1974.
- (197) *Function of Quinones in Energy Conserving Systems*, Trumpower, B. L., Ed.; Academic Press: New York, 1982.
- (198) Fisher, N.; Rich, P. R., *J. Mol. Biol.* **2000**, *296*, 1153-1162.
- (199) Prisner, T.; Rohrer, M.; MacMillan, F., *Annu. Rev. Phys. Chem.* **2001**, *52*, 279-313.
- (200) Zouni, A.; Witt, H. T.; Kern, J.; Fromme, P.; Krauss, N.; Saenger, W.; Orth, P., *Nature* **2001**, *409*, 739-743.
- (201) Ermler, U.; Fritsch, G.; Buchanan, S. K.; Michel, H., *Structure* **1994**, *2*, 925-936.
- (202) Zech, S. G.; van der Est, A. J.; Bittl, R., *Biochemistry* **1997**, *36*, 9774-9779.
- (203) Iwata, S.; Lee, J. W.; Okada, K.; Lee, J. K.; Iwata, M.; Rasmussen, B.; Link, T. A.; Ramaswamy, S.; Jap, B. K., *Science* **1998**, *281*, 64-71.
- (204) Xia, D.; Yu, C. A.; Kim, H.; Xia, J. Z.; Kachurin, A. M.; Zhang, L.; Yu, L.; Deisenhofer, J., *Science* **1997**, *277*, 60-66.
- (205) Hunte, C.; Koepke, J.; Lange, C.; Rossmann, T.; Michel, H., *Structure* **2000**, *8*, 669-684.
- (206) Iverson, T. M.; Luna-Chavez, C.; Cecchini, G.; Rees, D. C., *Science (Washington, D. C.)* **1999**, *284*, 1961-1966.
- (207) Li, R.; Bianchet, M. A.; Talalay, P.; Amzel, L. M., *Proc. Natl. Acad. Sci. U. S. A.* **1995**, *92*, 8846-8850.
- (208) Xia, Z.-X.; Dai, W.-W.; He, Y.-N.; White, S. A.; Mathews, F. S.; Davidson, V. L., *Journal of Biological Inorganic Chemistry* **2003**, *8*, 843-854.
- (209) Grimaldi, S.; Ostermann, T.; Weiden, N.; Mogi, T.; Miyoshi, H.; Ludwig, B.; Michel, H.; Prisner, T. F.; MacMillan, F., *Biochemistry* **2003**, *42*, 5632-5639.
- (210) Garcia-Horsman, J. A.; Barquera, B.; Rumbley, J.; Ma, J.; Gennis, R. B., *J. Bacteriol.* **1994**, *176*, 5587-5600.
- (211) Kranz, R. G.; Gennis, R. B., *J. Biol. Chem.* **1983**, *258*, 10614-10621.
- (212) Puustinen, A.; Finel, M.; Haltia, T.; Gennis, R. B.; Wikstrom, M., *Biochemistry* **1991**, *30*, 3936-3942.
- (213) Puustinen, A.; Wikstrom, M., *Proc. Natl. Acad. Sci. U. S. A.* **1991**, *88*, 6122-6126.
- (214) Puustinen, A.; Morgan, J. E.; Verkhovskii, M.; Thomas, J. W.; Gennis, R. B.; Wikstrom, M., *Biochemistry* **1992**, *31*, 10363-10369.
- (215) Sato-Watanabe, M.; Mogi, T.; Ogura, T.; Kitagawa, T.; Miyoshi, H.; Iwamura, H.; Anraku, Y., *J. Biol. Chem.* **1994**, *269*, 28908-28912.
- (216) Abramson, J.; Riistama, S.; Larsson, G.; Jasaitis, A.; Svensson-Ek, M.; Laakkonen, L.; Puustinen, A.; Iwata, S.; Wikstrom, M., *Nature structural biology* **2000**, *7*, 910-917.
- (217) Ingledew, W. J.; Ohnishi, T.; Salerno, J. C., *Eur. J. Biochem.* **1995**, *227*, 903-908.
- (218) Sato-Watanabe, M.; Itoh, S.; Mogi, T.; Matsuura, K.; Miyoshi, H.; Anraku, Y., *FEBS Lett.* **1995**, *374*, 265-269.
- (219) Veselov, A. V.; Osborne, J. P.; Gennis, R. B.; Scholes, C. P., *Biochemistry* **2000**, *39*, 3169-3175.
- (220) Hastings, S. F.; Heathcote, P.; Ingledew, W. J.; Rigby, S. E., *Eur. J. Biochem.* **2000**, *267*, 5638-5645.



- (221) Grimaldi, S.; MacMillan, F.; Ostermann, T.; Ludwig, B.; Michel, H.; Prisner, T., *Biochemistry* **2001**, *40*, 1037-1043.
- (222) Zandstra, P. J., *J. Chem. Phys.* **1964**, *41*, 3655-3656.
- (223) Hales, B. J., *J. Am. Chem. Soc.* **1975**, *97*, 5993-5997.
- (224) Himmo, F.; Babcock, G. T.; Eriksson, L. A., *J. Phys. Chem. A* **1999**, *103*, 3745-3749.
- (225) Grafton, A. K.; Wheeler, R. A., *J. Phys. Chem. A* **1997**, *101*, 7154-7166.
- (226) Boesch, S. E.; Wheeler, R. A., *J. Phys. Chem. A* **1997**, *101*, 5799-5804.
- (227) Wise, K. E.; Grafton, A. K.; Wheeler, R. A., *J. Phys. Chem. A* **1997**, *101*, 1160-1165.
- (228) Zhan, C.-G.; Chipman, D. M., *J. Phys. Chem. A* **1998**, *102*, 1230-1235.
- (229) Nonella, M., *J. Phys. Chem. B* **1998**, *102*, 4217-4225.
- (230) MacMillan, F.; Lendzian, F.; Lubitz, W., *Magn. Reson. Chem.* **1995**, *33*, 81-93.
- (231) Eichkorn, K.; Treutler, O.; Öhm, H.; Häser, M.; Ahlrichs, R., *Chem. Phys. Lett.* **1995**, *242*, 652-660.
- (232) Ahlrichs, R.; Bär, M.; Häser, M.; Horn, H.; Kölmel, C., *Chem. Phys. Lett.* **1989**, *162*, 165-169.
- (233) Ahlrichs, R.; von Arnim, M., *Chapter 13*; In *Methods and Techniques in Computational Chemistry*; Clementi, E., Corongiu, G., Eds.; Club European MOTTECC: 1995; pp 509.
- (234) Frisch, M. J.; Trucks, G. W.; Schlegel, H. B.; Scuseria, G. E.; Robb, M. A.; Cheeseman, J. R.; Montgomery, J. A., Jr., T. V.; Kudin, K. N.; Burant, J. C.; Millam, J. M.; Iyengar, S. S.; Tomasi, J.; Barone, V.; Mennucci, B.; Cossi, M.; Scalmani, G.; Rega, N.; Petersson, G. A.; Nakatsuji, H.; Hada, M.; Ehara, M.; Toyota, K.; Fukuda, R.; Hasegawa, J.; Ishida, M.; Nakajima, T.; Honda, Y.; Kitao, O.; Nakai, H.; Klene, M.; Li, X.; Knox, J. E.; Hratchian, H. P.; Cross, J. B.; Bakken, V.; Adamo, C.; Jaramillo, J.; Gomperts, R.; Stratmann, R. E.; Yazyev, O.; Austin, A. J.; Cammi, R.; Pomelli, C.; Ochterski, J. W.; Ayala, P. Y.; Morokuma, K.; Voth, G. A.; Salvador, P.; Dannenberg, J. J.; Zakrzewski, V. G.; Dapprich, S.; Daniels, A. D.; Strain, M. C.; Farkas, O.; Malick, D. K.; Rabuck, A. D.; Raghavachari, K.; Foresman, J. B.; Orti, J. V.; Cui, Q.; Baboul, A. G.; Clifford, S.; Cioslowski, J.; Stefanov, B. B.; Liu, G.; Liashenko, A.; Piskorz, P.; Komaromi, I.; Martin, R. L.; Fox, D. J.; Keith, T.; Al-Laham, M. A.; Peng, C. Y.; Nanayakkara, A.; Challacombe, M.; Gill, P. M. W.; Johnson, B.; Chen, W.; Wong, M. W.; Gonzalez, C.; Pople, J. A. *Gaussian 03*, Gaussian, Inc.: Wallingford CT, 2004.
- (235) Barone, V., In *Recent Advances in Density Functional Methods*; Chong, D. P., Ed.; World Scientific Publ. Co.: Singapore, 1996; Vol. Part I.
- (236) Hellwig, P.; Mogi, T.; Tomson, F. L.; Gennis, R. B.; Iwata, J.; Miyoshi, H.; Maentele, W., *Biochemistry* **1999**, *38*, 14683-14689.
- (237) Isaacson, R. A.; Abresch, E. C.; Lendzian, F.; Boullais, C.; Paddock, M. L.; Mioskowski, C.; Lubitz, W.; Feher, G., In *The reaction center of photosynthetic bacteria, structure and dynamics*; Michael-Beyerle, M.-E., Ed.; Springer-Verlag: Berlin, Germany, 1996; pp pp 353-367.
- (238) van den Brink, J. S.; Spoyalov, A. P.; Gast, P.; van Liemt, W. B. S.; Raap, J.; Lugtenburg, J.; Hoff, A. J., *FEBS Lett.* **1994**, *353*, 273-276.
- (239) Pushkar, Y. N.; Golbeck, J. H.; Stehlik, D.; Zimmermann, H., *J. Phys. Chem. B* **2004**, *108*, 9439-9448.

- (240) Pushkar, Y. N.; Ayzatulin, O.; Stehlik, D., *Applied Magnetic Resonance* **2005**, *28*, 195-211.
- (241) While the values given are simply averages over the data for the three different hydrogen atoms, a more complete averaging that rotates the methyl group in steps of  $10^\circ$  in a relaxed scan procedure (cf., e.g.: Mattar, S. M., *J. Phys. Chem. B* **2004**, *108*, 9449-9455) provided almost identical results in test calculations.
- (242) Rohrer, M.; MacMillan, F.; Prisner, T. F.; Gardiner, A. T.; Möbius, K.; Lubitz, W., *J. Phys. Chem. B* **1998**, *102*, 4648-4657.
- (243) MacMillan, F.; Teutloff, C.; Boullais, C.; Lubitz, W., *unpublished results*.
- (244) Teutloff, C.; Bittl, R.; Lubitz, W., *Applied Magnetic Resonance* **2004**, *26*, 5-21.
- (245) Pushkar, Y. N.; Stehlik, D.; van Gastel, M.; Lubitz, W., *J. Mol. Struct.* **2004**, *700*, 233-241.
- (246) O'Malley, P. J.; Babcock, G. T., *J. Am. Chem. Soc.* **1986**, *108*, 3995-4001.
- (247) Flores, M.; Isaacson, R. A.; Calvo, R.; Feher, G.; Lubitz, W., *Chem. Phys.* **2003**, *294*, 401-413.
- (248) Balzani, V.; Venturi, M.; Credi, A. *Molecular Devices and Machines: A Journey into the Nano World*; John Wiley & Sons: Chichester, UK, 2003; 500 pp.
- (249) Leigh David, A.; Wong Jenny, K. Y.; Dehez, F.; Zerbetto, F., *Nature* **2003**, *424*, 174-179.
- (250) Schalley, C. A.; Beizai, K.; Vögtle, F., *Acc. Chem. Res.* **2001**, *34*, 465-476.
- (251) Feringa, B. L., *Acc. Chem. Res.* **2001**, *34*, 504-513.
- (252) van Delden, R. A.; Hurenkamp, J. H.; Feringa, B. L., *Chemistry--A European Journal* **2003**, *9*, 2845-2853.
- (253) Kelly, T. R.; De Silva, H.; Silva, R. A., *Nature* **1999**, *401*, 150-152.
- (254) Kelly, T. R.; Silva, R. A.; De Silva, H.; Jasmin, S.; Zhao, Y., *J. Am. Chem. Soc.* **2000**, *122*, 6935-6949.
- (255) Kelly, T. R., *Acc. Chem. Res.* **2001**, *34*, 514-522.
- (256) Kim, H. G.; Lee, C.-W.; Yun, S.; Hong, B. H.; Kim, Y.-O.; Kim, D.; Ihm, H.; Lee, J. W.; Lee, E. C.; Tarakeshwar, P.; Park, S.-M.; Kim, K. S., *Organic Letters* **2002**, *4*, 3971-3974.
- (257) Weigend, F.; Häser, M., *Theor. Chem. Acc.* **1997**, *97*, 331-340.
- (258) Weigend, F.; Häser, M.; Patzelt, H.; Ahlrichs, R., *Chem. Phys. Lett.* **1998**, *294*, 143-152.
- (259) Schäfer, A.; Horn, H.; Ahlrichs, R., *J. Chem. Phys.* **1992**, *97*, 2571-2577.
- (260) Honda, Y.; Hada, M.; Ehara, M.; Nakatsuji, H., *J. Phys. Chem. A* **2002**, *106*, 3838-3849.
- (261) Mariam, Y. H.; Chantranupong, L., *Journal of Computer-Aided Molecular Design* **1997**, *11*, 345-356.
- (262) Mariam, Y. H.; Chantranupong, L., *THEOCHEM* **1998**, *454*, 237-258.
- (263) Stephens, P. J.; Devlin, F. J.; Chabalowski, C. F.; Frisch, M. J., *J. Phys. Chem.* **1994**, *98*, 11623-11627.
- (264) Schäfer, A.; Huber, C.; Ahlrichs, R., *J. Chem. Phys.* **1994**, *100*, 5829-5835.
- (265) Klamt, A.; Schüürmann, G., *Journal of the Chemical Society, Perkin Transactions 2* **1993**, *5*, 799-805.
- (266) Perdew, J. P., *Phys. Rev. B* **1986**, *34*, 7406.
- (267) Portmann, S.; Luthi, H. P., *Chimia* **2000**, *54*, 766-769.

- (268) Eichkorn, K.; Weigend, F.; Treutler, O.; Ahlrichs, R., *Theor. Chem. Acc.* **1997**, *97*, 119-124.
- (269) Yonezawa, T.; Kawamura, T.; Ushio, M.; Nakao, Y., *Bull. Chem. Soc. Jpn.* **1970**, *43*, 1022-1027.
- (270) Sinnokrot, M. O.; Valeev, E. F.; Sherrill, C. D., *J. Am. Chem. Soc.* **2002**, *124*, 10887-10893.
- (271) Tsuzuki, S.; Honda, K.; Uchimaru, T.; Mikami, M.; Tanabe, K., *J. Am. Chem. Soc.* **2002**, *124*, 104-112.
- (272) Tsuzuki, S.; Uchimaru, T.; Sugawara, K.-i.; Mikami, M., *J. Chem. Phys.* **2002**, *117*, 11216-11221.
- (273) Chipot, C.; Jaffe, R.; Maignet, B.; Pearlman, D. A.; Kollman, P. A., *J. Am. Chem. Soc.* **1996**, *118*, 11217-11224.
- (274) Braun, J.; Neusser, H. J.; Hobza, P., *J. Phys. Chem. A* **2003**, *107*, 3918-3924.
- (275) Stefov, V.; Pejov, L.; Soptrajanov, B., *J. Mol. Struct.* **2000**, *555*, 363-373.
- (276) Pejov, L., *Chem. Phys. Lett.* **2001**, *339*, 269-278.
- (277) Park, H.; Lee, S., *Chem. Phys. Lett.* **1999**, *301*, 487-492.
- (278) Hobza, P.; Riehn, C.; Weichert, A.; Brutschy, B., *Chem. Phys.* **2002**, *283*, 331-339.
- (279) Manojkumar, T. K.; Choi, H. S.; Tarakeshwar, P.; Kim, K. S., *J. Chem. Phys.* **2003**, *118*, 8681-8686.
- (280) Kim, K. S.; Suh, S. B.; Kim, J. C.; Hong, B. H.; Lee, E. C.; Yun, S.; Tarakeshwar, P.; Lee, J. Y.; Kim, Y.; Ihm, H.; Kim, H. G.; Lee, J. W.; Kim, J. K.; Lee, H. M.; Kim, D.; Cui, C.; Youn, S. J.; Chung, H. Y.; Choi, H. S.; Lee, C.-W.; Cho, S. J.; Jeong, S.; Cho, J.-H., *J. Am. Chem. Soc.* **2002**, *124*, 14268-14279.
- (281) Sjöberg, B.-M.; Reichard, P.; Gräslund, A.; Ehrenberg, A., *J. Biol. Chem.* **1977**, *252*, 536-541.
- (282) Sun, X.; Ollagnier, S.; Schmidt, P. P.; Atta, M.; Mulliez, E.; Lepape, L.; Eliasson, R.; Gräslund, A.; Fontecave, M.; Reichard, P.; Sjöberg, B.-M., *J. Biol. Chem.* **1996**, *271*, 6827-6831.
- (283) Young, P.; Andersson, J.; Sahlin, M.; Sjöberg, B.-M., *J. Biol. Chem.* **1996**, *271*, 20770-20775.
- (284) Mulliez, E.; Fontecave, M.; Gaillard, J.; Reichard, P., *J. Biol. Chem.* **1993**, *268*, 2296-2299.
- (285) Wagner, V. A. F.; Frey, M.; Neugebauer, F. A.; Schäfer, W.; Knappe, J., *Proc. Natl. Acad. Sci. U. S. A.* **1992**, *89*, 996-1000.
- (286) Krieger, C. J.; Roseboom, W.; Albracht, S. P. J.; Spormann, A. M., *J. Biol. Chem.* **2001**, *276*, 12924-12927.
- (287) Andrei, P. I.; Pierik, A. J.; Zauner, S.; Andrei-Selmer, L. C.; Selmer, T., *Eur. J. Biochem.* **2004**, *271*, 2225-2230.
- (288) Lehtio, L.; Gunter Grossmann, J.; Kokona, B.; Fairman, R.; Goldman, A., *J. Mol. Biol.* **2006**, *357*, 221-235.
- (289) Buis, J. M.; Broderick, J. B., *Arch. Biochem. Biophys.* **2005**, *433*, 288-296.
- (290) Selmer, T.; Andrei, P. I., *Eur. J. Biochem.* **2001**, *268*, 1363-1372.
- (291) Duboc-Toia, C.; Hassan, A. K.; Mulliez, E.; Ollagnier-de Choudens, S.; Fontecave, M.; Leutwein, C.; Heider, J., *J. Am. Chem. Soc.* **2003**, *125*, 38-39.
- (292) Carpenter, G. B.; Donohue, J., *J. Am. Chem. Soc.* **1950**, *72*, 2315-2328.
- (293) Saxebøl, G.; Melø, T. B.; Henriksen, T., *Radiat. Res.* **1972**, *51*, 31-44.
- (294) Miyagawa, I.; Kurita, Y.; Gordy, W., *J. Chem. Phys.* **1960**, *33*, 1599-1603.
- (295) Rega, N.; Cossi, M.; Barone, V., *J. Am. Chem. Soc.* **1997**, *119*, 12962-12967.

- (296) Himo, F.; Eriksson, L. A., *J. Chem. Soc., Perkin Trans. 2* **1998**, 305-308.
- (297) Krishnan, R.; Binkley, J. S.; Seeger, R.; Pople, J. A., *J. Chem. Phys.* **1980**, *72*, 650-654.
- (298) Clark, T.; Chandrasekhar, J.; Spitznagel, G. W.; Schleyer, P. v. R., *J. Comput. Chem.* **1983**, *4*, 294-301.
- (299) Gill, P. M. W.; Johnson, B. G.; Pople, J. A.; Frisch, M. J., *Chem. Phys. Lett.* **1992**, *197*, 499-505.
- (300) Frisch, M. J.; Pople, J. A.; Binkley, J. S., *J. Chem. Phys.* **1984**, *80*, 3265-3269.
- (301) Dunning, T. H., Jr., *J. Chem. Phys.* **1989**, *90*, 1007-1023.
- (302) Engström, M.; Vaara, J.; Schimmelpfennig, B.; Åagren, H., *J. Phys. Chem. B* **2002**, *106*, 12354-12360.
- (303) Patchkovskii, S.; Strong, R. T.; Pickard, C. J.; Un, S., *J. Chem. Phys.* **2005**, *122*, 214101-214109.
- (304) Chacko, V. P.; McDowell, C. A.; Singh, B. C., *J. Chem. Phys.* **1980**, *72*, 5228-5233.
- (305) Becker, A.; Fritz-Wolf, K.; Kabsch, W.; Knappe, J.; Schultz, S.; Volker Wagner, A. F., **1999**, *6*, 969-975.
- (306) Becker, A.; Kabsch, W., *J. Biol. Chem.* **2002**, *277*, 40036-40042.
- (307) Logan, D. T.; Andersson, J.; Sjöberg, B.-M.; Nordlund, P., *Science* **1999**, *283*, 1499-1504.
- (308) Owen, M. C.; Komaromi, I.; Murphy, R. F.; Lovas, S., *Journal of Molecular Structure: THEOCHEM* **2006**, *759*, 117-124.
- (309) Himo, F., *Chem. Phys. Lett.* **2000**, *328*, 270-276.
- (310) Himo, F.; Siegbahn, P. E. M., *Chemical Reviews (Washington, DC, United States)* **2003**, *103*, 2421-2456.
- (311) Amodeo, P.; Barone, V., *J. Am. Chem. Soc.* **1992**, *114*, 9085-9093.
- (312) Duboc-Toia, C., *Personal Communication*.

## ACKNOWLEDGMENTS

My first, and most earnest, acknowledgment goes to Martin Kaupp who has been a great supervisor. His ideas and support had a major influence on this thesis. I would like to thank him for introducing me to the subject and for guiding me through the research. I have learned a lot during this time and I am convinced that this knowledge will help me in the future.

Many thanks go to my colleagues for great time I had in our group. I enjoyed the atmosphere, the daily conversations, their friendship and their support. My thanks go to Sebastian Riedel, Christian Remenyi, Alexander Patrakov, James Asher, Roman Reviakine, Alexei Arbuznikov, Sandra Schinzel, Hilke Bahmann and Irina Malkin, as well as to our former group-member Michal Straka for great collaboration over the years. It was a pleasure to work with all these people and to benefit from their knowledge. Many thanks also to our neighbors, the group of Carsten Strohman, for contributing a lot to the great atmosphere of the fourth floor. A number of people have helped me in getting my manuscript to its final form, help for which I am very grateful.

This thesis has partly been supported by scholarship of the Graduate College “Magnetic Resonance” of the University of Stuttgart. This support is gratefully acknowledged.

I am also grateful to two people without whom I would never have come to Würzburg. Krzysztof Woliński, a professor at the University of Maria Curie-Skłodowska in Lublin, introduced me to the field of quantum chemistry and inspired my academic career. Tadeusz Andruniow, a friend, encouraged me to apply for the position here.

Last but not least, I am grateful to my parents and brother who have supported and believed in me over the years and all the friends who I have met along the way and who brightened my everyday life. Finally warm and special thanks go to Piotrek for putting up with me all that time.

Würzburg, 10 Juli 2006

Sylwia Kacprzak



# CURRICULUM VITAE

## PERSONAL DATA

---

Name: Mgr. Sylwia Małgorzata Kacprzak  
Date of birth: 3<sup>rd</sup> April 1977  
Place of birth: Puławy, Poland  
Family status: single, no children

## LOWER EDUCATION

---

09/1984-06/1992 A. Mickiewicz Primary School in Puławy, Poland  
09/1992-05/1996 A. J. Czartoryski High School in Puławy, Poland  
Leading subjects: Mathematics and Physics  
05/1996 Maturity examination (Abitur)

## UNIVERSITY EDUCATION

---

08/1996-07/2001 Chemistry Studies at the University of Maria Curie  
Sklódowska in Lublin, Poland  
08/2000-07/ 2001 Undergraduate research assistant at the University of  
Louisville, Louisville, KY, US with Dr. Paweł M.  
Kozłowski  
07/2001 Master of Science examination with Prof. Krzysztof  
Woliński  
Master of Science thesis:  
*„Theoretical Analysis of Shielding Tensors of CO  
Bound to Heme Group in Myoglobin and Hemoglobin”*  
08/2001-05/2002 Graduate research assistant at the University of  
Louisville, Louisville, KY, US with Dr. Paweł M.  
Kozłowski

## DOCTORAL EDUCATION

---

since 07/2002 Ph.D. student with Prof. Dr. M. Kaupp, Institute of  
Inorganic Chemistry, University of Würzburg,  
Würzburg, Germany.  
Ph.D. thesis:  
*„Investigations of the EPR Parameters of  
Bioradicals by Density Functional Methods“*

## LIST OF PUBLICATIONS

### LIST OF PUBLICATIONS INCLUDED IN THE THESIS

**Electronic g-Tensors of Semiquinones in Photosynthetic Reaction Centers. A Density Functional Study**, Kacprzak, S.; Kaupp, M., *J. Phys. Chem. B* **2004**, *108*, 2464-2469

**Protein-Cofactor Interactions and EPR Parameters for the Q<sub>H</sub> Quinone Binding Site of Quinol Oxidase. A Density Functional Study**, Kacprzak, S.; Kaupp, M.; MacMillan, F., *J. Am. Chem. Soc.* **2006**, *128*, 5659-5671

**Molecular Mechanical Devices Based on Quinone-Pyrrole and Quinone-Indole Dyads: A Computational Study**, Kacprzak, S.; Kaupp, M., *J. Phys. Chem. B* **2006**, *110*, 8158-8165.

**Understanding the EPR Parameters of Glycine-Derived Radicals. The Case of N-Acetylglycyl in the N-Acetylglycine Single-Crystal Environment**, Kacprzak, S.; Reviakine, R.; Kaupp, M., *J. Am. Chem. Soc.* **2006**, *submitted*

**Understanding the EPR Parameters of Protein-Bound Glycyl Radicals**, Kacprzak, S.; Reviakine, R.; Kaupp, M., *J. Am. Chem. Soc.* **2006**, *submitted*

### LIST OF OTHER PUBLICATIONS AND POSTERS

**Structure of the Nitrogen-Centered Radical Formed during Inactivation of E. coli Ribonucleotide Reductase by 2'-Azido-2'-deoxyuridine-5'-diphosphate: Trapping of the 3'-Ketonucleotide** Fritscher, J.; Artin, E.; Wnuk, S.; Bar, G.; Robblee, J. H.; Kacprzak, S.; Kaupp, M.; Griffin, R. G.; Bennati, M.; Stubbe, J., *J. Am. Chem. Soc.* **2005**, *127*, 7729-7738

**Calculation of g-Tensors for Bioradicals Using Density Functional Theory** Kacprzka, S., Kaupp, M. *European EPR Summer School*, Retie (Belgium), 2002, Poster



**Density Functional Theory Investigation of Electronic g-Tensor for Bioradicals**

Kacprzak, S., Kaupp, M., *40<sup>th</sup> Symposium for Theoretical Chemistry*, Suhl (Germany), 2004, Poster

**Density Functional Theory Investigation of EPR Parameters for Semiquinone**

**Radical Anions** Kacprzak, S., Kaupp, M. *1<sup>st</sup> Joint German/British Bioenergetics Conference “Mechanisms of Bioenergetic Membrane Proteins: Structures and Beyond”*, Wiesbaden (Germany), 2005, Poster

TALKS ON CONFERENCES

**Density Functional Theory Investigations of EPR Parameters of Glycyl**

**Radical. The Role of Intrinsic and Environmental Effects**, *Workshop of the Graduate College “Magnetic Resonance” of University of Stuttgart*, Hirschegg, Austria, 19-22 September 2005

Density Functional Studies of EPR Parameters for Semiquinone Radical Anions: from Biophysics to Materials, *X Stuttgarter Tag der Magnetischen Resonanz*, Stuttgart, Germany, 2005